

FACULDADE DE ENGENHARIA DA UNIVERSIDADE DO PORTO

Liquefaction resistance assessment of the TP-Lisbon sand in partially saturated conditions: Experimental evidence and physical modelling validation

Fausto Andrés Molina Gómez

U. PORTO

FEUP FACULDADE DE ENGENHARIA
UNIVERSIDADE DO PORTO

Thesis submitted to the Faculty of Engineering of the University of Porto
for obtaining the degree of Doctor in Civil Engineering

Supervisor: Prof. António Joaquim Pereira Viana da Fonseca

Advisor: Prof. Bernardo Caicedo Hormaza

Advisor: Dr. Cristiana Maria Fonseca Ferreira

November 22, 2023

**Liquefaction resistance assessment of the
TP-Lisbon sand in partially saturated
conditions: Experimental evidence and physical
modelling validation**

Fausto Andrés Molina Gómez

Thesis submitted to the Faculty of Engineering of the
University of Porto for obtaining the degree of Doctor in Civil
Engineering

November 22, 2023

Abstract

Earthquake-induced liquefaction is a phenomenon characterised by the loss of shear strength and stiffness of soils and is one of the more complex hazards of geotechnical engineering. This phenomenon typically occurs in loose and saturated sandy soil deposits during monotonic or cyclic loading. Earthquake-induced liquefaction is one of the most dramatic causes of damages and loss of functionality in buildings and infrastructures, as demonstrated in several case histories —Japan (2011), New Zealand (2010, 2011), Italy (2012, 2016) and Indonesia (2018). There are historical documents about earthquake-induced liquefaction in the greater Lisbon area after the 1755 earthquake. Such a catastrophic seismic event induced the generalised collapse of most buildings in the centre of Lisbon, including the King’s palace.

The damages caused by earthquake-induced liquefaction demand innovative alternatives to mitigate the effects caused by this phenomenon. Hence, in the last decades, relevant achievements in liquefaction mitigation have been developed by reducing pore pressure build-up and deformations in the ground surface. One of the most promising techniques for liquefaction mitigation is the induction of partial saturation (IPS). The mitigation techniques based on IPS have shown fruitful results in increasing the soil resistance against liquefaction. The suitability of IPS techniques for liquefaction mitigation is associated with the increment of fluid compressibility in partially saturated soils, which reduces the pore pressure build-up during seismic action.

This research aims to assess the liquefaction resistance and cyclic behaviour of sandy soils in partially saturated conditions to provide relevant insights about the mitigation by IPS of liquefaction effects. For this purpose, a detailed characterisation of an alluvial natural sand from the historical centre of Lisbon was carried out, namely TP-Lisbon sand. This soil was used as a case history due to the liquefaction reports after the 1755 earthquake. The characterisation allowed for the definition of the critical state parameters and wave propagation of TP-Lisbon. Besides, the liquefaction resistance in fully saturated conditions was assessed to obtain a reference for estimating the liquefaction resistance improvement by the partial saturation effects. Therefore, a novel approach combining experimental measurements of P-wave velocity and Biot’s theory was proposed to estimate the degree of saturation during element testing. On the other hand, a series of dynamic centrifuge tests were conducted to assess the site response of sandy soil deposits with different depths under

diverse degrees of saturation.

The liquefaction resistance improvement was analysed by a novel wave-based approach, which provides a reliable prediction of liquefaction resistance in partially saturated conditions. The suitability of IPS was attributed to the presence of occluded air bubbles in partially saturated soils, which significantly reduce the pore pressure build-up during cyclic loading. In addition, centrifuge test results indicated variations in the peak ground acceleration in free field with the change in degree of saturation, confirming the effects of induced partial saturation on the cyclic behaviour of TP-Lisbon sand, which can be replicated in the future for other sands.

Keywords: Liquefaction; Partial saturation; Mitigation; Laboratory tests; Wave propagation; Sands.

Resumo

A liquefação induzida por terremotos é um dos fenômenos mais complexos no campo da engenharia geotécnica devido à perda de resistência ao corte e rigidez dos solos. Esse fenômeno é comum em depósitos de solo arenoso solto e saturado durante carregamento monotônico ou cíclico. A liquefação induzida por terremotos é uma das causas mais dramáticas de perdas na funcionalidade de edifícios e infraestruturas, como demonstrado em diversos casos históricos —Japão (2011), Nova Zelândia (2010, 2011), Itália (2012, 2016) e Indonésia (2018). Existem documentos históricos sobre liquefação induzida por terremotos na região de Lisboa após o terremoto de 1755. Esse evento sísmico catastrófico causou o colapso generalizado do centro de Lisboa, incluindo grande parte dos edifícios e até mesmo o Palácio do Rei..

Os danos causados pela liquefação induzida por terremotos demandam alternativas inovadoras para mitigar os efeitos desse fenômeno. Portanto, nas últimas décadas, foram desenvolvidos avanços relevantes na mitigação da liquefação, visando reduzir o aumento de poro pressão e deformações na superfície do solo. Uma das técnicas mais promissoras para mitigação da liquefação é a indução de saturação parcial (ISP). As técnicas de mitigação baseadas em ISP têm mostrado resultados positivos no aumento da resistência do solo à liquefação. A adequação das técnicas ISP para a mitigação da liquefação está associada ao aumento da compressibilidade do fluido em solos parcialmente saturados, o que reduz a geração de poro pressão durante a ação sísmica.

Este trabalho de investigação tem como objetivo avaliar a resistência à liquefação e o comportamento cíclico de solos arenosos em condições parcialmente saturadas para fornecer informação relevante relativamente à mitigação dos efeitos da liquefação por meio da ISP. Para isso, foi realizada uma caracterização detalhada de uma areia aluvial natural proveniente do centro histórico de Lisboa, denominada areia TP-Lisbon. Esse solo foi escolhido como estudo de caso devido aos relatos de liquefação após o terremoto de 1755. A caracterização permitiu a definição dos parâmetros de estado crítico e propagação de ondas da areia TP-Lisbon. Além disso, a resistência à liquefação em condições totalmente saturadas foi avaliada para obter uma referência para estimar o aumento da resistência à liquefação devido aos efeitos da saturação parcial. Portanto, foi proposta uma abordagem inovadora que combina medições experimentais da velocidade de onda-P e a teoria de Biot para estimar o grau de saturação durante os ensaios elementares. Por outro lado, uma série de ensaios

dinâmicos de centrífugadora geotécnica foi realizada para avaliar a resposta do solo arenoso com várias profundidades e com diferentes graus de saturação.

O melhoramento da resistência do solo à liquefação foi analisada por meio de uma abordagem baseada em ondas, que fornece uma previsão confiável da resistência à liquefação em condições de saturação parcial. Os resultados experimentais confirmaram o aumento da resistência à liquefação pela indução de saturação parcial. A eficiência da ISP foi atribuída à presença de bolhas de ar dentro do fluido nos solos parcialmente saturados, o que reduz significativamente a geração de poro pressão durante o carregamento cíclico. Assim mesmo, os resultados na centrífugadora geotécnica indicaram variações na aceleração máxima do solo em campo livre com a mudança no grau de saturação, confirmando os efeitos da saturação parcial no comportamento cíclico da areia TP-Lisbon.

Palavras chave: Liquefação; saturação parcial; Mitigação; Ensaio de laboratório; Propagação de ondas; Areias.

Resumen

La licuación inducida por terremotos es uno de los riesgos más complejos de la ingeniería geotécnica debido a la pérdida de resistencia al corte y rigidez de los suelos. Este fenómeno es típico en depósitos de suelos arenosos sueltos y saturados durante cargas monótonas o cíclicas. La licuación inducida por terremotos es una de las causas más dramáticas de daños en construcciones e infraestructura, como se ha demostrado en varios casos históricos, como Japón (2011), Nueva Zelanda (2010, 2011), Italia (2012, 2016) e Indonesia (2018). Existen documentos históricos sobre la licuación inducida por terremotos en el área de Lisboa después del terremoto de 1755. Dicho evento sísmico catastrófico causó el colapso de varios edificios en el centro de Lisboa, incluyendo el palacio real del imperio.

Los daños causados por la licuación inducida por terremotos demandan alternativas innovadoras para mitigar los efectos de este fenómeno. Por lo tanto, en las últimas décadas, se han alcanzado logros relevantes en la mitigación de la licuación mediante la reducción del aumento de presión de poros y las deformaciones en la superficie del suelo. Una de las técnicas más prometedoras para la mitigación de la licuación es la inducción de la saturación parcial (IPS, por sus siglas en inglés). Las técnicas de mitigación basadas en IPS han mostrado resultados favorables en el aumento de la resistencia del suelo contra el aumento de la presión de poros. La implementación de las técnicas de la IPS para la mitigación de la licuación está asociada con el incremento de la compresibilidad del fluido en suelos parcialmente saturados, lo que reduce la acumulación de presión de poros durante la acción sísmica.

Esta investigación tiene como objetivo evaluar la resistencia a la licuación y el comportamiento cíclico de suelos arenosos en condiciones parcialmente saturadas para proporcionar información relevante sobre la mitigación de los efectos de la licuación mediante IPS. De esta manera, se realizó una caracterización detallada de una arena natural de origen aluvial proveniente del centro histórico de Lisboa, conocida como arena TP-Lisbon. Este suelo granular se utilizó como caso estudio, debido a los reportes históricos de licuación después del terremoto de 1755. La caracterización permitió definir los parámetros de estado crítico y la propagación de ondas en dicho suelo. Además, se evaluó la resistencia a la licuación en condiciones totalmente saturadas con el fin de obtener una referencia para estimar el incremento en la resistencia a la licuación debido a la disminución en el grado de saturación. Por lo tanto, se propuso un enfoque novedoso que combina resultados experimentales de la

velocidad de onda P y la teoría de Biot para estimar el grado de saturación durante los ensayos elementales. Por otro lado, se realizaron una serie de pruebas dinámicas en centrífuga geotécnica para evaluar la respuesta de sitio en depósitos de suelo arenosos superficiales bajo diferentes grados de saturación.

El aumento en la resistencia a la licuación se analizó mediante un enfoque novedoso basado en propagación de ondas, que proporciona una predicción confiable de la resistencia a la licuación en condiciones parcialmente saturadas. Los resultados experimentales confirmaron un aumento en la resistencia a la licuación mediante la inducción de la saturación parcial. La efectividad de la IPS se atribuyó a la presencia de burbujas de aire dentro del fluido en condiciones parcialmente saturadas, lo que reduce significativamente el aumento de presión de poros durante la carga cíclica. Además, los resultados de centrífuga geotécnica indicaron variaciones en la aceleración máxima del suelo en campo libre con el cambio en el grado de saturación, lo que valida los efectos de la inducción de saturación parcial en el comportamiento cíclico de la arena TP-Lisbon.

Palabras clave: Licuación; Saturación parcial; Mitigación; Ensayos de laboratorio; Propagación de ondas; Arenas.

Acknowledgements

This work has been possible thanks to the financial support of Portuguese Foundation for Science and Technology (Fundação para a Ciência e a Tecnologia – FCT) through the PhD Scholarship SFRH/BD/146265/2019, which is gratefully acknowledged. Additional resources were provided by CONSTRUCT – Institute of R&D in Structures and Construction, funded by the Portuguese national funds through the FCT/MCTES (PIDDAC), Portugal.

I am thankful for the support and assistance provided by many people during the development and completion of this work. I want to express my genuine gratitude to all of them for their invaluable contributions.

To Professor Viana da Fonseca, my supervisor and friend, whom I had the honour of being guided by him. His outstanding theoretical knowledge and practical experience have inspired me to be a vanguard engineer for the world. I have no words to express my gratefulness to received and supporting me all these years kindly, but more than this, thanks for his wonderful lessons and making me feel at home in Porto.

To Professor Bernardo Caicedo, my advisor, whom I was privileged to work with him. He is a remarkable person and engineer who has contributed extensively to the Colombian Geotechnics. I admire his practical solutions to any question or technical problem.

To Cristiana, my advisor. She always was available to review and discuss the research results and life with a coffee. Thanks for sharing your background with me and helping me become a better scientific writer. I appreciate your invitation to collaborate on the GEOLAB-CENLIMIT and InaWAVE projects.

To Professor Giovanni Cascante, from the University of Waterloo (Canada), whom I was privileged to show my work. Thank you for your generous contributions and feedback.

To Professors Giulia Viggiani and Stuart Haigh, from the University of Cambridge (United Kingdom), thanks for welcoming me to the Schofield Centre and sharing their experience in geotechnical centrifuge testing of liquefiable soils.

To Dr Sara Rios, from FEUP, who is an excellent example of good work, organisation and dedication.

Os resultados experimentais de qualidade não foram possíveis sem constante acompanhamento e generosidade da equipa do LabGEO. Por isso agradeço enormemente à Eng^a Daniela Coelho e ao Senhor Armando Pinto, dois profissionais incríveis dos quais estou a aprender sempre.

Também agradeço o apoio da Cláudia Pinto, da Paula Madeira e da Marta Poinhas nas questões e assuntos burocráticas do CONSTRUCT, do PRODEC e da Secção de Geotecnia, bem como a vossa simpatia e disponibilidade.

À Rita Rocha Lamas pelo apoio e motivação durante todo este tempo. Sempre estive disposta a dizer as palavras e conselhos certos. Isso e a tua confiança vou atesourar na vida toda.

A Davide, mi agradecimiento eterno por darme una mano amiga en momentos de crisis, permitiéndome trabajar con él. Estoy seguro que va a ser uno de los profesores que contribuirá enormemente al avance de la geotecnia en América.

Nesta fase conheci colegas e amigos do programa doutoral e do departamento de engenharia civil, Diana, Julieth, Rita, Diego, Joana, Pedro, Isabela, Claver, Rubens, Fabrizio, Catarina, Nelson, Candido e Rashid, à quem quero agradecer pela colaboração, as dicas e as risadas em muitos momentos.

Agradeço a Isabel e o Rui por terem-me acolhido na vossa casa durante todos estes anos.

A mi mamá y mi papá, por su excelente formación basada en amor, respeto y responsabilidad; sin los valores que me han inculcado desde niño, los logros de mi vida no hubiesen sido posibles.

A Sebas, gracias por ser parte esencial de mi vida siempre y su interés permanente por mi bienestar fuera de Colombia. Sus grandes capacidades e inteligencia me han inspirado en ser cada día mejor.

A Lenin, quién ha sido mi mejor amigo desde hace muchos años. Gracias por acompañar y motivar incondicionalmente esta etapa desde la distancia; pero, sobretudo por el ejemplo de calidad, sencillez, humildad y respeto.

Al Ing Javier Camacho, quien me motivó a ser geotecnista e iniciar una vida en Portugal. Gracias por el interés en conversar conmigo sobre aspectos técnicos o de investigación y preocupación constante por mi día a día en Portugal.

A Angélica por su amistad sincera y longeva; también, por motivarme durante muchos años a perseguir y cumplir mis sueños.

A las personas de la Universidad de los Andes, mi otra alma máter: Julieth, por compartir su destacada experiencia en el desarrollo de equipos y ayudarme incondicionalmente en los ensayos; a Jose Naranjo, por su constante disponibilidad y anécdotas graciosas; a mis Geoamigos, María Juliana y Juan Pablo, me acompañaron y brindaron su hospitalidad durante mi visita en la Universidad. Les agradezco por acogerme cálidamente en UniAndes.

A todos mis amigos, amigas y colegas, que son muchos, pero quiero mencionar a: Diani, Don Eduardo, Juan Carlos, Mónica, Juancho, Peppe, Carol, Ana Milena, Suli, Cristhian, Juan Camilo, Laura y Óscar.

¡Gracias totales!

*“Learn from yesterday, live for today, hope for tomorrow.
The important thing is not to stop questioning.”*

Albert Einstein

Contents

Abstract	i
Resumo	iii
Resumen	v
Acknowledgements	vii
1 Introduction	1
1.1 Context and research motivation	1
1.2 Research objectives	3
1.2.1 General objective	3
1.2.2 Specific objectives	3
1.3 Thesis structure	4
2 Perspectives of the effects of degree of saturation on soil liquefaction	7
2.1 Outline	7
2.2 Features of soil liquefaction	8
2.2.1 Mechanisms of soil liquefaction	8
2.2.2 Earthquake-induced liquefaction damages	13
2.2.3 Assessment and interpretation of liquefaction resistance	18
2.3 Saturation in soils and its measurements	32
2.3.1 States of saturation in soils	32
2.3.2 Experimental procedures to measure the degree of saturation in soils	34
2.4 Techniques for liquefaction mitigation	40
2.4.1 Conventional techniques for liquefaction mitigation	40
2.4.2 Techniques to induce partial saturation for liquefaction miti- gation	45
2.4.3 Applicability and performance of IPS techniques for liquefac- tion mitigation	54
2.5 Remarks	57
3 Materials, devices and experimental procedures	59
3.1 Outline	59

3.2	Studied soil	60
3.2.1	Geological setting of Terreiro do Paço site	60
3.2.2	Piezocone penetration tests and soil sampling	64
3.3	Testing devices	66
3.3.1	Bender elements	66
3.3.2	Triaxial apparatuses	71
3.3.3	Simple shear apparatus	76
3.3.4	Resonant-column and cyclic shear torsional apparatus	77
3.3.5	Geotechnical centrifuge apparatus	79
3.4	Experimental procedures	84
3.4.1	Specimen preparation	84
3.4.2	Element testing	85
3.4.3	Site response by centrifuge testing	86
3.5	Final considerations	87
4	Characterisation of the geomechanical properties of TP-Lisbon sand	89
4.1	Outline	89
4.2	Intrinsic properties	90
4.3	Compressibility	93
4.4	Stress-strain behaviour and critical state	98
4.5	Effects of particle shape and packing on critical state parameters	103
4.6	Stress–dilatancy assessment	105
4.7	Dynamic behaviour of TP-Lisbon sand	110
4.7.1	Shear modulus and damping curves	110
4.7.2	Stress and state dependency of wave propagation	119
4.8	Key findings	124
5	Liquefaction resistance of TP-Lisbon sand – fully saturated conditions	127
5.1	Outline	127
5.2	Liquefaction susceptibility from in situ testing	128
5.3	Liquefaction resistance assessment by advanced laboratory testing	131
5.4	Interpretation of liquefaction resistance within the CSSM framework	139
5.5	Key findings	142
6	Improvement of liquefaction resistance by induced partial saturation	145
6.1	Outline	145
6.2	Assessment of degree of saturation by a novel wave-based approach	146
6.2.1	Experimental procedure for monitoring the degree of saturation	146
6.2.2	Interpretation of wave signals	150
6.2.3	Analysis of elastic waves evolution in fluid saturated granular media	154
6.3	Liquefaction resistance assessment in partially saturated conditions	156
6.4	Analysis of liquefaction resistance improvement by wave-based approaches	165
6.5	Key findings	173

7	Site response of TP-Lisbon sand for different S_r by centrifuge testing	175
7.1	Outline	175
7.2	Features of site response in partially saturated sands	176
7.3	Experimental procedures	177
7.3.1	Centrifuge testing	177
7.3.2	Saturation and induction of partial saturation	180
7.4	Evaluation of stress-strain behaviour	182
7.5	Site response analysis	190
7.6	Volumetric strains	194
7.7	Key findings	196
8	Conclusions and further research	199
8.1	Concluding remarks	199
8.2	Further works	201
	References	205

List of Figures

2.1	Criteria of liquefaction susceptibility	9
2.2	Grain size boundaries proposed by Tsuchida (1970) to define liquefaction susceptibility	11
2.3	Illustration to define the state parameter, ψ	12
2.4	Liquefaction-induced damages illustration –tilt of building after 1964 Niigata earthquake (Kramer, 1996)	15
2.5	Effects of soil liquefaction in recent case histories: a) differential settlement of a house – Maule, Chile, 2010 (Bertalot et al., 2013); b) settlement and tilt of a store – Tokyo, Japan, 2011 (Ishihara, 2012); c) offset between an undamaged building and surrounding ground settlement – Urayasu, Japan, 2011 (Ishihara, 2012); d) car stuck in boiled mud and soil– Urayasu, Japan, 2011 (Yasuda et al., 2013); d) rutting pavement due to liquefaction– Urayasu, Japan, 2011 (Yasuda et al., 2013); f) spreading of sand over the road – Urayasu, 2011, Japan (Ishihara, 2012); g) sand boils – Benavente, 1909, Portugal (Teves-Costa et al., 2001); h) spreading of sand over the field – Itako, 1971, Japan (Ishihara, 2012), i) sandy soils transported hydraulically after liquefaction – Urayasu, 1971, Japan (Ishihara, 2012)	16
2.6	Soil response during cyclic element testing —based on experimental data: a) cyclic loading; b) evolution of shear strain; c) pore pressure build-up	19
2.7	Schematic of LRC from experimental data	21
2.8	Evolution of r_u evolution as a function of N/N_L (dashed lines denote the boundaries recommended by Booker et al., 1976)	23
2.9	Schematic representation of energy definitions and computation	24
2.10	Numerical integration to compute the energy during cyclic loading	25
2.11	Graphical illustration of PEC estimation (adapted from Green et al. 2000)	27
2.12	General law of normalised effective stress against the normalised volumetric strain of partially saturated soils subjected to cyclic loading (adapted from Mele and Flora 2019)	30
2.13	State of saturation in soil deposits (adapted from Zeybek and Madabhushi 2020)	33

2.14	Gas distribution in different soil states: a) unsaturated condition; b) partially saturated condition	33
2.15	Evolution of V_p in soils near the full saturation conditions (after Santamarina et al. 2005): a) effect of ν ; b) effect of n	38
2.16	Relationship between V_p and B -value (adapted from Yang 2002)	39
2.17	Influence of degree of saturation on the liquefaction resistance: a) Ottawa sand (after Sherif et al. 1977); b) Toyoura sand (after Yoshimi et al. 1989); c) Niigata sand (after Ishihara et al. 1998); d) Toyoura sand (after Tsukamoto et al. 2002	46
2.18	Normalised cyclic ratio for different sands (data from: Sherif et al. 1977; Yoshimi et al. 1989; Ishihara et al. 1998; Tsukamoto et al. 2002)	47
2.19	Potential volumetric strain vs liquefaction resistance ratio (adapted from Okamura and Soga 2006)	48
2.20	Schematic illustration of the air injection technique	51
2.21	Digital image of desaturated Ottawa sand using the drainage-recharge technique (Eseller-Bayat et al., 2013)	52
2.22	Reduction of nitrites and nitrates (Rebata-Landa and Santamarina, 2012)	53
2.23	S_r variation in time by microbial induced partial saturation for two temperatures (adapted from Mousavi and Ghayoomi 2021)	55
2.24	Relation between relative electrical conductivity and degree of saturation based on Archie's theory (adapted from Consentini and Foti 2014)	56
3.1	Illustrations of Terreiro do Paço site —images provided by the Lisbon Museum to Fundação Luso-Americana (2005): a) before 1755 earthquake; b) before 1755 earthquake	61
3.2	Lithological profile of Terreiro do Paço site (adapted from Salgado 2009, 2019)	63
3.3	Plan view and CPTu locations at Terreiro do Paço site	65
3.4	Profiles of primary CPTu data: a) cone tip resistance; b) sleeve friction c) pore-water pressure generated during the cone penetration	66
3.5	SBT and I_c simplified soil profiles: a) CPTu12; b) CPTu18; c) CPTu19	67
3.6	Integral samples of TP-Lisbon sand: a) collected soil; b) relative density profile at SI18; c) state parameter profile at SI18	68
3.7	Photograph of BE: a) Simple shear device; b) base cap of a triaxial cell	69
3.8	Schematic view of the Bender Element testing	69
3.9	Bender elements setup	70
3.10	Interpretation of BE test by the first arrival time method	71
3.11	Oversized lubricated end platens for triaxial tests (after Viana da Fonseca et al. 2021): a) photo with the implemented configuration; b) lateral view scheme	72
3.12	Embedded top-cap loading ram connection (after Viana da Fonseca et al. 2021): a) parts and scheme; b) implementation in the triaxial apparatus	72
3.13	Bishop-Wesley triaxial apparatus for stress-path testing of LabGEO	73

3.14	Cyclic triaxial apparatus of LabGEO	74
3.15	Local instrumentation by Hall-Effect transducers	75
3.16	Validation of Hall-Effect measurements: a) ε_v variation as a function of p'_0 ; b) Comparison between Hall-Effects and automatic volume gauge	76
3.17	Simple shear apparatus of LabGEO	77
3.18	Resonant column apparatus at Universidad Militar Nueva Granada	78
3.19	Mini geotechnical centrifuge at UniAndes	80
3.20	Scheme of the laminar box (Jara et al., 2020)	82
3.21	Instrumentation of micro shaking table and laminar box	83
3.22	Soil container equipped with Bender Elements	83
3.23	Schematic representation of the methods used for sampling remoulding: a) Dry Pluviation; b) Moist tamping	85
4.1	Grain size distributions: a) measurements at each meter; b) comparison against liquefaction boundaries	90
4.2	Particles of TP-Lisbon sand: a) Photograph of the particles taken with an optical microscope; b) Binary image of some selected particles	92
4.3	Graphical definitions of particle shape parameters: a) convexity, b) circularity; c) sphericity; d) roundness	93
4.4	Example of the analysis of particle shape –particle 1 of Figure 4.2: a) Diameter sphericity, b) width to length ratio sphericity; c) identification of particle corners; d) circle corner fitting of the particle	94
4.5	One-dimensional compression behaviour of TP-Lisbon sand	95
4.6	Isotropic consolidation of TP-Lisbon sand	97
4.7	Triaxial test results on TP-Lisbon sand: a) stress-strain behaviour in drained tests; b) stress-strain behaviour in undrained tests; c) change of volumetric strain in drained tests; d) pore-pressure change in undrained tests	101
4.8	Stress path and CSL on $q : p'$ invariant space: a) drained stress behaviour; b) undrained stress behaviour	102
4.9	Interpreted CSL with the inferred 1D-NCL for TP-Lisbon sand on $e : \log p'$ invariant space	103
4.10	Comparison of TP-Lisbon against other sands with similar intrinsic properties: a) GSD; b) CSL	104
4.11	Relationships between packing with critical state parameters: a) ϕ_{cs} vs. e_{max} ; b) ϕ_{cs} vs. e_{min} ; c) ϕ_{cs} vs. $e_{max} - e_{min}$; d) Γ vs. e_{max} ; e) Γ vs. e_{min} ; f) Γ vs. $e_{max} - e_{min}$; g) λ vs. e_{max} ; h) λ vs. e_{min} ; i) λ vs. $e_{max} - e_{min}$	106
4.12	Relationships between particle shape properties with critical state parameters: a) ϕ_{cs} vs. R ; b) ϕ_{cs} vs. S ; c) ϕ_{cs} vs. ρ ; d) Γ vs. R ; e) Γ vs. S ; f) Γ vs. ρ ; g) λ vs. R ; h) λ vs. S ; i) λ vs. ρ	107
4.13	Stress ratio relationships: a) stress ratio behaviour; b) dilation rate for drained tests; c) stress ratio plotted against the normalised pore pressure change for undrained tests	108
4.14	Peak stress ratio and maximum stress-dilatancy of TP-Lisbon sand	109

4.15	Maximum stress-dilatancy and state parameter relationship for TP-Lisbon sand	110
4.16	Typical results of transfer function computation (test in dry specimen at 100 kPa and 2 mV): a) magnitude; b) phase	112
4.17	Evolution of small-strain stiffness: a) shear modulus in dry conditions; b) damping in dry conditions; c) shear modulus in saturated conditions; d) damping in saturated conditions	113
4.18	Stiffness degradation curves: a) dry conditions; b) saturated conditions	114
4.19	Cyclic threshold as a function of the stress-state: a) dry conditions; b) saturated conditions	115
4.20	Normalised design curves and its comparison against the bounds proposed by Santos and Gomes Correia (2001) and Oztoprak and Bolton (2013): a) experimental data of TP; b) curve fitting of TP	116
4.21	Damping ratio of TP-Lisbon sand: a) dry conditions; b) saturated conditions	117
4.22	Normalised model of damping ratio in function of stiffness degradation.	118
4.23	Typical time-domain signals of BE: a) P-wave propagation in a dry sample; b) S-wave propagation in a saturated sample.	120
4.24	Stress-dependency of seismic wave velocities for TP-Lisbon sand.	121
4.25	Normalised shear modulus for TP-Lisbon sand	123
4.26	Relationships between particle shape properties with normalised small-strain stiffness parameters: a) Parameter C ; b) Exponent n	124
5.1	Liquefaction susceptibility based on in situ tests: a) CPTu12; b) CPTu18; c) CPTu19	130
5.2	Severity damage based on LPI and LSN from CPTu results	130
5.3	Typical results of cyclic triaxial testing ($p'_0 = 50$ kPa and $Dr = 30\%$)	133
5.4	Typical results of cyclic direct simple shear testing ($\sigma'_{v0} = 50$ kPa and $Dr = 50\%$)	135
5.5	Liquefaction resistance curves of TP-Lisbon sand: a) CTx test results; b) CDSS test results	136
5.6	Cyclic behaviour of TP-Lisbon sand compared against other liquefiable sands: a) CTx tests; b) CDSS tests	137
5.7	Liquefaction resistance curve of transformed for CTx loading ($p'_0 = 50$ kPa or $\sigma'_{v0} = 80$ kPa and $Dr = 50\%$)	139
5.8	Relation between ψ and CRR_{15} (database from: Jefferies and Been 2015)	141
6.1	Schematic representation of P-wave propagation in porous fluid saturated media (Astuto et al., 2023)	147
6.2	Void ratio changes inferred by Hall-Effects readings during saturation process: a) typical measurements (soil specimen with $Dr = 30\%$); b) variation of void ratio change during saturation phases, i.e. 0 (specimen assembling), 1st (carbon dioxide), 2nd water flusing and 3rd pressures increment	149

6.3	Interpretation of typical signals: a) P-wave analysis in the time-domain; a) P-wave analysis in the frequency-domain; c) S-wave analysis in the time-domain; d) S-wave analysis in the frequency-domain	151
6.4	P-wave propagation in water	152
6.5	P-wave propagation for different degrees of saturation —BE tests carried out for $Dr = 30\%$ and using 40 kHz input frequency	153
6.6	Relationship between B -value and V_P	154
6.7	Volumetric strains reported during B -value measurements	155
6.8	P-wave propagation for different degrees of saturation.	156
6.9	Soil-water characteristic curve of TP-Lisbon sand: a) $Dr = 30\%$; b) $Dr = 50\%$	158
6.10	Typical signals of wave propagation ($p' = 50$ kPa and $Dr \approx 30\%$): a) P-wave for $Sr = 100\%$; b) S-wave for $Sr = 100\%$; c) P-wave for $Sr = 96\%$; d) S-wave for $Sr = 96\%$; e) P-wave for $Sr = 91\%$; f) S-wave for $Sr = 91\%$	160
6.11	Relationship between degree of saturation and wave velocities: a) tests with $Dr \pm 30\%$; b) tests with $Dr \pm 50\%$	161
6.12	Cyclic behaviour for different degrees of saturation —typical CTx results for $Dr \pm 30\%$: a) $Sr = 100\%$; b) a) $Sr = 96\%$; c) $Sr = 91\%$	162
6.13	Liquefaction resistance curves for different Sr : a) test results under $Dr \pm 30\%$; b) test results under $Dr \pm 50\%$	163
6.14	Relationships between intercept coefficient and degree of saturation	164
6.15	$CSR_{CTx} : V_{s1}$ relationship for different Sr : a) test results under $Dr \pm 30\%$; b) test results under $Dr \pm 50\%$	167
6.16	Liquefaction resistance ratio as a function of V_P for different Sr in TP-Lisbon sand: a) test results under $Dr \pm 30\%$; b) test results under $Dr \pm 50\%$	169
6.17	Normalised cyclic strength ratio as a function of V_P	170
6.18	$LRR_{20} : V_P$ relationship for different liquefiable soils: a) TP-Lisbon sand $-Dr = 30\%$; b) TP-Lisbon sand $-Dr = 50\%$; c) Koshigaya sand; d) Niigata sand; e) Toyoura sand $-Dr = 40\%$; f) Toyoura sand $-Dr = 70\%$	172
7.1	Centrifuge testing in-flight setup: a) Micro shaking table; b) Container with piezoelectric transducers; c) Oscilloscope, Function generator and Amplifier	179
7.2	Illustration of saturation process in the geotechnical centrifuge	180
7.3	Illustration of the induced partial saturation process in the geotechnical centrifuge by soil desaturation	181
7.4	Results of the degree of saturation after induced partial saturation compared against the soil water characteristic curve	182
7.5	Variation of V_P as a function of Sr	183
7.6	Vibration modes of the laminar box — results of a dry sample tested at 30 g: a) 50 Hz (before resonance); b) 100 Hz (resonance); c) 200 Hz (after resonance)	186

7.7	Stress-strain loops for different frequencies —results of a dry sample tested at 30 g	187
7.8	Relation of CSR failure and state parameter for different effective centrifuge accelerations under fully saturated conditions	188
7.9	Stiffness degradation curves; comparison between C-ST tests against other testing methods and hyperbolic fitting by Ishibashi and Zhang (1993) for dry conditions and 30 kPa confinement	189
7.10	Example of amplification factor estimating —results of a sample with 87% degree of saturation and tested under 60g	191
7.11	Frequency-dependent of AF for various Sr : a) results under 30g; b) results under 60g; c) results under 80g	192
7.12	Site response analysis: a) maximum AF vs. depth; b) maximum AF vs. Sr ; c) f_R vs. depth; d) f_R vs. Sr	193
7.13	Typical measurements of surface settlements —results of a sample with 87% degree of saturation tested under 60 g and 500 Hz loading frequency	194
7.14	Frequency-dependent volumetric strain variation for various effective centrifuge accelerations: a) $Sr = 0\%$; b) $Sr = 71\%$; c) $Sr = 87\%$; d) $Sr = 100\%$	195

List of Tables

2.1	Recent liquefaction case histories (adapted from Geyin and Maurer 2020)	10
2.2	Summary of recently case history earthquake-induced liquefaction (NASEM, 2016)	17
2.3	CSR for different cyclic element testing	20
2.4	Reported logarithmic energy-based models for liquefaction assessment (adapted from Alavi and Gandomi 2012)	28
2.5	Summary of experimental studies on the V_p and B -value relationship	40
2.6	Factors influencing the applicability of mitigation techniques (adapted from Meslem et al. 2019)	42
2.7	Timeline of recent advances on the characterisation of soil liquefaction (Ishihara, 1993, 1996 ; Kramer, 1996 ; Towhata, 2008 ; Boulanger and Idriss, 2014 ; Towhata, 2021)	44
2.8	Principles of liquefaction mitigation (Towhata, 2021)	45
2.9	Studies on the liquefaction resistance of partially saturated sands	49
3.1	Seismic parameters for a return period of 475 years in the Lisbon area (CEN, 2010)	62
4.1	Physical properties of TP-Lisbon sand	91
4.2	Shape parameters of TP-Lisbon sand	94
4.3	Compressibility parameters	96
4.4	Details of the triaxial tests for critical state assessment	99
4.5	Fitting parameters of stress-dependency of seismic wave velocities	121
5.1	Values for estimating the relationship between ψ and CRR_{15}	140
6.1	Parameters defining the soil water characteristic curve of TP-Lisbon for different relative densities	159
6.2	Summary of average CTx and BE test results	164
6.3	Best fitting between intercept coefficient and degree of saturations	164
7.1	Scaling factors for centrifuge modelling (Taylor, 1995 ; Madabhushi, 2014)	178
7.2	Depth similitude of sandy soil deposit between prototype and model	190

Abbreviations and symbols

List of acronyms

1D-NCL	One dimensional normal consolidation line
AF	Amplitude factor
ASTM	American Society for Testing and Materials
B-value	Pore-pressure coefficient B
BE	Bender elements
BP	Back pressure during shear
CDSS	Cyclic direct simple shear
CEN	European Committee for Standardization
CONSTRUCT	Institute of Research and Development in Structures and Construction
CP	Cell pressure
CPT	Cone penetration test
CPT _u	Piezocone penetration test
CRR	Cycle resistance ratio
CRR ₁₅	Cycle resistance ratio for 15 cycles
CS	Critical state
CSCM	Critical state soil mechanics
CSL	Critical state line
CSR	Cycle stress ratio
CSR _{C_r}	Corrected cycle stress ratio
CSR _{CTx}	Cyclic stress ratio of triaxial test
CSR _{M_{7.5}}	Cyclic stress ratio for a 7.5 earthquake magnitude
CSR _{part}	Cyclic stress ratio in partially saturated conditions
CSR _{sat}	Cyclic stress ratio in fully saturated conditions
CSR _{SS}	Cyclic stress ratio of simple shear test
CSSM	Critical state soil mechanics
CTx	Cyclic triaxial test
D	Drain triaxial test condition
DA	Double strain amplitude
DEM	Discrete element methods
DMT	Dilatometer Marchetti test
EOTSF	End-of-test soil freezing
FFT	Fast Fourier transformation
FLAC	Fast Lagrangian analysis of continua
FS _{liq}	Factor of safety against liquefaction
GDS	Grain- size distribution
ICL	Intrinsic consolidation line
INEGI	Institute of Science and Innovation in Mechanical and Industrial Engineering

IPS	Introduced partial saturation
ISO	International Organization for Standardization
JGS	Japanese Geotechnical Society
LabGeo	Geotechnical Laboratory of Faculty of Engineering of University of Porto
LCL	Limiting compression line
LCR	Liquefaction curve resistance
LEP	Lubricate end platen
LIQ2PROEARTH	Liquefaction Assessment Protocols to Protect Critical Infrastructures against Earthquake Damage
LPI	Liquefaction potential index
LRC	Liquefaction resistance curve
LRC _{Cr}	Corrected liquefaction resistance curve
LRR	Liquefaction resistance ratio
LRR ₂₀	Liquefaction resistance ratio for 20 cycles
LSFD sand	Lower San Fernando Dam sand
LSN	Liquefaction severity number
LVDT	Linear vertical displacement transducer
MT	Moist Tamping
NB sand	New Brunswick sand
NCR	Normalised cyclic resistance
NSAEM	National Academies of Sciences, Engineering, and Medicine
P-wave	Primary or pressure wave
PEC	Pseudo-energy capacity
PGAB	Peak ground acceleration at the bedrock
PGAGS	Peak ground acceleration at the ground surface
PPA	Pressure plate apparatus
PRODEC	Programa doutoral em Engenharia Civil / Doctoral Program in Civil Engineering
P _v	Air pluviation
RC	Resonant column
S-wave	Secondary or shear wave
SAGI	Shape-angularity group indicator
SBT	Soil behaviour type
SDOF	Single-degree of freedom model
SGI	Swedish Geotechnical Institute
SPM	Suction plates method
SPT	Standard penetration test
SS	Simple shear
SWCC	Soil-water characteristic curve
TP	Terreiro do Paço
U	Undrain triaxial test condition
UMNG	Universidad Militar Nueva Granada
UniAndes	Universidad de los Andes
UP	Universidade do Porto / Porto University
USCS	Unified soil classification system
USR	Undrained shear resistance

List of symbols for physical properties and mathematical operators

$(A + B)$	Area of the particle when any convexity inside its perimeter are filled
$ H_{\theta T} $	Absolute value of the rotation-torque ratio
A/A_p	Area of particle
a_g	Design ground acceleration (m/s^2)
a_{gR}	Peak ground acceleration (m/s^2)
a_{\max}	Peak horizontal acceleration on the ground surface (m/s^2)
C	Material coefficient
Cc	Compression index
Ce	Ex
C_i	Circularity
Cr	Recompression index
c_r	Correction coefficient
C_u	Coefficient of uniformity
C_x	Coefficient of convexity
C_z	Coefficient of curvature
D	Diameter of particle (mm)
d	Dilatancy
D	Mass density
D_{50}	Mean diameter particle size (mm)
d_{\min}	Maximum dilatancy rate
Dr	Relative density (%)
e	Void ratio
e_0	Initial void ration
e_{cs}	Void ratio at critical state
e_f	Void ratio after test
e_{\max}	Maximum void rate
e_{\min}	Minimum void rate
F	Frequency (Hz)
$F(e)$	Void ratio function
FC	Fine content (%)
f_s	Sleeve friction (kPa)
g	Gravity (m/s^2)
G	Shear modulus (MPa)
G_0	Maximum shear modulus (MPa)
G_s	Specific gravity of solid particle
G_{soil}	Shear modulus of the soil (MPa)
h	Specimen hight (mm)
IC	Soil behaviour type index
J	Rotation mass inertia
J_a	Active rotation mass inertia
K_0	At-rest earth pressure coefficient
K_a	Bulk modulus of air (kPa)
K_{CO_2}	Bulk modulus of carbon dioxide (kPa)
K_f	Bulk modulus of pore fluid (kPa)
K_g	Bulk modulus of grain (kPa)
K_{sk}	Bulk modulus of soil skeleton (kPa)
K_{soil}	Bulk modulus of the soil (kPa)
K_{sus}	Bulk modulus of fluid and solid particle (kPa)
K_w	Bulk modulus of water (kPa)
LL	Liquid limit
L_{tt}	Travel length wave from tip-to-tip of BE
M	Critical friction ratio

M_W	Earthquake magnitude (Richter)
N	Multiply of Earth gravity or centrifuge scale factor
n	Porosity of soil skeleton
N_L	Number of cycles of liquefaction onset
p'	Mean effective stress (kPa)
p'_0	Initial mean effective stress (kPa)
p'_{cs}	Mean effective stress at critical state (kPa)
P_a	Atmospheric pressure
PI	Plasticity index
P_p	Perimeter of particle
q	Deviatoric stress (kPa)
q_c	Cone tip resistance (kPa)
$q_{c1N_{cs}}$	Normalised equivalent clean sand value (atm)
q_{cs}	Deviatoric stress at critical state (kPa)
R	Parameter depend of Poisson's ratio
r	Relative electrical resistivity
R	Roundness
R^2	Coefficient of determination
r_d	Stress reduction coefficient
r_{eq}	Radius of equivalent area of the analysed particle
r_i	Radius of particle corners
r_{max-in}	Maximum radius inscribed circle
$r_{min-cir}$	Minimum radius circumscribed circle
r_u	Pore pressure ratio
r_w	Relative electrical resistivity of water
S	Sphericity
S_f	elastic response spectrum parameter
S_{max}	ground soil factor
Sr	Degree of saturation (%)
Sr_0	Initial degree of saturation (%)
t	time
T_0	Amplitude
t_t	Wave propagation time
\ddot{u}	Acceleration
u	Displacement
u_2	Pore-water pressure during the cone penetration (kPa)
$u_{a,0}$	Initial pore air pressure
u_a	Pore air pressure
V_P	P-wave velocity (m/s)
V_S	S-wave velocity (m/s)
V_{S1}	Overburden stress-corrected S-wave velocity (m/s)
W	Elastic store energy (J)
W_a	Specific work to cause deformation of air (J)
W_d	Specific work cause by deviation strain (J)
W_r	Stored energy (J)
W_s	Normalised unit energy (J/m ³)
W_{sk}	Specific work to cause deformation of soil skeleton (J)
W_{tot}	Total specific energy (J)
W_v	Specific work to cause volume deformation (J)
W_w	Specific work to cause deformation of water (J)
Z	Specific soil deposit depth (m)
ΔW	Total dissipated energy per unit volume (J/m ³)
∇	Laplacian operator

Γ	Void ratio defined at $p' = 1$ kPa
γ	Shear strain
γ^*	Normalised strain
γ_I	Earthquake importance factor
γ_t	Cyclic threshold strain
ε_v^*	Potential volumetric strain
ε_a	Axial strain
ε_d	Deviation strain
$\varepsilon_{v,liq}$	Volumetric strain at liquefaction onset
ε_v	Volumetric strain
η	Stress ratio
η	Instability line
η_{\max}	Peak stress ratio
θ_0	Rotation level in RC test
θ_s	Saturated water content
θ_w	Volumetric water content
λ	Slope of CSL line
ν	Poisson's ratio
ν_{sk}	Poisson's ratio of soil skeleton
ξ	Damping ratio of RC system (%)
ξ_T	Total damping of RC system (%)
ρ	Regularity
ρ_{dry}	Mass density of dry soil (g/cm^3)
ρ_f	Mass density of fluid (g/cm^3)
ρ_{soil}	Mass density of soil grains (g/cm^3)
ρ_{sus}	Mass density of fluid and soil (g/cm^3)
ρ_w	Mass density of water (g/cm^3)
ρ_a	Mass density of the air (g/cm^3)
σ	Confining pressure (kPa)
σ'_v	Vertical effective stress (kPa)
σ'_{v0}	Initial vertical effective stress (kPa)
σ_{v0}	Vertical stress (kPa)
τ	Shear stress (kPa)
ϕ	Radians out of phase in RC test
ϕ'	Effective friction angle of soil
ϕ_{cs}	Critical state friction angle of soil
$\phi_{\theta T}$	Transfer function phase angle (rad)
χ	Dilatancy rate scaling parameter
Ψ	Matrix function
ψ	State parameter
ω	Water content
ω_R	Resonant frequency (Hz)
ω_f	Final water content

Chapter 1

Introduction

1.1 Context and research motivation

Earthquakes are one of the most destructive natural phenomena. During the past century, earthquakes caused the deaths worldwide and numerous damages in infrastructures, resulting in an estimated economic loss of EUR75 billion in the last quarter. Approximately half of this earthquake-induced was caused by liquefaction. Recent reports on liquefaction in Japan ([Boulanger, 2012](#)) and New Zealand ([Cubrinovski et al., 2011](#)) have clearly evidenced the risks to communities associated with liquefaction, providing an opportunity for improving public policies in various countries under similar risk. In May 2012, an energetic seismic sequence affected Northern Italy, despite the relatively moderate magnitude (around 5.9). This survey showed heavy damage in critical infrastructures essentially due to liquefaction or soil failure, as well as in old masonry constructions and recent constructions ([Viana da Fonseca et al., 2017](#)).

Recent works from FEUP geotechnical group of CONSTRUCT, within the scope of two projects financially supported by the Portuguese Foundation for Science and Technology (FCT) ‘Tools for performance-based design in liquefiable deposits’ (PTDC/ECM/103220/2008) and ‘Liquefaction Assessment Protocols to Protect Critical Infrastructures against Earthquake Damage: LIQ2PROEARTH’ (PTDC/ECM/-GEO/1780/2014), concluded in 2013 and 2019, have confirmed that liquefaction susceptibility can be essentially addressed by Critical State Soil Mechanics theory, both from static/monotonic and cyclic loading conditions. Furthermore, in-situ

testing was performed in four experimental sites in Portugal to identify liquefiable layers. In such experimental sites, high-quality samples of sandy soils were collected and which were subsequently tested in the laboratory using advanced procedures. Moreover, in European Project ‘LIQUEFACT’ (H2020 GA 700748), in which the geotechnical group of CONSTRUCT also participated, systems for IPS have been implemented in an experimental site in Pieve di Cento in Italy (Flora et al., 2020), where horizontal drains and air injection performed well as liquefaction mitigation measures (<http://www.liquefact.eu/>).

Therefore, it is of the utmost relevance to identify mitigation techniques to tackle liquefaction risk while satisfying the requirements of design reliability, environmental compatibility and cost-effectiveness. It is well-known that soil liquefaction is triggered in saturated conditions (Tatsuoka et al., 1986; Kokusho, 2013; He et al., 2014). Hence, reducing the saturation level can reduce liquefaction susceptibility (Soares and Viana da Fonseca, 2016; Wang et al., 2016). During element testing, the degree of saturation of the soil (S_r) can be estimated by measuring both Skempton’s B -value and P-wave velocity (Yang, 2002; Vieira Faria et al., 2006; Valle-Molina and Stokoe, 2012). However, P-wave velocity is advantageous to measure in the field and the laboratory, contrasting with other methods.

The induced partial saturation (IPS) technique is considered one of the most innovative and promising for increasing the liquefaction resistance of soils. IPS consists of introducing a certain amount of air/gas into the soil voids (Okamura et al., 2011; Eseller-Bayat et al., 2013). The air/gas insertion reduces the degree of saturation, and even a small decrease in saturation (from 100% to 95%) can increase the resistance to liquefaction by 30% (Yegian et al., 2007; Jafarzadeh and Sadeghi, 2012; Mele et al., 2019). The air in the voids prevents soil liquefaction due to a minor effect of the matric suction (Zhang et al., 2016; Tsukamoto, 2019) and the most relevant factor is the high-volumetric compressibility of air bubbles, even at micro-scale (Okamura and Soga, 2006; Tsukamoto et al., 2014; Mele and Flora, 2019). The partial saturation condition induces an increment of soil stiffness and a displacement of the critical state locus (Robertson et al., 2017). During undrained cyclic loading, the matric suction generates an additional strength, and the compression of air/gas minimises the pore pressure build-up in loose to medium-dense sands, which tend to contract (Mele et al., 2020). The instability of granular soils during cyclic loading is more pronounced in the presence of non-compressible fluids (Lirer and Mele, 2019). This effect can be controlled by increasing the compressibility of the voids

phase with specific fluids or by applying IPS techniques (e.g. remoulding partially saturated specimens). However, no integrated experimental procedure currently allows for the reliable measurement of the degree of saturation, controlled testing of sands under different degrees of saturation, and an approach to quantifying the IPS performance for liquefaction mitigation.

Furthermore, using a micro shaking table equipped with a piezoelectric actuator for centrifuge testing has significantly reduced testing time while providing reliable and small-scale models (Cabrera et al., 2012; Molina-Gómez et al., 2019). Therefore, a practical application for assessing site response (e.g., amplification factor and soil deformations) by integrating the micro shaking-table and geotechnical centrifuge for different degrees of saturation has not been proposed yet. Physical models in geotechnical centrifuges have been implemented in both dry and saturated sands. However, recently there has been an increased interest in studying geotechnical problems involving desaturated soils (Caicedo and Thorel, 2014). Prototypes for assessing liquefaction effects in shallow foundations and mitigation techniques have shown a reduction in the settlement after decreasing the degree of saturation of liquefiable layers (Yegian et al., 2007; Dashti et al., 2010; Olarte et al., 2017; Zeybek and Madabhushi, 2017, 2018).

1.2 Research objectives

1.2.1 General objective

To assess the cyclic behaviour of a sandy soil under different degrees of saturation by evaluating the performance of the induced partial saturation as a potential method to mitigate the effects of earthquake-induced liquefaction.

1.2.2 Specific objectives

- To characterise the physical, mechanical and dynamic properties of TP-Lisbon sand by an experimental plan in the laboratory, interpreting the geomechanical behaviour of such soil using the Critical State Soil Mechanics framework.
- To evaluate the liquefaction susceptibility of the liquefiable layer below the Terreiro do Paço site by combining advanced in situ and laboratory testing, analysing and comparing the results in the light of the state parameter concept.

- To propose a novel experimental method for estimating the degree of saturation during element testing, using elastic wave velocities and validated by the wave propagation theory on fluid-saturated granular media.
- To assess the liquefaction resistance of partially saturated sands using a cyclic triaxial apparatus equipped with piezoelectric transducers and local instrumentation, quantifying the soil improvement provided by the induced partial saturation by novel approaches.
- To perform a site response analysis of shallow sandy soil deposits by combining a micro shaking table and geotechnical centrifuge apparatuses, evaluating the seismic response for different degrees of saturation.

1.3 Thesis structure

This thesis is organised into eight chapters, representing all research work phases.

Chapter 1 presents the motivation, objectives and organisation of the thesis.

Chapter 2 contains a compilation of the main theoretical aspects related to the effects of degree of saturation on soil liquefaction. Therefore, this chapter covers a literature review of the mechanisms for earthquake-induced liquefaction, novel methods to interpret the cyclic behaviour of partially saturated sands, the wave propagation theory of fluid-saturated media and the techniques for inducing partial saturation.

Chapter 3 presents the materials and experimental methods used in this research. This chapter is divided into two main sections. The first one defines the selection of TP-Lisbon sand and its historical relevance for the Portuguese heritage. The second section describes the equipment and testing procedures implemented during the research.

Chapter 4 addresses the characterisation of the physical, mechanical and dynamic properties of TP-Lisbon sand. The characterisation results are interpreted in the light of the Critical State Soil Mechanics framework. Besides, the critical state parameters controlling the geomechanical behaviour of TP-Lisbon sand are correlated with the intrinsic properties and contrasted against similar sands.

Chapter 5 focuses on the assessment of the liquefaction susceptibility of TP-Lisbon

sand. The assessment is carried out by advanced in situ and laboratory testing, comprising reconstituted samples with relative densities representative of the liquefiable layer below the Terreiro do Paço site. The state parameter concept interprets the results between the diverse testing methods, predicting the liquefaction resistance for different stress and state conditions.

Chapter 6 covers the liquefaction resistance of TP-Lisbon sand in partially saturated conditions. In this chapter, two main contributions are introduced. The first contribution is proposing a novel experimental method to assess the degree of saturation during element testing by measuring mechanical wave velocities. The second contribution corresponds to the assessment of induced partial saturation to improve the liquefaction resistance of TP-Lisbon sand. The results of this method are validated by contrasting experimental results against theoretical predictions based on the wave propagation theory of fluid-saturated media.

Chapter 7 deals with a Site Response Analysis of shallow sandy soil deposits with different degrees of saturation. The Site Response Analysis comprises an advanced testing approach combining shaking table and centrifuge testing. This approach provides a series of frequency amplification spectra considering various testing conditions, namely the degree of saturation and effective centrifuge accelerations. The results obtained from centrifuge testing revealed the effects of the degree of saturation on the amplification factor, first resonant frequency and volumetric strains during cyclic loading for soil deposits with different depths.

Chapter 8 summarises the main findings and concluding remarks of the thesis, including the limitations and suggestions for further research works.

Chapter 2

Perspectives of the effects of degree of saturation on soil liquefaction

A version with the main content of this chapter has been submitted for publication to *Earth-Science Reviews*: Molina-Gómez, F.; Viana da Fonseca A.; Ferreira, C.; Caicedo, B. Earthquake-induced liquefaction mitigation based on induced partial saturation techniques: A review.

2.1 Outline

This chapter addresses a literature review on the mechanisms of soil liquefaction and the progress of induced partial saturation (IPS) techniques to mitigate this phenomenon. The review method covers a systematic search for research works aimed at selecting: (i) fundamental aspects regarding the liquefaction susceptibility; (ii) desaturation methods currently used to induce partial saturation in soils; and (iii) experimental evidence about the effectiveness of IPS techniques. On the other hand, methods to measure the degree of saturation in soils are also presented in this chapter. These methods highlight the propagation of P-wave in fluid-saturated media using Biot's theory. The review discusses the most notable achievements, limitations and challenges of IPS techniques. Therefore, relevant findings that propose interesting and valuable concepts are conferred in this chapter. Further literature about the explored ideas and concepts will be given in the main text of each chapter.

2.2 Features of soil liquefaction

2.2.1 Mechanisms of soil liquefaction

Liquefaction is an instability phenomenon characterised by the rapid loss of the strength and stiffness of soil. Effective stress tends to zero during liquefaction due to the generation of pore pressure build-up. This phenomenon may occur in saturated soil deposits subjected to rapid undrained loading, including monotonic conditions (e.g. seepage, water level rise or accelerated overloading) and cyclic conditions (e.g. earthquakes, machine vibration or traffic action). Once the soil liquefies, it presents similar characteristics and behaviour to a non-Newtonian fluid. Physically, liquefaction causes the loss of contact between soil particles. For this reason, liquefaction is one of the most complex phenomena occurring in granular soils. Besides, it is one of the causes of severe damage in operational facilities and natural ecosystems.

Any soil capable of generating pore pressure build-up is susceptible to trigger liquefaction. Therefore, one of the main aspects of assessing the liquefaction susceptibility of soil deposits is to establish whether the soil is liquefiable or not. [Kramer \(1996\)](#) classified the liquefaction susceptibility through the criteria, covering four broad categories. [Figure 2.1](#) presents the criteria for identifying the liquefaction susceptibility in soil deposits, based on the criteria indicated by [Kramer \(1996\)](#), mentioning their main peculiarities.

The historical criterion addresses seismic activity and involves factors like magnitude, acceleration and duration of the earthquake in a specific zone or region. Historical evidence about earthquake-induced liquefaction provides relevant insights into the liquefaction susceptibility of natural soil deposits. Furthermore, such information allows developing and validating methods to mitigate liquefaction and, thus its consequences or effects. [Table 2.1](#) summarises a series of recent liquefaction case histories worldwide.

The geological environment plays a relevant role in liquefaction susceptibility. Loose to medium sands with a uniform grain size distribution are the soils most susceptible to trigger liquefaction. Such types of soils are typical in alluvial, colluvial and aeolian soil deposits. In addition, the grain size, particle shape and grading curve of the soil have a strong influence on liquefaction resistance since these factors restrain the volume change of soils and control the development of pore pressure build-up required for liquefaction triggering ([Yang and Wei, 2012](#); [Wei and Yang, 2014](#);

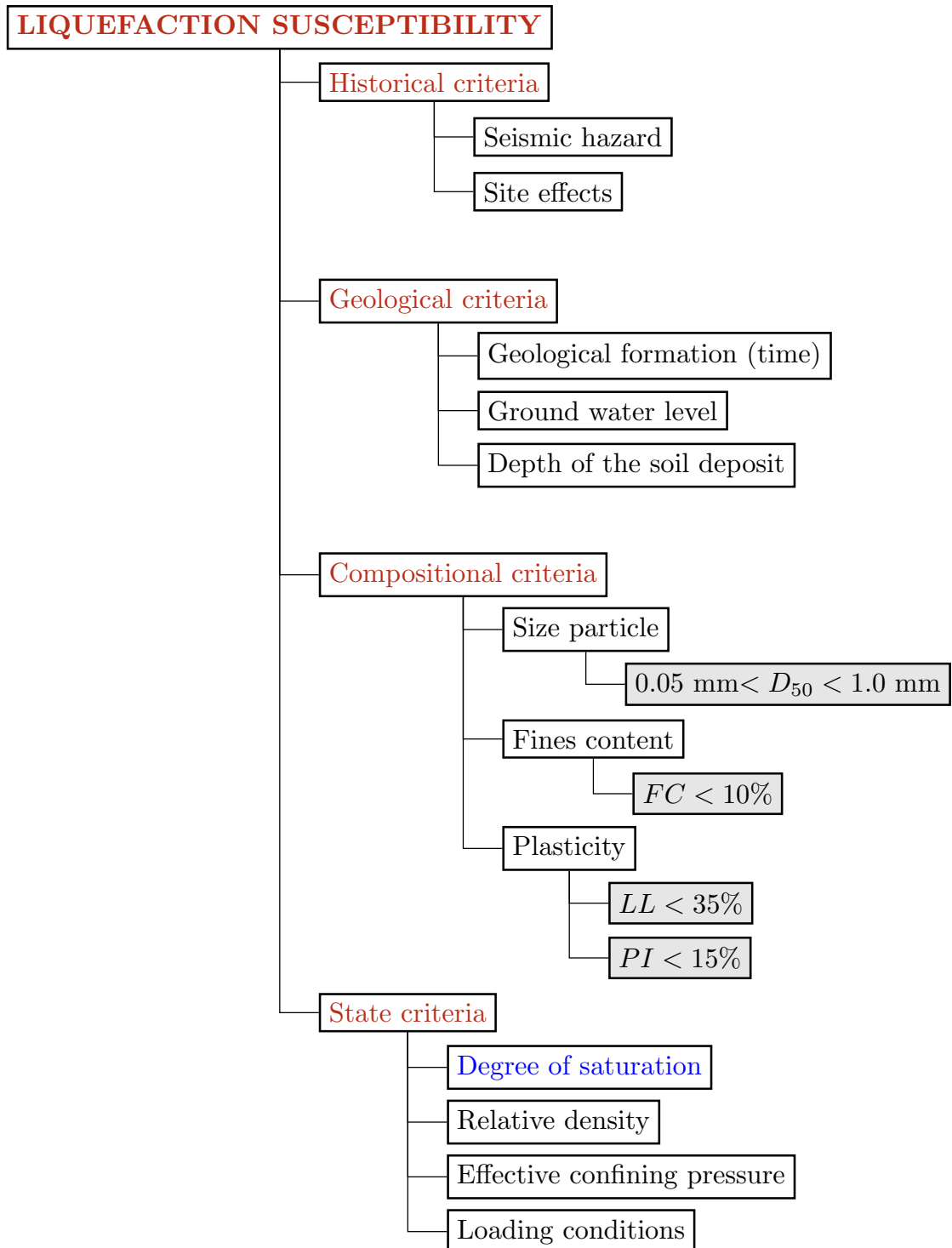


Figure 2.1: Criteria of liquefaction susceptibility

Table 2.1: Recent liquefaction case histories (adapted from [Geyin and Maurer 2020](#))

Date	Earthquake	Country	Magnitude (M_w)
16/6/1964	Niigata	Japan	7.6
09/2/1971	San Fernando	United States	6.6
04/2/1975	Haicheng	China	7.0
27/7/1976	Tangshan	China	7.6
15/10/1979	Imperial Valley	United States	6.5
09/5/1980	Victoria (Mexicali)	Mexico	6.3
26/4/1981	Westmoreland	United States	5.9
26/5/1983	Nihonkai-Chubu	Japan	7.7
28/10/1983	Borah Peak	United States	6.9
02/3/1987	Edgecumbe	New Zealand	6.6
24/11/1987	Elmore Ranch	United States	6.2
24/11/1987	Superstition Hills	United States	6.5
18/10/1989	Loma Prieta	United States	6.9
17/1/1994	Northridge	United States	6.7
16/1/1995	Hyogoken-Nambu	Japan	6.9
17/8/1999	Kocaeli	Turkey	7.5
20/9/1999	Chi-Chi	Taiwan	7.6
8/6/2008	Achaia-Ilia	Greece	6.4
27/2/2010	Maule	Chile	8.8
04/4/2010	El Mayor-Cucapah	Mexico	7.2
04/10/2010	Darfield	New Zealand	7.1
22/2/2011	Christchurch	New Zealand	6.2
11/3/2011	Tohoku	Japan	9.0
20/5/2012	Emilia Romagna	Italy	6.1
14/2/2016	Christchurch	New Zealand	5.7

[Lashkari et al., 2020](#)). Soils with rounded particle shapes have lower shear strength resistance than soils composed of angular particles, meaning liquefaction resistance is higher in angular-grained soils.

[Tsuchida \(1970\)](#) proposed a series of grain size boundaries to identify soils susceptible to the phenomenon based on historical earthquake-induced liquefaction cases. Such bounds establish that fine sands and poorly graded are the most liquefiable soils, while silts and coarse sands are potentially liquefiable soils. Figure 2.2 presents the compositional criterion proposed by [Tsuchida \(1970\)](#) to identify soils susceptible to liquefaction.

The composition criterion proposed by [Tsuchida \(1970\)](#) has been implemented for the characterisation of soil deposits recently experienced liquefaction in Italy ([Monaco](#)

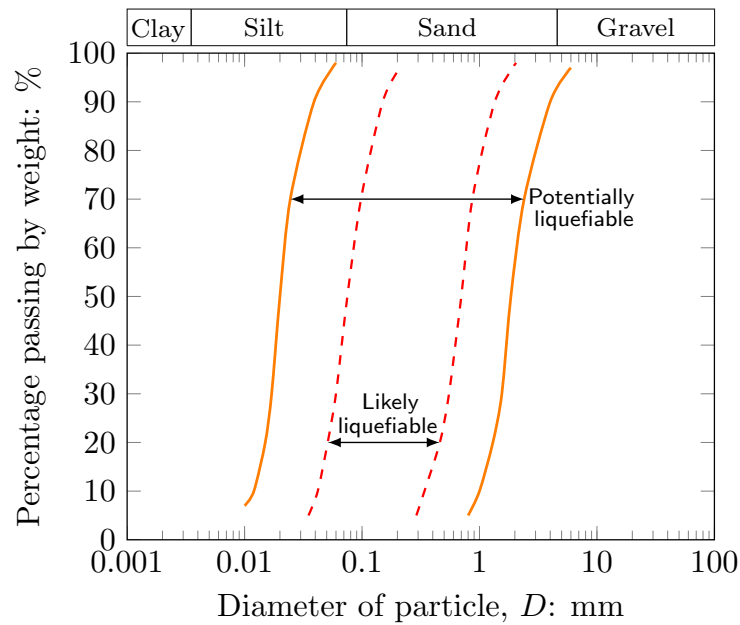


Figure 2.2: Grain size boundaries proposed by Tsuchida (1970) to define liquefaction susceptibility

et al., 2011) and New Zealand (Villamor et al., 2016). Besides, it has been used as a first approach to identify the causes of the collapse of B1 tailings dam, in Brazil, (Cambridge and Shaw, 2019). These contrasts showed a good agreement with the composition criterion in term of liquefaction susceptibility for both static and cyclic loading conditions.

Park and Kim (2013) and Boulanger and Idriss (2014) recognise that soils with a high content of plastic and fine particles, such as clays, are less susceptible to liquefy due to the difficulty of particle rearrangement and the additional shear strength given by the electrostatic forces between particles of plastic soils. Notwithstanding, the plasticity index (PI) is a better indicator of liquefaction susceptibility than fines content. Hence, non-plastic silts and clayey silts with $PI < 12\%$ are susceptible to liquefy, but clayey silts and silty clays with $12\% < PI < 18\%$ can also undergo liquefaction (Bray and Sancio, 2006). On the other hand, coarse sands and gravels are less susceptible to trigger liquefaction because of their high permeability, which allows the drainage and then eliminates the development of pore-water pressure build-up. However, these soil types can trigger liquefaction under high loading solicitations or at a large number of cycles (Dhakal et al., 2020).

On the other hand, the tendency to generate pore pressure excess is strongly influenced by the state of the soil; i.e. stress, density and saturation conditions. Hence,

liquefaction susceptibility depends on the initial state, even if the soil satisfies all previous criteria. Both stress and density define the dilative or contractile behaviour of soil. Been and Jefferies (1985) defined the state parameter (ψ) to establish the dilative or contractile behaviour of soil by applying the critical-state soil mechanics framework. Equation 2.1 defines the state parameter.

$$\psi = e - e_{cs} \quad (2.1)$$

where e is the current void ratio of the soil, and e_c is the void ratio of the critical state at the current mean stress –measuring the vertical distance between the initial state of the soil and its critical-final state. Therefore, ψ can simultaneously quantify the influence of the relative density (void ratio) and the stress level on the behaviour of granular soils. Besides, it allows defining whether the soil has dilative or contractile behaviour. Soils with positive state parameter ($\psi > 0$) have contractile behaviour (covering very loose to loose soils under low stress). In contrast, soils with negative state parameter ($\psi < 0$) have dilative behaviour (typically comprising medium to dense soils under high stress). Figure 2.3 represents the definition of ψ and the location of contractile and dilative behaviours in the $e : \log(p')$ space.

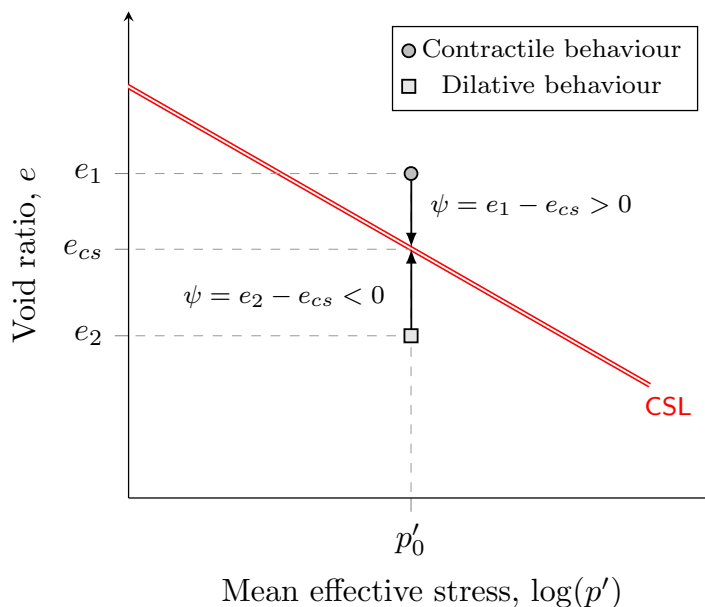


Figure 2.3: Illustration to define the state parameter, ψ

Soil behaviour, represented in terms of ψ , provides relevant insights on the liquefaction susceptibility since this parameter can be associated with the tendency of soil to generate pore pressure built-up (Ishihara, 1993; Jefferies and Been, 2015).

Soils with positive state parameter tend to pack the particles close together, aiding the pore pressure build-up during loading. On the other hand, soils with dilative behaviour tend to separate the particles during loading, reporting, in some cases, negative excess of pore pressure. Therefore, soils with contractile behaviour are more susceptible to trigger soil liquefaction than soils with dilative behaviour. To practical engineers, the value of the ψ approach is that many soil properties and behaviours are simple functions of normalised parameters in terms of this parameter (Jefferies and Been, 2015; Giretti et al., 2018). Hence, it turns out that ψ is fundamental to constitutive models of soil that integrate invariant properties with soil density and stress level (Jefferies, 1993).

Loose or medium-dense granular soils tend to be more susceptible to soil liquefaction under full saturation conditions. However, earthquake-induced liquefaction may also occur in partially saturated soils. Experimental evidence reported by Tsukamoto et al. (2002); Zeybek and Madabhushi (2017); Mele et al. (2019) showed that a reduction of the degree of saturation has a relevant influence on the liquefaction susceptibility. The above is because of two effects of air into soil voids: (i) the matric suction that increases the initial effective stress of soil (Zhang et al., 2016; Robertson et al., 2017; Tsukamoto, 2019) and (ii) the less capability of generating pore pressure build-up during loading (Yoshimi et al., 1989; Yang, 2002; Eseller-Bayat et al., 2013).

The effects of degree of saturation (S_r) on liquefaction resistance are the focus of this research; thus, these will be thoroughly addressed in this document in order to understand and explain the soil behaviour under partially saturated conditions and the influence of induced partial saturation on liquefaction resistance of sandy soils.

2.2.2 Earthquake-induced liquefaction damages

The consequences of soil liquefaction may be catastrophic. Earthquake-induced liquefaction has caused significant damage in critical infrastructures and building collapses, causing the loss of its operation and functionality (Viana da Fonseca et al., 2017). In Portugal, local liquefaction-induced damage dates from 1344, 1531, 1755 and 1909, when distant and local intraplate earthquakes ($M_w \approx 6.0 - 8.5$) stroke the country, mainly affecting the greater Lisbon area (Viana da Fonseca et al., 2019; Ferreira et al., 2020). Major damages were reported after in 1755 and 1909 earthquakes. The 1st November 1755 earthquake ($M_w = 8.5$) is probably the greatest

seismic disaster of Western Europe since it almost destroyed the Lisbon centre, killed up to 100 000 people and injured more than 40 000 people (Soares, 2015). The characterisation of the liquefiable layers composing the historical centre is thoroughly addressed in this study. On the other hand, the 23 April 1909 earthquake ($M_w = 6.0$) destroyed the small municipality of Benavente and affected surrounding towns, being the largest crustal earthquake in the Iberian Peninsula during the 20th century (Teves-Costa and Batlló, 2011).

Well-documented studies about earthquake-induced liquefaction are available after the Niigata earthquake ($M_w = 7.3$ on 16 June 1964), which severely damaged Niigata city. Niigata is located on the west coast of Japan and lies over 30 m of fine alluvial sand from the Shinano River. The most relevant liquefaction-induced damage due to the Niigata earthquake resulted in ground deformations and tilting on a set of apartment buildings located in Kawagishi in Niigata city (Jefferies and Been, 2015) – now a frequently used illustration of the results of liquefaction (see Figure 2.4). The tilting of such buildings was because of an excessive settlement and a bearing capacity failure in the liquefied ground, affecting the building foundation without degrading its structure. Yoshimi and Kuwabara (1973) pointed “after the earthquake, water from the ground flowed due to the dissipation of pore pressure in the areas of the city that experienced liquefaction”. It is supposed that at such time the buildings probably settled (Yoshimi and Tokimatsu, 1977).

In addition to excessive settlements and tilting on buildings, liquefaction can produce the following damages:

- loss of bearing capacity;
- differential settlements in bridges;
- lateral spreading;
- ground failures and large deformations in transport infrastructures;
- large deformations in energy infrastructures and pipelines;
- increments of active lateral earth pressures behind retaining walls;
- flotation of underground structures (i.e. tunnels and pipelines);
- loss of passive resistance in anchor systems.



Figure 2.4: Liquefaction-induced damages illustration –tilt of building after 1964 Niigata earthquake (Kramer, 1996)

Figure 2.5 displays some liquefaction-induced damages evidenced after case histories. The Niigata incident highlighted the effects of soil liquefaction and the relevance of assessing its susceptibility, especially in sandy soil deposits in areas with moderate to high seismic risk. However, it was not until 1964 that liquefaction became considered one of the main concerns in geotechnical engineering (Towhata, 2008).

NASEM (2016) compiled liquefaction triggering case history databases for level-ground conditions of different historical earthquakes in Chile, Japan and the United States. From such a compilation, these authors defined the bases for the most common correlations used to assess liquefaction susceptibility by different types of in-situ tests. Table 2.2 summarises the results of number of case histories, presenting the earthquake magnitude and reporting the number of cases in which liquefaction was triggered during the seismic events. Besides, Table 2.2 shows the parameters of soil resistance for an equivalent earthquake of $M_W = 7.5$ estimated by different in-situ tests methods (e.g. SPT, CPT and seismic tests) and the critical depth —with the lowest factor of safety against liquefaction— together with its corresponding vertical effective stress.

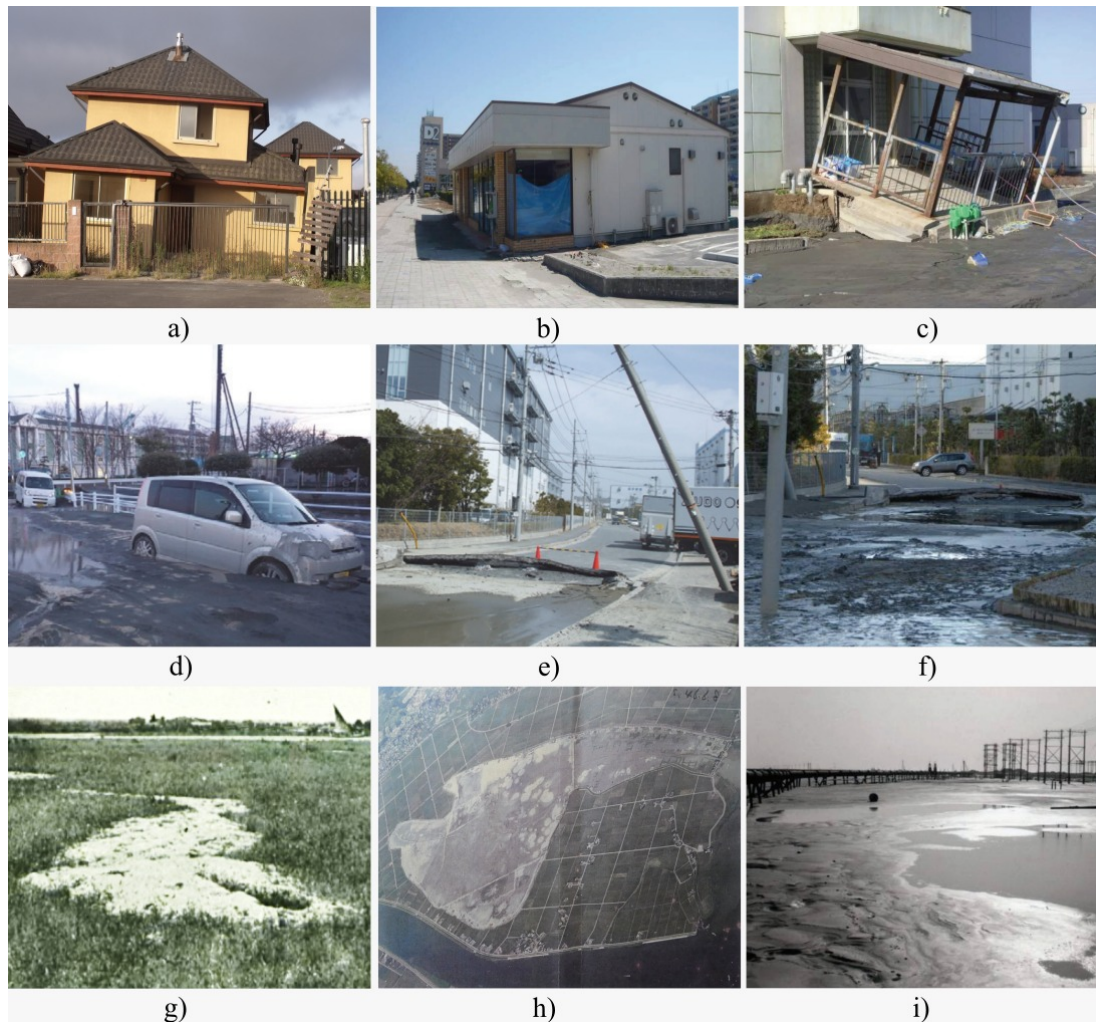


Figure 2.5: Effects of soil liquefaction in recent case histories: a) differential settlement of a house – Maule, Chile, 2010 ([Bertalot et al., 2013](#)); b) settlement and tilt of a store – Tokyo, Japan, 2011 ([Ishihara, 2012](#)); c) offset between an undamaged building and surrounding ground settlement – Urayasu, Japan, 2011 ([Ishihara, 2012](#)); d) car stuck in boiled mud and soil– Urayasu, Japan, 2011 ([Yasuda et al., 2013](#)); d) rutting pavement due to liquefaction– Urayasu, Japan, 2011 ([Yasuda et al., 2013](#)); f) spreading of sand over the road – Urayasu, 2011, Japan ([Ishihara, 2012](#)); g) sand boils – Benavente, 1909, Portugal ([Teves-Costa et al., 2001](#)); h) spreading of sand over the field – Itako, 1971, Japan ([Ishihara, 2012](#)), i) sandy soils transported hydraulically after liquefaction – Urayasu, 1971, Japan ([Ishihara, 2012](#))

Table 2.2: Summary of recently case history earthquake-induced liquefaction (NASEM, 2016)

Parameter	Standard penetration test, SPT		Cone penetration test, CPT		Seismic test
	Cetin et al. (2004)	Boulanger and Idriss (2014)	Moss et al. (2006)	Boulanger and Idriss (2014)	
Liquefaction triggered	109	133	139	180	287
No liquefaction triggered	88	118	44	71	124
Yes/No liquefaction	3	3	0	2	4
Critical depth (m)	1.1-20.5	1.8-14.3	1.4-14.0	1.4-11.8	1.1-18.5
Vertical effective stress, σ'_v (kPa)	8-199	20-171	14-145	19-147	11-176
Fines content (% by weight)	0-92	0-92	–	0-85	–
$(N_1)_{60cs}$; q_{c1Ncs} (atm); V_{s1} (m/s)	2.2-66.1*	4.6-63.7	11.2-252.0	16.1-311.9	81.7-362.9
Equivalent cyclic stress ratio, $CSR_{M7.5}$	0.05-0.66	0.04-0.69	0.08-0.55 [‡]	0.06-0.65	0.02-0.73 [‡]
Earthquake magnitude, M_w	5.8-8.0	5.9-8.3	5.8-8.0	5.9-9.0	5.9-9.0

Note: * $(N_1)_{60}$; [‡]values of cyclic stress ratio (CSR)

2.2.3 Assessment and interpretation of liquefaction resistance

The identification of liquefaction onset is the main concern in the assessment of such phenomena. In current design practice, the number of cycles necessary to trigger liquefaction for a representative load of an earthquake is used to define the liquefaction susceptibility of soils. Eurocode 8 (CEN, 2010) recommends the simplified procedure proposed by Seed and Idriss (1971) to define the earthquake-induced loading, considering the seismic wave propagation in a soil column.

The movement induced by the peak horizontal acceleration on the ground surface (a_{max}) generates a shear stress (τ), which acts at the bottom of the soil column. Seed and Idriss (1971) indicates that the movement induced by the seismic wave propagation is assumed to be completely horizontal. This simplified procedure allows estimating the cyclic stress ratio (CSR) at a specific depth, Z , during an earthquake of magnitude $M_w = 7.5$. Equation 2.2 describes the simplified procedure proposed by Seed and Idriss (1971).

$$CSR = \frac{\tau_{cyc}}{\sigma'_{v0}} = 0.65 \cdot \frac{a_{max}}{g} \cdot \frac{\sigma_{v0}}{\sigma'_{v0}} \cdot r_d \quad (2.2)$$

where τ_{cyc} is the amplitude of cyclic shear stress, σ'_{v0} is the vertical effective stress, σ_{v0} is the vertical stress, and r_d is stress reduction coefficient that considers the depth of soil deposit (Z) and the earthquake magnitude (M_w) (see equation 2.3).

$$r_d = \exp[\alpha(Z) + \beta(Z)M_w] \quad (2.3)$$

where:

$$\alpha(Z) = -1.012 - 1.126 \sin\left(\frac{Z}{11.73} + 5.133\right) \quad (2.4a)$$

$$\beta(Z) = 0.106 + 0.118 \sin\left(\frac{Z}{11.28} + 5.142\right) \quad (2.4b)$$

From the simplified procedure, the cyclic shear stress at the surface caused by the seismic action can be estimated. There are different methods based on in situ test results have been proposed to estimate the cyclic resistance ratio (CRR) of

the soils susceptible to earthquake-induced liquefaction –discussed below. However, to characterise the liquefaction susceptibility of soils, it is necessary to assess the number of cycles to trigger liquefaction (N_L) for different earthquake-induced loads; that is, the assessment of N_L for different CSR, representing the cyclic resistance ratio (CRR) of the soil. This characterisation is conducted in the laboratory by element testing. During element testing, a soil sample is subjected to an undrained and uniform sinusoidal cyclic loading to measure the evolution of shear strain and pore pressure build-up (see Figure 2.6).

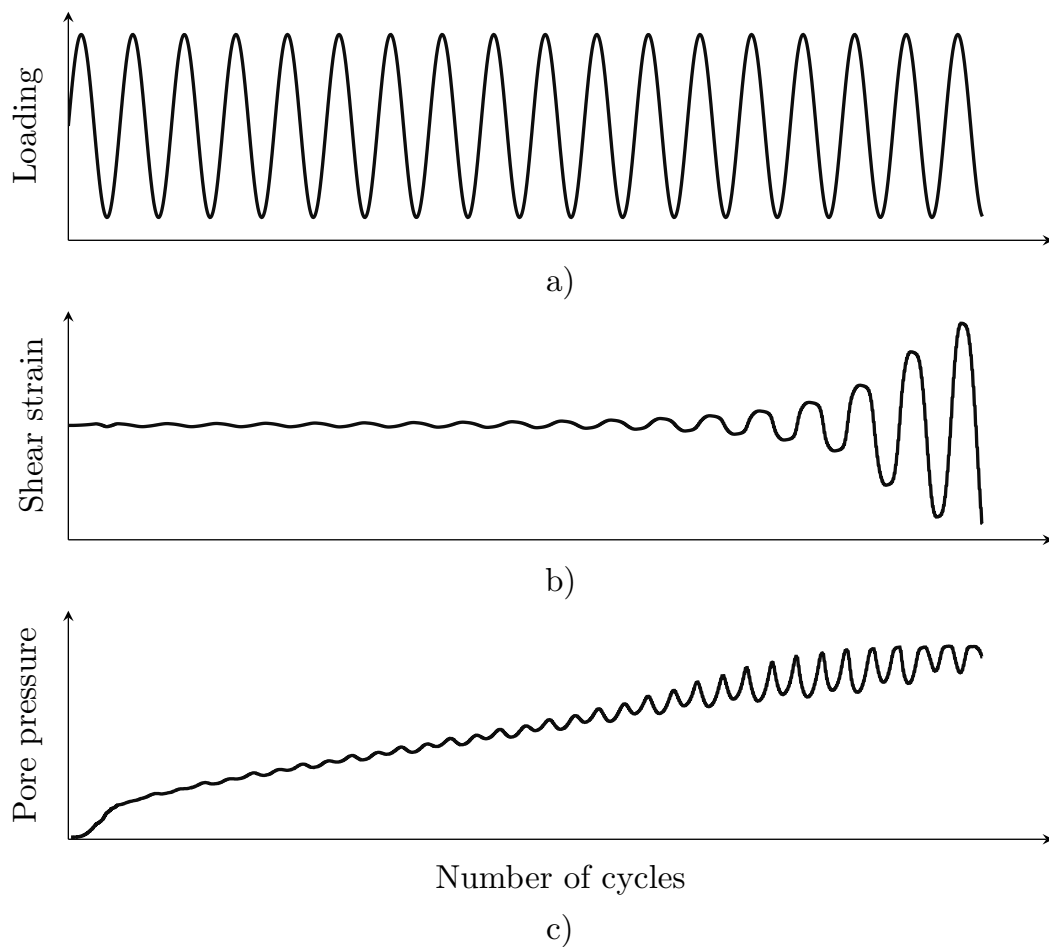
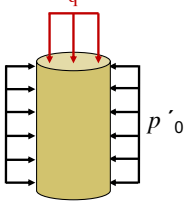
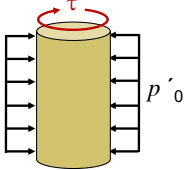
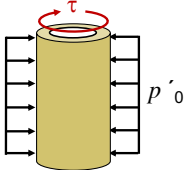
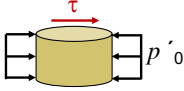
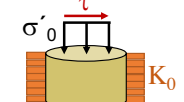


Figure 2.6: Soil response during cyclic element testing —based on experimental data: a) cyclic loading; b) evolution of shear strain; c) pore pressure build-up

Cyclic element testing can be performed in a triaxial, torsional, hollow cylinder or simple shear apparatus. According to the type of test, the cyclic stress ratio (CSR) is obtained differently. The CSR computation depends on the nature of loading during element testing, e.g. axial, torsional or tangential. Besides, CSR depends on the type of consolidation, that is, p'_0 or σ'_0 . Both loading and consolidation depend on the

Table 2.3: CSR for different cyclic element testing

Test type	CSR and r_u computation	DA value*
Triaxial 	$CSR = \frac{q}{2p'_0} \quad r_u = \frac{\Delta u}{p'_0}$	$\varepsilon_a = 5.0\%$
Torsional shear 	$CSR = \frac{\tau}{p'_0} \quad r_u = \frac{\Delta u}{p'_0}$	$\gamma = 7.5\%$
Hollow cylinder 	$CSR = \frac{\tau}{p'_0} \quad r_u = \frac{\Delta u}{p'_0}$	$\gamma = 7.5\%$
Cyclic simple shear 	$CSR = \frac{\tau}{p'_0} \quad r_u = \frac{\Delta u}{p'_0}$	$\gamma = 7.5\%$
Cyclic direct simple shear ⁺ 	$CSR = \frac{\tau}{\sigma'_0} \quad r_u = \frac{\Delta \sigma}{\sigma'_0}$	$\gamma = 7.5\%$

* Values suggested by [Ishihara \(1996\)](#)

⁺ in this testing condition the variation of vertical stress ($\Delta\sigma$) is assumed as equivalent to the pore pressure built-up

apparatus configuration used for cyclic testing. Usually, the liquefaction triggering occurs when the pore pressure build-up is equal to the actual effective stress of the soil. The assessment of liquefaction triggering based on the pore pressure build-up is known as the stress criterion and uses the pore pressure ratio (r_u). However, the soil deforms progressively during cyclic loading as the pore pressure approaches the effective confining pressure ([Ishihara, 1996](#)). Such an evolution of strains provides another liquefaction criterion, the strain criterion. The strain criterion considers the onset of liquefaction from a specific value of double strain amplitude (DA), which changes according to the loading type. Table 2.3 shows the procedures to compute cyclic stress ratio (CSR) and r_u , together with the DA value for different testing methods and apparatuses in the laboratory.

In element testing, the incremental pore pressure build-up and evolution of strains are measured along with the number of loading/stress cycles. Therefore, the test results for liquefaction assessment cover the number of cycles necessary to trigger liquefaction (N_L) for each CSR. During element testing, the CSR is equivalent to CRR since the testing aim is to identify the liquefaction onset for a specific loading condition. The number of cycles can be estimated using the r_u or DA strain criteria. Experimental data provide a series of points that compose the liquefaction resistance curve (LRC).

Figure 2.7 illustrates the LRC and its derivation from experimental data. Figure 2.7 shows that CSR above LRC designates liquefaction manifestation, while CSR below LRC designates non-liquefaction onset. Nevertheless, the LRC curve depends on the soil state; that is, an LRC only represents the cyclic behaviour of a specific ψ or Sr . Usually, the LRC follows a power rule in the form of equation 2.5 (Boulanger and Idriss, 2014), where a and b are curve fitting parameters, and N_L represents the number of cycles for liquefaction onset.

$$CRR = a(N_L)^{-b} \quad (2.5)$$

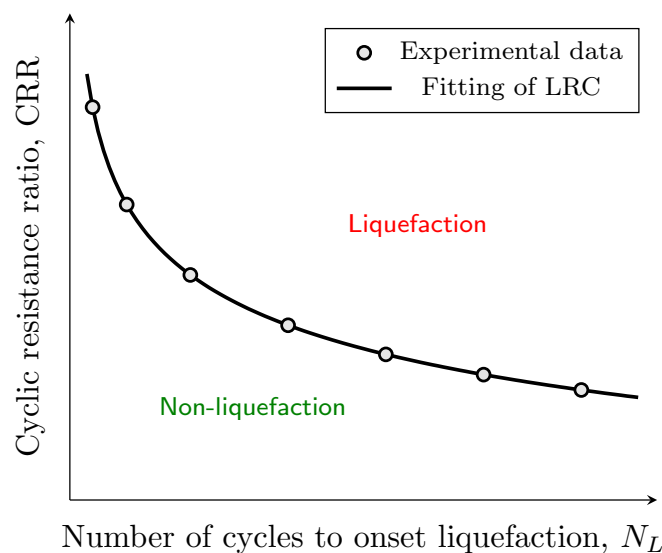


Figure 2.7: Schematic of LRC from experimental data

For loose sands, the liquefaction onset can be unquestionably taken as a state of softening because large deformations are produced suddenly with complete loss of strength during or immediately following the $r_u = 1$. In contrast, for medium dense to dense sand, a state of softening is also generated with a pore water pressure

build-up of almost $r_u = 1$, accompanied by about double strain amplitude criterion (Ishihara, 1993). Viana da Fonseca et al. (2015); Giretti and Fioravante (2017) observed the same number of cycles to trigger liquefaction, N_L , for stress and strain criteria in loose sands. However, these authors showed that the difference between the number of cycles between both criteria increases with increasing relative density, identifying higher values of N_L for the DA strain criterion. Therefore, the assessment of liquefaction susceptibility from r_u measurements provides more conservative results, which is conceptually consistent since soil liquefaction is strongly linked to pore pressure build-up.

Due to the relevance of stress criterion, models to predict the pore pressure build-up in granular soils have been explored by several authors (Lee and Albaisa, 1974; Seed et al., 1975; Booker et al., 1976; Polito et al., 2008; Park et al., 2015; Khashila et al., 2018; Chiaradonna and Flora, 2020). These models allow predicting the pore pressure build-up by the pore pressure ratio (r_u), denominating these models as stress-based methods. The stress-based have been proposed by fitting experimental data of cyclic element tests and following the formulation developed by Seed et al. (1975) to predict the r_u as a function of the cycle ratio, N/N_L . Such a formulation uses a coefficient, β , which depends on the soil type and state. Equation 2.6 describes the formulation of Seed et al. (1975).

$$r_u = \frac{1}{2} + \frac{1}{\pi} \arcsin \left[2 \left(\frac{N}{N_L} \right)^{1/\beta} - 1 \right] \quad (2.6)$$

From equation 2.6, it can be inferred that β controls the shape of the curve describing r_u evolution. Booker et al. (1976) recommended $\beta = 0.7$ and $\beta = 1.4$ as lower and upper boundaries, respectively, for clean sands. Figure 2.8 shows the r_u evolution as a function of N/N_L and compares different values of β . Note that dashed lines denote the boundaries recommended by Booker et al. (1976). Due to the association of β with soil type and testing conditions, Polito et al. (2008) introduced a correlation relating β to fines content (FC), relative density (Dr) and cyclic stress ratio (CSR), as follows:

$$\beta = C_1 \cdot FC + C_2 \cdot Dr + C_3 \cdot CSR + C_4 \quad (2.7)$$

where C_1 , C_2 , C_3 and C_4 are regression coefficients. Polito et al. (2008) indicated

that for soils with $FC < 35\%$, $C_1 = 0.01166$, $C_2 = 0.007397$, $C_3 = 0.01034$ and $C_4 = 0.5058$; while for soils with $FC \geq 35\%$, $C_1 = 0.002149$, $C_2 = -0.0009398$, $C_3 = 1.667$ and $C_4 = 0.4285$.

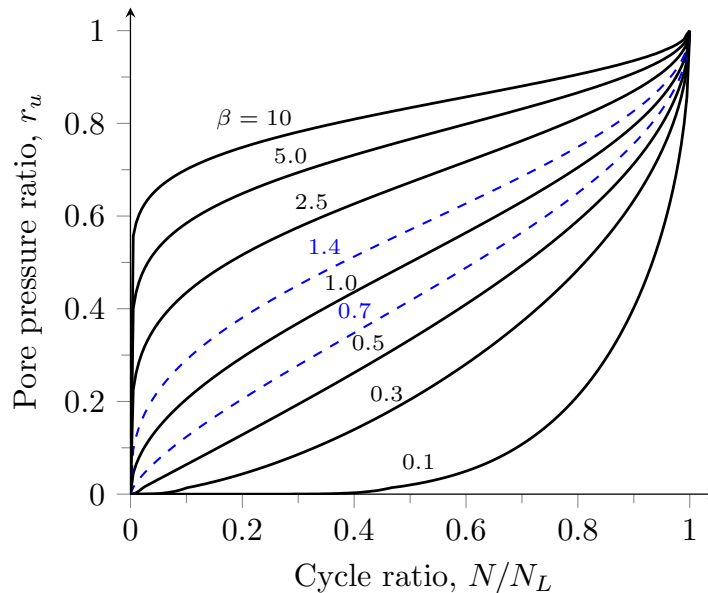


Figure 2.8: Evolution of r_u evolution as a function of N/N_L (dashed lines denote the boundaries recommended by Booker et al., 1976)

The main drawback of the models predicting the pore pressure build-up is that it is challenging to implement them in a coupled dynamic numerical analysis (Park et al., 2015). The above is because N/N_L has to be specified a *prior* and such type of analysis seeks to establish the stability, deformations and possible damages induced by pore pressure increments in geotechnical structures (Chiaradonna et al., 2018). Accordingly, to overcome the limitations of stress-based and strain-based methods, energy-based methods have been recently introduced for analysing earthquake-induced liquefaction (Millen et al., 2020). Energy-based methods for evaluating soil liquefaction were introduced as an alternative to stress-based procedures for analysing historical earthquake cases. The energy approach proposed by Nemat-Nasser and Shokooh (1979) was proposed based on seismological application to estimate the soil densification for drained conditions and pore pressure build-up for undrained conditions. Besides, it is based on the idea that the soil deforms as it dissipates part of the energy during cyclic loading (Figueroa et al., 1994).

The energy-based procedures use various measures of energy, including the elastic stored energy (W), stored energy (Wr) and total dissipated energy per unit volume (ΔW), which is appropriate since cyclic response involves energy transformation

(Liang, 1995; Green, 2001). For liquefaction assessment, the dissipated energy per unit volume of all cycles before liquefaction triggering is linked to the pore pressure built-up (Nemat-Nasser and Shokoh, 1979; Khashila et al., 2021). Figure 2.9 schematises the graphical definition of W , W_r and ΔW for one stress-strain hysteresis loop.

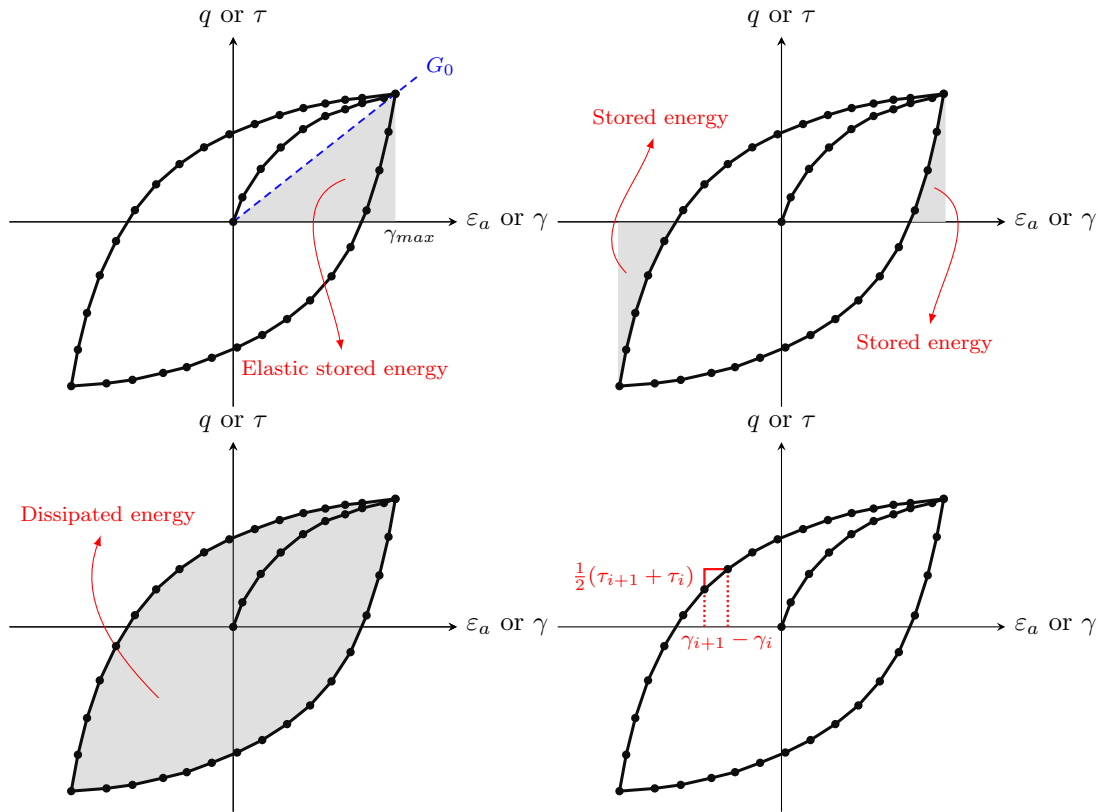


Figure 2.9: Schematic representation of energy definitions and computation

Equation 2.8 allows quantifying ΔW by relating the stresses and incremental strains (note that both the stress and incremental strain tensors are symmetrical), as follows:

$$\Delta W = \int dW = \int \sigma'_x d\varepsilon_x + \sigma'_y d\varepsilon_y + \sigma'_z d\varepsilon_z + \tau_{xy} d\gamma_{xy} + \tau_{xz} d\gamma_{xz} + \tau_{yz} d\gamma_{yz} \quad (2.8)$$

where dW is the incremental dissipated energy per unit volume; σ'_x , σ'_y and σ'_z are the effective stresses acting parallel to the x , y and z axes, respectively; $d\varepsilon_x$, $d\varepsilon_y$ and $d\varepsilon_z$ are the incremental axial strains in the x , y and z directions, respectively; τ_{xy} , τ_{xz} and τ_{yz} are the shear stresses acting on planes having normal vectors in the

x , y and z directions, respectively; and ε_{xy} , ε_{xz} and ε_{yz} are the incremental shear strain resulting from τ_{xy} , τ_{xz} and τ_{yz} , respectively.

Equation 2.8 can be solved by numerical integration (e.g. using the trapezoidal rule), as illustrated in Figure 2.10. The numerical solution allows deriving the normalised unit energy (Ws), which is the parameter used for liquefaction assessment (Green, 2001; Polito et al., 2013; Khashila et al., 2021). Equations 2.9a, 2.9b and 2.9c present the numerical derivation of Equation 2.8 for estimating Ws from experimental data obtained from cyclic triaxial, cyclic torsional (for solid and hollow soil specimens) and cyclic direct simple shear tests, respectively:

$$Ws = \frac{1}{2p'_0} \sum_{i=1}^{n-1} (q_i + q_{i+1}) (\varepsilon_{a,i} - \varepsilon_{a,i+1}) \quad (2.9a)$$

$$Ws = \frac{1}{2p'_0} \sum_{i=1}^{m-1} (\tau_i + \tau_{i+1}) (\gamma_i - \gamma_{i+1}) \quad (2.9b)$$

$$Ws = \frac{1}{2\sigma'_0} \sum_{i=1}^{n-1} (\tau_i + \tau_{i+1}) (\gamma_i - \gamma_{i+1}) \quad (2.9c)$$

where i represents the load/stress increment, n is the total number of increments to trigger liquefaction; q and τ are deviator and shear stresses, respectively; ε_a and γ are axial and shear strains, respectively; and p'_0 and σ'_0 are mean effective and vertical stresses, respectively, which represent the stress confinement of the soil.

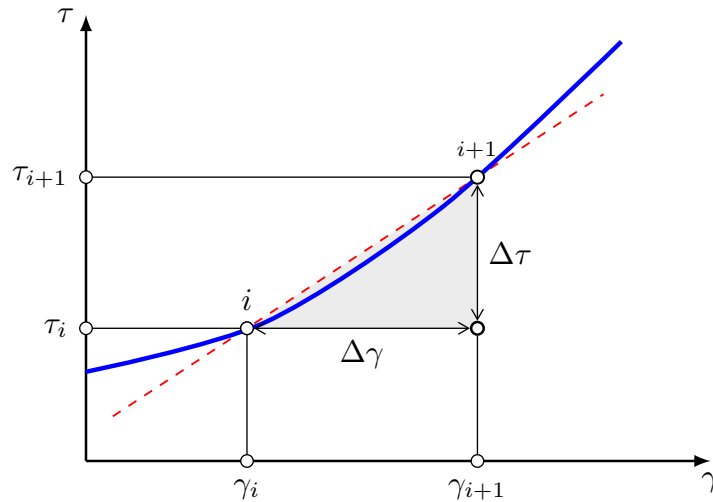


Figure 2.10: Numerical integration to compute the energy during cyclic loading

Figuroa et al. (1994), Azeiteiro et al. (2017), Khashila et al. (2018) and Rios et al. (2022) observed that the strain amplitude and location of the peak loading cycle have no effects on the results of energy-based methods. Since the dissipated energy required to trigger liquefaction is independent of the applied loading pattern (uniform or non-uniform), energy-based methods are very promising for liquefaction assessment. Therefore, energy-based methods allow for comparing results of different laboratory test procedures and predicting pore pressure generation in the field (Kokusho, 2013).

Another advantage of energy-based methods is associating the energy applied during cyclic loading with the pore pressure build-up. Green et al. (2000) proposed Equation 2.10, which provides an empirical expression for relating r_u to the Ws of soil and calibration parameter denominated as the pseudo-energy capacity (PEC):

$$r_u = \sqrt{\frac{Ws}{PEC}} \quad (2.10)$$

Such a model was developed using experimental data from cyclic element tests carried out on non-plastic silt-sand mixtures, which ranged in fines contents from clean sands to pure silts. The calibration parameter PEC is estimated from cyclic test data by plotting r_u versus the square root of Ws or calculated as follows (Green et al., 2000):

$$PEC = \frac{Ws, r_u=0.65}{(0.65)^2} = \frac{Ws, r_u=0.65}{0.4225} \quad (2.11)$$

The term pseudo-energy capacity or PEC indicates that the calibration parameter has a physical significance rather than just being a fit parameter (Polito et al., 2008). Consequently, PEC represents the normalised unit energy dissipated at the point of the liquefaction onset (Green, 2001). Figure 2.11 presents a graphical illustration of the PEC estimation.

Energy-based methods provide a powerful approach for assessing earthquake-induced liquefaction from historical cases, in-situ testing, cyclic element testing and physical modelling. This is because energy-based methods use parameters to quantify the load imposed on the soil by the earthquake and the capacity required to induce liquefaction, contrary to stress-based and strain-based methods (Alavi and Gan-

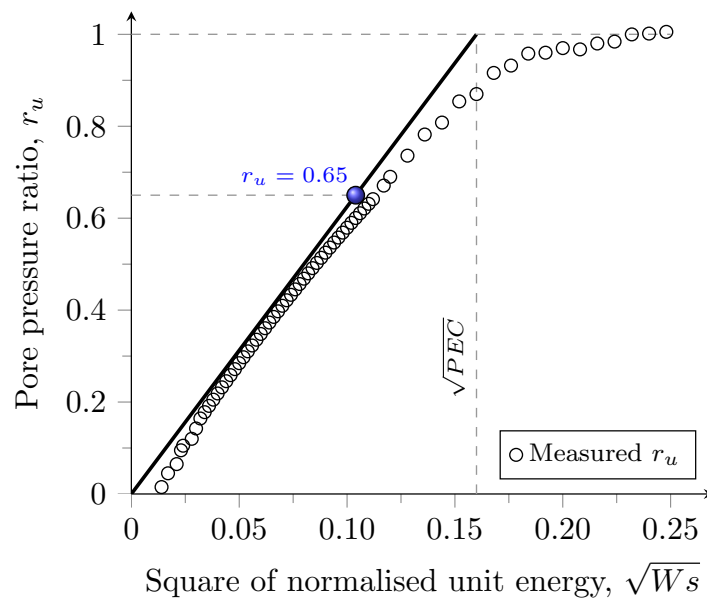


Figure 2.11: Graphical illustration of PEC estimation (adapted from Green et al. 2000)

domi, 2012). Moreover, the energy-based methods have shown more advantages than stress-based methods since their formulation allows estimating the liquefaction onset under irregular loading conditions (Rios et al., 2022), such as the cyclic loading induced in the ground during earthquakes. Therefore, several models involving an energy-based approach have been developed to relate the soil energy to trigger the liquefaction of sands with the shear strain amplitude and the state of soil (e.g. mean effective stress or confinement pressure and relative density).

Table 2.4 summarises a series of logarithmic regression models to estimate the accumulated energy required for triggering liquefaction as a function of the mean effective stress and relative density for diverse sands and based on different testing procedures, including element testing and physical models, involving different stress-state and relative densities. These models are also independent of the loading conditions, providing a reasonable estimation of liquefaction onset using element testing and physical modelling.

Table 2.4: Reported logarithmic energy-based models for liquefaction assessment (adapted from Alavi and Gandomi 2012)

Reference	Model	Testing apparatus	Testing method	Soil
Figueroa et al. (1994)	$\log Ws = 2.002 + 0.0048p'_0 + 0.0116Dr$	Cyclic torsional shear	Stress control	Reid Bedford sand
Liang (1995)	$\log Ws = 2.062 + 0.0039p'_0 + 0.0124Dr$	Cyclic torsional shear	Strain control	Reid Bedford sand
Liang (1995)	$\log Ws = 2.484 + 0.0047p'_0 + 0.0005Dr$	Cyclic torsional shear	Strain control	LSFD sand
Figueroa et al. (1999)	$\log Ws = 2.055 + 0.0048p'_0 + 0.0127Dr$	Cyclic torsional shear	Strain control	LSI-30 sand
Figueroa et al. (1999)	$\log Ws = 1.330 + 0.0061p'_0 + 0.0219Dr$	Cyclic torsional shear	Stress control	Nevada sand
Dief and Figueroa (2001)	$\log Ws = 2.459 + 0.0045p'_0 + 0.0012Dr$	Geotechnical centrifuge	60 g	Reid Bedford sand
Dief and Figueroa (2001)	$\log Ws = 1.164 + 0.0124p'_0 + 0.0209Dr$	Geotechnical centrifuge	60 g	Nevada sand

Note: Ws is the accumulated energy required for triggering liquefaction (in J/m^3); p'_0 is the initial mean effective stress; Dr is the relative density of soil.

For partially saturated soils, the total specific energy (W_{tot}) approach is used to assess the liquefaction susceptibility (Mele and Flora, 2019). The main feature of W_{tot} approach is the incorporation of the volumetric deformations during cyclic loading, which are mainly controlled by the fluid compressibility, corresponding to the mixture of gas and liquid .

Okamura and Soga (2006) proposed a theoretical formulation to relate the volumetric strain at liquefaction onset ($\varepsilon_{v,\text{liq}}$) with the initial degree of saturation (Sr_0) based on Boyle's law. Such a formulation also involves the initial void ratio (e_0), the initial air pressure ($u_{a,0}$) and the initial effective confinement stress (p'_0). The effective confinement stress can be assessed using the model proposed by Bishop and Blight (1963), which is valid for any Sr . Equation 2.12 describes the model to compute the $\varepsilon_{v,\text{liq}}$ of partially saturated soils.

$$\varepsilon_{v,\text{liq}} = \frac{e_0}{1 + e_0} (1 - Sr_0) \left(1 - \frac{u_{a,0}}{p'_0} \right) \quad (2.12)$$

Note that when $Sr_0 = 1.0$, the volumetric strain is zero. In such case, the energy-based methods referred to in Figure 2.9 provide a good estimation of liquefaction susceptibility. Moreover, Equation 2.12 indicates that there is a unique value of $\varepsilon_{v,\text{liq}}$, for specific values of e_0 (or Dr) and Sr_0 , which is consistent with the experimental evidence reported by Mele et al. (2019). Hence, these authors observed that during undrained cyclic tests, the relationship between p'/p'_0 and $\varepsilon_v/\varepsilon_{v,\text{liq}}$ does not depend on soil intrinsic and state properties, following the general law of Equation 2.13 (see also Figure 2.12).

$$\frac{p'}{p'_0} = 1 - \left(\frac{\varepsilon_v}{\varepsilon_{v,\text{liq}}} \right)^{1.7} \quad (2.13)$$

However, to apply Boyle's law to partially saturated soils, the system must follow the subsequent thermodynamic hypotheses (Mele et al., 2019):

- the process is isothermal; that is, no heat is generated or lost during the test;
- the mass of the system is constant; that is, no increase or decrease of the mass of air, water or soil in the specimen during the test;

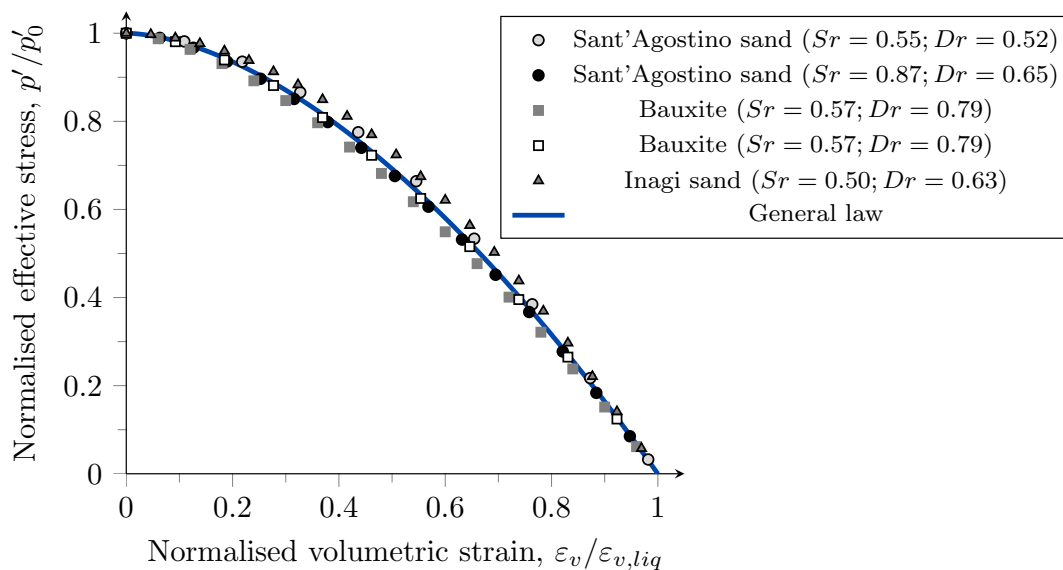


Figure 2.12: General law of normalised effective stress against the normalised volumetric strain of partially saturated soils subjected to cyclic loading (adapted from Mele and Flora 2019)

- the system is thermodynamically open; that is, within the specimen, the deformation process implies internal flows of air and water;
- the pore gas (air) can be treated as an ideal gas.

Under the hypotheses of Boyle's law, Equation 2.13 can be formally rewritten using the Helmholtz function (represented by Ψ). Li (2007) proposed the following equation to represent the gradient $d\Psi$ as a function of the internal energy during cyclic loading at a constant temperature, Equation 2.13 adopts the form:

$$d\Psi = [(p' - u_a\delta) + sSr\delta] : d\varepsilon - \frac{e}{1+e}sdSr + \frac{e_0}{1+e_0}(1 - Sr_0)u_a d(\ln \rho_a) \quad (2.14)$$

where the term $(p' - u_a\delta)$ is the net stress, u_a is the pore air pressure, s is the suction, Sr is the degree of saturation, e is the void ratio, the subscript 0 indicates the initial value, and ρ_a is the mass density of the air. In accordance with Li (2007), the incremental dissipation is neglected.

Mele et al. (2019) incorporated Helmholtz function (Equation 2.14) in the concept of total specific energy to assess the liquefaction resistance of partially saturated soils.

Such a new energy-based approach considers the sum of three components: (i) the work associated with the deformation of the soil skeleton; (ii) the work caused by the flow of water mass; and (iii) the work induced by the air into the porous media. Hence, W_{tot} can be expressed as:

$$W_{\text{tot}} = W_{sk} + W_w + W_a \quad (2.15)$$

where W_{sk} , W_w and W_a represent the specific work to cause deformation of the soil skeleton, water and air, respectively. W_{sk} covers the work due to change in volume (W_v) and the work caused by deviatoric strains (W_d), as follows in Equation 2.16:

$$W_{sk} = W_{v,sk} + W_{d,sk} \quad (2.16)$$

Considering the measured volumetric strains during element testing and incorporating thermodynamic hypotheses of Boyle's law, the elements of equations 2.15 and 2.16 can be evaluated as:

$$W_{v,sk} = \int_0^{\varepsilon_{v,\text{liq}}} [(p' - u_a) + sSr] d\varepsilon_v \quad (2.17)$$

$$W_{d,sk} = \int \int_{\Delta W} dq d\varepsilon_d \quad (2.18)$$

$$W_w = - \int_{Sr_0}^{Sr,\text{liq}} \left(\frac{eSr}{1 + eSr} sSr \right) dSr \quad (2.19)$$

$$W_a = \frac{e_0}{1 + e_0} (1 - Sr_0) u_{a,\text{liq}} d(\ln \rho_{a,\text{liq}}) \quad (2.20)$$

Mele et al. (2019) stated that $W_{v,sk}$ depends on the soil state (that is, p'_0 , e_0 and Sr) and is independent of CSR; whereas $W_{d,sk}$ only comprises the dissipated strain energy. Therefore, it can be estimated from the sum of the areas of all loading cycles (as indicated in Figure 2.9). Besides, these authors observed that W_w associates the liquefaction of partially saturated soils with the variations of Sr , which can

be attributed to the volumetric deformations during cyclic loading. Finally, W_a describes the effect of pressure variation in the gas phase.

2.3 Saturation in soils and its measurements

2.3.1 States of saturation in soils

Soils comprise an assemblage of grains —forming the soil skeleton— and fluid material. The fluid material (liquid or gas) fills the pores of the soil skeleton. In natural deposits, the soil can present all or some of the following conditions: ‘dry’, ‘unsaturated’, ‘partially saturated’ and ‘fully saturated’ according to the volume of liquid (typically water) in the pores of the soil skeleton (Zeybek and Madabhushi, 2020).

Dry soils are typically located on the ground surface or in the shallow layers of the natural deposits, but this condition is weather dependent (Fredlund and Rahardjo, 1993). Unsaturated soils are the most common materials in natural deposits and cover a saturation state in which the soil voids are water and air. Besides, these soils are above the current or historical groundwater level, having pores filled with air and menisci of water. In such menisci, pore water pressures are usually negative due to capillary suction (Fredlund, 2006). Partially and fully saturated soils are located below the current groundwater level. In both conditions, soil voids are primarily filled with water. The difference between these conditions is that partially saturated soils have air bubbles in the fluid (Zeybek and Madabhushi, 2017). Therefore, the S_r of partially saturated soils is relatively low compared to fully saturated soils. Although the voids are filled with water, occluded air bubbles in the fluid have no direct contact between the solid particles and the gas. Figure 2.13 illustrates the saturation states in soil deposits. Moreover, this figure displays how liquefaction resistance increases from saturated to dry conditions.

Dry and fully saturated soils comprise only two phases, including the soil skeleton and gas or liquid. In these saturation conditions, the gas or liquid is in a continuous phase, directly interacting with the soil grains (Fernandes, 2017). Unsaturated and partially saturated soils have three phases: soil skeleton, gas and liquid. The unsaturated condition includes a continuous gas phase (commonly composed of air), which creates a series of water meniscus between the grains contacts. On the other hand, in the partially saturated condition, the gas exists as occluded bubbles surrounded by

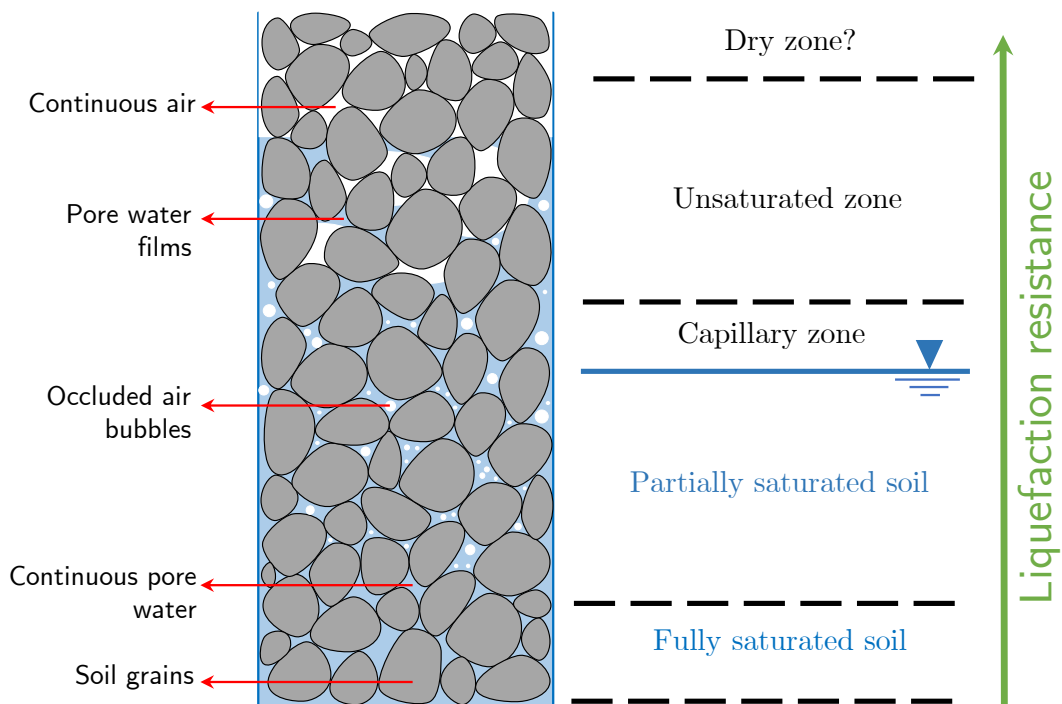


Figure 2.13: State of saturation in soil deposits (adapted from Zeybek and Madabhushi 2020)

the pore fluid. Such a condition was established for higher S_r values, i.e., between 80% and 99% (Okamura and Soga, 2006). Figure 2.14 shows the distributions of phases in unsaturated and partially saturated soils.

By using enlarged and high-quality images, Zeybek and Madabhushi (2017) observed that the size of the air bubbles was generally smaller than or in the same order as the size of the sand particles. These authors identified that these air bubbles are in discrete forms and fit the pore spaces without interacting with the soil grains.

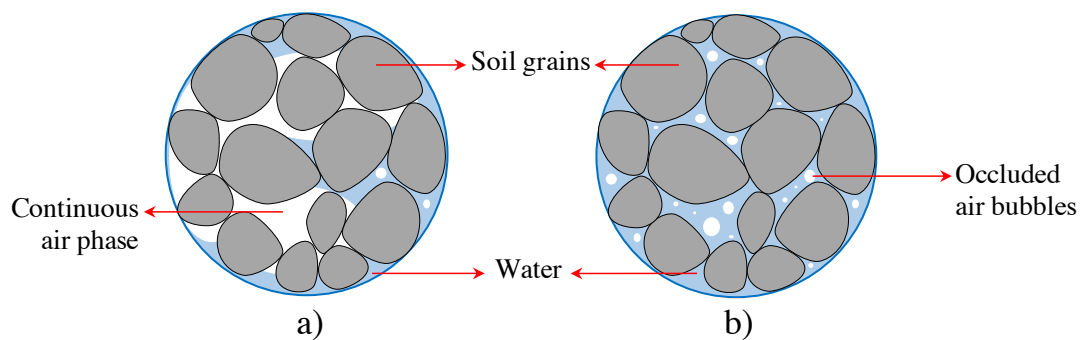


Figure 2.14: Gas distribution in different soil states: a) unsaturated condition; b) partially saturated condition

Therefore, the matric suction is negligible in partially saturated sandy soils since pore water and pore air pressures can be considered almost equal (Zeybek and Madabhushi, 2020). This effect is because occluded air bubbles are in equilibrium with the surrounding pore fluid.

The occluded air bubbles increase the volumetric compressibility of the medium, even at the micro-scale, reducing the pore pressure build-up during cyclic loading and, consequently, the liquefaction susceptibility of partially saturated sandy soils (Okamura and Soga, 2006; Tsukamoto et al., 2014; Mele and Flora, 2019). Studies developed by Yoshimi et al. (1989); Yang (2002); Eseller-Bayat et al. (2013); Tsukamoto (2019) demonstrated that the degree of saturation (S_r) influences the pore pressure build-up during earthquake-induced liquefaction. Physical models conducted by Zeybek and Madabhushi (2017) in dynamic centrifuge tests on partially saturated sand models also validate these conditions. Therefore, such experimental evidence confirmed the influence of S_r on liquefaction resistance, which increases from saturated to dry conditions and has optimal values in the partially saturated condition.

2.3.2 Experimental procedures to measure the degree of saturation in soils

During element testing, the saturation of the soil sample can be estimated by measuring the value of the pore pressure coefficient B (or B -value). Skempton (1954) defined the B -value as the ratio between the increment of the isotropic confining pressure ($\Delta\sigma$) with the corresponding increment of pore pressure (Δu) under undrained conditions, as follows in equation 2.21.

$$B = \frac{\Delta u}{\Delta\sigma} \quad (2.21)$$

In fully saturated conditions, B -value is about 1.0 —that is, $\Delta\sigma \approx \Delta u$. This response is due to the volumetric compressibility of granular media, which corresponds to a combination between the bulk modulus of soil skeleton, K_{sk} , and the bulk modulus of the pore fluid, K_f , (Skempton, 1954). However, the estimation of B -value considers two assumptions: (i) the soil remains incompressible when applying $\Delta\sigma$; and (ii) the porosity of soil skeleton (n) does not change with the increment of cell pressure. Equation 2.22 presents the model to estimate B -value based on the

volumetric compressibility of granular media.

$$B = \left(1 + n \frac{K_{sk}}{K_f}\right)^{-1} \quad (2.22)$$

Equation 2.22 considers the fluid in the soil skeleton as a mixture of liquid and gas, which typically corresponds to water and air (Ishihara, 1970). Hence, K_f can be computed from the bulk modulus of water and air (K_w and K_a) for a given degree of saturation, Sr (see equation 2.23).

$$K_f = \left(\frac{Sr}{K_w} + \frac{1 - Sr}{K_a}\right)^{-1} \quad (2.23)$$

Emerson and Foray (2006); Leong and Cheng (2016) suggested values of K_w and K_a equal to 2.18×10^6 kPa and 142 kPa, respectively. By combining equation 2.22 and equation 2.23, B -value can be estimated as a function of Sr and bulk moduli of the granular media (i.e. K_{sk} , K_w and K_a), as follows in equation 2.24.

$$B = \left[1 + n \cdot K_{sk} \left(\frac{Sr}{K_w} + \frac{1 - Sr}{K_a}\right)\right]^{-1} \quad (2.24)$$

Ensuring B -values higher than 0.97 is particularly important in undrained element tests for assessing liquefaction resistance (Soares and Viana da Fonseca, 2016). However, measurements of B -value cannot be carried out during physical modelling (e.g. shaking table and geotechnical centrifuge tests) or in the field due to the lack of control of undrained conditions (Kokusho, 2000; Naesgaard et al., 2007; Rebata-Landa and Santamarina, 2012; Eseller-Bayat et al., 2013; Gu et al., 2021; Zhang et al., 2021). Therefore, Sr must be estimated by implementing alternative methods for physical modelling and field applications.

Studies conducted by Tsukamoto et al. (2002); Emerson and Foray (2006); Conte et al. (2009); Kumar and Madhusudhan (2012); Kim et al. (2021) showed that changes in Sr lead to variations in the propagation of primary wave (or P-wave) velocity, V_p . Such a response is a consequence of the environment in which the P-wave is propagated; that is, the existence of water in the voids. The above means that P-wave is preferably propagated through the fluid and not by the soil grains (Foti et al., 2002). Therefore, the V_p values in saturated soils are higher than 1482

m/s since the wave propagation is mainly controlled by the water in the pores of soil skeleton (Santamarina et al., 2001).

Biot (1956a; 1956b) proposed a series of relationships involving the characteristic linear poroelasticity parameters to estimate the wave propagation in fluid-saturated granular media, which is only valid if relative movement between soil grains does not occur (Ishihara, 1970). These relations involve the bulk modulus (K_{soil}), the shear modulus of the soil (G_{soil}), and mass density (ρ_{soil}) of the propagation medium, in this case, the soil, as follows in equation 2.25:

$$Vp = \sqrt{\frac{K_{\text{soil}} + \frac{4}{3}G_{\text{soil}}}{\rho_{\text{soil}}}} \quad (2.25)$$

$$K_{\text{soil}} = K_{\text{sus}} = K_{sk} + K_f \quad (2.26)$$

where K_{soil} is the sum of the bulk modulus of the suspension composed of the fluid and solid particles (K_{sus}) with the bulk modulus of soil grains (K_{sk}). For unsaturated soils, the bulk modulus of the suspension, K_{sus} , can be computed from the porosity of soil (n), the bulk modulus of the grains (K_g) and the bulk modulus of the fluid (K_f), which depends on Sr , K_w and K_a (see equation 2.23). Equation 2.27 defines the computation of K_{sus} .

$$K_{\text{sus}} = \left(\frac{1-n}{K_g} + \frac{n}{K_f} \right)^{-1} \quad (2.27)$$

In addition, considering that the shear stiffness in the fluid is null, K_{sk} can be computed using the equation 2.28.

$$K_{sk} = \frac{2}{3}G_{\text{soil}} \frac{1 + \nu_{sk}}{1 - 2\nu_{sk}} \quad (2.28)$$

where ν_{sk} is the Poisson's ratio of soil skeleton. This parameter can be obtained in dry conditions by estimating as a function of both P-wave velocity (Vp) and S-wave velocity (Vs), as follows:

$$\nu_{sk} = \frac{\frac{1}{2} \left(\frac{Vp}{Vs} \right)^2 - 1}{\left(\frac{Vp}{Vs} \right)^2 - 1} \quad (2.29)$$

The Equation 2.29 also provides an approximate estimation of Poisson's ratio of the soil (ν) for different Sr since the soil is a homogeneous non-continuous porous media with fluid. On the other hand, there is an influence of n on ρ_{soil} (equivalent to density of the suspension ρ_{sus}) since it is the parameter controlling the volume of fluid that saturates the soil. Therefore, the bulk mass density of fluid-saturated porous media is defined by:

$$\rho_{\text{soil}} = \rho_{\text{sus}} = (1 - n) \rho_g + n \rho_f \quad (2.30)$$

where ρ_g is the bulk mass density of the soil grains and ρ_f is the mass density of the fluid, which depends on the degree of saturation (Sr), the density of the air (ρ_a) and density of the water (ρ_w), as follows:

$$\rho_f = (1 - Sr) \rho_a + Sr \rho_w \quad (2.31)$$

Based on the equations of motion governing the propagation of P-wave, Equation 2.32 can be derived to assess Vp in fluid-saturated soils (Yang and Sato, 2001; Foti et al., 2002):

$$Vp = \sqrt{\frac{K_{sk} + \frac{1}{n} K_f + \frac{4}{3} G_{\text{soil}}}{(1 - n) \rho_{\text{soil}} + n \rho_f}} \quad (2.32)$$

Figure 2.15 applies Biot's theory to describe the evolution of Vp as a function of the degree of saturation by varying both ν and n . The computations of Figure 2.15 were conducted by adopting $Vs = 230$ m/s, $K_g = 3.5 \times 10^9$ kPa and $\rho_g = 2.65$ g/cm³ (Santamarina et al., 2005).

The results of Biot's model showed a notable influence of Sr on Vp , particularly for Sr higher than 90%. In such a range, Vp sharply increases, reaching values of about

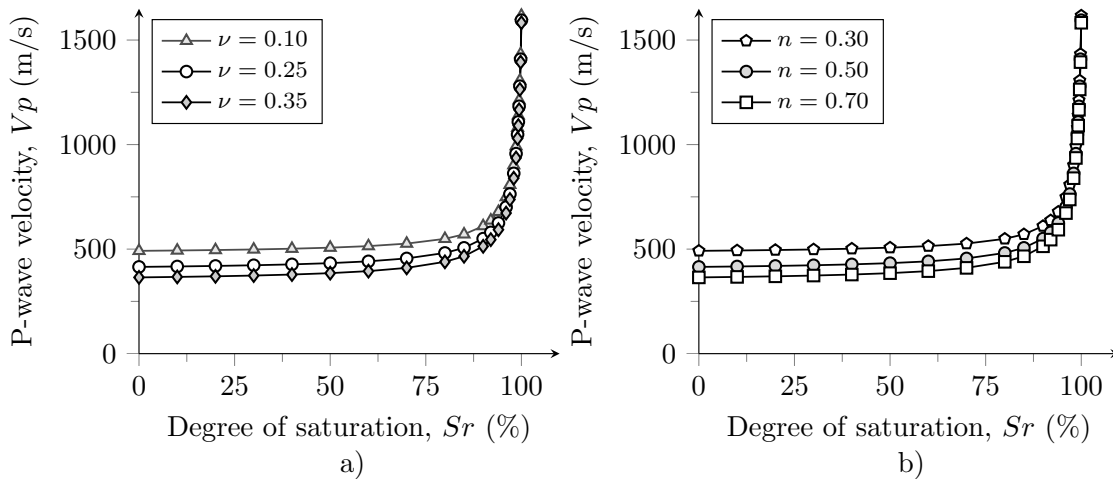


Figure 2.15: Evolution of V_p in soils near the full saturation conditions (after [San-tamarina et al. 2005](#)): a) effect of ν ; b) effect of n .

1500 m/s. The above is consistent with the experimental findings reported by [Nakagawa et al. \(1997\)](#); [Valle-Molina and Stokoe \(2012\)](#); [Leong and Cheng \(2016\)](#).

Based on this principle, Equation 2.33 allows estimating V_P as a function of B -value in granular media ([Yang, 2002](#)):

$$V_p = \sqrt{\frac{\frac{4}{3}G_{\text{soil}} + \frac{K_{sk}}{1+B}}{(1-n)\rho_{\text{soil}} + n\rho_f}} \quad (2.33)$$

Note that Equation 2.33 satisfies the principles of the continuum mechanics ([Biot, 1956a,b](#)), providing a robust theoretical framework to correlate the degree of saturation of the soil obtained from different measurement methods. This has a particular interest and application to assess techniques for liquefaction mitigation based on induced partial saturation since it allows correlating results of in situ and laboratory testing ([Yang, 2002](#); [Tsukamoto et al., 2002](#)).

Figure 2.16 illustrates the variation of V_p and B -value, by adopting the same soil parameters of Figure 2.15 for different n . From Figure 2.16, it can be observed that V_p remains constant for B -values lower than 0.50, and then it slowly increases until a B -value of about 0.85. Afterwards, V_p sharply tends toward (or even exceeds) the V_p value in water (i.e. > 1482 m/s), indicating the full saturation condition of the soil for B -values higher than 0.975. The literature reports studies focused on assessing the V_p and B -value relationship. Table 2.5 summarises the details of

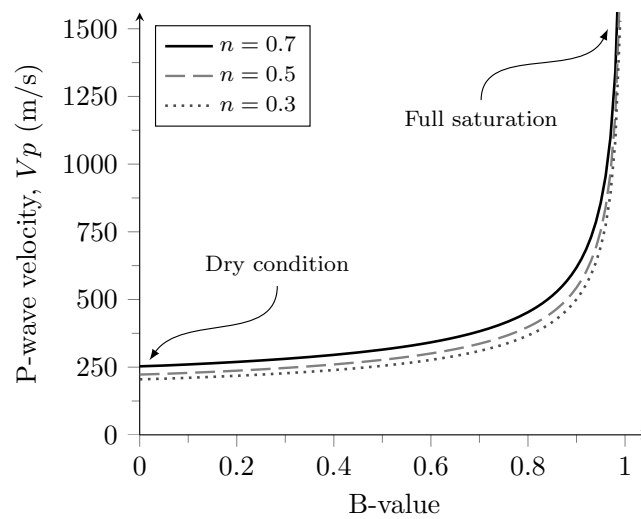


Figure 2.16: Relationship between V_p and B -value (adapted from Yang 2002)

experimental studies carried out to validate the relation between V_p and B -value using Equation 2.33 in sandy soils.

Tsukamoto et al. (2002) and Leong and Cheng (2016) reported a good agreement between experimental measurements and the theoretical approach of Equation 2.33, showing differences for B -values from 0.50 to 0.95. In these studies, V_p tends to a value of about 1500 m/s for B -values higher than 0.97, as observed by Soares and Viana da Fonseca (2016). The evolution of V_p as a function of B -value agrees with the results reported by Kokusho (2000). Tamura et al. (2002) stated that the discrepancies between laboratory measurements and theoretical predictions are due to the size and solubility of air bubbles in the pore-water. Naesgaard et al. (2007) conducted a series of numerical modelling in FLAC to assess the effects of the homogeneous and non-homogeneous distribution of gas-phase in the evolution of V_p as a function of B -value. These authors observed that the size of air bubbles affects the V_p and B -value relationship; that is, a good fitting between experimental measurements and theoretical approach when simulating a homogeneous distribution of air into the fluid (e.g. occluded air bubbles) and important differences of V_p evolution in models involving a continuous three-phase of soil (the unsaturated condition).

Gu et al. (2021) explored the effects of the types of pore air and pore fluid on the relationship between V_p and B -value (i.e. CO₂ flushing, tap water and de-aired water). These authors observed that V_p measurements were independent of the B -value for the specimens with de-aired water, while V_p increased as B -value increased

Table 2.5: Summary of experimental studies on the V_p and B -value relationship

Reference	Soil	Dr (%)	p' (kPa)	B -value	V_p (m/s)
Tamura et al. (2002)	Toyouura sand	64 - 84	49	0.36 - 0.97	660 - 1643
Tsukamoto et al. (2002)	Toyouura sand	30 - 70	98	0.00 - 0.90	400 - 1770
Naesgaard et al. (2007)	Fraser sand	20	30	0.36 - 0.99	1415 - 1557
Kumar and Madhusudhan (2012)	*	40 - 80	100 - 300	0.94 - 1.00	512 - 1756
Leong and Cheng (2016)	River sand	*	30	0.56 - 0.97	200 - 1688
Gu et al. (2021)	Fujian sand	70.5	30	0.36 - 0.99	340 - 1720

Note: *do not reported

for the soil specimens containing tap water. These differences are because tap water has more air than de-aired water. Therefore, the higher content of occluded air bubbles in the tap water affects the measurements of B -values, which does not allow for correctly reproducing the in situ state of the soil/fluid interface.

From the conclusions of these previous studies, it can be drawn that: (i) V_p increases as the B -value increases for the low and full saturation condition, following a parallel tendency between experimental measurements and the theoretical approach; and (ii) evolution of P-wave propagation and B -value is significantly affected by the compressibility of the pore fluid type and distribution of gas bubbles (occluded or in a continuous phase) in the soil skeleton.

2.4 Techniques for liquefaction mitigation

2.4.1 Conventional techniques for liquefaction mitigation

Many techniques to mitigate soil liquefaction have been developed in the last decades. However, recent earthquake-induced liquefaction events (e.g. 1999 Adapazari (Turkey), 2010 Maule (Chile), 2011 Christchurch (New Zealand) and 2011 Great East (Japan) earthquakes) indicate that the problems have not yet been solved, motivating research about the improvement of liquefaction resistance and mitigation techniques. Techniques for mitigation of soil liquefaction aim to prevent the 100% development of excess pore water pressure (Towhata, 2008).

Techniques for liquefaction mitigation comprise the enhancement of soil fabric or the modification/change of the soil state. Nevertheless, liquefaction mitigation methods face three main problems (Huang and Wen, 2015): (i) how to achieve non-disruptive mitigation of liquefaction risk at developed sites susceptible to liquefaction, especially under vulnerable structures; (ii) how to achieve liquefaction mitigation in large areas at low cost; and (iii) how to combine liquefaction mitigation with environmental friendliness and low-carbon economy.

The selection of mitigation techniques mainly depends on the existence of structures in the liquefiable soil deposit. In-built areas (for new or with existing structures), the mitigation techniques aim to prevent the onset of liquefaction, whereas, for free-field areas, mitigation techniques deal with the reduction of liquefaction-induced damage (Towhata, 2008; Huang and Wen, 2015). Hence, installation of mitigation techniques before construction has a clear and straightforward procedure, while it is more complex in areas with existing structures. Towhata (2021) stated that when the implementation of technologies for soil improvement is not feasible, structural reinforcements are the best solution to reduce or mitigate liquefaction-induced damage. Usually, such reinforcements deal with enhancing the foundation systems by increasing the soil stiffness, which may eventually amplify the seismic action reaching the surface.

Other factors for selecting the mitigation technique cover the soil type, stratigraphy, depth of liquefiable layer(s), area size to be improved, foundation type, constraints, subsurface obstructions, and environmental compatibility. Meslem et al. (2019) classified the level of importance to the applicability criteria and weighted accordingly all factors presented herein. Table 2.6 shows the list of the factors considered by Meslem et al. (2019) to select the mitigation techniques.

Table 2.6: Factors influencing the applicability of mitigation techniques (adapted from Meslem et al. 2019)

Factors	Level of importance	Weight	Details
Site conditions	Very important	18.2%	It comprises the free-field condition or the presence of existing structures.
Soil type	Very important	18.2%	Soil type affects the performance of some technologies, affecting the suitability of the mitigation techniques.
Stratigraphy	Medium important	9.1%	It links the suitability of techniques due to the presence of interlaying or crust.
Depth of the treatment zone	Very important	18.2%	It affects the suitability of techniques because of the equipment capacity for the technical implementation in the field.
Size of the treatment area	Less important	4.5%	It controls the economic costs of techniques implementing. Size area classification: Small Area (less than 1000 m ²); Medium Area (between 1000 and 5000 m ²); High Area (more than 5000 m ²).
Foundation	Less important	4.5%	The foundation type allows sorting of technologies based on the usefulness of the ground improvement techniques to the specific foundation type (shallow or deep).
Project constraints	Medium important	9.1%	It allows selecting technologies considering the following cases: (i) low overhead clearance: there is no accessibility of the equipment to reach the site; (ii) adjacent structures: some technologies could damage the adjacent structures – adjacent buildings and structures must be monitored; (iii) existing utilities, i.e. the technology may be acceptable if there are some existing utilities –this could affect the ground improvement.
Subsurface obstructions	Medium important	9.1%	It can affect the selected technique. Some examples: cobbles, boulders or construction debris, water-bearing sands, organic layers and very stiff surface deposits can significantly impact the type of ground improvement technologies that can be selected.
Environmental compatibility	Medium important	9.1%	It may include disposal of spoils from ground improvement technologies, disposal of waste materials, protection of the site from erosion, protection of surface and ground waters from pollution, inducing vibrations, noise and dust.

To properly discuss the mitigation of soil liquefaction, it is essential to identify the triggering mechanism, the characterisation of liquefiable soils (by in-situ and laboratory testing) and the procedures to assess the liquefaction resistance in soil deposits. Table 2.7 summarises the advancements to characterise the earthquake-induced liquefaction after the Niigata earthquake. This table provides a better understanding of the recent advances regarding liquefaction phenomena. Besides, Table 2.8 presents an association between the processes towards soil liquefaction with methods to prevent them, providing initial insights about the fundamentals for liquefaction mitigation.

Based on a comprehensive literature review (e.g. Kramer 1996; Yegian et al. 2007; Rebata-Landa and Santamarina 2012; He et al. 2013; Huang and Wen 2015; Marasini and Okamura 2015; Bao et al. 2019; Salvatore et al. 2020; Towhata 2021; Seyedi-Viand and Eseller-Bayat 2021) the following classification of liquefaction mitigation techniques is proposed:

- soil improvement;
- drainage;
- soil densification;
- induced partial saturation.

The soil improvement techniques deal with the change of soil fabric. Within such techniques, the artificial cementation and addition of fines are highlighted. The soil reinforcement techniques cover the artificial cementation methods to increase the soil stiffness, whereas adding fines decreases the soil permeability, limiting the pore pressure build-up (Kramer, 1996). On the other hand, the implementation of drainage systems (e.g. horizontal and vertical drains) allows rapid dissipation of the pore pressure build-up during seismic action, reducing the liquefaction susceptibility. The drains can be implemented in free-field or in areas with existing buildings. Nevertheless, their implementation depends on the geometry and direction, that is, horizontal or vertical. Therefore, drainage is a promising concept to consider in shallow layers (not deeper than 10 m) using diameters less than 30 cm (Fasano et al., 2019). However, the main limitation of drainage systems lies in controlling soil deformations or settlements during cyclic loading.

Table 2.7: Timeline of recent advances on the characterisation of soil liquefaction (Ishihara, 1993, 1996; Kramer, 1996; Towhata, 2008; Boulanger and Idriss, 2014; Towhata, 2021)

Topics	Years	Remarks	Advancements
Case histories	1960s–now	Investigation on earthquake damages and site response	Identification of liquefaction-induced damages due to significant reduction of effective stress during seismic loading.
Consequences of liquefaction	1960s–2000s	Damages in buildings and critical infrastructures	Permanent deformations, settlements, subsidence, tilting, floating, landslides, lateral spreading, and its combinations.
Assessment of liquefaction susceptibility	1970s–now	In situ testing	Correlations of liquefaction resistance with SPT, CPT, DMT and geophysical results.
	1980s–now	Laboratory testing	Shear tests under undrained cyclic loading up to large strains.
High-quality samples	1990s–now	Advanced sampling techniques	Collecting undisturbed and representative samples in liquefiable soil deposits.
Mechanisms of liquefaction	1970s–2000s	Factors affecting liquefaction susceptibility of soils	Association of liquefaction susceptibility with morphology (grain size distribution and particle shape), fines content, plasticity and permeability.
Prediction of deformations and pore pressure build-up	1980s–now	Numerical tools	Development of computational codes and numerical modelling.
	1990s–now		Formulation of constitutive laws.
	2000s–now	Physical modelling	Scaled tests in shaking table and geotechnical centrifuge.
	2000s–now		Benchmarks and instrumentation of case histories.
Mitigation of liquefaction susceptibility and effects	1970s–now	Soil improvement	Implementation of techniques such as compaction/densification, jet grouting, deep mixing, horizontal/vertical drains and induced partial saturation.
	1990s–now	Protection of new and existing structures	Construction of deep foundations or retaining walls and structural reinforcement.

Table 2.8: Principles of liquefaction mitigation (Towhata, 2021)

Process toward liquefaction	Principles of mitigation
Loose packing of particles	Compaction/densification
Falling of particles into big voids	Bonding/grouting of grains
Notable cyclic motion of particles	Constraints against ground motion
Long time needed for drainage	Installation of water channel; drains
Incompressibility of pore water	Dewatering or injection of gas bubbles

On the other hand, densification and induced partial saturation (IPS) are the most common methods for modifying the state of the soil. The densification methods allow increasing the shear strength of the improved soil deposit. In contrast, the IPS methods increase the volumetric compressibility due to the presence of gas bubbles, which significantly reduce the pore pressure build-up during cyclic loading (Okamura and Soga, 2006). Since this research focuses on assessing induced partial saturation (IPS) techniques for liquefaction mitigation, only techniques for IPS will be thoroughly addressed in the next section.

2.4.2 Techniques to induce partial saturation for liquefaction mitigation

The techniques to induce partial saturation (IPS) allow for improving the resistance of soils against liquefaction by increasing the compressibility of the pore fluid with the generation of some amount of gas. The presence of the gas (e.g. air) creates occluded air bubbles in the pore fluid, inducing a condition of partial saturation in the soil, as described in Section 2.3. As the gas content of the fluid increases, liquefaction resistance increases (Rebata-Landa and Santamarina, 2012). Hence, the number of cycles to trigger liquefaction in partially saturated soils is higher than in fully saturated soils.

Figure 2.17 compiles results of experimental studies comparing the cyclic liquefaction resistance of well-characterised sands at different degrees of saturation, including the full-saturation condition. On the other hand, Figure 2.18 presents the normalised cyclic resistance (NCR), which is a normalisation of liquefaction resistance for different S_r concerning liquefaction resistance reported in fully saturated conditions (Ishihara et al., 1998; Tsukamoto et al., 2002). NCR was obtained using the data reported in Figure 2.17 and by estimating the CSR corresponding to 15 cycles to trigger liquefaction for each sand. From Figure 2.18, it can be observed that a

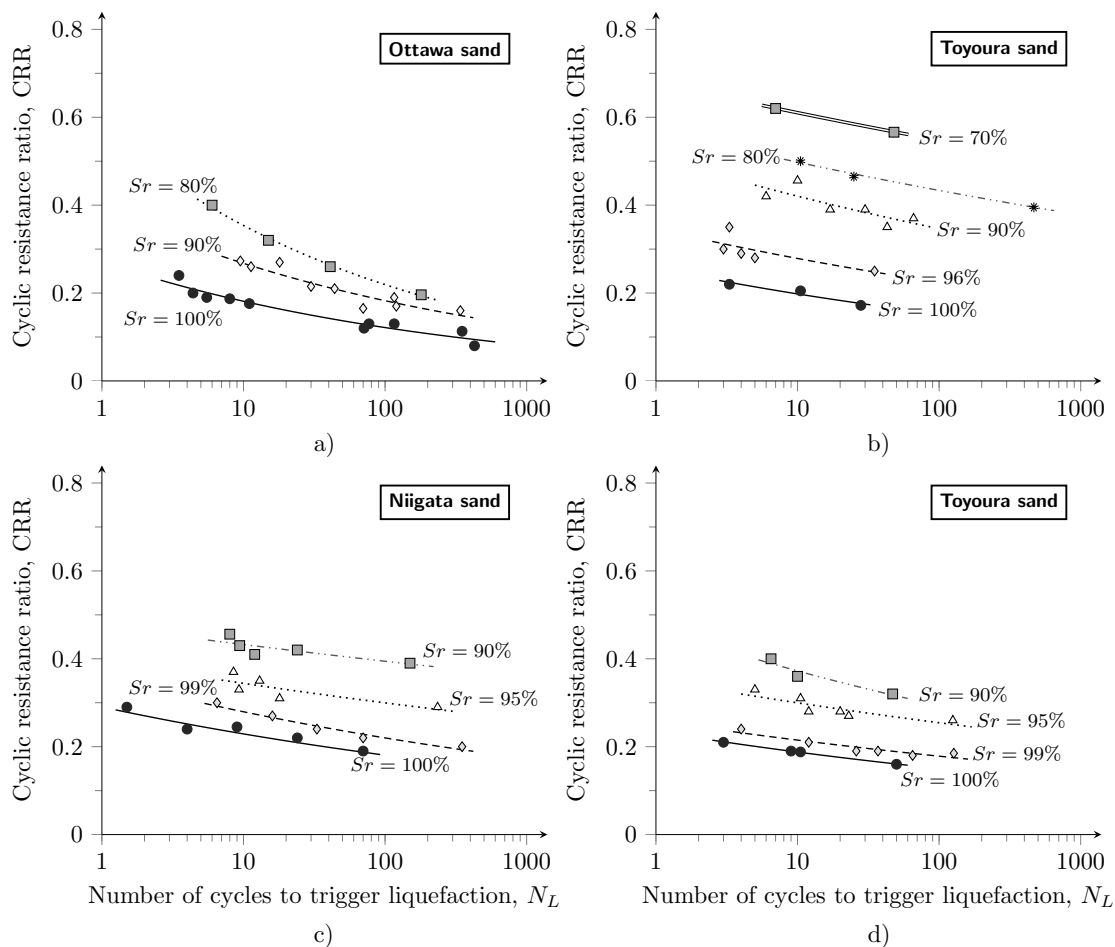


Figure 2.17: Influence of degree of saturation on the liquefaction resistance: a) Ottawa sand (after Sherif et al. 1977); b) Toyoura sand (after Yoshimi et al. 1989); c) Niigata sand (after Ishihara et al. 1998); d) Toyoura sand (after Tsukamoto et al. 2002)

reduction of S_r from 100% to 90% doubled the liquefaction resistance, providing experimental evidence about the effectiveness of IPS as a liquefaction mitigation technique.

The improvement of liquefaction resistance in partially saturated soils is due to the following mechanisms: (i) the matric suction; and (ii) the reduction of the fluid compressibility. The matric suction increases the effective stress and, consequently, the stiffness and strength of the soil (Bishop and Blight, 1963). However, the matric suction can be considered negligible for liquefaction resistance since the maximum matric suction of clean sands is about 4 kPa (Fredlund, 2006). These suction values are not relevant compared to the effective stress in natural soil deposits. Therefore, reducing fluid compressibility is the main mechanism that increases the liquefaction

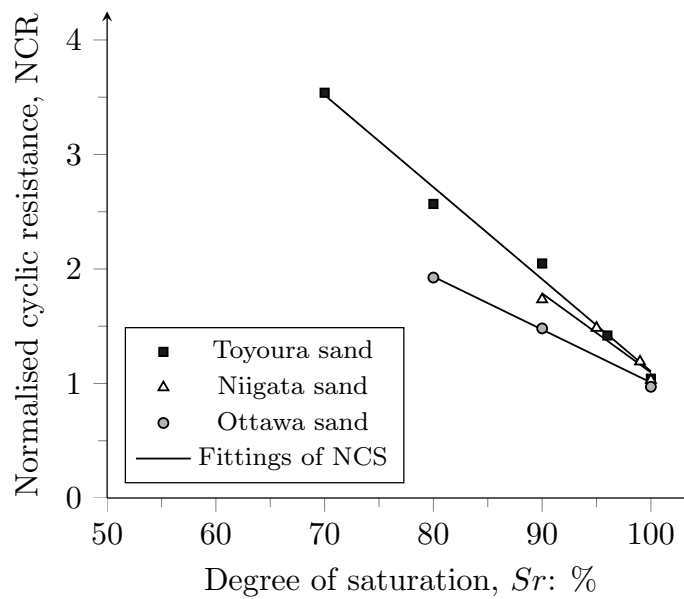


Figure 2.18: Normalised cyclic ratio for different sands (data from: Sherif et al. 1977; Yoshimi et al. 1989; Ishihara et al. 1998; Tsukamoto et al. 2002)

resistance of clean sands. This is because the occluded air bubbles allow absorbing the pore pressure build-up generated during seismic action by reducing the soil volume (Pietruszczak and Pande, 1996). The enhancement of soil resistance is due to the reduction of the bulk modulus of the pore fluid —caused by the presence of air bubbles.

Okamura and Soga (2006) proposed a method for assessing the effect of gas compressibility on liquefaction resistance by estimating the relationship between the liquefaction resistance ratio (LRR) with potential volumetric strains (ε_v^*) achieved at $r_u = 1$. These authors defined LRR by normalising the liquefaction resistance obtained in partially and fully saturated soil specimens, and ε_v^* through Equation 2.34:

$$\varepsilon_v^* = \frac{p'_0}{BP + p'_0} (1 - Sr) \frac{e}{1 + e} \quad (2.34)$$

where p'_0 corresponds to the initial mean effective stress, BP denotes the back pressure of during shearing (also designated as absolute fluid pressure), Sr is the degree of saturation, and e is the void ratio of the soil. Such a method involved the compilation of triaxial test results conducted in Toyoura sand under different effective confinement stresses (from 50 kPa to 200 kPa), relative densities (from 40% to 90%)

and degrees of saturation (from 70% to 100%). Figure 2.19 presents the relation between potential volumetric strains with the liquefaction resistance ratio proposed by Okamura and Soga (2006).

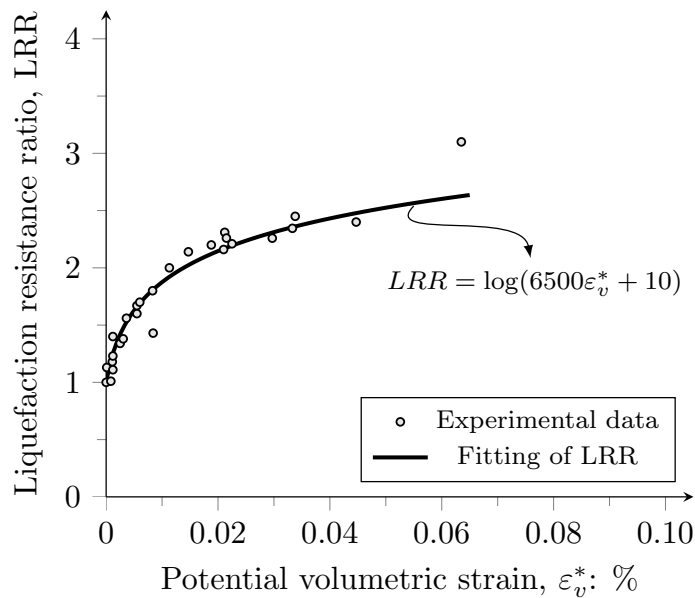


Figure 2.19: Potential volumetric strain vs liquefaction resistance ratio (adapted from Okamura and Soga 2006)

Experimental studies addressing the gas compressibility on the liquefaction resistance of partially saturated soils have reported several element tests and physical models subjected to static and dynamic loading. Table 2.9 reviews such experimental studies for assessing the liquefaction resistance in partially saturated sands. Indeed, there is an effect of the degree of saturation on the liquefaction resistance, demonstrating the great potential and plausibility of the application of IPS for liquefaction mitigation.

Table 2.9: Studies on the liquefaction resistance of partially saturated sands

Reference	Experimental setup	Range tested of Sr	Evaluation of liquefaction resistance
Yoshimi et al. (1989)	Cyclic triaxial	70% to 100%	B-value decreases; N_L increases
Ishihara et al. (1998)	Cyclic triaxial	90% to 100%	B-value decreases; V_p increases; N_L increases
Tsukamoto et al. (2002)	Cyclic triaxial	90% to 100%	B-value decreases; V_p increases; N_L increases
Okamura and Soga (2006)	Cyclic triaxial	70% to 100%	ε_v increases; N_L increases
Yegian et al. (2007)	Shaking table	72% to 100%	Sr decreases; r_u decreases
Unno et al. (2008)	Cyclic triaxial	12% to 100%	s increases; N_L increases
Eseller-Bayat et al. (2013)	Shaking table	40% to 100%	Sr decreases; γ decreases; r_u decreases
He et al. (2013)	Shaking table	84% to 100%	Sr decreases; γ decreases; r_u decreases
Tsukamoto et al. (2014)	Cyclic triaxial	42% to 100%	s increases; ε_v ; N_L increases
Marasini and Okamura (2015)	Geotechnical centrifuge	85% to 100%	Sr decreases; r_u decreases
Wang et al. (2016)	Cyclic and monotonic triaxial	68% to 100%	Sr decreases; ε_v increases; N_L increases
Zeybek and Madabhushi (2017)	Geotechnical centrifuge	85% to 100%	Sr decreases; r_u decreases
Mele et al. (2019)	Cyclic triaxial	54% to 100%	Sr decreases; ε_v increases; W_{tot} increases; N_L increases
Tsukamoto (2019)	Cyclic and monotonic triaxial	41% to 100%	Sr decreases; USR increases; N_L increases
Wang et al. (2020)	Cyclic and monotonic triaxial	83% to 100%	Sr decreases; USR increases; N_L increases

Note: Sr is degree of saturation; N_L is the number of cycles required to liquefaction; V_p is P-wave velocity; ε_v is volumetric strain; r_u is pore pressure ratio; s is matric suction; γ is shear strain; W_{tot} is the total specific energy; and USR is undrained shear resistance.

Despite the beneficial effects of reducing Sr to increase the liquefaction resistance of soils, this concept as a countermeasure of earthquake-induced liquefaction has yet to be thoroughly studied [Flora et al. \(2020\)](#). IPS has emerged as a new cost-effective and environment-friendly liquefaction mitigation technique ([Pietruszczak et al., 2003](#); [Okamura et al., 2011](#); [Zeybek and Madabhushi, 2018](#)). This method is relatively inexpensive as it involves only injection or production of gas in the soil deposit ([He et al., 2014](#)). The partial saturation condition enhances the liquefaction resistance by inducing gas bubbles, which can be applied in soil deposits using the following techniques:

- air injection;
- water electrolysis;
- chemical desaturation;
- bio-desaturation or microbial desaturation.

The air injection technique relies on artificial air injection into the saturated and liquefiable soil deposits. The principle of this technique considers the application of pressurised air into the ground to introduce small-sized air bubbles in the voids, reducing the degree of saturation of the soil deposit ([Marasini and Okamura, 2015](#)). Nevertheless, the air must be injected at pressures that will not cause hydro-fracture. Hence, the air pressure must overcome the value enabling air (equal to the sum of the hydrostatic and capillarity pressures) to penetrate through pore water to guarantee the airflow in the soil deposit. [Figure 2.20](#) schematises the in-situ air injection technique. [Okamura et al. \(2011\)](#) achieve a desaturation zone ranging from 68% to 98% degree of saturation by injecting air in-situ, which is compatible with the range reported by [Zeybek and Madabhushi \(2017\)](#) in physical models —74% to 99% degree of saturation. The main drawback of the current air injection technique is the incapability to create a homogeneous distribution of gas bubbles in the soil. Besides, the air injected into the soil may not be stable; thus, ensuring constant saturation over time is challenging.

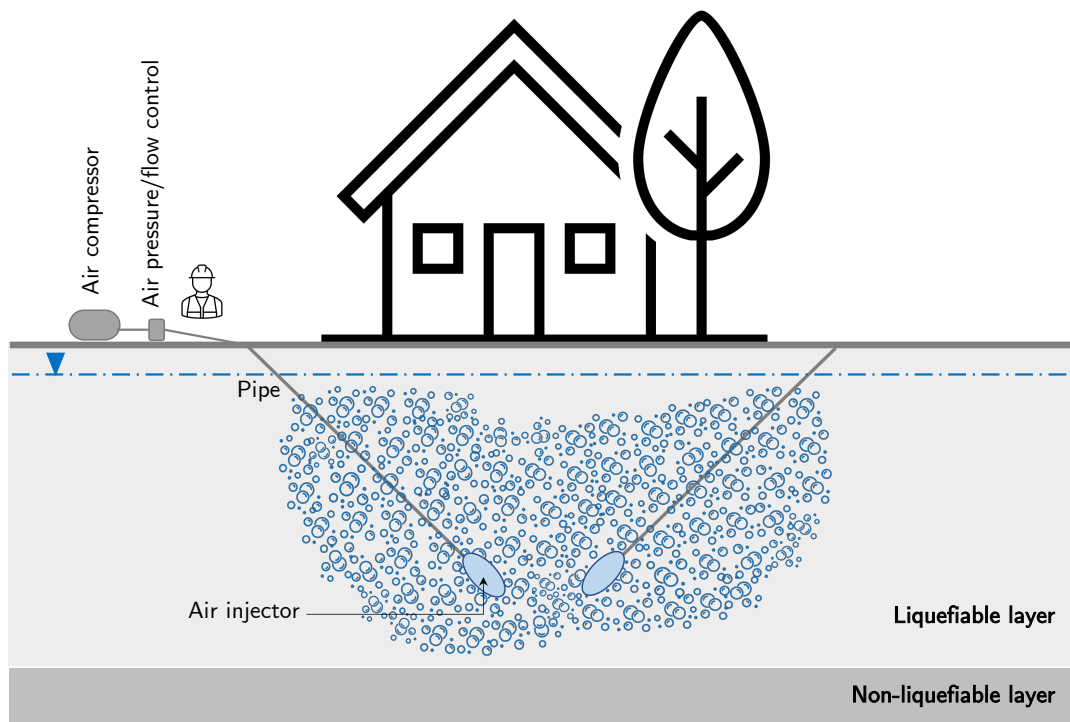
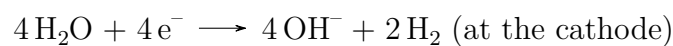
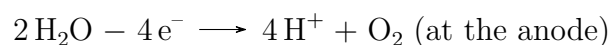


Figure 2.20: Schematic illustration of the air injection technique

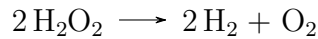
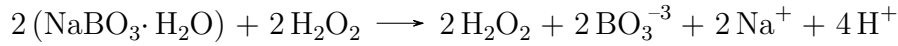
The water electrolysis technique involves ionising hydrogen and oxygen gases by sending water electrodes to entrap gas molecules in saturated soils. In contrast to the air injection technique, this technique does not require the application of an external pressure to induce partial saturation (Yegian et al., 2007). Water electrolysis produces oxygen and hydrogen gases at the anode and cathode by ensuring the following chemical reactions:



The electrolysis process should be maintained until hydrogen bubbles are generated, which migrate from the cathode to the anode through the soil. The amount of produced gas (mainly H_2) is significant enough to change the degree of saturation without compromising any safety hazard associated with explosions (Yegian et al., 2007). However, the in situ implementation of the water electrolysis technique is expensive because of its monitoring and maintenance.

Similarly to the water electrolysis technique, the chemical desaturation technique promotes chemical reactions to generate gas. Eseller-Bayat et al. (2013) used sodium

perborate monohydrate ($\text{NaBO}_3 \cdot \text{H}_2\text{O}$) to induce a partial saturation condition in Ottawa sand. This technique was referred to as drainage-recharge. $\text{NaBO}_3 \cdot \text{H}_2\text{O}$ reacts with water (H_2O) to generate hydrogen peroxide (H_2O_2), which is a ready source produce (H_2) and oxygen (O_2), as follows:



The results reported by [Eseller-Bayat et al. \(2013\)](#) revealed uniform distribution of gas bubbles. Figure 2.21 presents a digital image of the desaturated soil after applying the drainage-recharge technique. The digital imaging results indicated that gas bubbles were smaller in size (0.1–0.3 mm diameter) than the observed void space (0.6 mm in equivalent diameter as observed on the digital image). However, the degree of saturation of this technique was limited to 82–86%. Therefore, using sodium perborate monohydrate in liquefiable soils reduces the degree of saturation by about 80%

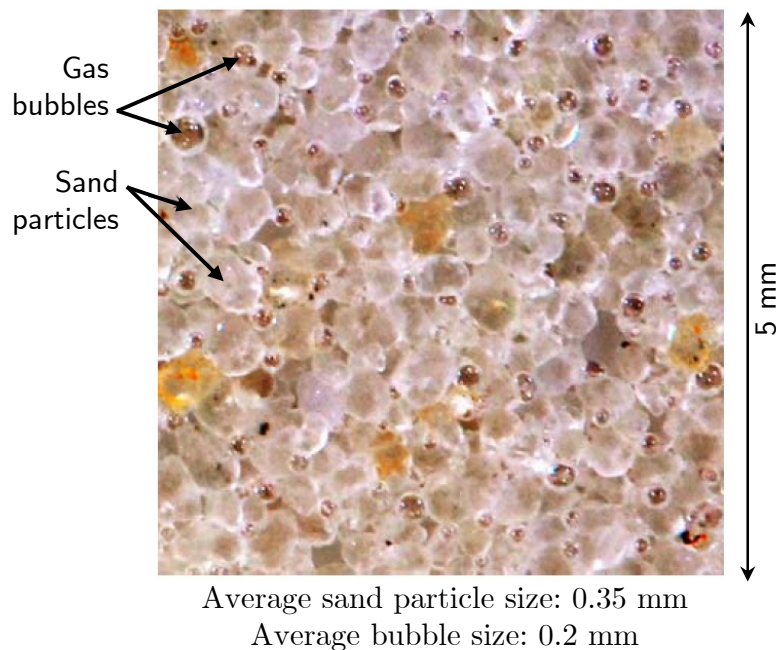


Figure 2.21: Digital image of desaturated Ottawa sand using the drainage-recharge technique ([Eseller-Bayat et al., 2013](#))

Finally, the generation of biogas to desaturate the soil has been explored as a liquefaction mitigation technique ([Rebata-Landa and Santamarina, 2012](#); [He et al., 2013](#);

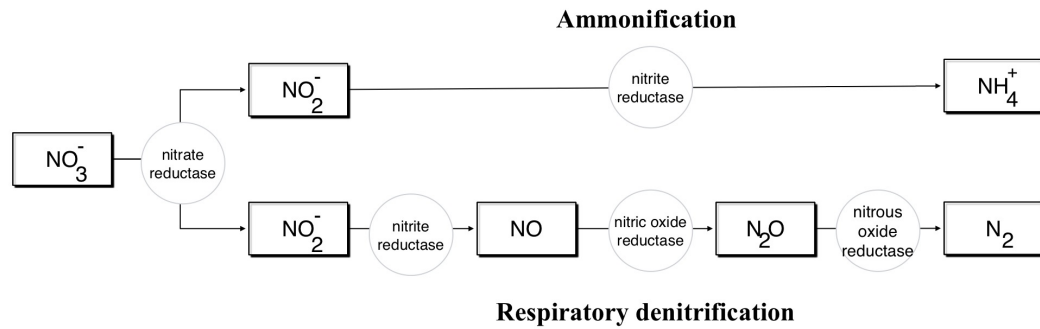


Figure 2.22: Reduction of nitrites and nitrates (Rebata-Landa and Santamarina, 2012)

Wang et al., 2020; Astuto, 2021). The biochemical process for inducing partial saturation leads to the nucleation of gas bubbles within the soil pores by the activity of the microorganisms (e.g. archaea, fungi or bacteria), which generates gas as a product of their metabolism. This activity leads to the formation of different gases, according to the type of microorganisms and bio-chemical reaction involved in the process.

The gases produced during the biochemical reaction are carbon dioxide (CO_2), carbon monoxide (CO), nitrogen (N_2), nitrous oxide (N_2O) and methane (CH_4). The biochemical reaction involves different activities of microorganisms, such as nitrogen fixation, dissimilatory nitrate reduction to ammonia, nitrification, Anoxic-Ammonia-Oxidation (An-Amm-Ox), and denitrification. The above activities correspond to biological and anoxic processes that are simultaneously carried out. Notwithstanding, denitrification is the process most used to induce the partial saturation in liquefiable soils due to the formation of soluble nitrogen oxides, which afterwards are reduced to N_2 (Rebata-Landa and Santamarina, 2012; Astuto, 2021). Figure 2.22 presents the reduction of nitrites and nitrates during microorganisms activities.

He et al. (2013) and Astuto (2021) observed degrees of saturation lower than 80% using the denitrification of bacteria in quartz sands. Such results were obtained from physical models specially adapted to apply such an IPS technique. Moreover, these authors concluded that the in-situ application of bio-desaturation by bacteria denitrification for liquefaction mitigation is feasible due to the degrees of saturation experimentally achieved and N_2 is a gas with low solubility in water, chemically inert and of low environmental impact. However, it is effective for shallow layers, with

a maximum depth of about 7 m below the groundwater level. Such a limitation is because the microorganisms cannot generate enough gas under relatively high pressure or vertical stresses ([Astuto, 2021](#)).

2.4.3 Applicability and performance of IPS techniques for liquefaction mitigation

The interest in the IPS techniques for liquefaction mitigation has grown due to its ability to increase the liquefaction resistance by inducing a minimal disturbance to the soil and its simple implementation in free field conditions and urban areas. The applicability of IPS saturation techniques depends on different factors. These factors are presented as follows:

- area and depth of treated zone;
- technology and equipment the induction of partial saturation;
- the monitoring of S_r in the long-term;
- maintaining of the IPS systems.
- durability of the induced partial saturation.

The area and depth of the treated zone should be considered the specific IPS technique to implement. Therefore, in the case of air injection systems, the air pressure must be higher than the sum of the pressure associated with the head of water and the capillary pressures at the point of injection, and not it must exceed the effective stresses at that point to avoid failure or cracking of the material ([Marulanda et al., 2000](#)). Considering these factors, the air injectors can desaturate areas with about 5 m radius, as observed by [Ishihara et al. \(2003\)](#) in centrifuge tests. Numerical simulations performed by [Nateghi and Shamy \(2022\)](#) validated these results.

For the case of chemical and bio-desaturation techniques, the results depend on the concentration of the components [Rebata-Landa and Santamarina \(2012\)](#); [Wang et al. \(2020\)](#). The concentration generates occluded air bubbles with different diameters that control the final S_r of the soil. However, the main limitation of these methods lies in the depth at which the denitrification process is conducted, restricting their implementation for soil deposits below 7 m depth [Astuto \(2021\)](#). Besides, the efficiency of this technique may change with the temperature, as observed by

Mousavi and Ghayoomi (2021), affecting the time to achieve the lowest possible S_r by microbial-induced partial saturation (see Figure 2.23).

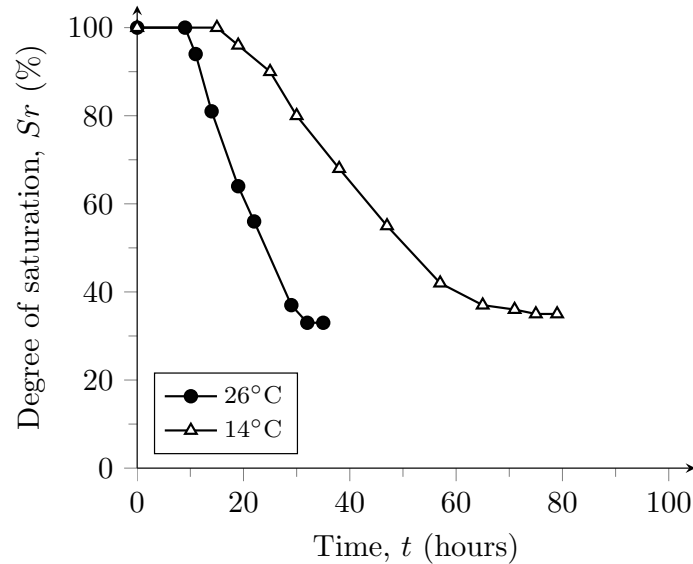


Figure 2.23: S_r variation in time by microbial induced partial saturation for two temperatures (adapted from Mousavi and Ghayoomi 2021)

A pertinent question regarding the IPS techniques is whether or not gas bubbles in sands can remain for a long time. Therefore, before answering that question, it is necessary to establish a method for measuring S_r during the operation of any IPS technique, which is critical in assessing IPS performance.

In the laboratory, the B -value is the most common parameter to estimate the S_r . However, this parameter does not provide a reliable estimation of S_r in the field since, in free field conditions, the undrained condition cannot be guaranteed. Therefore, alternative methods involving the electrical conductivity or P-wave velocity have demonstrated good results in estimating S_r by both in situ and laboratory testing (Consentini and Foti, 2014; Chen et al., 2021; Astuto, 2021).

Wave velocities and electrical resistivity in soils depend on the saturation and other parameters, such as the porosity, fabric, stress, mineralogy, pore fluid and temperature (Santamarina et al., 2005). Hence, P-wave velocity (V_P) and relative electrical conductivity (r) can be used as reliable estimators of S_r . Figure 2.24 shows the theoretical approaches based on the electrical resistivity theories (Archie, 1942), which complements the wave-based approach of Biot's theory (Biot, 1956a,b) of Figure 2.15.

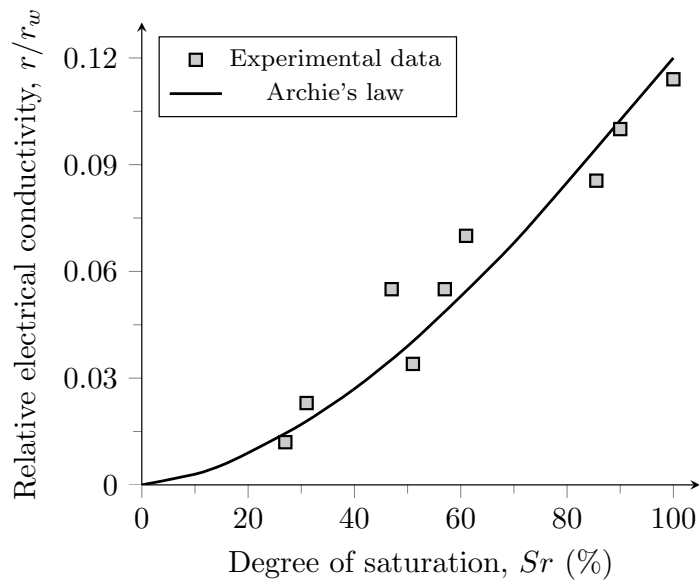


Figure 2.24: Relation between relative electrical conductivity and degree of saturation based on Archie's theory (adapted from [Consentini and Foti 2014](#))

After establishing the procedure to estimate S_r , the durability of IPS is examined. [Yegian et al. \(2007\)](#) observed a change in the degree of saturation from 82% to 84% during 442 days. Similar tests were also carried out by [He et al. \(2013\)](#) using biogas. [Okamura et al. \(2011\)](#) collected high-quality undisturbed frozen samples from six different experimental sites where the IPS was implemented. Analyses of these samples in the laboratory revealed a slight increment in the degree of saturation concerning the degree of saturation reported after the IPS application. These authors concluded that the gas bubbles injected into the soil remained for more than 26 years, demonstrating the long-term durability of the soil improvement by the IPS. Notwithstanding, the durability results referred to above are limited for hydrostatic conditions.

[Hu et al. \(2020\)](#) carried out a series of tests under hydraulic gradient flow to assess the stability of biogas generated by bacteria denitrification. In the seepage condition, degrees of saturation increased from 84.7% to 85.5%. No biogas bubble aggregation occurred, and no biogas bubbles were observed to flow away from the sample. Hence, these authors attributed the biogas bubbles decreasing to the gas dissolution caused by the seepage. The performance of IPS techniques in hydrostatic and seepage conditions is not significantly affected by the void ratio (or relative density) of the soil ([Mousavi et al., 2021](#); [Zeybek, 2022](#)).

2.5 Remarks

This chapter presented the mechanisms of liquefaction, the earthquake-induced liquefaction damages worldwide and describes novel approaches to interpret the undrained cyclic behaviour and liquefaction resistance of soils. This novel interpretation addresses stress-based and energy-based methods. The energy-based methods provide a promising framework to assess the liquefaction resistance of partially saturated soils because of the incorporation of fluid compressibility effects during cyclic loading.

Compilation of experimental results disclosed that the liquefaction resistance tends to increase by decreasing the degree of saturation (Sr). Such results revealed that soils with $Sr = 90\%$ have cyclic resistance (or the number of cycles to trigger liquefaction) of about twice that of soils with $Sr = 100\%$. The enhancement of liquefaction resistance in partially saturated soils is due to the effects of occluded air bubbles, which reduce the bulk modulus of fluid. The bulk modulus reduction increases the volumetric strains of soil deposits and reduces the pore pressure build-up during cyclic loading. The effects of matric suction have been considered negligible in clean sands since its maximum value is of about 4 kPa—a non-relevant value compared to the mean effective stress on the field. This confirms the Sr effects on the liquefaction resistance, which indicates the plausibility of reducing Sr to increase the cyclic resistance of liquefiable soils, demonstrating the great potential of IPS techniques for liquefaction mitigation.

The induced partial saturation (IPS) has been receiving increasing interest as an alternative technique for liquefaction mitigation because of the gas generation in fully saturated soils. The presence of gas bubbles increases the fluid compressibility and significantly reduces pore pressure build-up during cyclic loading. Different techniques, such as air injection, water electrolysis, chemical desaturation and bio-desaturation can generate gas bubbles. These techniques are environmentally friendly. Besides, its implementation causes a minimal soil disturbance, in contrast to other mitigation techniques that improve the cyclic resistance of the soil (e.g. vibro compaction), which is suitable for both free-field conditions and urban areas.

The use of P-wave velocity and the application of Biot's theory for estimating Sr have several advantages, including the real-time monitoring of Sr in different experimental setups, a precise comparison between Sr measured in the field and the

laboratory, the detection of small Sr changes in partially saturation conditions (e.g. $Sr > 85\%$), and a reliable correlation between Vp and B -value which are parameters that can be correlated with the liquefaction resistance for soils with different Sr .

Energy-based methods provide a promising framework to assess the liquefaction resistance of partially saturated soils and represent an alternative to the conventional approach interpreting liquefaction resistance (e.g. stress-based methods), due to the incorporation of fluid compressibility effects on the soil behaviour during cyclic loading. Moreover, energy-based methods allow for comparing results obtained from different procedures for characterising the liquefaction resistance of soils in the laboratory, including several types of element testing and centrifuge modelling.

Chapter 3

Materials, devices and experimental procedures

3.1 Outline

This chapter describes the materials and the testing apparatuses used in this research. This study focuses on a historically liquefiable sand from the Lisbon centre. Hence, the geological setting description and sampling of such a sandy soil are presented herein. Most parts of the experimental program were carried out in the Geotechnical Laboratory (LabGEO) of the Civil Engineering Department at the Faculty of Engineering of the University of Porto (Portugal), and complementary advanced tests were conducted in the ‘Centre for Advanced Studies of Road Infrastructure and Geotechnics’ at the Universidad Militar Nueva Granada. The physical modelling by geotechnical centrifuge tests was developed in the ‘Geotechnical Models Laboratory’ at Universidad de los Andes (Colombia). The tests carried out in the centrifuge focused on the assessment of the site response of TP-Lisbon sand under different stress states and degrees of saturation. Hence, this chapter also describes the instrumentation of the models. On the other hand, this chapter includes a description of testing devices and experimental procedures adopted for characterising the behaviour of TP-Lisbon sand. A special focus is given to a series of novel adaptations in the apparatuses to estimate the soil state during element testing. These adaptations allow for a proper definition of the critical state parameters and liquefaction resistance of sandy soils.

3.2 Studied soil

3.2.1 Geological setting of Terreiro do Paço site

In Portugal, local liquefaction-induced damage dates from 1344, 1531, 1755 and 1909 when distant and local intraplate earthquakes (with a magnitude M_w between 6.0 and 8.5) stroke the Portuguese onshore mainland, mainly affecting the greater Lisbon area (Jorge and Vieira, 1997; Teves-Costa and Batlló, 2011; Lai et al., 2020). Relevant damages were reported after in 1755 and 1909 earthquakes. Notwithstanding, the 1st of November 1755 earthquake ($M_w = 8.5$) is probably the greatest seismic disaster in Western Europe since it almost destroyed the Lisbon centre, killed up to 100,000 people and injured more than 40,000 people (Oliveira, 2008). Therefore, the characterisation of the cyclic behaviour of liquefiable layers composing the soil deposits of Lisbon centre is of utmost importance to prevent damage and possible collapse of buildings, facilities and critical infrastructures in this area.

This seismic event is a well-known major earthquake ($M_w = 8.5$) that impacted the Portuguese continental mainland. The 1755 earthquake, which originated in the depths of the Atlantic Ocean, induced the collapse of several buildings in Lisbon, including the Ribeira Palace—the most important royal complex in Portugal, considered the centre of the empire. Historical reports indicated that earthquake-induced liquefaction caused lateral spreading and affected the stability of the foundations of the surrounding buildings at this site (Salgado, 2019). The combination of liquefaction effects with a tsunami from the Tagus River induced significant damage to several buildings in the city centre. Figure 3.1 shows two representations of Terreiro do Paço site before and after of 1755 earthquake. This figure illustrates well the damages and effects of such an earthquake on this site.

After the 1755 earthquake, a plaza was constructed. This plaza was named ‘Praça do Comércio’ and is now one of the historically significant sites in Portugal and one of the most beautiful plazas in Europe. Due to the previous location of the palace, the Portuguese people referred to the site as ‘Terreiro do Paço’, which in English means yard of the palace, instead of using the name Praça do Comércio. The Terreiro do Paço site is surrounded on three sides by distinctive yellow Pombaline architecture—a superb Portuguese heritage (Couto et al., 2020)—with the decorative ‘Arco da Rua Augusta’ located on the north side, serving as the focal point of the plaza. Facing the Arco da Rua Augusta, Terreiro do Paço opens up to the Estuary of the Tagus River. This site is one of the main transportation hubs in Lisbon as



a)



b)

Figure 3.1: Illustrations of Terreiro do Paço site —images provided by the Lisbon Museum to [Fundação Luso-Americana](#) (2005): a) before 1755 earthquake; b) before 1755 earthquake

it includes a significant commuter ferry terminal, offering departures south across the Tagus River. The site also serves as a departure location for the tram network heading towards the Belem district or the Basílica da Estrela. Furthermore, the bus and metro stations are adjacent to the river terminal, providing connections between central Lisbon and other parts of the city.

Terreiro do Paço site is located in the mainland region with probably the greater seismic risk of Portugal. This region is affected by the occurrence of large magnitude ($M_w > 8$) distant earthquakes and medium magnitude ($M_w > 6$) near earthquakes due to its proximity to the boundary of African and Eurasian plates. An example of a distant event is the 1755 earthquake ($M_w > 8.5$) generated in the Eurasian-Nubia plate boundary zone (Jorge, 1993). However, local intraplate earthquakes ($M_w \approx 6 - 7$) have occurred more frequently, in 1344, 1531 and 1909 (Ferreira et al., 2020). The assessment of liquefaction susceptibility in this region can be done by using the parameters of EC8-NA (CEN, 2010), for a return period of 475 years and a seismic action Type 1 and Type 2, as summarised in Table 3.1

Table 3.1: Seismic parameters for a return period of 475 years in the Lisbon area (CEN, 2010)

	Seismic action Type 1	Seismic action Type 2
Seismic zone	1.3	2.3
M_w	7.5	5.2
a_{gR} (m/s ²)	1.5	1.7
γ_I	1	1
a_g	1.0	1.7
Ground type	D	D
S_{max}	2	2
S_f	1.83	1.77
a_{max} (m/s ²)	2.75	3.00
a_{max} (g)	0.28	0.31

The geological profile at the Praça do Comércio site corresponds to the alluvial materials of the Tagus River valley, in the south of Portugal. The lithology of this region is composed by widespread deposits of fine-grained sands, which were sedimented in the late Quaternary and are resting over Miocene deposits of stiff clays. Shallow layers mainly consist of fine clean sands and sandy silts with intercalations of plastic soils. However, these layers contain the remaining resulting from older civilisations that occupied Lisbon and the wreckage caused by the 1775 earthquake (Teves-Costa et al., 2001). Such intercalations indicate that the valley was infilled

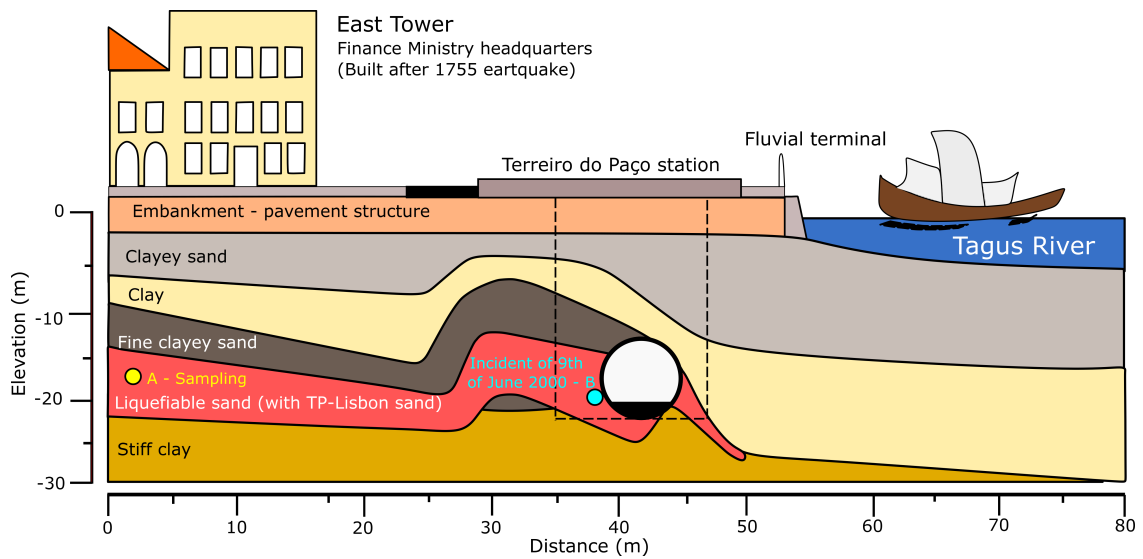


Figure 3.2: Lithological profile of Terreiro do Paço site (adapted from Salgado 2009, 2019)

in a heterogeneous process, which included water level variations of the Tagus River. Besides, the thick shallow layers of sandy soils below the Praça do Comércio site are susceptible to trigger liquefaction (Salgado, 2009). Figure 3.2 schematises the lithology of the Praça do Comércio site.

The main interest in studying this site is related two factors. The first is assessing earthquake-induced liquefaction susceptibility of the sandy soils composing this zone. The second one is the characterisation of the soil involving the incident that occurred during the construction of the underground Lisbon blue line tunnel of ‘Metropolitano de Lisboa’ (point **B** in Figure 3.2), which was constructed with a large boring machine passing onshore through the Tagus River, on 9th of June 2000. This underground tunnel sought to extend the blue line, passing by the riverfront of the Terreiro do Paço. The geotechnical design of the tunnel included soil improvement with the jet grouting technique in 250 holes for its construction. However, mud and water began to erupt uncontrollably from the 13th hole during the excavation of such holes, and settlements started to occur at the surface that affected the buildings around the excavation (Salgado, 2019). This incident caused settlements at the surface, affecting several surrounding buildings, including some of the old heritage Pombalino masonry buildings (Couto et al., 2020). Detailed work carried out by Salgado (2009) indicates that this incident was induced by flow liquefaction of the alluvial soils, which compose the affected area.

The main interest in studying this site is related to two factors. The first is assessing earthquake-induced liquefaction susceptibility of the sandy soils composing this zone. The second one is the characterisation of the soil involving the incident that occurred during the construction of the underground Lisbon blue line tunnel of ‘Metropolitano de Lisboa’ (point **B** in Figure 3.2), which was constructed with a large boring machine passing onshore through the Tagus River, on 9th of June 2000. This underground tunnel sought to extend the blue line, passing by the riverfront of the Terreiro do Paço. The geotechnical design of the tunnel included soil improvement with the jet grouting technique in 250 holes for its construction. However, mud and water began to erupt uncontrollably from the 13th hole during the excavation of such holes, and settlements started to occur at the surface that affected the buildings around the excavation (Salgado, 2019). This incident caused settlements at the surface, affecting several surrounding buildings, including some of the old heritage Pombalino masonry buildings (Couto et al., 2020). Detailed work by Salgado (2009) indicates that this incident was induced by flow liquefaction of the alluvial soils, which compose the affected area.

3.2.2 Piezocone penetration tests and soil sampling

For the design and construction of the underground Lisbon blue line tunnel of ‘Metropolitano de Lisboa’, nine piezocone tests (CPTu) were performed, including four into the square of the Praça do Comércio site and five next to the Tagus River. The tests were performed before this research according to the standard procedure ASTM D5778 (ASTM International, 2017). The groundwater level was measured in each location, varying from 2.3 m to 8.4 m. The variations of the groundwater level position were conferred to the tidal effects of the Tagus River. Figure 3.3 shows the location of the tests.

Only the results of CPTu112, CPTu118 and CPTu119 are discussed in this document due to the central location of these tests. CPTu were conducted from 8 m until 30 m depth. The starting point (corresponding to 8 m depth) of Penetration testing was selected due to the presence of remains from the old palace and compacted materials used for the embankment and the pavement structure surrounding Praça do Comércio site. Figure 3.4 presents the primary data of the CPTu tests, that is cone tip resistance (q_c), sleeve friction (f_s) and pore-water pressure generated during the cone penetration (u_2).

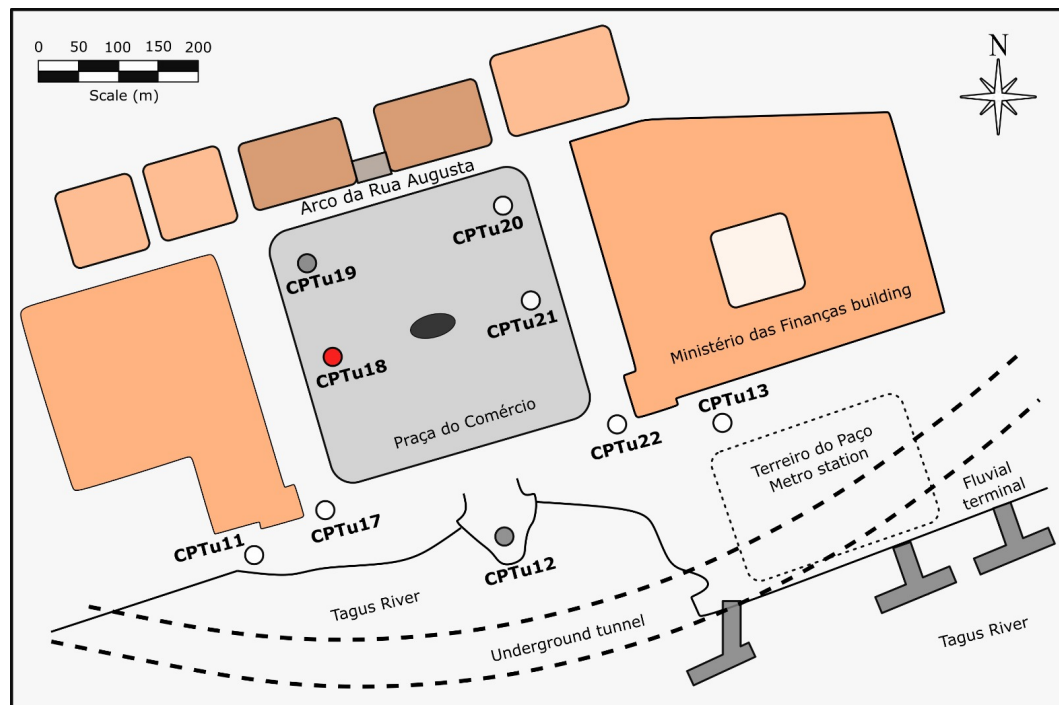


Figure 3.3: Plan view and CPTu locations at Terreiro do Paço site

Primary data were analysed regarding the soil behaviour type (SBT) methodology proposed by Robertson (1990). In addition, a simplified soil profile has been defined for practical purposes by approximating the original soil behaviour type index (I_c) by constant values, where similar behaviour is expected. As proposed by Cubrinovski et al. (2019), the simplified soil profile considers gravel and coarse sand ($I_c < 1.3$); clean sand ($1.3 \leq I_c \leq 1.8$); sands with low fines content ($1.8 \leq I_c \leq 2.1$); silty sand, sandy silt and non-plastic silt ($2.1 \leq I_c \leq 2.6$); and non-liquefiable silt or clay ($I_c > 2.6$). This alternative classification method focuses on soil response concerning earthquake-induced liquefaction (Ferreira et al., 2020). Figure 3.5 illustrates a preliminary soil profile and the simplified soil profile, based on the proposal of Robertson (1990) and Cubrinovski et al. (2019), respectively.

Based on the in situ characterisation results, a sampling campaign was carried out to collect representative and integral soil samples at Praça do Comércio site. These samples were obtained by Keller Groundbau GmbH Company using a rotary probe attached to a Shelby sampler device able to retrieve integral samples of 110 mm diameter in the vertical direction. The samples corresponding to TP-Lisbon sand were collected between 13 to 23 m depth in a site investigation point next to CPTu18 located inside Praça do Comércio at the coordinates $38^\circ 42' 26.61'' N - 9^\circ 8' 13.37'' W$ (point A in Figure 3.2). Figure 3.6 exhibits the integral samples of TP-Lisbon sand

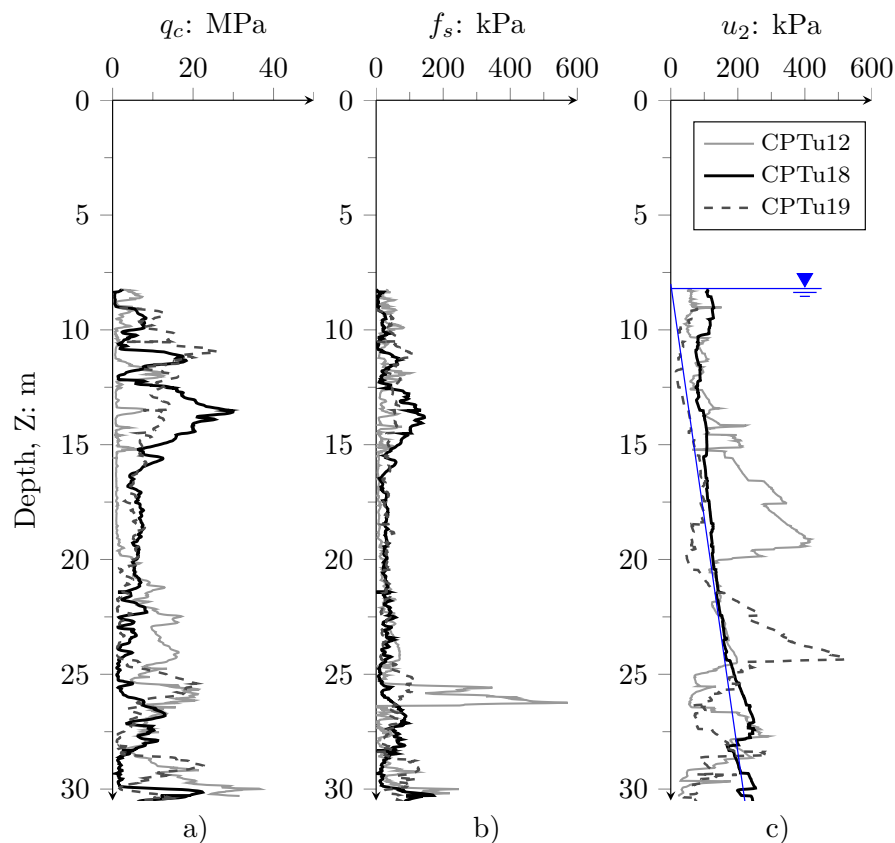


Figure 3.4: Profiles of primary CPTu data: a) cone tip resistance; b) sleeve friction c) pore-water pressure generated during the cone penetration

and shows the profiles of relative density (Dr) and state parameter (ψ) derived from CPTu data. These profiles were estimated based on the correlations proposed by Robertson (2009), which are widely used for soils with $I_c < 2.6$.

3.3 Testing devices

3.3.1 Bender elements

A bender element (BE) is a piezoceramic transducer able to transmit or receive a mechanical perturbation. It comprises two thin plates, rigidly bonded to a central metallic sheet and two electrodes on its outer surfaces. BE can be installed virtually in any soil testing apparatus, including the oedometer (Lee and Santamarina, 2005), triaxial (Viana da Fonseca et al., 2009), resonant-column (Camacho-Tauta, 2011), true triaxial or cubical devices (Ferreira, 2009) and geotechnical centrifuges (Murillo et al., 2009). Besides, BE can also be used in bench tests, similarly to other ultrasonic

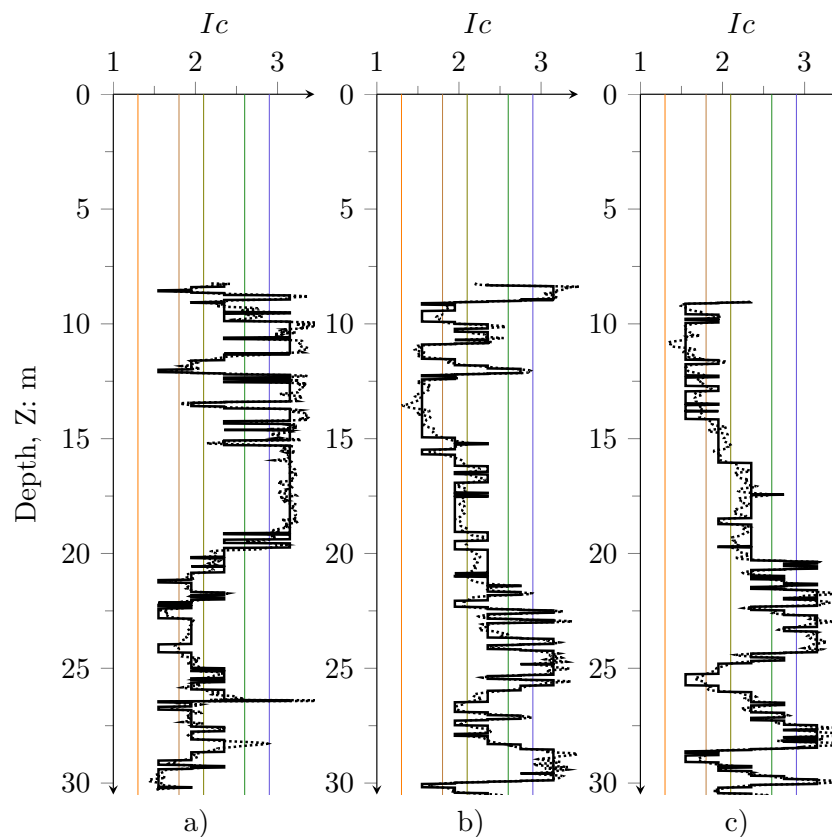


Figure 3.5: SBT and I_c simplified soil profiles: a) CPTu12; b) CPTu18; c) CPTu19

transducers, for rapid assessment and monitoring of soil stiffness (Silva et al., 2013). Figure 3.7 shows a BE installed in advanced geotechnical testing apparatuses.

BE behaves as a simple cantilever beam, fixed at the base and free at the other end. For soil testing, a couple of such transducers are used at two locations of the soil specimen, allowing the generation or detection of a mechanical perturbation. The BE transmitter generates such disturbance and travels thru the soil specimen until the other end, where the BE receiver converts the mechanical perturbation into a voltage signal (Rio, 2006). The mechanical perturbation is in the range of small-strain and is similar to a seismic wave. Figure 3.8 illustrates the operation of BE tests.

For BE tests, a sine pulse was used as an input signal to excite the BE transmitter. However, different electrical signals can generate distortion in the BE transmitter, such as square, impulse, forced oscillation, continuous sine with constant frequency, sine sweep or stochastic random noise (Viggiani and Atkinson, 1995; Santos, 1999; Ferreira, 2009; Camacho-Tauta, 2011). The BE test set-up used in this research

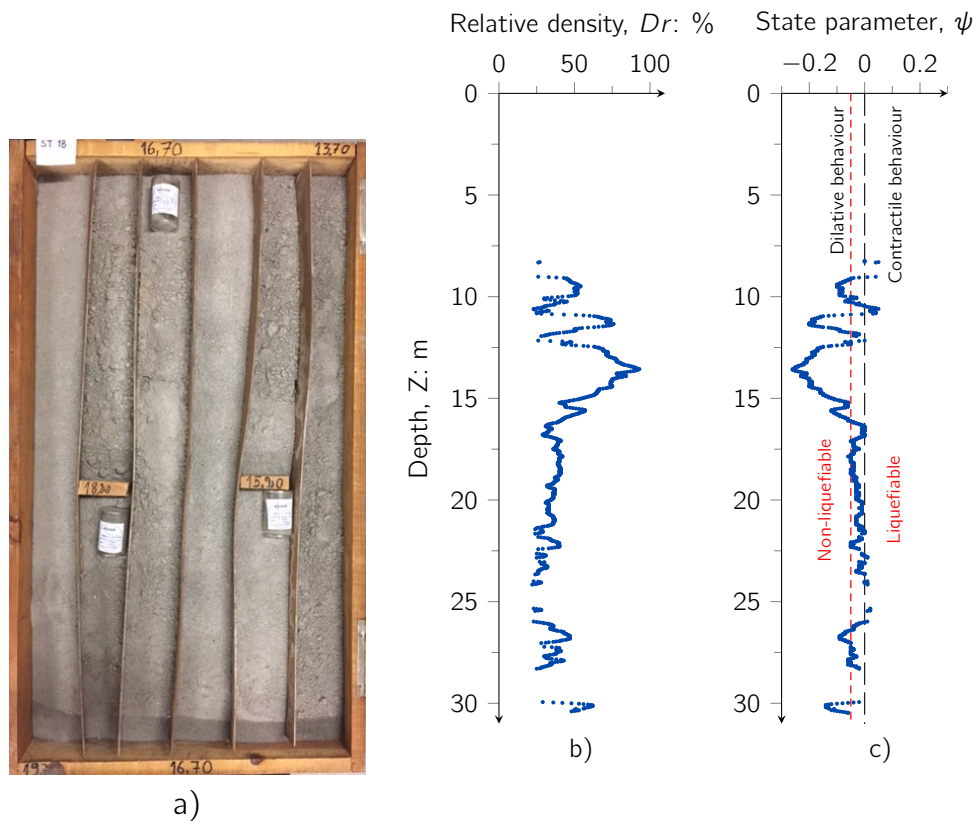


Figure 3.6: Integral samples of TP-Lisbon sand: a) collected soil; b) relative density profile at SI18; c) state parameter profile at SI18

consists of a function generator (TTi TG1010), two input-output amplifiers (designed at the University of Western Australia), an oscilloscope (Tektronix TDS 220) and a computer with WaveStar software to acquire the wave signals. All the BE used in this research were manufactured in the Geotechnical Laboratory of FEUP (LabGEO). Figure 3.9 presents the BE set-up used in the LabGEO.

The wave velocity from BE tests was obtained by computing the ratio between the travel length and the wave propagation time. The travel length (L_{tt}) corresponds to the tip-to-tip distance between BE (Camacho-Tauta et al., 2015). On the other hand, the wave propagation time (t_t) was obtained using the first arrival time method Viggiani and Atkinson (1995). Figure 3.10 presents a representation of the wave propagation time and the interpretation by the first arrival time method. In this figure, it can be observed three different times, represented by three arrows to consider the first arrival point, O' . Due to the differences between these times, determining the arrival time is controversial. Lee and Santamarina (2005) and Ferreira (2009) suggest considering arrival the time in the time indicated by

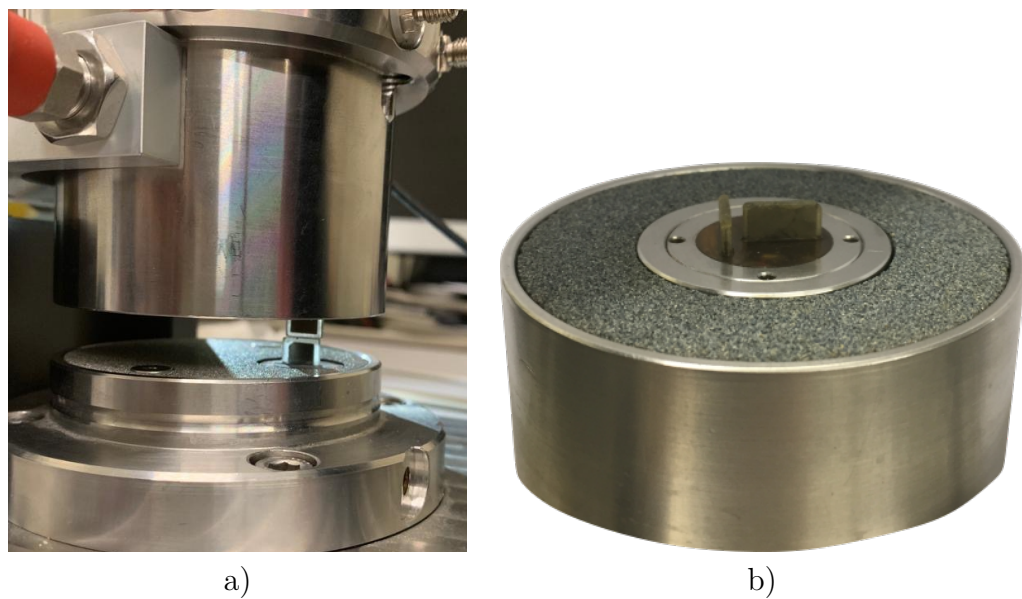


Figure 3.7: Photograph of BE: a) Simple shear device; b) base cap of a triaxial cell

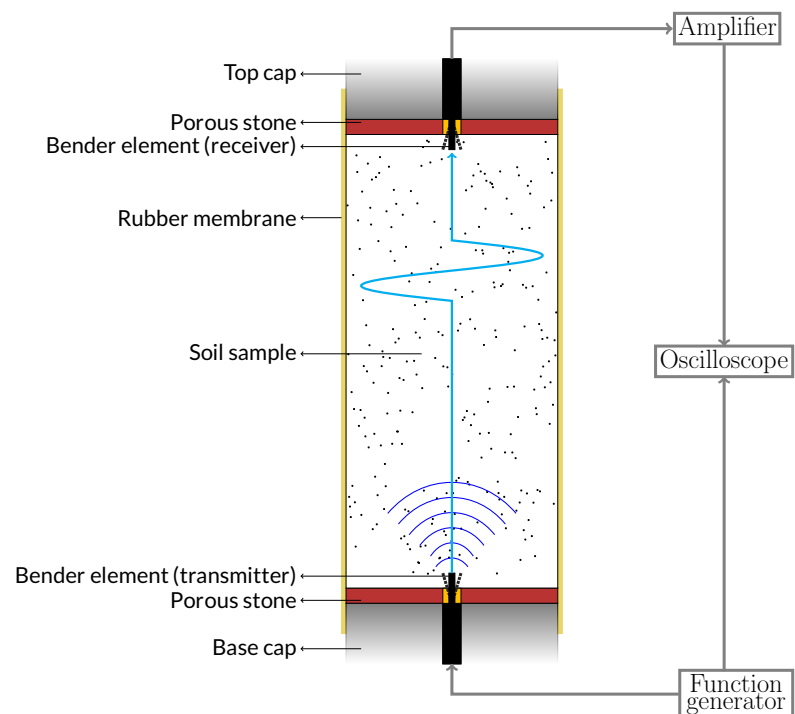


Figure 3.8: Schematic view of the Bender Element testing

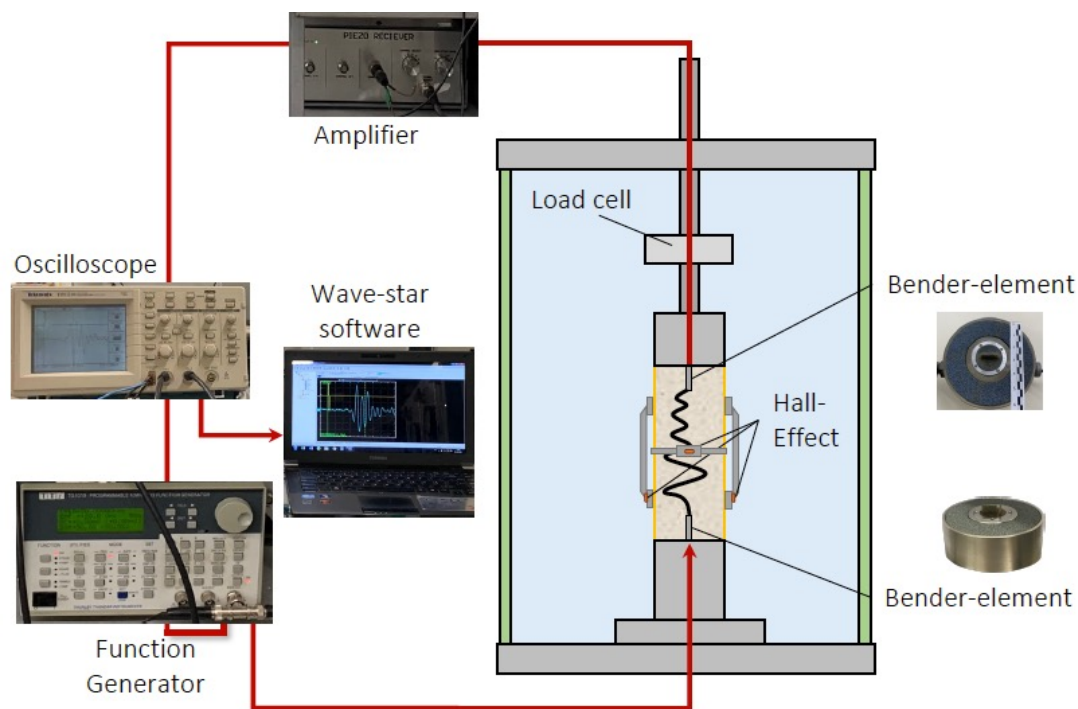


Figure 3.9: Bender elements setup

the arrow 3. Such a consideration is because arrows 1 and 2 indicate a change in the polarity of the signal, which is related to near-field effects. In contrast, arrow 3 corresponds to the point at which the BE receiver starts to detect the mechanical distortion. [Viana da Fonseca et al. \(2009\)](#) recommended measuring wave propagation time by applying several input signals at different frequencies to avoid misinterpretations during BE testing.

[Ferreira et al. \(2021\)](#) demonstrated by laser vibrometer results that BE can generate concurrent P-waves and S-waves without installing additional transducers in the testing device (i.e. bender extender elements and flat disk-shaped piezoceramic transducers). These authors proposed an experimental methodology using high-frequency excitation pulses for detecting P- and S-wave velocities using a single BE pair. During BE testing, detecting the P-wave arrival is possible when high frequencies are used because high frequencies excite higher BE vibration modes, having relatively higher displacements in the vertical direction than lower vibration modes. Such vibrations create compression-extension movements, which generate a stronger P-wave front. The high-frequency laser vibrometer measurements of the actual BE deformation showed that P-wave and S-wave can be induced by applying frequencies between 20 to 100 kHz and 1 to 10 kHz, respectively. The methodology proposed by [Ferreira et al. \(2021\)](#) was implemented in this research to assess the P- and S-wave

velocities of liquefiable sands to control its soil state during element testing in dry, partially and fully saturated conditions.

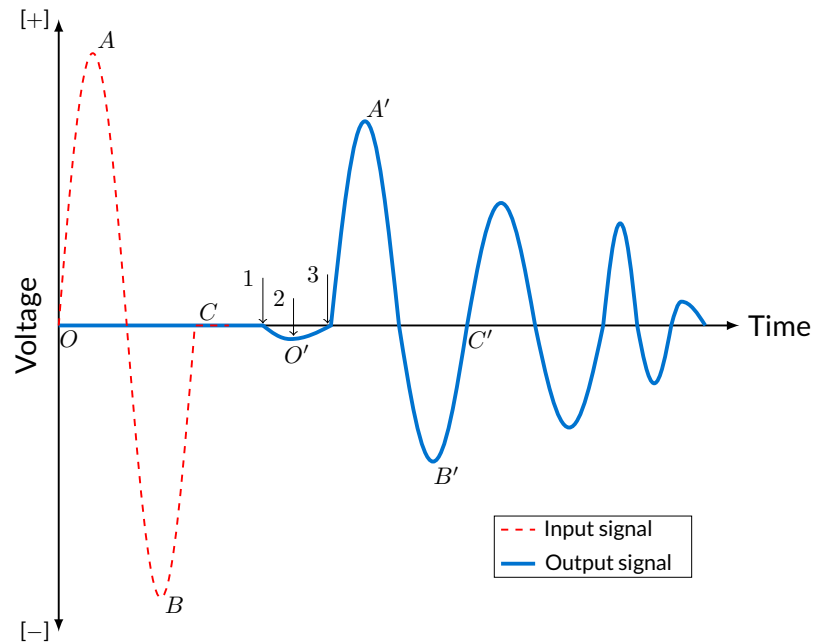


Figure 3.10: Interpretation of BE test by the first arrival time method

3.3.2 Triaxial apparatuses

In this research, three triaxial equipment configurations were used. The first configuration corresponds to triaxial cells with lubricated oversized end platens and an embedded connection piston into the top cap. The second configuration comprises a Bishop-Wesley type stress-path triaxial cell equipped with piezoelectric ceramic instruments. Finally, the third configuration is a cyclic triaxial apparatus fabricated in the Institute of Science and Innovation in Mechanical and Industrial Engineering (INEGI) of FEUP.

The first triaxial configuration was used to characterise critical state parameters of TP-Lisbon sand, as recommended by [Viana da Fonseca et al. \(2021\)](#). The use of lubricated end platens allows reducing the influence of platen restraint on stresses in the soil specimen during triaxial testing, which induces uniform radial strains and helps to keep the cylindrical shape of the specimen at large axial strain levels. Hence, the oversized platens ensure the full support of the soil specimen, avoiding any overhang and allowing a uniform radial deformation during shear. The embedded connection piston significantly reduces specimen ‘tilting’ of the top cap during all phases of triaxial testing, providing more reliable test results for assessing

shear-strain behaviour and CSL of soils (Reid et al., 2021). Figure 3.11 shows the configuration of the oversized lubricated end platens. Figure 3.12 shows the system and configuration of the embedded top-cap loading ram connection in the triaxial apparatus. An automatic volume change gauge measured the volume change during testing.

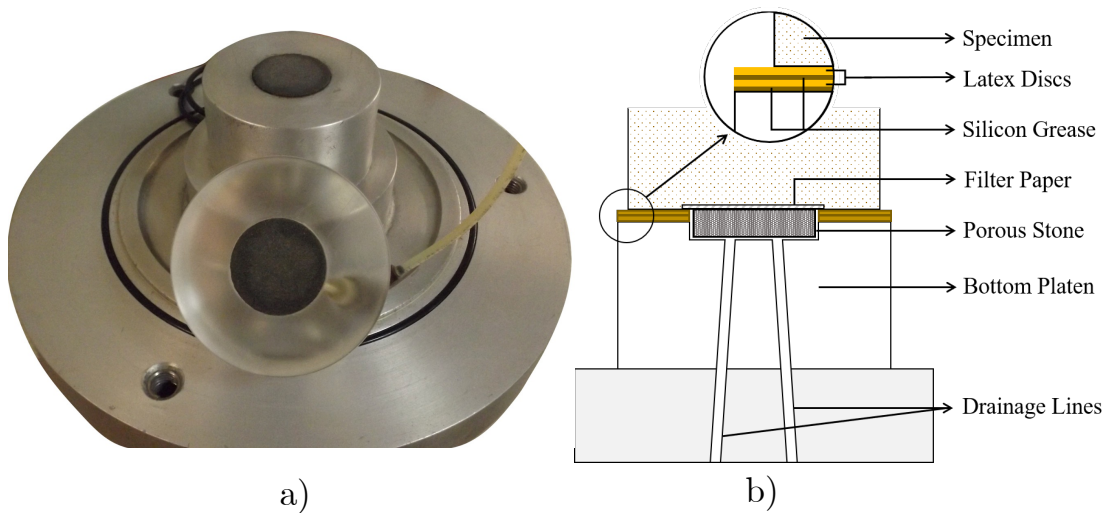


Figure 3.11: Oversized lubricated end platens for triaxial tests (after Viana da Fonseca et al. 2021): a) photo with the implemented configuration; b) lateral view scheme

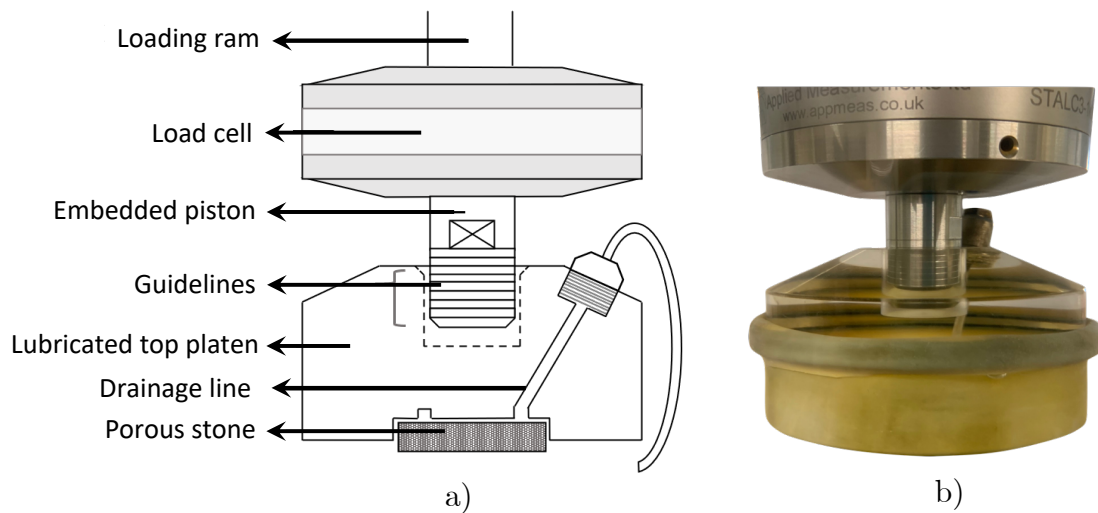


Figure 3.12: Embedded top-cap loading ram connection (after Viana da Fonseca et al. 2021): a) parts and scheme; b) implementation in the triaxial apparatus

The second triaxial configuration was used for evaluating the stress-dependency of small-strain stiffness of different granular soils addressed in this research. Nevertheless, the Bishop-Wesley triaxial apparatus of LabGEO can apply different stress-path

stress during testing. Such a particular feature of this type of equipment also applies to the control of deformations. Therefore, this advanced equipment allows for the advanced characterisation of soils subjected to complex stress conditions, such as anisotropic consolidations, extension shearing and pore water pressure increments. The stress-path cell allows for conducting automatic tests by TRIAX software, which controls stresses and displacements using a set of pressure transducers and an LVDT (Linear Vertical Displacement Transducer). The system transfers the pressure from an air compressor to the Bishop-Wesley cell through a series of air/water interfaces. Besides, the equipment has a submersible load cell and a volume gauge to measure/control the axial load and volume changes during testing. Figure 3.13 shows the Bishop-Wesley triaxial apparatus for stress-path testing of LabGEO.

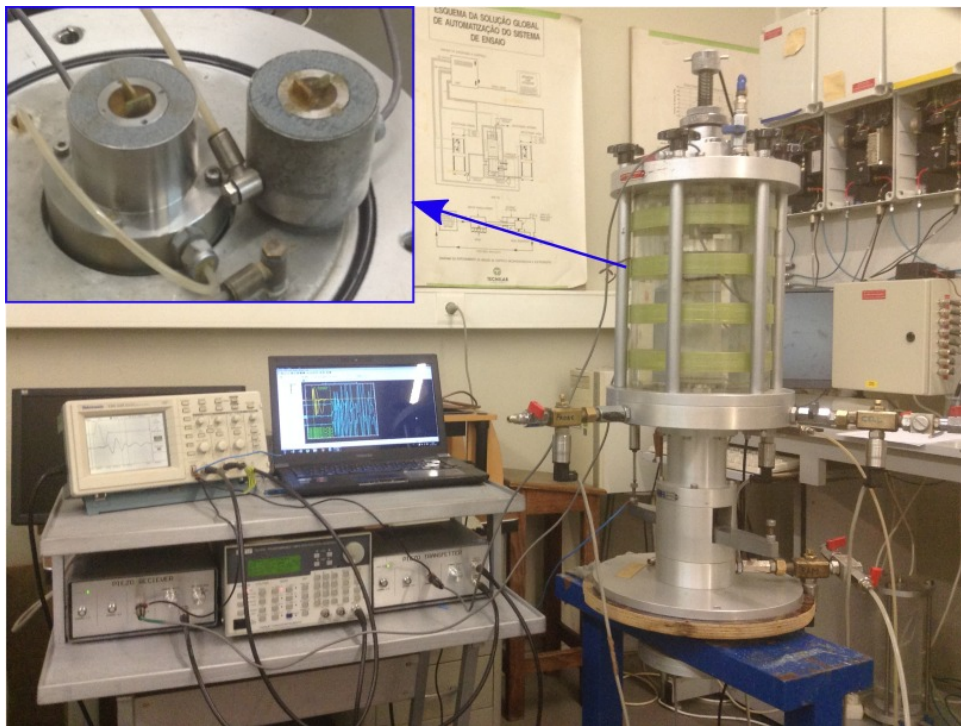


Figure 3.13: Bishop-Wesley triaxial apparatus for stress-path testing of LabGEO

The third triaxial configuration is a cyclic triaxial apparatus used for assessing the liquefaction resistance of soils. Such a configuration covers a conventional triaxial cell equipped with piezoelectric transducers to measure the seismic wave velocities and local Hall-Effect transducers to accurately measure the axial and radial strains of soil specimens in all testing phases. Figure 3.14 shows a general overview of the cyclic triaxial apparatus of LabGEO.

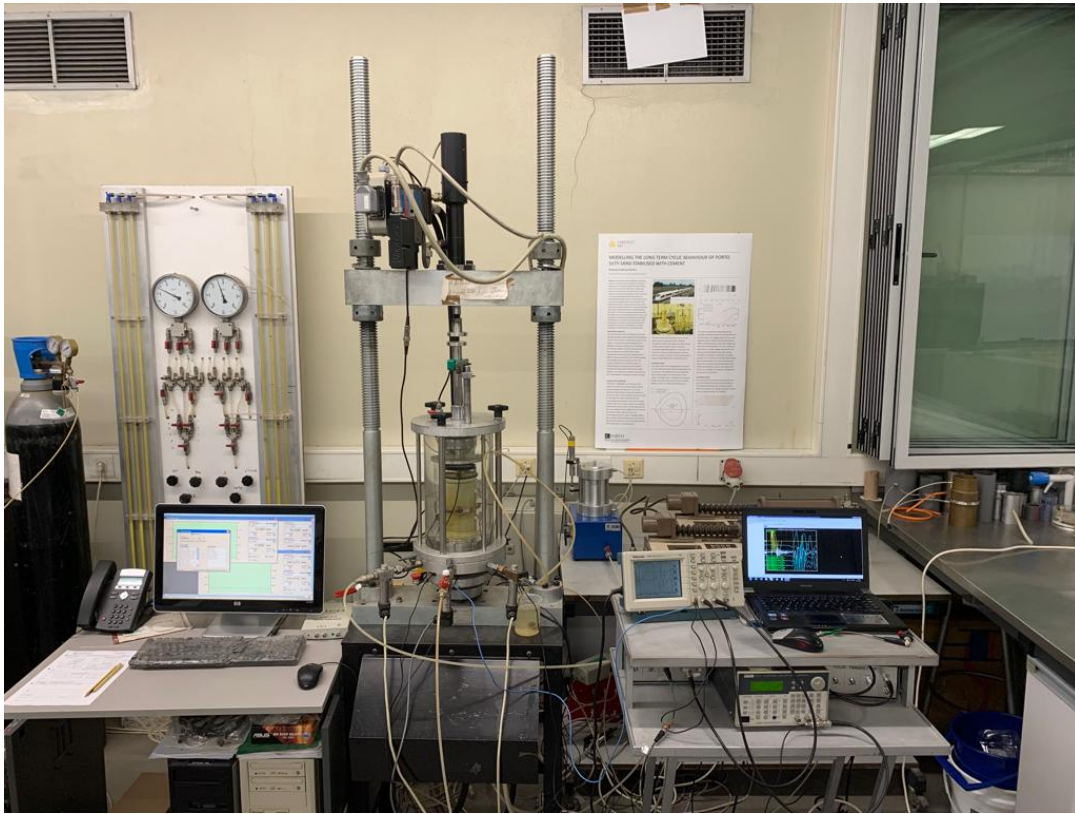


Figure 3.14: Cyclic triaxial apparatus of LabGEO

The cyclic loading is applied by a servo-actuator composed of a hydraulic piston with displacement and load transducers, which allows varying the loading frequency between 0.001 and 2 Hz. This hydraulic system is powered by an oil pump, which allows applying a maximum load of 10 kN. However, the maximum load that can be applied during testing is limited to the capacity of the load cell. In this research, a load cell of 1 kN was used. On the other hand, a rubber V-ring was used to ensure the contact between the top cap and the hydraulic piston during cyclic loading (Ramos, 2021), warranting the inversion of principal stresses during the cyclic testing in this equipment.

The cell and back pressures were controlled by a pair of GDS Advanced Pressure/Volume Controllers, which automatically increment both pressures during the saturation and consolidation of soil specimens by a step-by-step motor. The cyclic triaxial apparatus includes connections to a panel with air/water interfaces connected to a motorised air compressor system, which manually operates until 600 kPa constant pressure. The air/water interfaces were connected to the triaxial cell during the shearing phase to allow for a correct application of cyclic loading and then obtaining a reliable measurement of soil behaviour during testing, as recommended by Liu

et al. (2022). An automatic volume gauge was used to measure the volume changes in fully saturated conditions during testing.

The local instrumentation comprises four Hall-Effect transducers, two to measure axial strains and two to measure radial strains directly installed in the soil specimen (see Figure 3.15). The Hall-Effect transducers consist of a magnetic conductor encapsulated in epoxy resin. Hall Effect conductors measure magnetic flux density across a metallic plate almost in contact with a magnet. The transducers are directly glued to the soil specimen thru a caliper assembly, which allows the movement —at low friction— of all transducers without inducing additional deformations in the soil specimen. These transducers were selected for this research since they are very light (≈ 12 g), which is an advantage during the testing of loose sands. This configuration allows for accurately estimating the volumetric strains of soil specimens in all testing phases, highlighting the saturation and cyclic shearing phases.



Figure 3.15: Local instrumentation by Hall-Effect transducers

The local instrumentation with the Hall-Effect transducers was implemented to measure the volumetric strains of soil specimens in dry and partially saturated conditions during testing. The validation of the measurements by Hall-Effect transducers was carried out through a comparison between the volumetric strains (ε_v) reported by these transducers against the measurements reported using the automatic volume

gauge measurements. This validation was performed using a fully saturated soil specimen of TP-Lisbon sand with a relative density of 30%. During such a test, the evolution of ε_v was examined for different mean effective stresses. Figure 3.16 compares the ε_v measurements between Hall-Effects transducers and automatic volume gauge. This figure reveals a good agreement between the measurements with a maximum difference of about 10%. The results comparison validates the suitability of using the Hall-Effects transducers to measure ε_v in partially saturated sands.

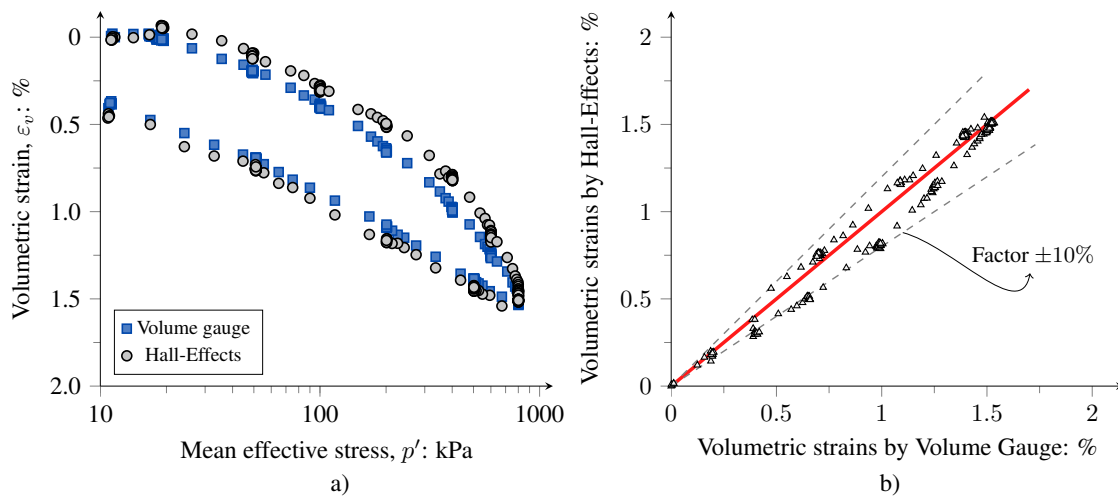


Figure 3.16: Validation of Hall-Effect measurements: a) ε_v variation as a function of p'_0 ; b) Comparison between Hall-Effects and automatic volume gauge

3.3.3 Simple shear apparatus

The simple shear (SS) apparatus used in this research is an advanced fully automatic simple-shear apparatus manufactured by Willie Geotechnik, which comprises an automatic system composed of a servo controller for applying cell and back-pressure increments and two high-quality servomotor drives for vertical and horizontal loading. The apparatus also includes a series of LVDT transducers to measure vertical and horizontal displacements and a multi-axis load cell, with the capacity for a maximum vertical force of 5 kN and maximum horizontal force of 4 kN. This system allows for conducting static and monotonic tests at strain and stress control. This apparatus also includes piezoelectric transducers for BE testing, which were installed during the development of this research. Figure 3.17 shows the SS apparatus of LabGEO.



Figure 3.17: Simple shear apparatus of LabGEO

The device can carry out static and cyclic tests in samples of 63 mm and 70 mm diameter. These samples are confined by a rubber membrane and a series of stacked copper rings —SGI configuration— which keep the area constant but allow the shear distortion of the specimen (Ramos, 2021). In this research, cyclic direct simple shear (CDSS) tests were conducted. Therefore, during CDSS, the soil specimen is subjected to cyclic shear stresses (or horizontal loading), ensuring a constant height of the specimen. Due to this test condition and the null radial deformations, this type of test is considered a test at constant volume state, which replicates the undrained shear conditions of the soil specimen (Dyvik et al., 1987). The main advantage of CDSS tests is the rotation of principal stresses during loading, which allows better replicating the in situ solicitation of the soil during a seismic event.

3.3.4 Resonant-column and cyclic shear torsional apparatus

The resonant-column (RC) apparatus used in this study is of bottom-fixed and top-free configuration or Stokoe type manufactured by Wykeham Farrance, which is in the ‘Centre for Advanced Studies of Road Infrastructure and Geotechnics’ at the

Universidad Militar Nueva Granada (Cajicá, Colombia). This apparatus allows applying a sinusoidal voltage to the coils attached to the cell body without an external function generator. Such sinusoidal voltage is proportional to the torque produced in the specimen top. In addition, the apparatus software has a routine to conduct the saturation and consolidation phases automatically. The pressures for these phases are controlled by a pneumatic system, which generates both cell pressure and back-pressure using air/water interfaces. The apparatus instrumentation consists of an axial LVDT transducer, a volume change apparatus, three pressure transducers, two Eddy current displacement sensors (with a miniaturised driving system) and a MEMS accelerator. This apparatus can perform tests in soil specimens of 50 mm diameter and 100 mm height. Figure 3.18 shows a photograph and scheme of the RC equipment.

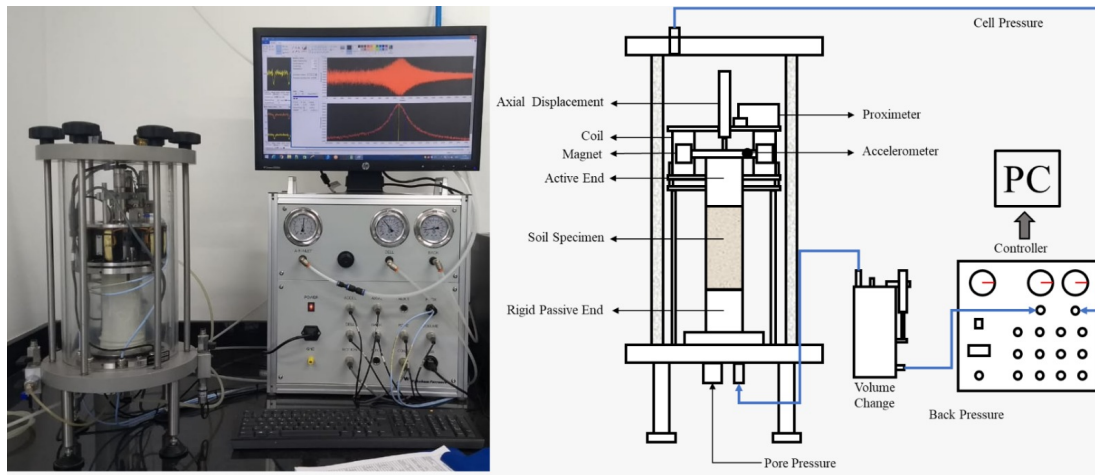


Figure 3.18: Resonant column apparatus at Universidad Militar Nueva Granada

The phenomenon of propagation of shear waves in an isotropic, homogeneous and elastic medium is represented by the wave equation expressed in Equation 3.1. Such an equation describes the movement of a particle located at any position of the medium.

$$\frac{\partial^2 u}{\partial t^2} = V_s^2 \cdot \nabla^2 u \quad (3.1)$$

where V_s is the shear wave velocity, ∇^2 is the Laplacian operator in cylindrical coordinates of the displacement component u .

Santos (1999) derived the generalised equilibrium Equation 3.2 for a Stokoe-type resonant-column apparatus, in which a specimen with height h , mass density ρ and

known rotational mass inertia J is subjected to forced vibration. This equation represents the small-strain visco-elastic response of a homogeneous, isotropic and elastic soil tested in this type of resonant column. The amplitude T_0 and frequency ω of the torque are controlled while a motion transducer measures the resulting rotation level θ_0 , which is ϕ radians out of phase with respect to the torque. The dynamic properties of the active platen (*i.e.* rotational mass inertia of the active pattern J_A) are determined by equipment calibration.

$$\frac{T_0}{\theta_0} \exp^{i\phi(\omega)} = \frac{J\omega^2}{\left(\frac{\omega}{V_s\sqrt{(1+i2\xi)}}\right) \tan\left(\frac{\omega}{V_s\sqrt{(1+i2\xi)}}\right)} - J_A\omega^2 \quad (3.2)$$

This model is valid for any frequency within the experimental range under small-strain loading. Since Equation 3.2 has a complex component, solving it by an iterative process requires an initial estimated value. The model solution converges if such initial values are close to the final results. Camacho-Tauta (2011) derived Equation 3.3 for estimating V_s and consequently G from measurable variables (e.g. resonant frequency, ω_R , and the total damping of the system, ξ_T), and then used them as the initial values to compute Equation 3.2. This proposal approximates the RC system into a single-degree-of-freedom model (SDOF) Khan et al. (2011).

$$V_s = \omega_R \cdot h \sqrt{\frac{J_A}{J} + \frac{1}{3}} \quad (3.3)$$

3.3.5 Geotechnical centrifuge apparatus

The geotechnical centrifuge apparatus used in this study is a mini geotechnical centrifuge located in the ‘Geotechnical Models Laboratory’ at Universidad de los Andes (Bogotá, Colombia). This apparatus corresponds to a beam-type centrifuge with a nominal radius of 56.5 cm. A beam centrifuge consists of horizontal structural beams that carry the payload at one end and a counterweight at the other end (Taylor, 1995). The horizontal beams are attached either by welds or bolts and act as a single structural beam. The main feature behind this configuration is the development of fast tests due to the preparation of small soil models lower than 4 kg (Garzón et al., 2015). Figure 3.19 shows the mini geotechnical centrifuge at Universidad de los Andes (Uniandes).

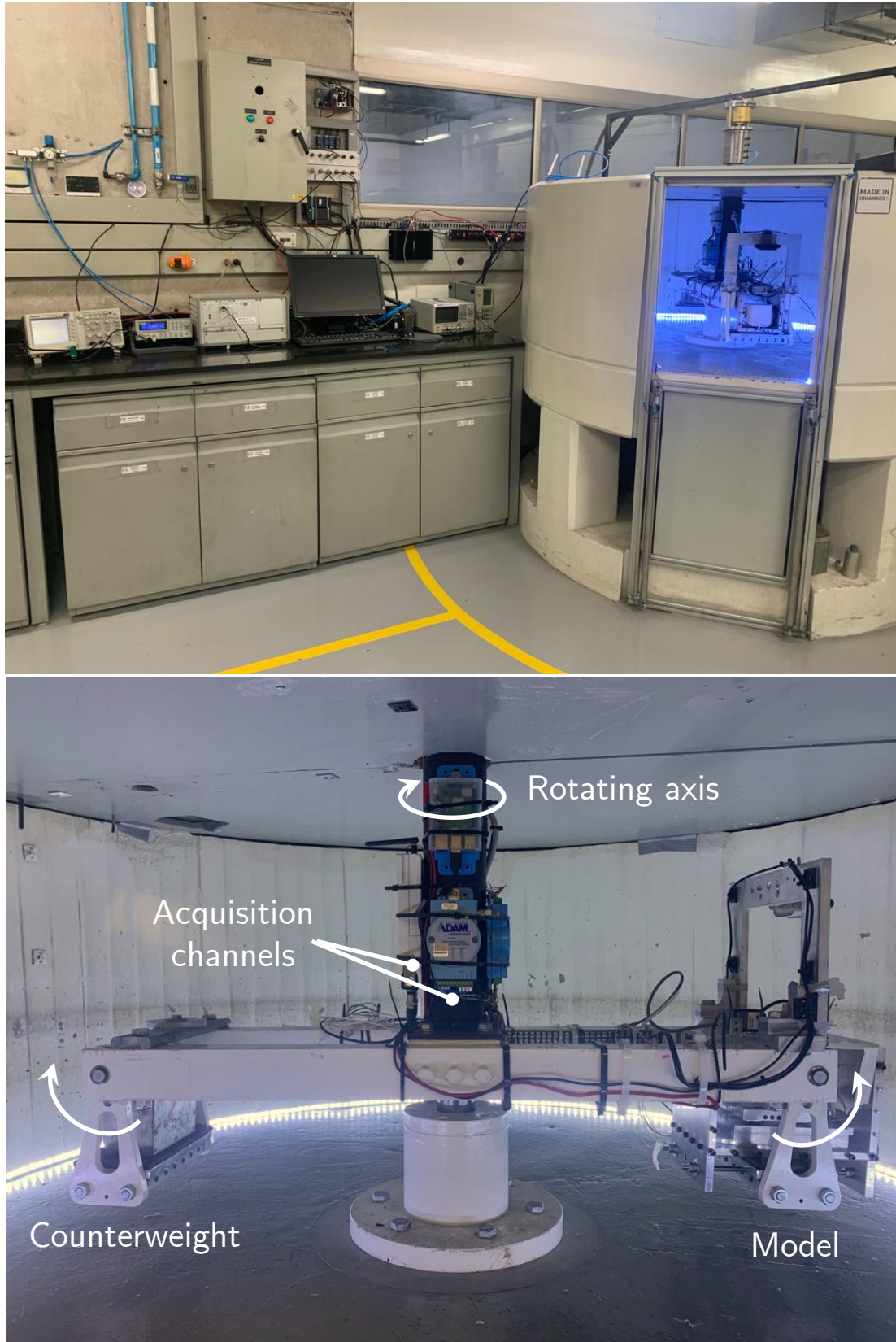


Figure 3.19: Mini geotechnical centrifuge at UniAndes

The centrifuge apparatus of UniAndes incorporates an in-flight micro shaking table and a laminar box system. The laminar box system was selected for dynamic testing since it to minimises boundary effects and allows for uniform wave propagation through the soil and container, as indicated by [Esmailpour et al. \(2023\)](#). This system allows for conducting dynamic tests on the acceleration and frequency of representative seismic events in the field. The novel design of this apparatus allows for quick preparation of numerous soil models ([Molina-Gómez et al., 2019](#)). The movement of the micro shaking table is applied by a Piezoelectric Actuator (CEDRAT APA ML120), which receives an input signal produced by a function generator (PROTEK B8003FD). The signal is then amplified by an amplifier device (CEDRAT LA75). This actuator is fixed at one end to the aluminium support and constrained at the other end by the payload over the shaking table base plate, serving as a ground motion source.

The centrifuge and micro shaking table setup allows for replicating the stress-state conditions and seismic loading at the model base, which represents the action at the bedrock of the soil deposit. The dynamic loading at the base is usually applied by a sinusoidal continuous signal, which can comprise different combinations of accelerations and displacements (induced by changing the input voltage and frequency of the Piezoelectric Actuator). However, the dynamic action is not limited to sinusoidal signals; it can be induced by different excitations depending on the capabilities of the function generator or the focus of the evaluated model.

The laminar box consists of six rectangular hollow frames stacked with two mini-linear bearings (SEBS3AY, Nippon Bearing). The frames have external dimensions of $\times 90 \text{ mm} \times 95 \text{ mm}$, and internal dimensions of $52 \text{ mm} \times 85 \text{ mm}$. The frame thickness is 8 mm, but each frame is separated by 1 mm to avoid any possible friction. This novel design allows free movement (at very low friction), ensuring the macro-gravity field without deforming or self-sliding. Inside the laminar box a latex membrane was incorporate to prevent any leak during testing of saturated or wet soils. [Figure 3.20](#) schematises the mini shaking table and laminar box system.

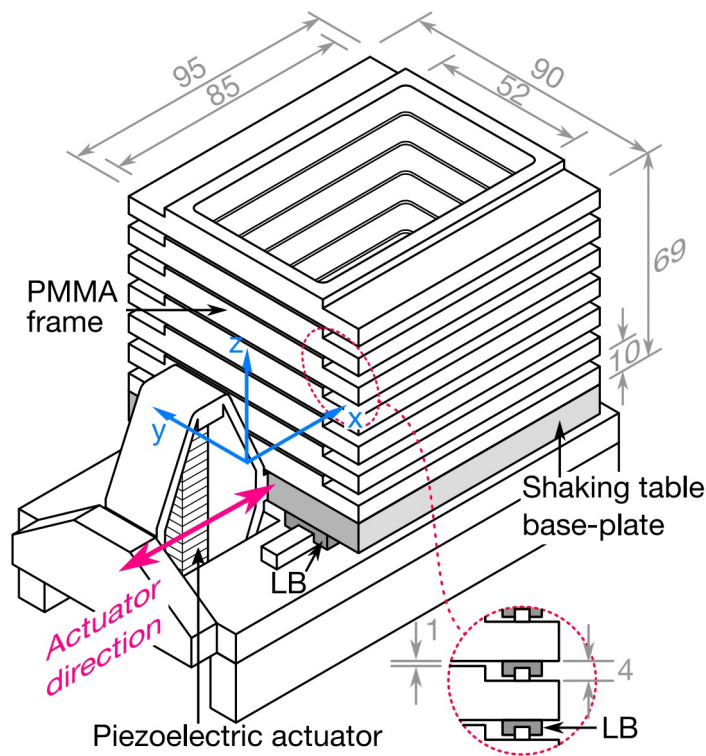


Figure 3.20: Scheme of the laminar box (Jara et al., 2020)

For dynamic testing, a series of transducers were used. The system instrumentation comprises three accelerometers (ACC104A OMEGA) positioned in the base, middle and top of the laminar box (i.e. 0 mm, 37 mm and 72 mm height, respectively), a pore pressure transducer (Honey Well 40PC0156) to measure up to 150 kPa and a laser to measure the vertical displacements (settlements) at the soil surface. The accelerometers allow registering the soil response during the dynamic testing, while the pore is connected directly to the box bottom to measure the pore pressure build-up of the soil when applying dynamic loading. Figure 3.21 presents the system instrumentation.

On the other hand, seismic wave measurements are fundamental for dynamic response assessment soils. This assessment can be performed by interpreting the hysteresis cycles obtained during in-flight shaking table testing. The dynamic properties change with the stress or strain level induced in the soil. For this reason, the use of ultrasonic methods or piezoelectric transducers is fundamental to characterise the small-strain stiffness of soil. However, these methods cannot be implemented in the laminar box since the elements may interfere with the free movement at low friction of the system. Therefore, a new container was specially designed to

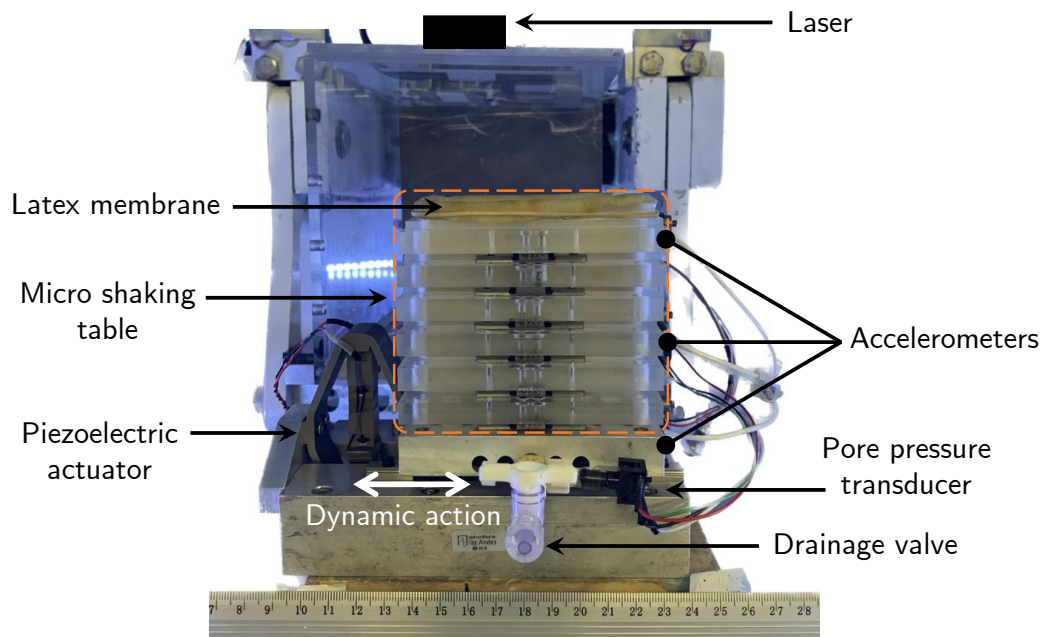


Figure 3.21: Instrumentation of micro shaking table and laminar box

be equipped with a pair of bender elements. The bender elements (BE) allow for the measurement of P-wave and S-wave velocities in-flight during centrifuge testing. This container was fabricated with Teflon due to its low weight and versatility during the manufacture of the box in the workshop. Moreover, this container has the same internal dimensions as the laminar box to replicate the same state of the soil during centrifuge testing. Figure 3.22 shows the soil container equipped with BE.

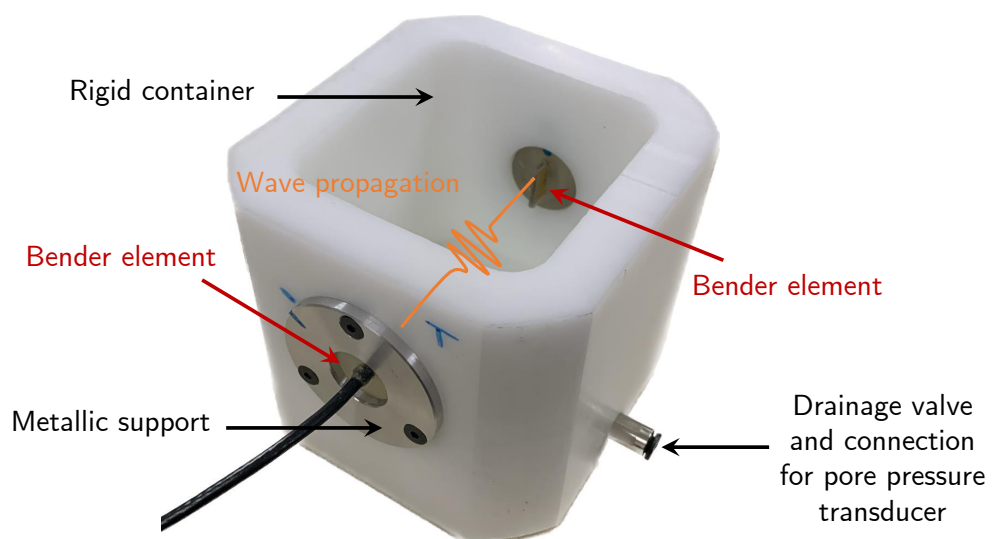


Figure 3.22: Soil container equipped with Bender Elements

3.4 Experimental procedures

3.4.1 Specimen preparation

Two of the features that guarantee the representability of the tests carried out in the laboratory are soil preparation and sampling remoulding. The soil preparation involved the blending of the sandy soil collected below the Praça do Comércio site at 13 to 23 m depth (point **A** Figure 3.2). Furthermore, it comprised the oven-drying and randomising of all studied soils using the standard procedure C702 (ASTM International, 2018), to obtain homogeneous and representative samples for element testing.

For this study, the dry pluviation method was adopted for remoulding the soil specimens. Notwithstanding, few specimens were remoulded using the moist tamping method for further comparisons and assessments of the fabric effect on the soil behaviour of the studied soils. The dry pluviation method ensures reasonably homogeneous soil specimens with an initial soil fabric similar to the one encountered in alluvial soil deposits (Miranda et al., 2020). Soil remoulding of soil using dry pluviation method comprised the procedure suggested by Yamashita et al. (2009). This procedure is done by rotating and lifting a long-neck funnel with dry soil. During the process, such a funnel is risen at a constant rate to maintain a constant drop height from the soil surface. In this study, there are no sieves in front of the funnel to regulate the flow, due to it was being controlled by the diameter of the funnel nozzle (≈ 8 mm). The dry pluviation method provides soil specimens with uniform density, which ranges from 25% to 75% if varies the drop height. This method was used in all testing setups, i.e. triaxial, simple shear and centrifuge apparatuses.

For the case of the specimens remoulded using the moist tamping method, the soil was mixed with water until achieve a specific of water content —usually 5% for sandy soils (Soares and Viana da Fonseca, 2016). Afterwards, the wet soil was divided into six or three layers to be compacted in the triaxial and simple shear chamber, respectively. The soil compaction was carried out by applying the under compaction method (Ladd, 1977) because it reduces the segregation of soil grains and allows obtaining uniform layers with the same density. In this study, a percent under compaction equal to 2% was adopted. Figure 3.23 schematises the remoulding methods used in this research.

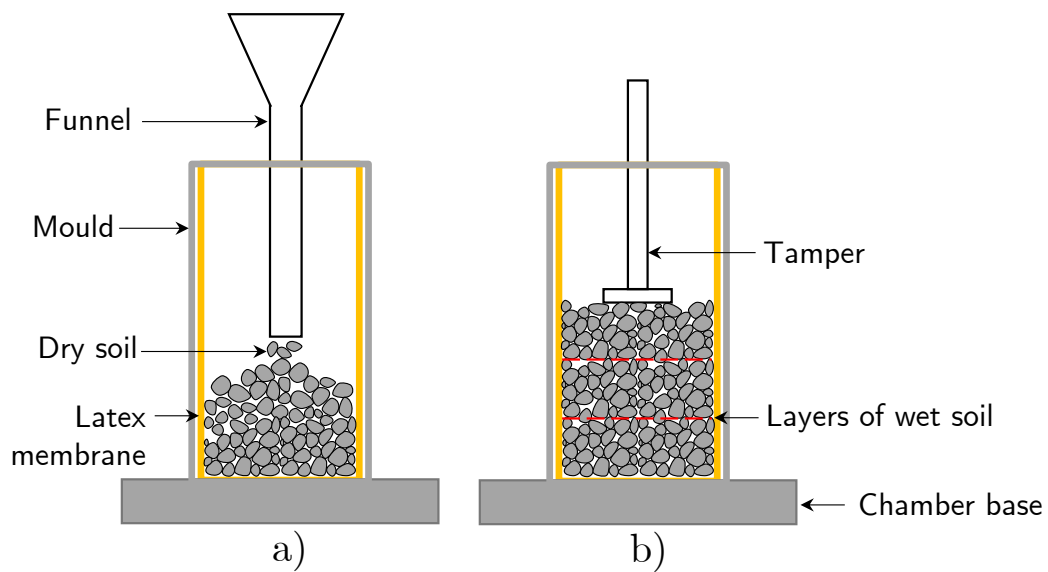


Figure 3.23: Schematic representation of the methods used for sampling remoulding: a) Dry Pluviation; b) Moist tamping

3.4.2 Element testing

The saturation process is fundamental for the assessment of liquefaction resistance of soils. In this research, a novel experimental approach have been proposed to assess the cyclic behaviour of sands under diverse Sr . This procedure mainly involves the monitoring of the degree of saturation by measuring the evolution of P-wave velocity (Vp) during testing with an accuracy control of total and water volume changes was carried out by means of local instrumentation (Hall-Effect transducers) installed directly in the soil specimen (see Figure 3.15) and an automatic volume change gauge. The details of this approach are in Chapter 6 due to the effects of Sr on liquefaction resistance.

The consolidation of soil specimens involved different procedures based on the the degree of saturation of the soil and type of element testing. Therefore, four procedures were implemented, according to the degree of saturation for soil testing and the type of element testing, two per condition, respectively. The procedure for fully saturated conditions consists of flushing of carbon dioxide and de-aired water through the sample and then gradually increasing the pressures using a ramp increment of 50 kPa/h. The procedure for soil testing in partially saturated conditions is described below in Chapter 6. On the other hand, the soil consolidation depended on the test type and device configuration. For triaxial testing, all soil specimens were isotropically consolidated at different confining effective stress (p'_0). Whereas, for direct

simple shear testing, the samples were consolidated by increasing the vertical load and restricting the radial strains by a series of stacked copper rings, inducing the K_0 condition. During this stage, in both element test type, an automatic volume gauge measured the specimen volume changes, the axial displacement was quantified with a Linear Variable Differential Transformer (LVDT) —attached to the load piston— or local instrumentation, when available.

The monotonic/static shear was conducted at 0.025 mm/min. This shear velocity is compatible with the rate of excess pore pressure dissipation of granular soils. For the case of cyclic tests, diverse combinations of cyclic stress ratio (CSR) were adopted. The cyclic loading was applied using a continuous sinusoidal signal at 1 Hz frequency and constant amplitude. To ensure the accuracy of the results, all tests were carried out by using internal submersible load cells. Besides, data was corrected for membrane restraint using the method as indicated in the standard procedure ISO/TS 17892-9 (ISO, 2004).

Regardless the type of test performed, an accurate void ratio determination is essential for the proper interpretation of results (Ramos, 2021). Therefore, at the end of the shear stage, all specimens tested in the triaxial cell with lubricated end platens were frozen to ensure a very accurate measurement of the final void ratio of the soil after testing, as observed by Soares and Viana da Fonseca (2016); Reid et al. (2021). For the case of the tests conducted in the devices equipped piezoelectric ceramic instruments (i.e. stress path, cyclic triaxial and simple shear), the specimens were carefully removed from the cell, avoiding possible loss of soil particles and water as suggested by Verdugo and Ishihara (1996); Murthy et al. (2007), for a correct measurement of the final void ratio after testing based on the final water content. The freezing was not used during the tests conducted in the apparatuses with BE to avoid damages in the piezoelectric ceramic instruments. This procedure, if used correctly, may be equally accurate to the EOTSF.

3.4.3 Site response by centrifuge testing

The characterisation of local site effects by site response analysis provides relevant insights for the assessment and mitigation of earthquake-induced damages. Moreover, this characterisation is important for the earthquake-resistant design of infrastructures and heritage preservation, such as the Pombaline architecture of the Terreiro do Paço site (located at the historical centre of Lisbon). Usually, local site effects studies focus on the assessment of three main factors during an earthquake:

i) amplification factor; *ii*) ground deformations; and *iii*) pore-pressure build-up (or liquefaction susceptibility). These parameters can be obtained after seismic events in instrumented sites or by dynamic centrifuge testing (Dashti et al., 2010; Bertalot et al., 2013; Fioravante et al., 2021).

Dynamic centrifuge testing allows for the assessment of site response of soil deposits due to its capacity to assess the soil behaviour under numerous combinations of testing conditions, e.g. stress state, cyclic loading and Sr . Such a type of testing can provide valuable insights that help in the proposal of alternatives to mitigate the effects caused by earthquake-induced damage due to its capabilities in replicating the site conditions without affecting the existing infrastructure. Therefore, in this research, an advanced experimental program that focuses on the site response Analysis of shallow sandy soil deposits with different Sr using a mini centrifuge equipped with a micro shaking table is carried out.

A novel procedure to perform site response analyses combining shaking table and geotechnical centrifuge testing is proposed in this research. This procedure addresses the application of diverse dynamic loading, as well as a method for the saturation and desaturation of the soil. However, this procedure is detailed in Chapter 7 since it is a novel contribution to the advancement of centrifuge testing methods, which enhances the characterisation of site response under partially saturated conditions.

3.5 Final considerations

This chapter has outlined the criteria used to select a specific type of sand for investigation in this research based on a liquefaction case history. Moreover, it provides a detailed description of the testing devices and experimental procedures employed to characterise the behaviour of TP-Lisbon sand. The reliability of the experimental results obtained in this research relies on the quality of these procedures. As a result, various equipment enhancements, such as the novel connection for the embedded top-cap loading ram (monotonic triaxial apparatus), piezoelectric actuator and transducers (cyclic triaxial and centrifuge apparatuses), rail miniature linear guide with low friction (micro shaking table), and others, have been implemented. On the other hand, specific details for soil testing, including the use of different input frequencies for the Bender Element (BE) tests and the measurement of the end-of-test void ratio, among other factors, have been applied in this research. These enhancements and refinements ensure the accuracy of the obtained results.

Chapter 4

Characterisation of the geomechanical properties of TP-Lisbon sand

A version with the main content of this chapter has been published in:

Molina-Gómez, F. and Viana da Fonseca A. (2021) Key geomechanical properties of the historically liquefiable TP-Lisbon sand. *Soils and Foundations* 61(3): 836-856. doi: 10.1016/j.sandf.2021.03.004 and Molina-Gómez, F.; Viana da Fonseca, A.; Ferreira, C.; Camacho-Tauta, J. (2020) Dynamic properties of two historically liquefiable sands in the Lisbon area. *Soil Dynamics and Earthquake Engineering* 140: 106101. doi: 10.1016/j.soildyn.2020.106101

4.1 Outline

This chapter presents the results of a comprehensive experimental study aimed at characterising the geomechanical properties of TP-Lisbon sand. For this purpose, a comprehensive experimental plan was conducted in the laboratory using accurate testing procedures, addressing: (i) the evaluation of the particle shape from a large number of particles using a computational geometry algorithm and statistical procedures; (ii) the estimation of the minimum and maximum void ratio through two standard methods; (iii) the assessment of the stress-strain behaviour by triaxial tests using lubricated end platens and an embedded connection piston, and (iv) and void ratio measurements by end-of-test soil freezing. Besides, resonant column and bender element tests assessed the small-strain properties (shear modulus and damping). The main features of the behaviour of TP-Lisbon sand are interpreted within

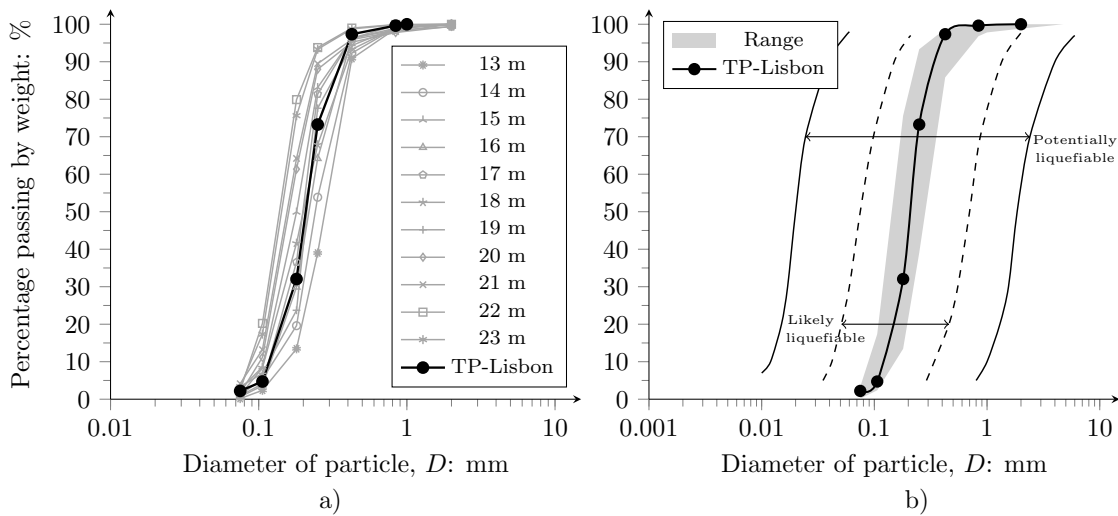


Figure 4.1: Grain size distributions: a) measurements at each meter; b) comparison against liquefaction boundaries

the critical state soil mechanics framework. In addition, critical state parameters are compared and thoroughly discussed against selected data from other sands. Therefore, the results of this chapter provide a detailed geotechnical database to add new experimental evidence about the mechanical behaviour of sandy soils, highlighting the effects of the particle shape and granular packing on the geomechanical properties of TP-Lisbon sand.

4.2 Intrinsic properties

TP-Lisbon sand corresponds to a historically liquefiable soil, which was collected below Praça do Comércio at 13 to 23 m depth (point **A** Figure 3.2), as described in Chapter 3. Therefore, a series of particle-size analyses using the sieve method ASTM D422 was carried out for samples located at each meter depth. Figure 4.1 presents the grain size distribution of the collected soil in each depth and the blended material—giving to TP-Lisbon sand. Due to the low variability of the grain size distribution (GSD) of the sandy soils that compose the liquefiable layer bellow Praça do Comércio, these samples were blended. The GSD of blended soil provides a good representation of the range of grain sizes in the field. In addition, Figure 4.1 presents a comparison of the grain size distributions against the boundaries proposed by Tsuchida (1970) to estimate the liquefaction susceptibility based on the compositional criteria of the soil. This comparison showed that the grain size distribution of TP-Lisbon sand fall within the boundaries of a soil likely liquefiable.

Table 4.1: Physical properties of TP-Lisbon sand

Parameter	Units	Value
G_s	-	2.66
e_{max}	-	1.01* ; 1.01 ⁺
e_{min}	-	0.63* ; 0.64 ⁺
$e_{max} - e_{min}$	-	0.38* ; 0.39 ⁺
D_{50}	mm	0.21
C_z	-	1.13
C_u	-	1.69
Fines content	%	2.21

Note: *ASTM method; ⁺JGS method

As mentioned before TP-Lisbon sand is a natural sand with an alluvial origin from the Tagus River. The mineralogy of this sand is 78% Quartz, 8% Orthoclase 8% Muscovite and 6% Albite. Table 4.1 summarises the physical properties measured in the laboratory of TP-Lisbon sand, such as specific gravity of solid particles (G_s) mean diameter (D_{50}), maximum and minimum void ratio (e_{max} and e_{min}). Moreover, Table 4.1 indicates the parameters of the grain size distribution of TP-Lisbon sand, namely the coefficient of curvature (C_z) and the coefficient of uniformity (C_u). According to the unified soil classification system (USCS) TP-Lisbon sand was classified as poorly-graded (SP) with low values of C_u and C_z —indicating a uniform particle size distribution.

Due to the interest in studying the effect of soil package on the mechanical behaviour of this soil, e_{max} and e_{min} were estimated by the ASTM and Japanese Geotechnical Society (JGS) standard procedures (D4253 2016a; D4254 2016b; JGS 0161 2009). For measuring e_{max} , these standard procedures address the air pluviation technique using a funnel located as close as possible to the soil surface to achieve its loosest condition. The main differences between these procedures are related to the use of moulds with different dimensions – 2830 cm³ for ASTM procedure and 113 cm³ for JGS procedure. For measuring e_{min} , ASTM and JGS procedures use the same moulds before mentioned and involve a vertical vibrating table and the application of horizontal blows, respectively. Since the total applied energy during testing, e_{min} values obtained from the JGS method yields slightly higher values than e_{min} values obtained from the ASTM (Lunne et al., 2019). Non-significant differences resulted by using both standard procedures for e_{max} and e_{min} . Void ratio range ($e_{max} - e_{min}$) agree with the values claimed by Ishihara et al. (2016) for clean sands. The results obtained by means of the ASTM methods will be used for further comparisons

because these are more universal.

The particle shape has a strong influence on the extreme void ratios and various mechanical properties like the small-strain stiffness sand shear strength of sands (Cho et al., 2006; Altuhafi et al., 2016; Sarkar et al., 2020). The shape of particles was assessed through extensive morphological imaging analysis, including samples with of about 15000 sand particles. The equipment used in this research was a Morphologi G3-ID, produced by Malvern Panalytical Company, which can measure individual particles with sizes between $1.3 \mu\text{m}$ and 1.0mm . This equipment can identify the length, width, perimeter, area and elongation of the particles. A macro photograph displaying the particles of TP-Lisbon sand is shown in Figure 4.2. Based on the macro photographs, the shape of the particles was estimated using a MATLAB algorithm implemented by Zheng and Hryciw (2015). The procedure involved a careful observation of individual grains robust using numerical methods based on computational geometry to estimate the traditional values from two-dimensional images using the binary form of particles, as shown in Figure 4.2b.

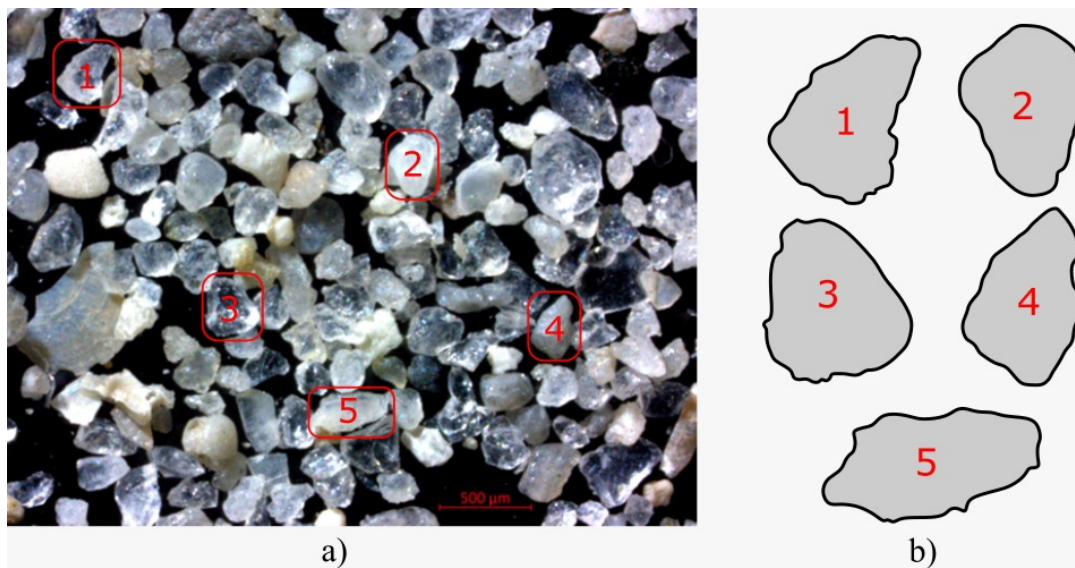


Figure 4.2: Particles of TP-Lisbon sand: a) Photograph of the particles taken with an optical microscope; b) Binary image of some selected particles

The computational algorithm used in this study assessed about 1000 random particles. The particle shape was defined by mean values of the convexity (Cx), circularity (Ci), sphericity (S), roundness (R) and regularity (ρ). Figure 4.3 presents the definition of these morphological parameters. Cx is the ratio between the area of the particle (A) with the area of the particle when any convexity inside its perimeter are filled ($A + B$), providing a measure of the compactness of the particle (Altuhafi

et al., 2016). Ci is a function of a projected area and perimeter of the particle, A_p and P_p respectively. Both A_p and P_p are computed by estimating the radius (r_{eq}) of a circle with an equivalent area of the analysed particle (Lashkari et al., 2020). S quantifies how close a particle's largest projected area is to a perfect circle (Zheng and Hryciw, 2015). Therefore, computation of S covers the ratio of the radius of the maximum inscribed circle (r_{max-in}) to the radius of the minimum circumscribed circle ($r_{min-cir}$). R describes the sharpness of particles corners (N) by estimating the ratio of the average radius of curvature of such corners (r_i) to r_{max-in} (Zheng et al., 2017). ρ is the average value between S and R (Cho et al., 2006).

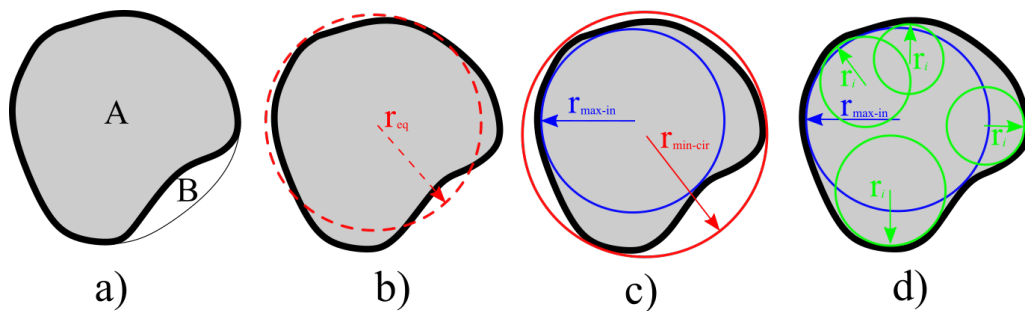


Figure 4.3: Graphical definitions of particle shape parameters: a) convexity, b) circularity; c) sphericity; d) roundness

Figure 4.4 illustrates the procedure for assessing the particle shape. Table 4.2 summarises the results of the particle shape analysis. Results showed that the particles of TP-Lisbon sand are predominately subangular according to Shape-Angularity Group Indicator (SAGI = 11.76) proposed by Altuhafi et al. (2016). This classification indicated that the particles composing TP-Lisbon sand have a morphology similar to well-characterised silica natural sands, namely Ticino and Toyoura sands, as reported by Altuhafi et al. (2016).

4.3 Compressibility

The compressibility of TP-Lisbon sand was investigated by a series of one-dimensional oedometer compression tests by apparatuses capable of testing specimens of 50 mm and 70 mm diameter. The one-dimensional consolidation tests were conducted using front-loading oedometer frames. These tests included the testing of soil samples under dry and full saturation conditions, prepared through the dry pluviation and moist tamping methods. All the specimens were remoulded for an initial void ratio value close to the e_{max} (indicated in Table 4.1). Moreover, the tests were conducted

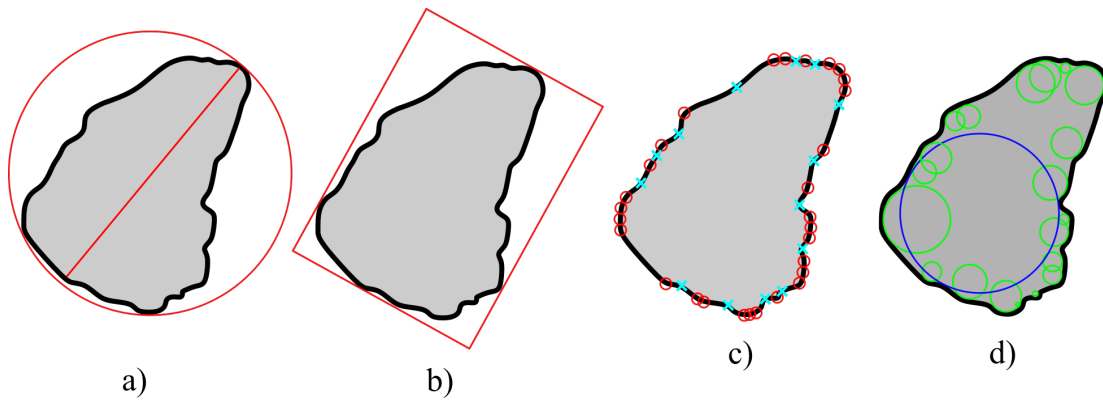


Figure 4.4: Example of the analysis of particle shape –particle 1 of Figure 4.2: a) Diameter sphericity, b) width to length ratio sphericity; c) identification of particle corners; d) circle corner fitting of the particle

Table 4.2: Shape parameters of TP-Lisbon sand

Particle shape parameter	Mathematical definition	Value
Convexity	$C_x = \frac{A}{A + B}$	0.95
Circularity	$C_i = \frac{2\sqrt{\pi A_p}}{P_p}$	0.88
Roundness	$R = \frac{\sum_{i=1}^N (r_i/N)}{r_{ins}}$	0.41
Sphericity	$S = \frac{r_{max-in}}{r_{min-cir}}$	0.56
Regularity	$\rho = \frac{S + R}{2}$	0.49

under dry and full saturation conditions, corresponding to one dry test with a specimen prepared using dry pluviation method and three saturated tests with specimens prepared using both methods. Of these three saturated tests, two were conducted using soil specimens 50 mm diameter and one was performed using a specimen 70 mm diameter. The samples reached a high degree of saturation by inundating the oedometer cell with deaired water and waiting for 12 hours. The maximum applied vertical effective stress (σ'_v) in one-dimensional oedometer compression tests was reached at 6400 kPa in the specimens of 50 mm diameter. Figure 4.5 presents the compressibility curves obtained from one-dimensional compression tests.

Compressibility curves revealed a very similar shape between for the specimens

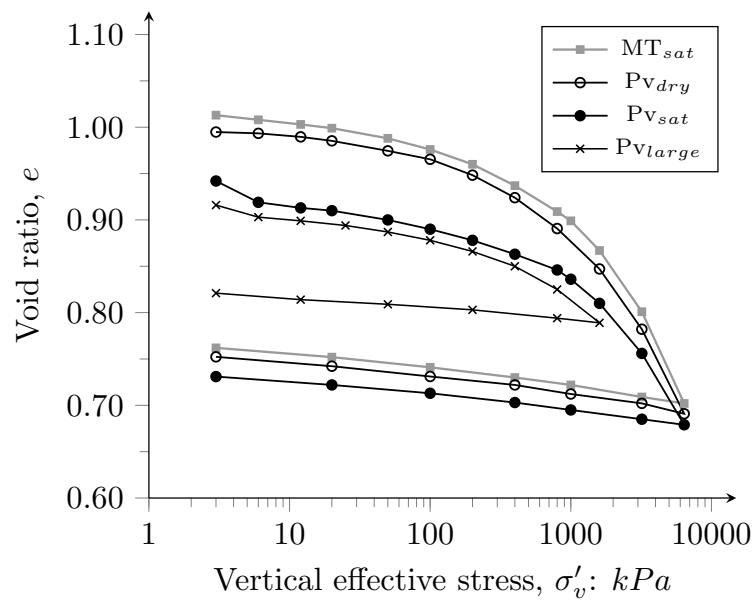


Figure 4.5: One-dimensional compression behaviour of TP-Lisbon sand

prepared by dry pluviation and moist tamping. In addition, these curves indicated that the oedometer compressibility behaviour of TP-Lisbon sand is similar under dry and saturated conditions for close initial void ratios, even when using different methods of preparation. A comparison between the curves of the specimens of 50 mm and 70 mm diameter showed that there is not an important effect of the specimen size on the oedometer compressibility behaviour of TP-Lisbon sand. On the other hand, from Figure 4.5, it can be observed that the curves of the samples prepared using the dry pluviation method and tested under saturated conditions presented a ‘collapse’ after the first load stage.

A grain size distribution analysis was carried out after finishing the test of specimen 70 mm diameter to assess the particle crushing and its influence on the compressibility behaviour of TP-Lisbon sand. GSD was not assessed for the specimens of 50 mm due to the minimum amount of material established in ASTM D6913 standard [ASTM International \(2007\)](#). The test results revealed that the GSD does not change after testing, showing that there is not crushing of particles of TP-Lisbon sand when applying σ'_v lower than 1600 kPa. Notwithstanding, from Figure 4.5, it can be observed that for σ'_v between 1600 kPa and 6400 kPa the slope of curves increases, that is, an indication of crushing onset of particles in such range of stresses. Therefore, results obtained in the σ'_v range between 6 kPa to 1600 kPa was considered to interpret the compressibility curves. Table 4.3 summarises the compressibility parameters obtained from the one-dimensional consolidation curves for the different

initial void ratios and preparation methods.

Table 4.3: Compressibility parameters

Test	e_0	C_c	Cr	C_e	Cr/C_c
MT _{sat}	1.01	0.1466	0.0176	0.0172	0.1208
PV _{dry}	0.99	0.1422	0.0153	0.0149	0.1045
PV _{sat}	0.94	0.1325	0.0174	0.0173	0.1311

Values of Table 4.3 indicates that there are no significant differences between the results of the four oedometer tests. Results of C_c values reported in Table 4.3 agrees with the compression parameters observed by Mesri and Vardhanabhuti (2009), which vary from 0.03 to 0.63 for σ'_v between 1000 and 10000 kPa in very loose conditions. This range is suitable for angular to subangular quartz sands; such as Mol sand, which is a sandy soil with similar intrinsic properties of TP-Lisbon sand ($Cu = 1.75$ and $D_{50} = 0.20$ mm).

Moreover, the compressibility of TP-Lisbon sand was explored through isotropic triaxial tests. Such tests will be further discussed in the following sections of this chapter. For silica sands, intrinsic consolidation line (ICL) is non-unique and multiple ICLs exist depending on the initial void ratio, e_0 , (Jefferies and Been, 2000). However, in many cases, these ICLs converge to a single line known as limiting compression line (LCL), which becomes apparent at a high-stress level and before the onset of grain crushing (Pestana and Whittle, 1995). Figure 4.6 shows a series of end consolidation points obtained in the triaxial tests. Besides, Figure 4.6 presents three characteristic isotropic consolidation paths obtained for e_0 of about 0.96, 0.91 and 0.86, which end at 200, 500 and 800 kPa, respectively. These isotropic consolidation paths well-represent the ICL of the referred e_0 , as confirmed by the end consolidation points obtained for similar initial states.

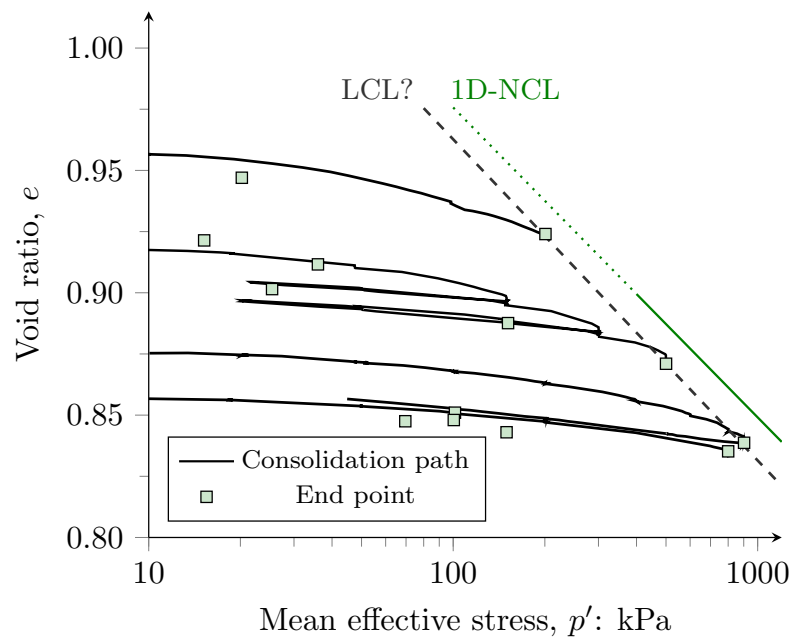


Figure 4.6: Isotropic consolidation of TP-Lisbon sand

From isotropic consolidation paths, a possible limiting compression line (LCL) was inferred for TP-Lisbon sand. LCL was estimated by considering LCL the endpoint of three isotropic consolidation paths. In Figure 4.6, it can be observed that the LCL line is almost parallel to a 1D-NCL deduced from the one-dimensional compressibility. The parallelism between such lines is consistent regarding the behaviour observed in granular materials (Li et al., 2018; Qadimi and Coop, 2007). 1D-NCL was obtained from the compression curve of the tests Pv_{dry} within the range 400 kPa and 1600 kPa. This range was selected because at these stresses TP-Lisbon sand does not experience crushing of particles.

The definition of ICLs for e_0 values close to e_{max} (that is, $e_0 > 0.96$) was not possible due to the volume reduction of the specimens during de-aired water flushing after CO_2 flushing, as also observed in the assessment of the one-dimensional oedometer compression tests (see Figure 4.5). Similar behaviour was described by Jefferies and Been (2000) since these authors reported a significant volume reduction during the saturation of very loose sandy samples. Therefore, soil collapse during water flushing did not allow obtaining soil specimens with Dr higher than 0.14 at the end of the consolidation phase. Although the convergence of some ICLs to a single line, additional triaxial tests involving high-stress levels are required to confirm the LCL inferred in this study.

4.4 Stress-strain behaviour and critical state

A total of 19 monotonic triaxial compression tests were conducted on loose and medium dense specimens ($D_r < 63\%$). The experimental plan included 14 tests under drained conditions and 5 tests under undrained conditions. These tests were carried out by combining the equipment configurations and the two methods for specimen preparation —described in section 3.4.1. Table 4.4 summarises the details and final results of triaxial tests. Figure 4.7 presents the results of the triaxial tests on TP-Lisbon sand. From Figure 4.7, it can be observed that the stress-strain curves have a similar shape for the drained and undrained tests. Most of the tests were sheared to axial strains up to 25% to reach the critical state, except for TxU15-300 test that concluded close to 20% axial strain because the triaxial apparatus reached its maximum displacement.

On the other hand, for the undrained tests, the phase transformation occurs within the range 1-2% axial strain. This transformation generates an increase in deviatoric stress and a reduction in the pore pressure, increasing the shear strength of soil. In addition, once the initial peak deviatoric stress occurs, in about 25-27% axial strain, the stabilisation of the deviatoric stress and pore pressure keep constant, indicating that the soil reached its the critical state. Figure 4.7 shows that the stress-strain and shear-induced pore pressure curves of the undrained test are parallel; even for Tx-300, which does not reach the critical state. Analogous evolution of shear-induced pore pressure was observed by [Giretti and Fioravante \(2017\)](#) in alluvial liquefiable deposits.

Table 4.4: Details of the triaxial tests for critical state assessment

Test name	Triaxial cell	Method of preparation	Test condition	Mean confining effective stress, p'_0 : kPa	Relative density after consolidation, Dr : %	Deviatoric stress at CS, q_{cs} : kPa	Mean effective stress at CS, p'_{cs} : kPa	Void ratio at CS, e_{cs}
TxD1-10	LEP	Pv	D	10	22	28	20	0.9681
TxD2-15	LEP	Pv	D	15	24	37	28	0.9649
TxD3-20	LEP	Pv	D	20	18	52	39	0.962
TxD4-25	LEP	Pv	D	25	29	62	47	0.9498
TxD5-35	LEP	Pv	D	35	27	95	70	0.9386
TxD6-50	LEP	Pv	D	51	49	143	100	0.9161
TxD7-50	LEP	MT	D	50	19	121	87	0.9303
TxD8-70	LEP	Pv	D	70	44	185	134	0.8998
TxD9-100	LEP	Pv	D	100	43	273	192	0.8821
TxD10-150	LEP	Pv	D	149	62	362	271	0.8631
TxD11-150	LEP	MT	D	151	32	355	268	0.8765
TxD12-150	BE	MT	D	150	45	320	257	0.8808
TxD13-200	LEP	MT	D	200	23	487	362	0.8592
TxD14-500	BE	Pv	D	500	38	1279	928	0.806
TxU15-100	LEP	Pv	U	100	43	460	350	0.8511
TxU16-150	LEP	Pv	U	150	41	445	331	0.8597
TxU17-300	BE	Pv	U	300	56	*	*	*
TxU18-400	LEP	Pv	U	400	49	638	496	0.8299
TxU19-500	LEP	Pv	U	500	52	805	632	0.8172

Note: LEP is lubricated end platen; BE is bender element; D is drained; U is undrained; CS is critical state; * do not reach the CS.

The results of all the drained and undrained triaxial tests considered to have reached the critical state were used to define the critical state parameters of TP-Lisbon sand. Critical state was confirmed by assessing the stress-dilatancy evolution in all tests, as is shown below in the next section. Figure 4.8 presents the stress path on the $q : p'$ invariant space derived from triaxial tests results. From Figure 4.8, it can be observed that the end points all define a unique critical state line (CSL) in the $q : p'$ space, which is clearly represented by a straight line passing through the origin. The CSL projection $q : p'$ space defines the strength parameter M equal to 1.37. Therefore, the angle of shearing resistance at large strains or in the critical state (ϕ_{cs}) of TP-Lisbon Sand is 34° . Similar findings were reported by Gajo and Wood (1999) for Hostun sand, a sandy soil with intrinsic properties very close to TP-Lisbon sand (e.g. $Cu = 1.80$, $e_{max} = 1.00$ and $e_{min} = 0.65$).

On the other hand, Figure 4.8.b presents the undrained stress behaviour of TP-Lisbon sand under monotonic load. This behaviour is interpreted by the phase transformation point and the undrained instability point. Murthy et al. (2007) define the phase transformation point as the point at which the sand response changes from contractive to dilative, and the undrained instability point as the point at which q reaches a local and temporary maximum value. For TP-Lisbon sand, it was observed that the phase transformation point is close to the CSL, indicating soil dilatation once the soil reached a stable frictional state. Besides, although no liquefaction was triggered in undrained tests, it was possible to identify the instability points for each test. Such instability points allowed defining an instability line (η_L), with a slope of about 0.80.

Figure 4.9 shows the best-fit CSL for TP-Lisbon sand in $e : \log p'$ space. Solid diamond symbols represent the starting of drained shearing, while solid squares symbols represent the same for undrained tests. Open circles indicate the end of the triaxial tests at critical state condition, which were used to define the CSL. From Figure 4.9, it can be observed that CSL is curved at low stresses, being relatively flat for $p' < 30$ kPa, but subsequent it converges to a unique linear gradient. This effect is typical in granular soils due to soil packing effect represented by e_{max} value and flow instability at low-stress levels and high void ratio of this type of geomaterials (Verdugo and Ishihara, 1996; Murthy et al., 2007; Carrera et al., 2011; Li et al., 2018). Although the experimental evidence showed that the CSL of TP-Lisbon sand is curvilinear, in this study, only the straight-linear part of the CSL will be considered to describe the behaviour of this particular sandy soil. Such an assumption was

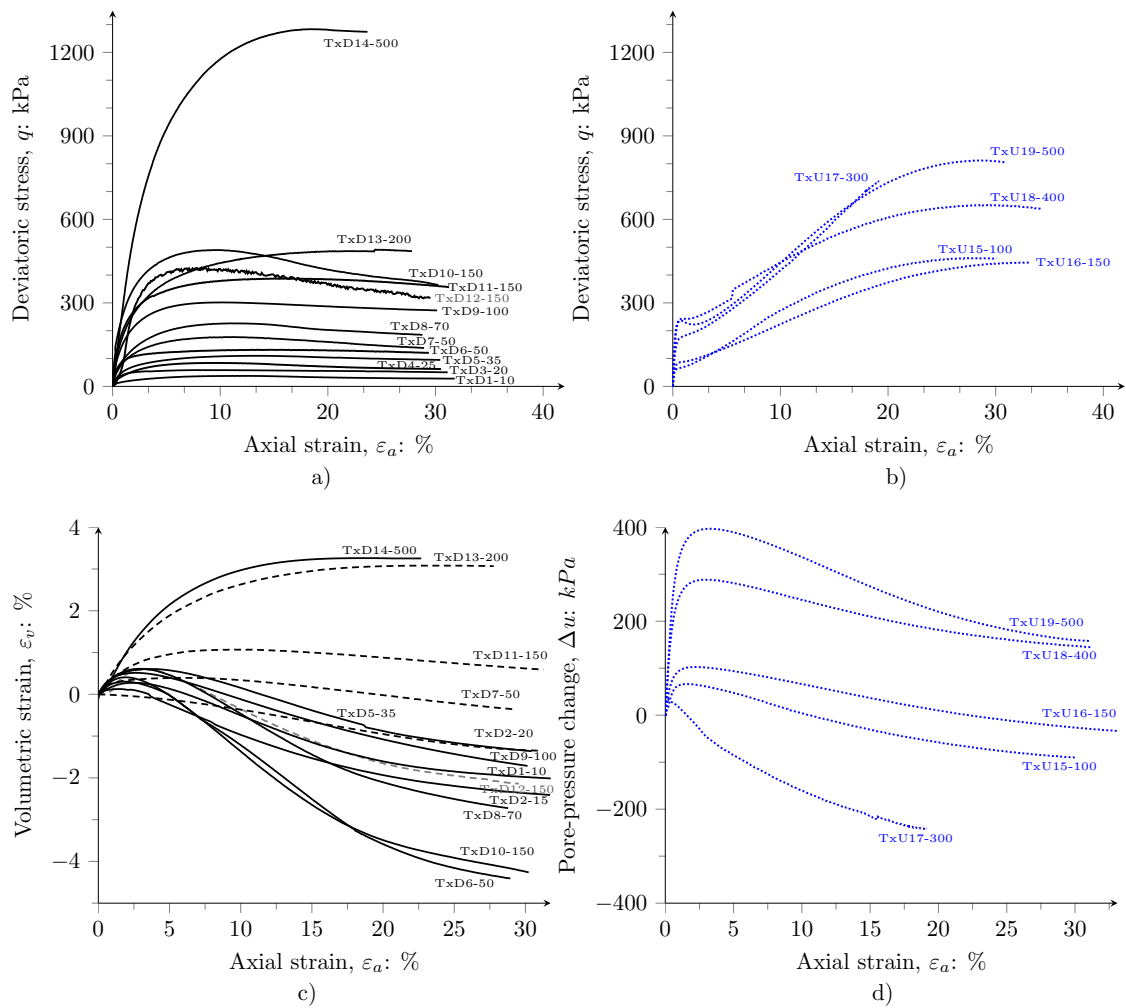


Figure 4.7: Triaxial test results on TP-Lisbon sand: a) stress-strain behaviour in drained tests; b) stress-strain behaviour in undrained tests; c) change of volumetric strain in drained tests; d) pore-pressure change in undrained tests

implemented because the stress and relative density states of the curve part of CSL of TP-Lisbon sand are unlikely in practical engineering applications.

The the general form of Equation 4.1 was adopted to define the CSL in the straight-linear part.

$$e_{cs} = \Gamma - \lambda \ln p' \quad (4.1)$$

where e_{cs} is the critical state void ratio, Γ is the void ratio defined at $p' = 1$ kPa and λ is the slope of the CSL in the $e : \log p'$ space. Tests results allowed defining a unique CSL with a higher correlation coefficient ($R^2 > 0.97$) for TP-Lisbon sand

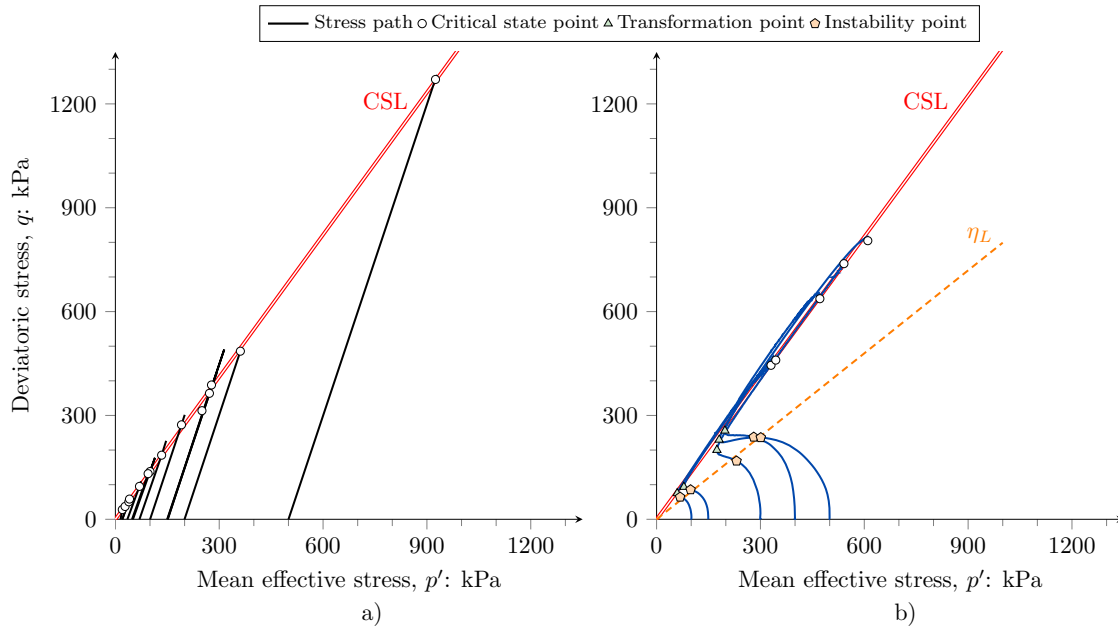


Figure 4.8: Stress path and CSL on $q : p'$ invariant space: a) drained stress behaviour; b) undrained stress behaviour

with $\Gamma = 1.155$ and $\lambda = 0.052$. The linear approach of the equation 4.1 provides the best-fit to describe the behaviour of TP-Lisbon sand for p' from 40 kPa to 1000 kPa and e from 0.7821 to 0.9616. These ranges well represent the possible stress-state conditions that this sandy soil may experience in the field.

In Figure 4.9, the drained state paths have a hooked shape since the void ratio change during shearing. The orientation of the hooked shape varies according to the position of the initial void ratio with respect to the CSL (i.e. above or below). Test-paths with similar shapes were observed for drained tests with both contractile and dilative behaviour. On the other hand, Figure 4.9 showed that the undrained state paths are horizontal lines, displaying minimum values of p' different to their corresponding p'_0 . This effect is due to the positive change of pore pressure caused by their initial contractile behaviour.

A comparison of the CSL for TP-Lisbon sand with other quartz sands is shown in Figure 4.10. The parameters of the best-fit CSL for TP-Lisbon sand are comparable to several of other natural sands reported by Cho et al. (2006) and Altuhafi et al. (2016). Compared to sands with similar intrinsic properties (e.g. D_{50} , Cu , e_{max} and e_{min}), TP-Lisbon CSL sand has similar λ value and higher Γ value, indicating that the CSL is parallel and lies in a different position to the reference sands. In sands with roundness values lower than 0.45, such as Ticino sand, Blasting sand

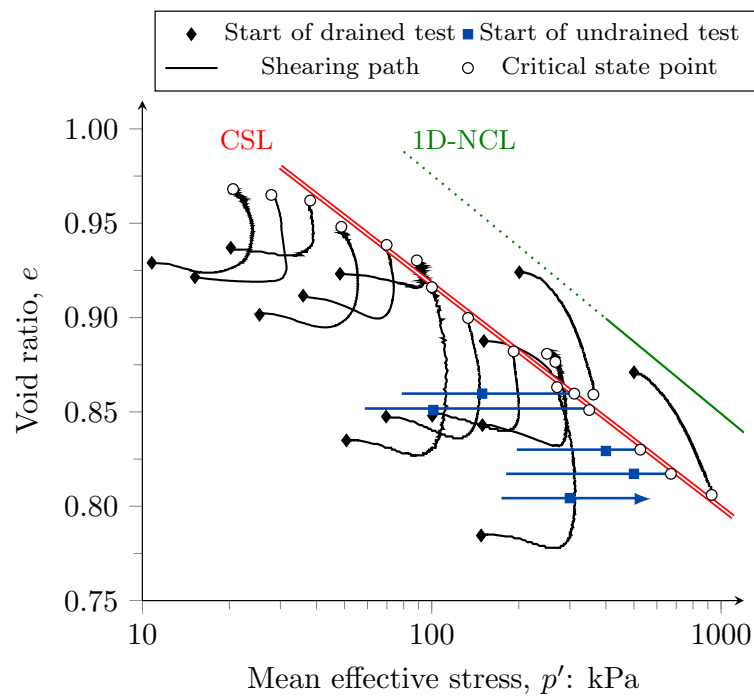


Figure 4.9: Interpreted CSL with the inferred 1D-NCL for TP-Lisbon sand on $e : \log p'$ invariant space

and TP-Lisbon sand, Γ values higher than e_{max} values were observed. According to Cho et al. (2006); Yang and Luo (2015); Altuhafi et al. (2016); Sarkar et al. (2020), a decreasing in particle roundness and regularity lead to an increase in the Γ parameter, meaning the CSL is located above when the sand is composed of angular particles. Therefore, the relatively high position of the TP-Lisbon CSL is attributed to the subangular shape of its particles, as also found by Ramos et al. (2019).

4.5 Effects of particle shape and packing on critical state parameters

Overall, the position of the CSL of granular soils is independent of initial soil fabric (Been et al., 1991; Ishihara, 1993; Carrera et al., 2011; Li et al., 2018). However, CSL and behaviour of sands depend on some intrinsic properties, which are represented by the particle dimension, particle shape and the granular packing. Previous studies showed that particle shape and soil packing characteristics affect the critical state and small-strain stiffness parameters of sands and non-plastic soils (Cubrinovski and Ishihara, 2002; Santamarina and Cho, 2004; Park and Santamarina, 2017; Torres-Cruz and Santamarina, 2020). Cho et al. (2006); Yang and Luo (2015); Altuhafi

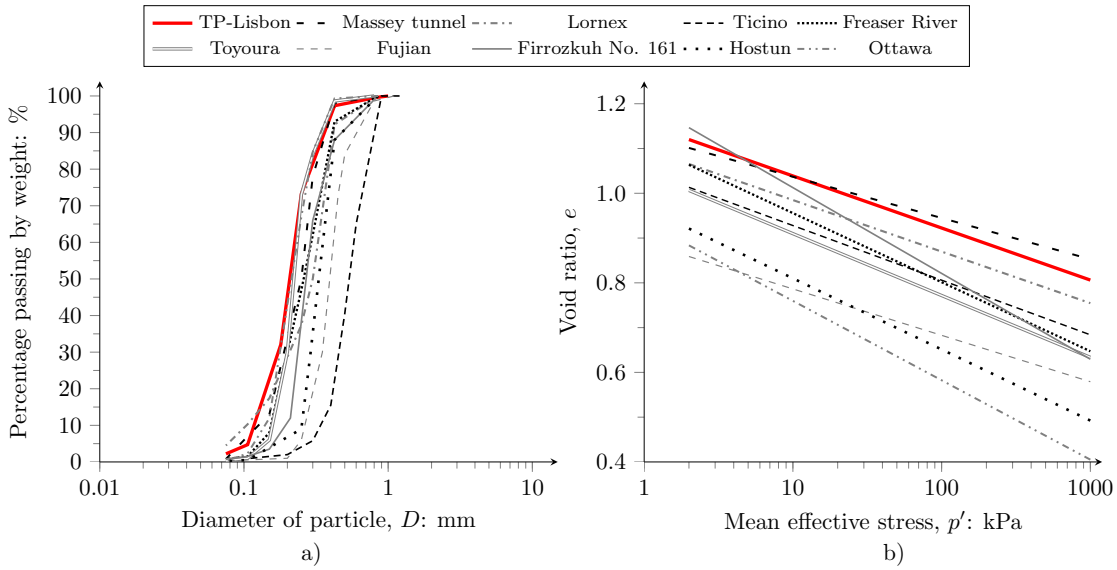


Figure 4.10: Comparison of TP-Lisbon against other sands with similar intrinsic properties: a) GSD; b) CSL

et al. (2016); Sarkar et al. (2020); Lashkari et al. (2020) proposed correlations between critical state parameters with the particle shape of sands. The main findings of these studies were similar –particle shape can significantly alter the critical state parameters of granular soils– although included the measurement of morphological properties by different methods (e.g. visual approach and advanced imaging analysis).

The effects of particle shape on critical state parameters were recently validated by numerical simulations comprising discrete element methods, DEM, (e.g. Jiang et al. 2018; Nguyen et al. 2020). Consequently, the morphological properties provide micromechanical approximations toward explaining complex phenomena of granular materials interpreted by the CSSM framework, such as soil liquefaction (Yang and Wei, 2012; Wei and Yang, 2014) and dilatancy (Winter et al., 2017; Xiao et al., 2019). The particle shape also has a strong influence on the packing of granular materials (Cubrinovski and Ishihara, 2002; Santamarina and Cho, 2004; Sarkar et al., 2020); for example, non-spherical and uniform-sized sands tend to have larger values of e_{max} and e_{min} than rounded, spherical, and well-graded sands (Zheng and Hryciw, 2016; Zheng et al., 2017). Soil packing, represented by the extreme void ratios in sandy soils, captures the underlying role on the volumetric compression potential and allows identifying the potential position of CSL (Torres-Cruz and Santamarina, 2020). In addition, it is well-known that the soil packing together with the particle shape has a strong influence on the stress-dependency of small-strain stiffness of

sands because of the contact-type and arrangement of soil particles (Cho et al., 2006; Altuhafi et al., 2016; Liu and Yang, 2018). Therefore, there is an interest on the part of geotechnical research in assessing the influence of the morphology of soil particles on the geomechanical properties of granular geomaterials.

Figure 4.11 presents the relationships between packing with critical state parameters, indicating a positive linear increment of all critical state parameters when increasing the values of packing parameters. Results indicated that the relationships with best agreement are ϕ_{cs} and Γ with the three packing parameters. Besides, Figure 4.11 shows that the spread in e_{max} is lower than that in e_{max} and void ratio range $e_{max} - e_{min}$.

Figure 4.12 presents the relationships between particle shape properties with critical state parameters. From Figure 4.12, it was observed that the sands composed of angular particles have higher values of critical state parameters (i.e. ϕ_{cs} , Γ and λ) than the sand with spherical particles. R and ρ presented the best fitting with ϕ_{cs} and Γ . Note that there is no clear clustering of λ as a function of particle shape properties, as also observed by Cho et al. (2006); Torres-Cruz and Santamarina (2020). Therefore, the packing and shape of particles have a strong influence only in the ϕ_{cs} and Γ parameters of sandy soils.

For the specific case of TP-Lisbon sand, e_{max} , R and ρ are the best parameters for describing the relatively high position of the CSL since particle shape and packing affect the intercept of the CSL in the $e : \log p'$ space, but not the slope of the CSL. This effect induces and controls the predominant dilative behaviour of this sandy soil in the low-pressure range. In addition, it was observed that the particles shape of TP-Lisbon sand controls the shearing resistance at large strains and its critical state.

4.6 Stress–dilatancy assessment

Stress-dilatancy refers to the volumetric changes in sands as a result of mobilised shear strains and applied stresses. Stress–dilatancy is a concept regarding plastic strain rates since shear stress does not generate elastic volume change. The soil dilatation is estimated by computing the ratio between the volumetric strain increment and deviatoric strain increment ($d = \delta\varepsilon_v/\varepsilon_s$), providing relevant elements to assess the behaviour of granular materials. For undrained conditions, the soil dilata-

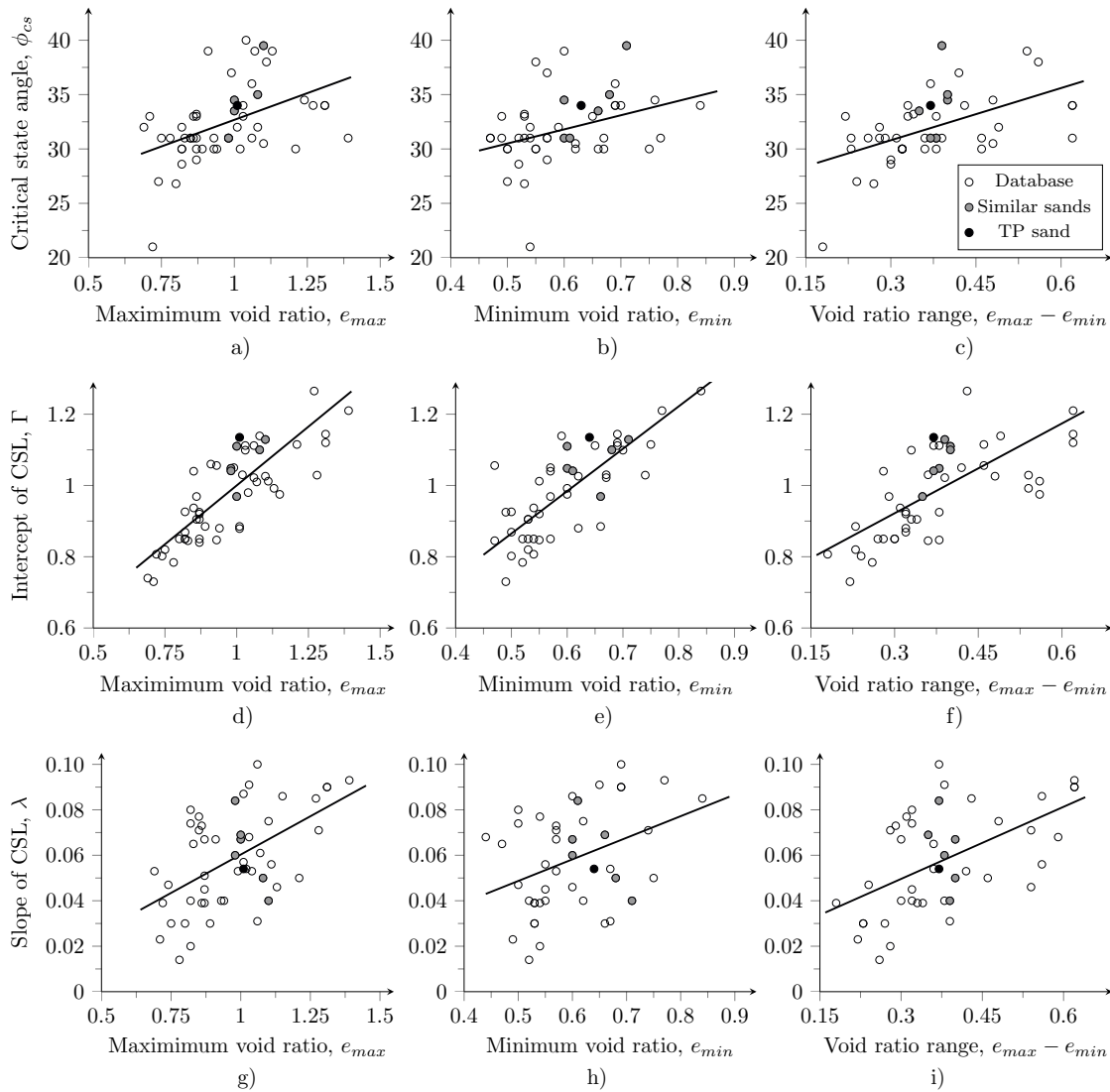


Figure 4.11: Relationships between packing with critical state parameters: a) ϕ_{cs} vs. e_{max} ; b) ϕ_{cs} vs. e_{min} ; c) ϕ_{cs} vs. $e_{max} - e_{min}$; d) Γ vs. e_{max} ; e) Γ vs. e_{min} ; f) Γ vs. $e_{max} - e_{min}$; g) λ vs. e_{max} ; h) λ vs. e_{min} ; i) λ vs. $e_{max} - e_{min}$

tion is estimated by the rate of change of the deviatoric strain increment ($\delta\Delta u/\varepsilon_a$), where $\varepsilon_a = \varepsilon_s$ since there is no volume change in undrained testing. Soil dilatancy only considers the plastic volumetric strains because the elastic volumetric strains are very small and then negligible (Been and Jefferies, 2004). Figure 4.13 presents the development of the stress ratio ($\eta = q/p'$) with the axial strain, the evolution of stress-dilatancy (for drained tests) and the normalised pore pressure in terms of volumetric strains (for undrained tests).

From Figure 4.13.a, it can be observed a convergence of the stress ratio to a single η value of about 1.37 at large axial stains, for both drained and undrained tests,

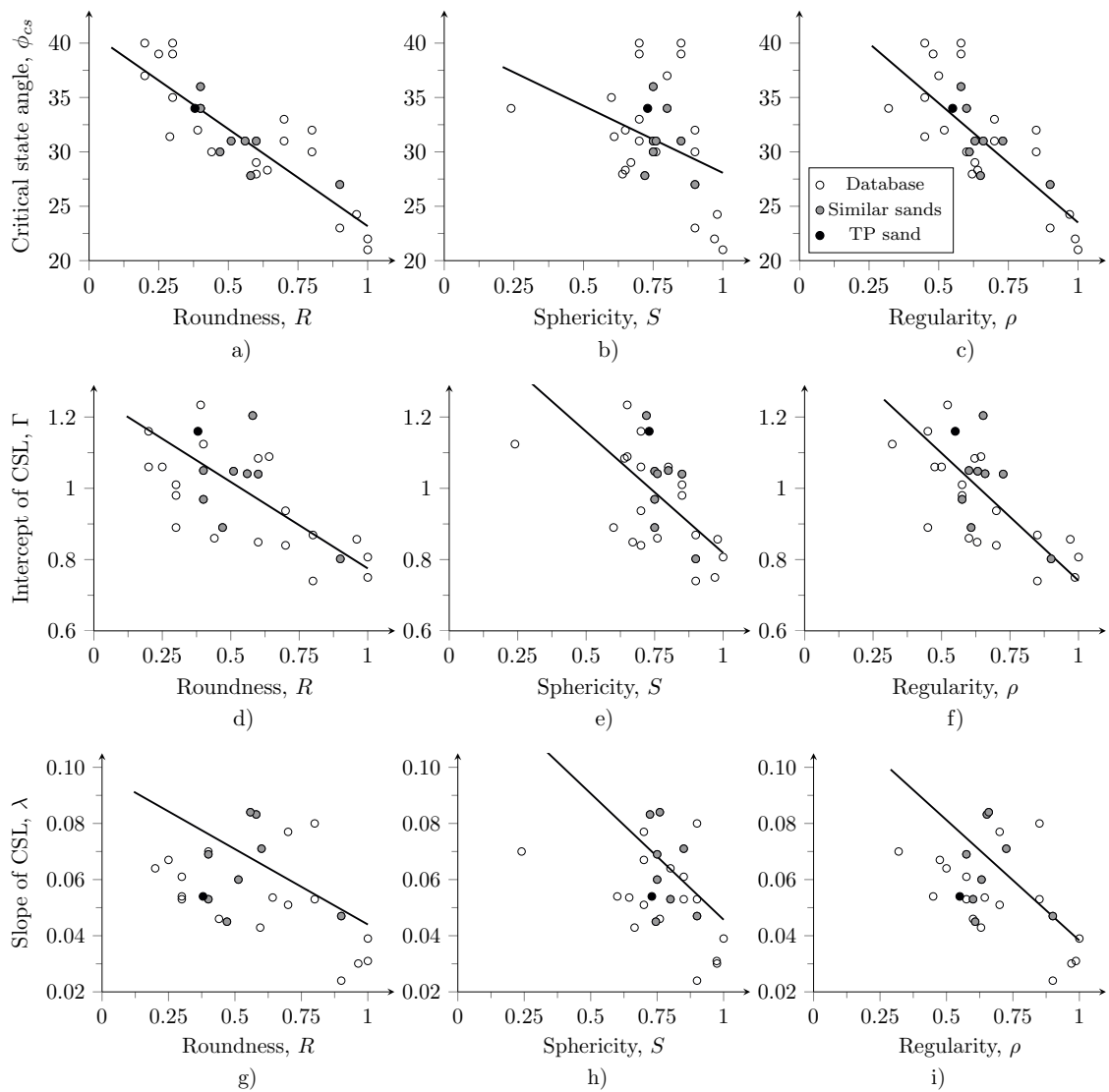


Figure 4.12: Relationships between particle shape properties with critical state parameters: a) ϕ_{cs} vs. R ; b) ϕ_{cs} vs. S ; c) ϕ_{cs} vs. ρ ; d) Γ vs. R ; e) Γ vs. S ; f) Γ vs. ρ ; g) λ vs. R ; h) λ vs. S ; i) λ vs. ρ

corresponding to the M value already identified in Figure 4.8. Such a convergence occurs when $\varepsilon_v/\varepsilon_s$ and $\delta\Delta u/\varepsilon_a$ are zero, confirming that all tests reached the critical state condition for both drained and undrained conditions, except TxU17-300. On the other hand, negative dilation rates are evidenced in Figure 4.13.b with peak strengths higher than the final value achieved at the end of the tests, indicating the effects of stress-dilatancy on specimens with states below the critical state line. Figure 4.13.c plots the stress-ratio results of undrained tests, showing that when the pore pressure rate is zero ($\delta\Delta u/\varepsilon_a$) the soil moves upwards until the maximum shear strength value and then moves downwards to the critical state condition.

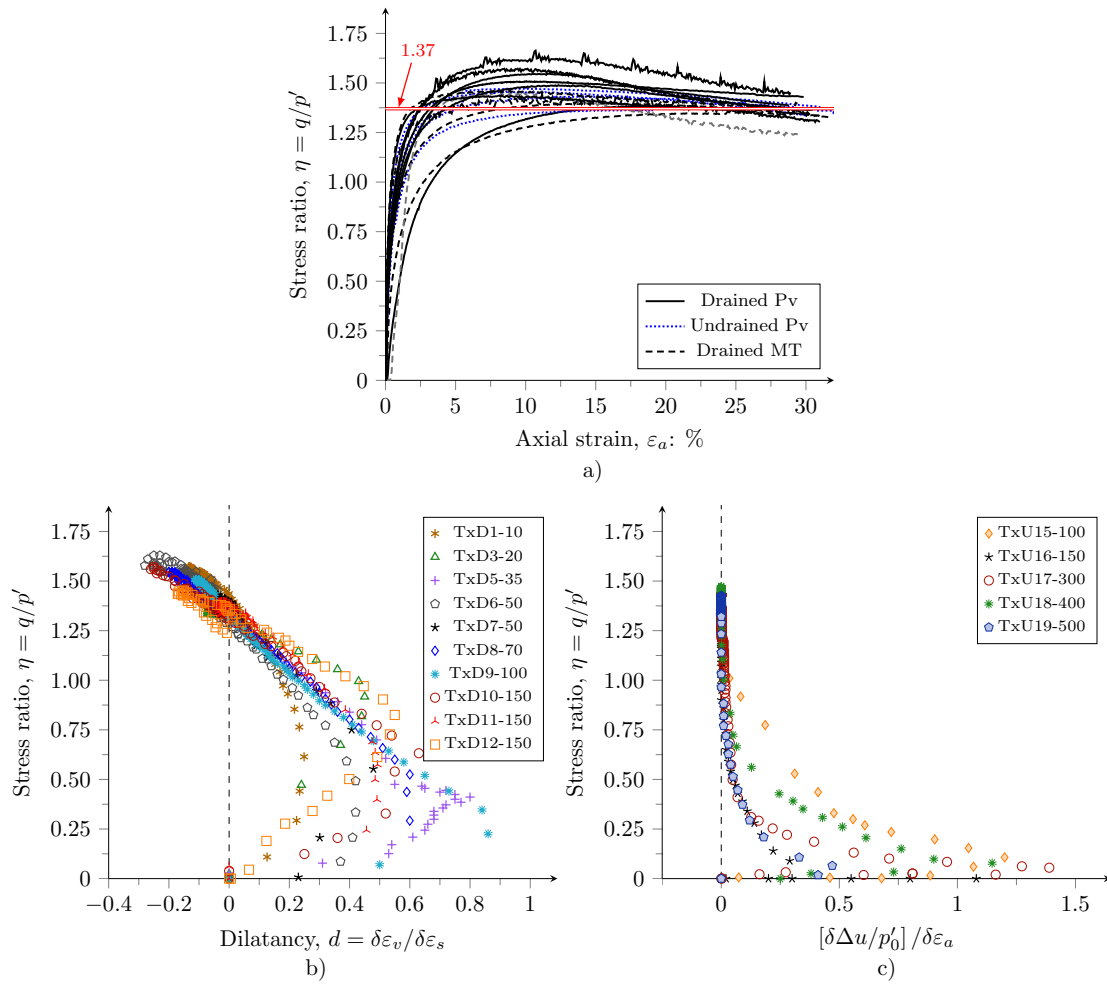


Figure 4.13: Stress ratio relationships: a) stress ratio behaviour; b) dilation rate for drained tests; c) stress ratio plotted against the normalised pore pressure change for undrained tests

The stress-dilatancy curves of TP-Lisbon sand revealed a clear reversal once the soil reaches the peak stress ratio (η_{max}), following afterwards to the critical state (see Figure 4.13.b). This behaviour was observed in the negative values of volumetric strains rate, indicating the maximum dilation rate (d_{min}) of all tests. Experimental data shows that TP-Lisbon sand is highly dilatant, mainly at lower values of confinement stress, which is typical of angular and subangular sands (Nguyen et al., 2020). This behaviour was also observed by Been and Jefferies (2004) for loose quartz sands.

The soil stress-dilatancy behaviour of sands can be represented by plotting the η_{max} of the drained tests as a function of d_{min} (Nova, 1982). This relation incorporates a volumetric coupling parameter (N), as follows.

$$\eta_{max} = M - (1 - N)d_{min} \quad (4.2)$$

Equation 4.2 provides an inverse linear relationship between both variables, that is, higher values of η_{max} for lower values of d_{min} . For TP-Lisbon sand, it was found that $N = 0.17$ provides the best fitting to describe the evolution of η_{max} in terms of d_{min} . Figure 4.14 shows the relationship between η_{max} and d_{min} of TP-Lisbon sand in the same triaxial test compared against the model of equation 4.2. Moreover, Figure 4.14 indicates that the intercept at zero dilatancy is 1.37, which corresponds to the same value of M inferred in Figure 4.8.

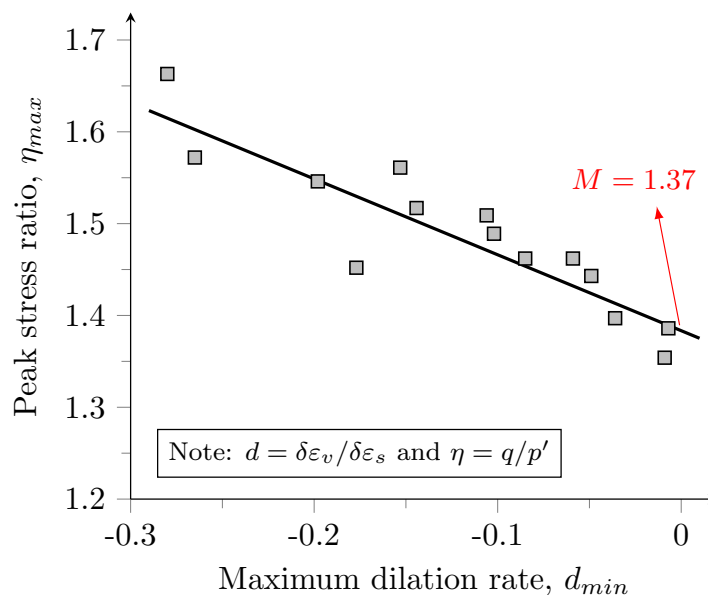


Figure 4.14: Peak stress ratio and maximum stress-dilatancy of TP-Lisbon sand

Another way to interpret the stress-dilatancy behaviour of granular materials using the CSSM framework is the combining of d_{min} with the state parameter (ψ)—defined as the difference or distance between the current void ratio and the void ratio on the CSL at the same stress-state (Been and Jefferies, 1985). This novel interpretation allows estimating the rate of dilation through the dilatancy rate scaling parameter (χ), which is the line slope of obtained from the d_{min} values and their corresponding ψ at which d_{min} occurs. Jefferies and Been (2015) claimed that χ is a material property that captures the maximum dilatation of the soil and ranges typically from 2 to 5. However, for uniform and clean sands, this parameter ranges from 3.5 to 4.0 according to the particle shapes. Figure 4.15 shows the derivation of $\chi = 3.79$,

indicating a good agreement to the typical values for quartz sands usually assumed as 3.5 (Giretti et al., 2018).

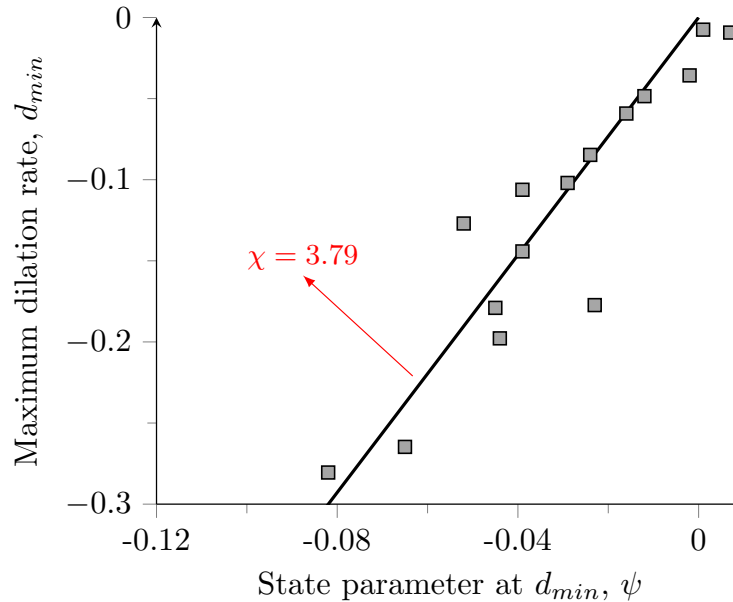


Figure 4.15: Maximum stress-dilatancy and state parameter relationship for TP-Lisbon sand

4.7 Dynamic behaviour of TP-Lisbon sand

4.7.1 Shear modulus and damping curves

The soil behaviour during seismic events and wave propagation is correlated to the dynamic properties of soils often expressed in terms of shear modulus and damping ratio. These dynamic properties are estimated commonly in the laboratory by bender-element and resonant-column tests. Bender-element test works at very small-strain level, i.e. $\gamma \leq 10^{-5}$ (Ishihara, 1996), while resonant-column test allows measuring the dynamic properties in the small to medium strain levels ($10^{-5} < \gamma < 10^{-3}$) (Camacho-Tauta, 2011). For this reason, both tests are complementary since it is well known that the stress-strain behaviour of soil is highly non-linear, and soil stiffness may decay with strain increment. However, the limit values of both tests range below the strains for triggering soil liquefaction.

The shear modulus (G) is a stiffness parameter, which is related to the mass density of the soil (ρ) and the shear wave velocity (V_S). V_S is a soil property, which can be measured both in the field and in the laboratory, offering the advantage of providing

comparable results from the two types of testing (Ferreira, 2009). Equation 4.3 presents the most common procedures to compute analytically G . On the other hand, the damping ratio (ξ) is defined as the ratio of the energy loss per cycle (ΔW) to the elastic stored energy (W) (see Equation 4.4). The energy concepts were previously introduced in Figure 2.9.

$$G = \rho \times V_s^2 \quad (4.3)$$

$$\xi = \frac{\Delta W}{2 \times \pi \times W} \quad (4.4)$$

In an initial phase, the dynamic response of TP-Lisbon sand was investigated by resonant-column (RC) tests, using the equipment described in Section 3.3.4. RC tests were conducted for dry and saturated conditions under different mean effective confinement pressure; that is, p'_0 equal to 30, 50, 100, 150 and 200 kPa. Besides, these tests were conducted in remoulded specimens of 50 mm diameter with $Dr \approx 0.30$, which corresponds to the in situ relative density. The dynamic excitation was applied by generating a sine-sweep, which ranged ± 25 Hz of the resonant frequency. This procedure was repeated ten times for input voltages between 1 mV and 1000 mV to reduce the uncertainties of measurements.

RC measurements allowed obtaining the resonant frequency (ω_R). Such a value was related to V_S and then G , as well as with ξ (Khan et al., 2011). Experimental data were interpreted by applying Equation 3.3, the seed values for the computation of Equation 3.2 were obtained for each amplitude. Figure 4.16 shows the typical results of the transfer function computation. In such a Figure, the system response variation is presented as a function of the different frequencies of the sine-sweep signal during RC testing. In all tests, ω_R was defined where the transfer function of the absolute value of the Rotation-Torque ratio, $|H_{\theta T}|$, exhibits a sharp peak that indicates the resonant point (see Figure 4.16.a) and the phase angle, $\phi_{\theta T}$, is equal to $-\pi/2$ rad (see Figure 4.16.b). Besides, from Figure 4.16, it can be observed a good fitting between experimental data and theoretical model, demonstrating the applicability of the function transfer.

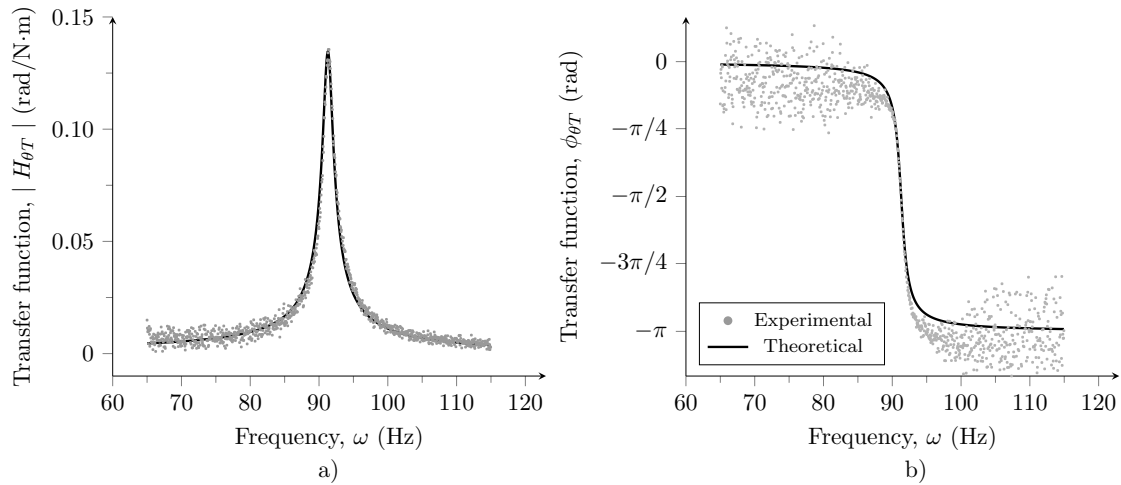


Figure 4.16: Typical results of transfer function computation (test in dry specimen at 100 kPa and 2 mV): a) magnitude; b) phase

Figure 4.17 presents the curves of shear modulus and damping ratio obtained from RC tests in the range of small to medium strains ($10^{-6} < \gamma < 10^{-3}$) for samples remoulded for $Dr = 30\%$ and tested under dry and saturated conditions. For both dry and saturated, G values increased when γ increased and remained constant in the strain range of $\gamma < 10^{-5}$. Furthermore, in Figure 4.17, it was recognised greater values of G for higher p'_0 , as was expected. However, slightly higher values were observed for G of saturated soil. These differences can be attributed to small variations in the relative density of tested samples. On the other hand, in Figure 4.17, it can be recognised that ξ values increase as γ increases. The higher ξ values were achieved for $p'_0 = 30$ kPa. As in the shear modulus curves, significant differences between ξ results were not identified in dry and saturated conditions.

Since G changes according to the strain level induced to the soil, it can be normalised in terms of the maximum shear modulus (G_0) to represent the reduction of the soil stiffness at different γ . G_0 describes the elastic response of soil at small-strain levels. Normalised shear modulus curve or stiffness degradation curve allows identifying the soil stiffness under cyclic loading at very small, small, medium and large strains ranges. Such ranges establish the dynamic response of the soil, as well as the model that best represents the cyclic soil behaviour for each strain level (Ishihara, 1996). RC tests provided the normalised decay of soil stiffness G/G_0 or shear modulus degradation curves and damping ratio evolution. Figure 4.18 presents the stiffness degradation curves for the different stress-state conditions for dry and saturated conditions of TP-Lisbon sand.

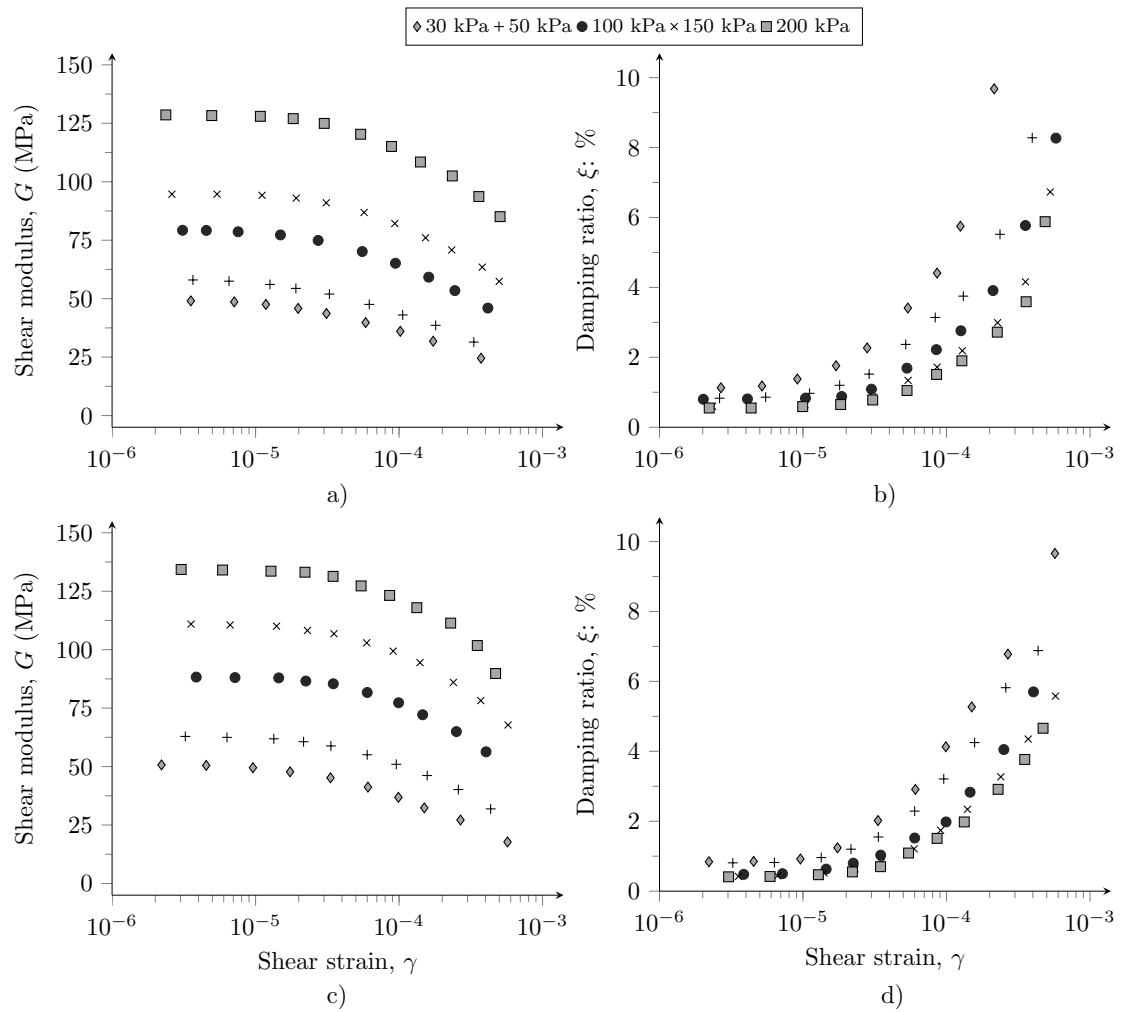


Figure 4.17: Evolution of small-strain stiffness: a) shear modulus in dry conditions; b) damping in dry conditions; c) shear modulus in saturated conditions; d) damping in saturated conditions

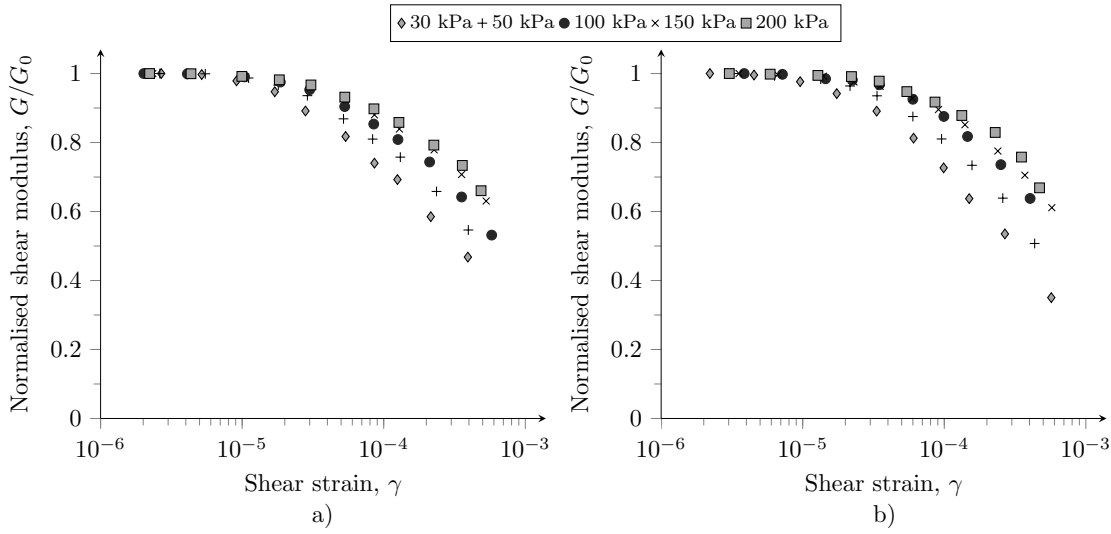


Figure 4.18: Stiffness degradation curves: a) dry conditions; b) saturated conditions

From experimental results, it was identified that the stiffness degradation in dry and saturated conditions is similar for TP-Lisbon sand. The main factor affecting the stiffness degradation is the confinement stress. Therefore, the soil behaviour presented in Figure 4.18 clearly represents the effect of the stress-state on the particle contact and then its influence on the stiffness increase in granular soils stated by Cascante and Santamarina (1996).

In addition, the shear modulus reduction curves allowed estimating the limit of elastic behaviour or cyclic threshold strain (γ_t) in all RC tests, which is the limit between small and medium strains is defined as the shear strain. γ_t allows identifying the strain in which the microstructure is irreversibly altered by cyclic loading, indicating the transition from the linear elastic to the nonlinear elastic behaviour (Vucetic, 1994). Such values can be obtained by applying the interpolation method to find γ corresponding to $G/G_0 = 0.7$ (Santos, 1999). The results revealed that the elastic behaviour for TP-Lisbon sand ranges about $\gamma < 10^{-5}$ and γ_t is located in the medium strain level. Besides, more pronounced plastic deformations were identified at lower confining pressures. Figure 4.19 shows the γ_t evolution with p' .

Given the different forms of soil behaviour at the small-strain range, Santos and Gomes Correia (2001) defined normalised relationships that allow assessing the shear modulus degradation of soils at very-small to medium strain levels ($10^{-6} < \gamma < 10^{-4}$). They demonstrated, based on experimental values, that the data occupied a narrow zone delimited by the curves given by Equations 4.5 and 4.6.

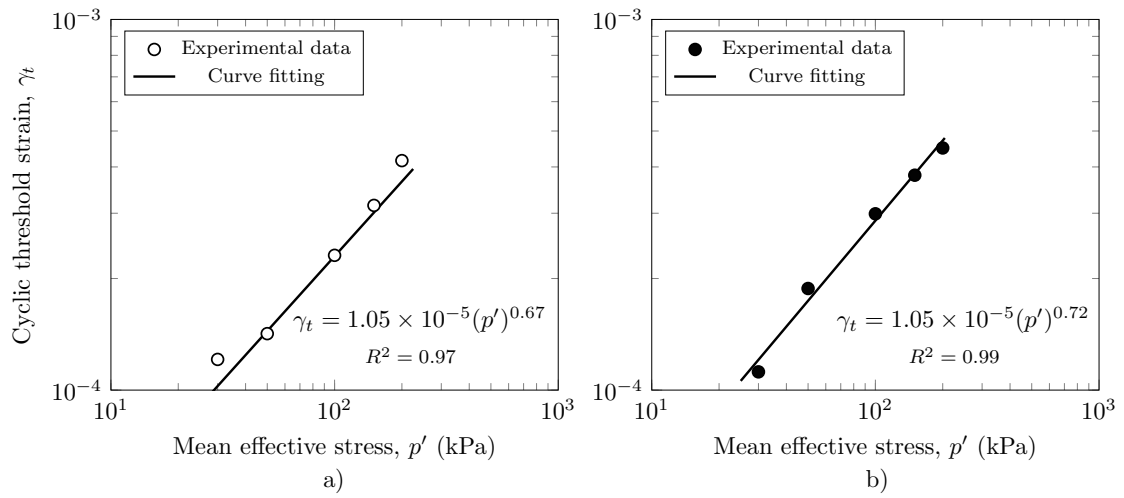


Figure 4.19: Cyclic threshold as a function of the stress-state: a) dry conditions; b) saturated conditions

$$\text{Lower bound} \begin{cases} \frac{G}{G_0} = 1 & \text{for } \gamma^* \leq 10^{-2} \\ \frac{G}{G_0} = 0.5 \left[1 - \tanh \left(0.48 \frac{\gamma^*}{1.9} \right) \right] & \text{for } \gamma^* > 10^{-2} \end{cases} \quad (4.5)$$

$$\text{Upper bound} \begin{cases} \frac{G}{G_0} = 1 & \text{for } \gamma^* \leq 10^{-1} \\ \frac{G}{G_0} = 0.5 \left[1 - \tanh \left(0.46 \frac{\gamma^* - 0.1}{3.4} \right) \right] & \text{for } \gamma^* > 10^{-1} \end{cases} \quad (4.6)$$

where γ^* is the normalised strain, defined as γ/γ_t .

Gomes Correia et al. (2001) defined Equation 4.7 to adjust the data within the narrow zone of the lower and upper unified bounds using the least-squares method. This model includes the reduction curves for experimental data of plastic and cohesionless soils.

$$\frac{G}{G_0} = \frac{1}{1 + 0.385\gamma^*} \quad (4.7)$$

RC results of TP-Lisbon sand were fitted into the lower and upper bounds of the normalised model for shear modulus reduction curves proposed by Santos and Gomes Correia (2001). Besides, the results were compared against the database presented by Oztoprak and Bolton (2013). Figure 4.20 shows the results of such

a fitting. From Figure 4.20, it can be observed that all experimental values are within the curves proposed by Santos and Gomes Correia (2001) and fall into the narrow zone of the database of Oztoprak and Bolton (2013). Therefore, the normalised curves model allows describing the dynamic behaviour of TP-Lisbon sand for different confinement conditions. In this study, the regression method of nonlinear (weighted) least-squares was applied to estimate the model describing the normalised design curve of TP-Lisbon sand (see Figure 4.20.b). The regression model revealed a value of $R^2 = 0.99$ and a coefficient equal to 0.421, which is slightly different to the coefficient found by Gomes Correia et al. (2001).

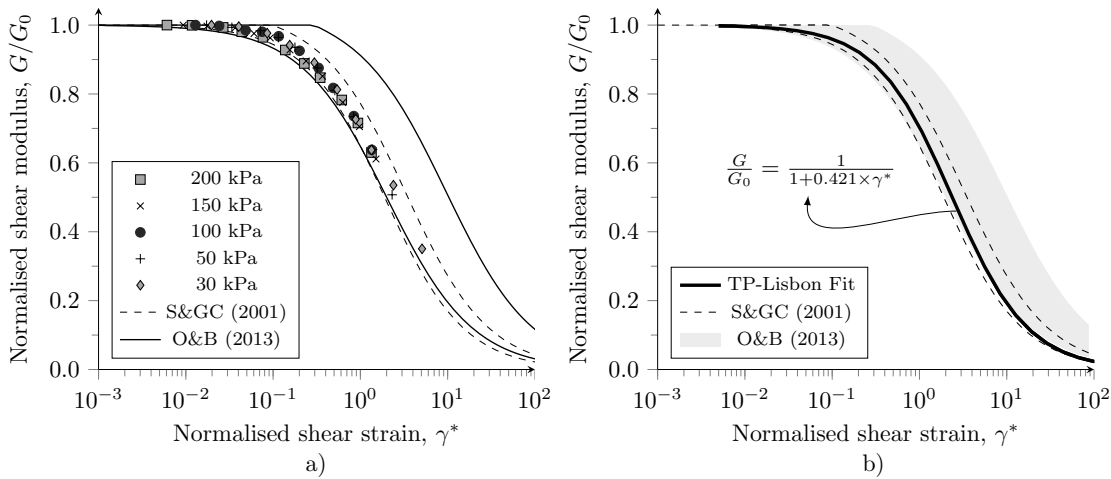


Figure 4.20: Normalised design curves and its comparison against the bounds proposed by Santos and Gomes Correia (2001) and Oztoprak and Bolton (2013): a) experimental data of TP; b) curve fitting of TP

The damping ratio curves were compared against the boundaries proposed by Rollins et al. (1998). Such boundaries were selected considering its good agreement stated by Senetakis et al. (2013) for quartz soils. As Figure 4.21 indicates, quartz is the main mineral that composes the sands of this study. The curves proposed by Rollins et al. (1998) do not describe satisfactorily the response of TP-Lisbon sand in the range of very small to small strains. In such strain levels, all ξ values were outside of the literature curves. This is partially attributed to the higher linearity that the sands exhibit in the range of $\gamma < 10^{-5}$ and the differences between the grain size distribution of the materials used to obtain such model, which are more coarse than the sands evaluated in this study. However, for p' equal to 30 and 50 kPa ξ values were located in the narrow zone for shear-strain levels above 10^{-5} . In addition, a good fit was observed between the damping curves for $p' = 100$ kPa and the lower

bound. Experimental results showed an overestimation of ξ for p' conditions higher than 100 kPa.

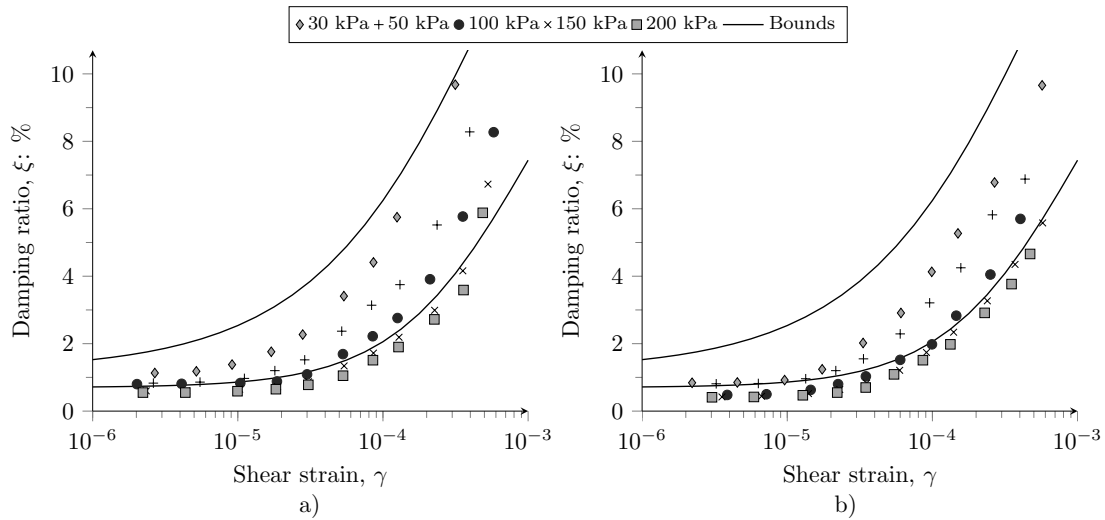


Figure 4.21: Damping ratio of TP-Lisbon sand: a) dry conditions; b) saturated conditions

As in the shear modulus reduction curves, significant differences between ξ results were not recognised for dry and saturated conditions. ξ increases as the strain level increases, thus it can be assessed in parallel of shear modulus degradation curve. ξ can be expressed as a function of G/G_0 . [Hardin and Drnevich \(1972\)](#) stated that the combination of stiffness degradation and damping results provides a normalised model capable of removing the density and confinement effects, which significantly affects the dynamic properties in sandy soils. By compilation of data, [Ishibashi and Zhang \(1993\)](#) proposed a normalised model to estimate ξ , in percentage, using G/G_0 values obtained from the stiffness degradation curves (see Equation 4.8).

$$\xi = 19.51 \left(\frac{G}{G_0} \right)^2 - 51.51 \left(\frac{G}{G_0} \right) + 33.3 \quad (4.8)$$

To provide a model that describes the ξ evolution of each sand, experimental data were contrasted against the normalised model of Equation 4.8. Figure 4.22 shows a comparison between experimental data against the normalised model, and presents the data fitting of the results obtained in this study with the narrow zone compiled by [Ishibashi and Zhang \(1993\)](#) using ξ values from other different sands.

From Figure 4.22, it can be observed that the experimental data of TP-Lisbon sand do not match to the normalised model. The variability of these results is attributed

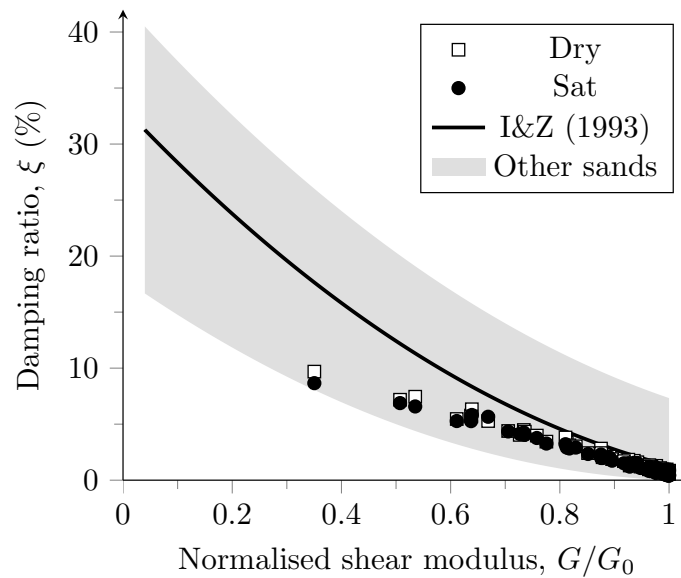


Figure 4.22: Normalised model of damping ratio in function of stiffness degradation.

to the different procedures used to estimate ξ for each strain level. However, the data of the studied material is within the zone of the values reported in the literature. Furthermore, significant differences between the results of both sands were not identified. Equation 4.9 describes the evolution of ξ as a function of G/G_0 for TP and NB sands, respectively. This Equation was obtained under R^2 value higher than 0.97.

$$\xi = -1.91 \left(\frac{G}{G_0} \right)^2 - 10.19 \left(\frac{G}{G_0} \right) + 12.61 \quad (4.9)$$

Normalised curve, to estimate the relationship between ξ and G/G_0 , allowed estimating the dynamic properties, eliminating the density and confinement effects. Negligible differences were observed between the results obtained for dry and saturated conditions. Nevertheless, further studies are needed to characterise the response in shear-strain levels above 10^{-3} .

4.7.2 Stress and state dependency of wave propagation

Stress-dependency of small-strain stiffness of TP-Lisbon sand was investigated by means of bender element (BE) tests. These tests were conducted for dry and saturated conditions under different confining stresses. Besides, specimens were prepared using the dry pluviation method for relative densities of 30% and 50%, corresponding to the state of TP-Lisbon sand on the field. The wave propagation time (t_t) between BE tip-to-tip distance (L_{tt}) at each p'_0 was assessed using the first arrival method, for both shear and compression waves. To minimise the uncertainty and subjectivity associated with the interpretation of test results (e.g. cross-talk or near-field effect), four input signals with frequencies between 1-8 kHz and 25-125 kHz were applied to assess V_S and V_P , respectively (Viana da Fonseca et al., 2009). Figure 4.23 presents some typical results of BE measurements for both P-wave and S-wave at different test conditions.

BE tests have been analysed to derive the best fit of wave velocities (V_S and V_P) stress-dependency using Equations 4.10 and 4.11.

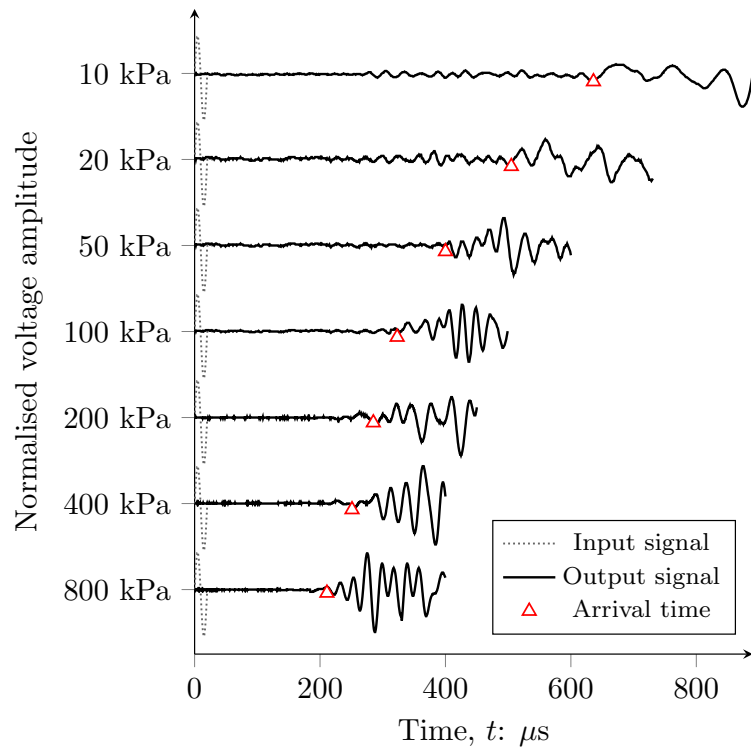
$$V_S = \alpha (p')^\beta \quad (4.10)$$

$$V_P = \theta (p')^\beta \quad (4.11)$$

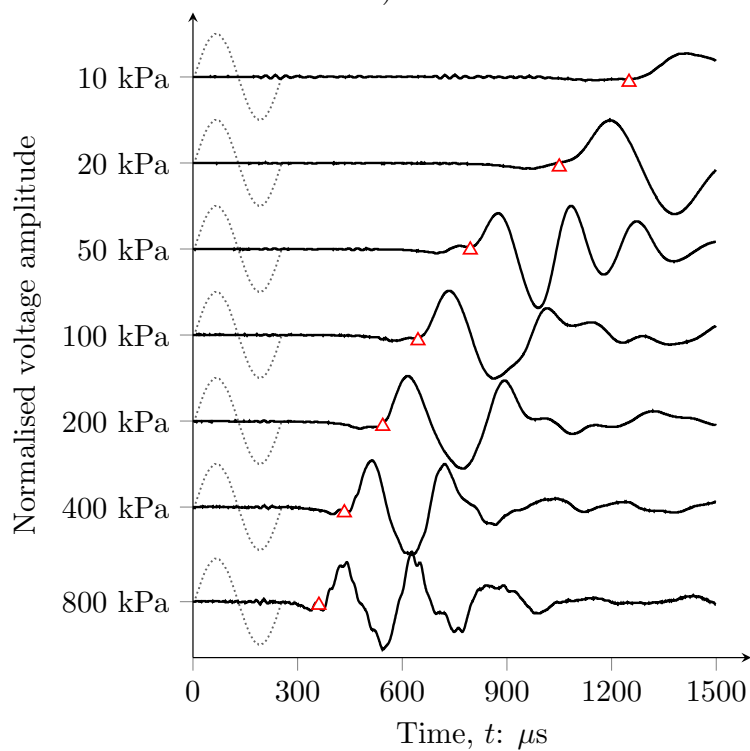
where α and θ are the values of V_S and V_P at 1 kPa, respectively, and β is the exponent of the stress-state dependency law of wave propagation velocities.

The V_P values obtained for saturated conditions ranged from 1495 m/s to 1513 m/s, corresponding to typical results for fluid-saturated granular media (Biot, 1956a). Therefore, the stress-dependency model of V_P for saturated conditions was not estimated. The V_S results obtained from BE tests were contrasted against V_S values obtained from the resonant-column tests. Figure 4.24 shows the stress-dependent seismic wave velocities of V_S and V_P for TP-Lisbon sand. Table 4.5 presents the values of the stress-dependency fitting parameters.

Results of stress-dependency seismic wave velocities for TP-Lisbon sand showed very close β values for all tests, revealing a parallel evolution of the wave velocities as a function of the stress-state. It should be noted that V_S and V_P values obtained



a)



b)

Figure 4.23: Typical time-domain signals of BE: a) P-wave propagation in a dry sample; b) S-wave propagation in a saturated sample.

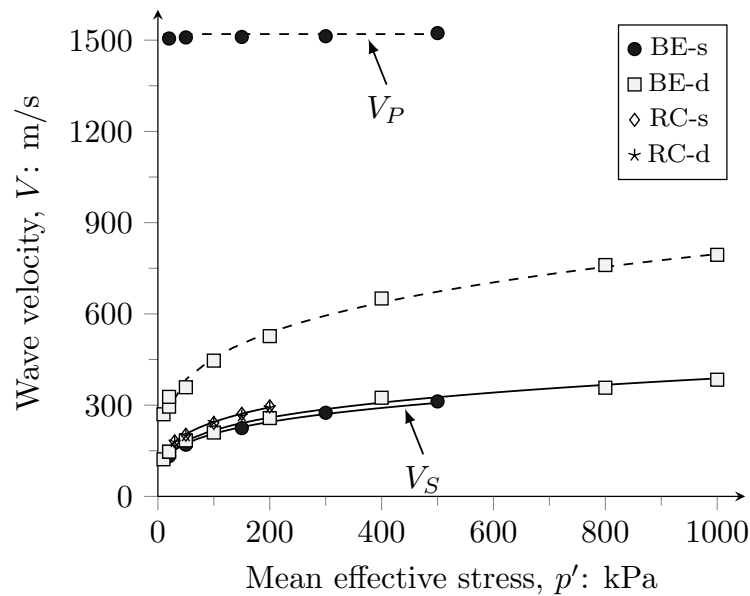


Figure 4.24: Stress-dependency of seismic wave velocities for TP-Lisbon sand.

Table 4.5: Fitting parameters of stress-dependency of seismic wave velocities

Test name	Seismic wave type	α or θ : m/s	β : dimensionless
BE-s	V_S	68.75	0.2484
BE-d	V_S	65.68	0.2505
BE-d	V_P	148.40	0.2433
RC-s	V_S	74.31	0.2588
RC-d	V_S	73.74	0.2576

from the measurements in dry conditions have the same evolution but with higher values in V_P . Furthermore, from the BE-d results, the Poisson ratio was computed for each mean stress, finding a mean value of 0.31 with a coefficient of variation equal to 5% for loose conditions. Moreover, similitude between results for the same testing method were observed, which shows that BE and RC measurements allow estimating the small-strain stiffness of sands (Camacho-Tauta et al., 2015).

It is well-known that V_S is affected by void ratio and confining stress. Hence, the small-strain stiffness of soils should be represented by a normalised model. Equation 4.12 introduces a generalised stress-state model for describing the small-strain stiffness of TP-Lisbon sand. This model is based on the stress-dependency of shear wave velocity, but expressed in terms of maximum shear modulus (G_0). The maximum shear modulus (G_0), considered elastic when describing the response of soils at small-strain levels, is strongly dependent on the void ratio (e) and the mean effective stress (p'). Therefore, a void ratio function, $F(e)$, allows eliminating the effect of soil

state when estimating the soil stiffness at small-strain levels. $F(e)$ can be classified into hyperbolic and exponential functions.

Lo Presti et al. (1997) demonstrated that exponential functions are compliant with Hertz's theory, which deals on the particles contact. This theory establishes that the plastic deformations in granular materials are related to the changes in the arrangement of particles. Equation 4.12 shows the general form of the exponential void ratio function.

$$G_0 = Vs^2D = F(e) \times C \times \left(\frac{p'}{\text{Pa}} \right)^n \quad (4.12)$$

where D is mass density, p' is mean effective stress, Pa is the atmospheric pressure (used as reference stress), $F(e)$ is a void ratio function, C is a material coefficient that captures the influence of the particle shape and bonding or cementation of the particles and n is a power exponent that reflects the sensitivity of the stiffness modulus to the confining pressure.

Figure 4.25 presents a comparison between the normalised shear modulus computed from BE and RC data. The computation of Equation 4.12 required the previous estimation of D . This estimation considered the degree of saturation of the soil specimens, that is, D for dry and saturated conditions, respectively. The experimental evidence in Figure 4.25 defined $F(e) = e^{-1.79}$, $C = 65.11$ MPa and $n = 0.48$ for TP-Lisbon sand. The stress-state models were obtained under a $R^2 > 0.98$. Note that x values are close between them and quite different to the most common value $x = 1.29$ reported by Lo Presti et al. (1997). However, Senetakis et al. (2013) obtained from RC tests different x values for three sandy soils, which suggested that x is characteristic for each soil type. The exponents n of both sands are close to 0.5, which is the 'typical' value reported by Hardin and Richart (1963); Vardanega and Bolton (2013); Goudarzy et al. (2018) to describe the effect of confining pressure on small-strain stiffness.

A contrast between results from dry and saturated specimens revealed that there are no substantial differences in the normalised small-strain stiffness of TP-Lisbon sand for these conditions. On the other hand, a good agreement between BE and RC results with the normalised model was found. The use of the stress-state model is conceptually more consistent for describing the small-strain stiffness of granular materials due to the double normalisation, which eliminates the effects of void ratio

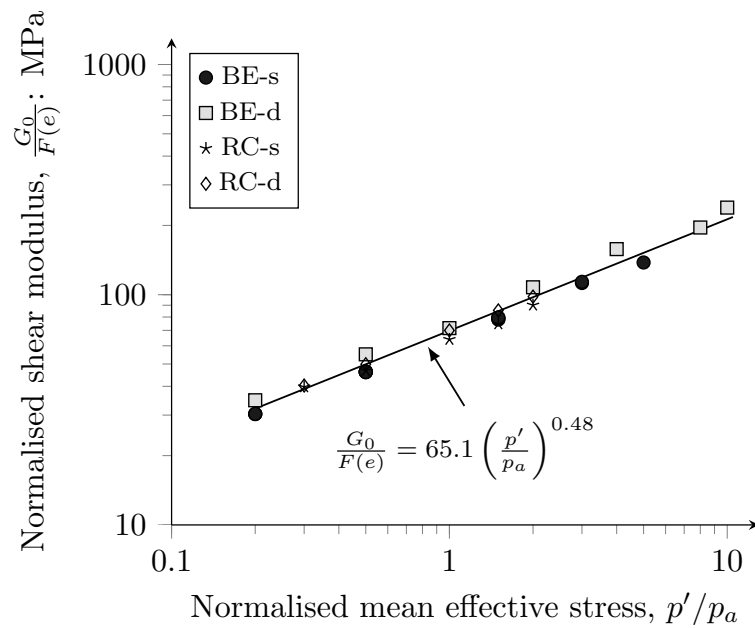


Figure 4.25: Normalised shear modulus for TP-Lisbon sand

and confinement stress. Besides, the application of such a model allows comparing the small-strain stiffness of TP-Lisbon sand against other sandy soils at different relative densities and stress-states.

Figure 4.26 shows a comparison between parameters describing the normalised small-strain stiffness and particle shape of TP-Lisbon sand (referred in Figure 4.25 and Table 4.2). This comparison includes values reported by Liu and Yang (2018). A good correlation between parameter C and exponent n with sphericity, circularity and convexity was observed. These correlations revealed that an increment of shape parameter causes a decreasing of parameter C , while an increment of shape parameter causes a decreasing of exponent n . Hence, experimental results validate the effects of particle shape on the behaviour of TP-Lisbon sand.

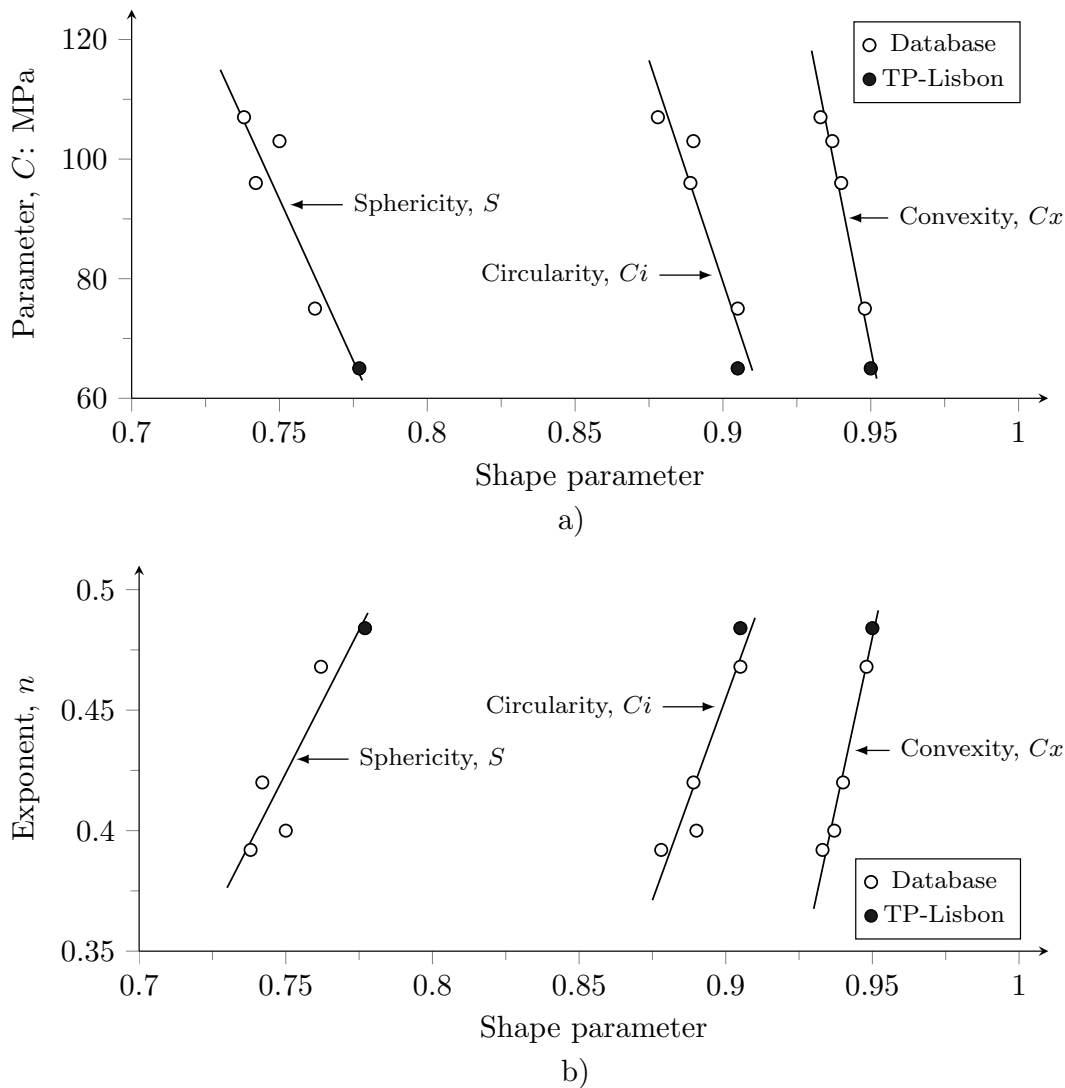


Figure 4.26: Relationships between particle shape properties with normalised small-strain stiffness parameters: a) Parameter C ; b) Exponent n

4.8 Key findings

This chapter provided a characterisation of the key geomechanical properties of TP-Lisbon sand. The well-controlled and accurate test procedures (e.g. lubricated end platens, top cap-loading ram connection and end-of-test soil freezing) were implemented. Moreover, this chapter presented a detailed characterisation of the dynamic properties of TP-Lisbon sand. The analysis focused on the soil state effects on the small-strain stiffness, damping and wave propagation on such a sandy soil by resonant column and bender element tests on triaxial testing conditions. Experimental results led to the following findings:

- TP-Lisbon sand presented the highest critical state locus position (higher value of Γ) in comparison with the data of the other similar sands. However, Γ is a slither higher, inducing a predominant dilative behaviour of TP-Lisbon sand during monotonic/static loading.
- There is a strong correlation between the normalised shear modulus of TP-Lisbon sand with its particle shape parameters, namely e_{max} , R and ρ , confirming the influence of particle shape on the behaviour of TP-Lisbon sand. This may explain the high CSL position of TP-Lisbon sand.
- TP-Lisbon achieves its peak deviatoric stress and maximum shear strength in about 10-15% axial strain, while its volumetric strain stabilises after 25% axial strain. It was observed that, for undrained conditions, the phase transformation of TP-Lisbon sand occurred at 1-2% axial strain and the deviatoric stress stabilisation at about 20-25% axial strain.
- The power laws that estimate the evolution of G_0 as a function of the stress state were obtained for both sands in saturated conditions from BE tests in triaxial conditions, which included load-unload-reload stages, thus eliminating the soil state effect. The exponent values, n , obtained in this study agree well with those reported in the literature for sandy soils with cone-to-plane contacts (about 1/2). The void ratio functions, $F(e)$, which follow Hertzian contact particle law, showed a specific value for x parameter for each sand. Such values differ from the typical values reported in the literature.
- The experimental data of TP-Lisbon sand were found to be suitable in comparison with the normalised curves proposed by Santos and Gomes Correia (2001). In addition, the experimental results fall into the narrow zone of the database presented by Oztoprak and Bolton (2013). Normalised results were fitted using a modified hyperbolic relationship. This simple approximation could be applied to different stress-state conditions in similar soils.
- The RC results showed that the damping ratio increases with strain level in the range $\gamma > 10^{-5}$ in both sands. Furthermore, results showed that ξ decreases as p' increases. The bounds proposed by Rollins et al. (1998) do not describe well the damping ratio evolution for confining stresses above 100 kPa. Moreover, ξ results exhibited slightly lower values in comparison to such bounds in the small-strain level ($\gamma < 10^{-5}$).

- Normalised curves to estimate the relationship between ξ and G/G_0 were obtained for each sand. The model allows estimating the dynamic properties, eliminating the density and confinement effects. Nevertheless, further studies are needed for shear-strain levels above 10^{-3} .

The the intrinsic properties, CSL parameters and small-strain stiffness sand identified in this chapter will be used further to describe the liquefaction resistance of TP-Lisbon soil and the efficiency of induced partial saturation to mitigate the effects of this granular soil.

Chapter 5

Liquefaction resistance of TP-Lisbon sand – fully saturated conditions

The main content of this chapter has been published in Viana da Fonseca, A., Molina-Gómez, F. and Ferreira, C. (2023) Liquefaction resistance of TP-Lisbon sand: a critical state interpretation using in situ and laboratory testing. *Bulletin of Earthquake Engineering*, 21(2), pp. 767-790. doi:10.1007/s10518-022-01577-8.

5.1 Outline

This chapter addresses the assessment of earthquake-induced liquefaction (known herein as liquefaction resistance) of TP-Lisbon sand. The characterisation was carried out by combining in situ with laboratory tests. The results of in situ tests allowed obtaining the factor of safety profiles against liquefaction, liquefaction potential index and liquefaction severity number. On the other hand, an experimental programme conducted in the laboratory allowed defining of the cyclic resistance ratio for different relative densities and mean effective stresses of TP-Lisbon sand. Moreover, the effects of inversion and rotation of principal stresses on liquefaction resistance were examined by advanced testing procedures (i.e. cyclic triaxial and cyclic direct simple shear tests). The results of this study were analysed within the critical state soil mechanics framework by comparing the state parameter reported by in situ and laboratory testing, particularly when using remoulded soil specimens. The data presented in this study provide a database for numerical analyses and cyclic or seismic geotechnical design, following a framework appropriate to natural

sands susceptible to liquefaction phenomena.

5.2 Liquefaction susceptibility from in situ testing

Based on the in situ characterisation, which comprised a series of CPTu soundings (see Figures 3.3 and 3.4), an assessment of liquefaction susceptibility based on CPTu results was carried out using the simplified procedure proposed by Boulanger and Idriss (2014), considering the factor of safety against liquefaction (FS_{liq}). The method was originally introduced by Seed and Idriss (1971) and nowadays is recommended in Eurocode 8 (CEN, 2010):

$$FS_{liq} = \frac{CRR}{CSR} \quad (5.1)$$

The CRR refers to the cyclic resistance ratio and CSR corresponds to the cyclic stress ratio. Therefore, CRR represents the resistance of soil to liquefy derived from CPTu data. On the other hand, CSR denotes the design seismic action at a specific location in depth Seed and Idriss (1971). The procedure to estimate CRR from CPTu data is:

$$CRR = \exp \left[\frac{q_{c1Ncs}}{113} + \left(\frac{q_{c1Ncs}}{1000} \right)^2 - \left(\frac{q_{c1Ncs}}{140} \right)^3 + \left(\frac{q_{c1Ncs}}{137} \right)^4 - 2.8 \right] \quad (5.2)$$

where q_{c1Ncs} is the normalised equivalent clean sand values, as suggested by Boulanger and Idriss (2014). According to these authors, a clean sand is considered to have a fines content (FC) below 5%. The FC of TP-Lisbon sand is 2.21% (see Table 4.1).

Moreover, the procedure proposed by Seed and Idriss (1971) to estimate the in situ CSR is:

$$CSR = \frac{\tau_{cyc}}{\sigma'_{v0}} = 0.65 \cdot \frac{a_{max}}{g} \cdot \frac{\sigma_{v0}}{\sigma'_{v0}} \cdot r_d \quad (5.3)$$

where τ_{cyc} is the amplitude of cyclic shear stress, σ'_{v0} is the initial vertical effective stress, σ_{v0} is the vertical stress, and r_d is stress reduction coefficient that considers the depth of soil deposit (Z) and the earthquake magnitude (M_w), as follows:

$$r_d = \exp^{[\alpha(Z) + \beta(Z)M_w]} \quad (5.4)$$

where:

$$\alpha(Z) = -1.012 - 1.126 \sin\left(\frac{Z}{11.73} + 5.133\right)$$

$$\beta(Z) = 0.106 + 0.118 \sin\left(\frac{Z}{11.28} + 5.142\right)$$

Figure 5.1 shows the FS_{liq} profiles of SI12, SI18 and SI19 for the Type 1 seismic action. From Figure 5.1, it can be observed a thick liquefiable layer in all profiles, highlighting the in SI18 and SI19 sites at 13 to 23 m depth. Besides, interlayers of soil with lower liquefaction susceptibility or non-liquefaction is observed in all profiles at 14 to 15 m and 25 m depth. The results of FS_{liq} are coincident with the layers of sandy soils inferred from the SBT analysis (see Figure 3.5). Besides, the results at SI18 matched with ψ profile (Figure 3.6), in which sandy soils with contractile behaviour —materials more susceptible to liquefaction— were identified in the critical zones in this site, that is, $FS_{liq} < 1$.

Moreover, alternative approaches to liquefaction assessment have been performed, namely the Liquefaction Potential Index (LPI) and Liquefaction Severity Number (LSN). These approaches are quantitative indexes, which allow estimating the liquefaction-induced damages. Both approaches were proposed by Iwasaki et al. (1978) and Tonkin & Taylor (2013), respectively. LPI allows estimating the liquefaction susceptibility of the soil deposit by combining the results of FS_{liq} until 20 m depth. In addition, LSN represents the expected damage effects of shallow liquefaction on direct foundations, based on post-liquefaction volumetric deformations that are associated with reconsolidation settlements (Iwasaki et al., 1978). Figure 5.2 presents the results of the LPI and LSN, considering the seismic action type 1.

Iwasaki et al. (1978) defined intervals for LPI classification, classifying liquefaction potential as low when LPI is lower than 5, high when LPI is between 5 and 15 and very high if LPI is higher than 15. As shown in Figure 5.2, LPI values fall on the high liquefaction severity, except for SI12, where the LPI is low. Complementary, Tonkin & Taylor (2013) defined LSN ranges for liquefaction effects, classifying the expression of liquefaction as little to none for values lower than 10, minor for values from 10 to 20, moderate for values from 20 to 30, moderate to severe for values

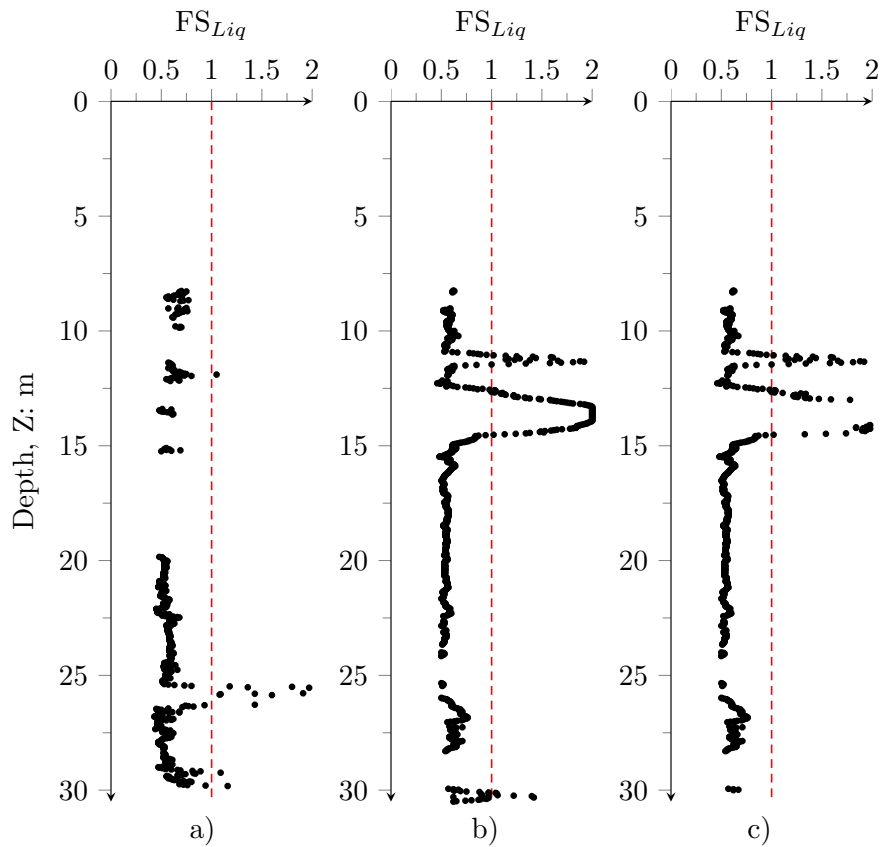


Figure 5.1: Liquefaction susceptibility based on in situ tests: a) CPTu12; b) CPTu18; c) CPTu19

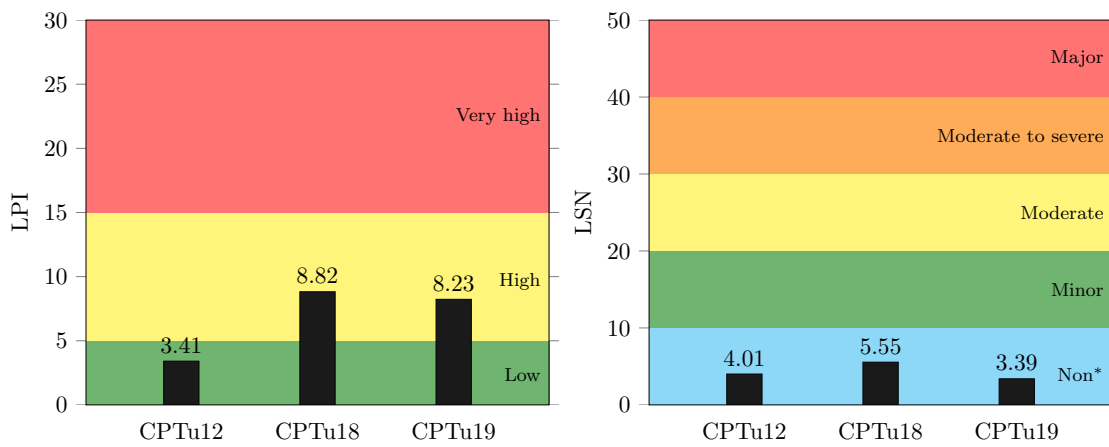


Figure 5.2: Severity damage based on LPI and LSN from CPTu results

from 30 to 40, major for values from 40-50 and severe damage for values higher than 50. LSN results showed in Figure 5.2 fall within the little to non-expression of liquefaction class, below 10, in the three SI.

The results in Figure 5.2 showed high probability of damage potential from liquefaction onset in SI18 and SI19 locations, which are attributed to the presence of soil layers composed of fine loose sandy between 15 m and 23 m depth. However, the post-liquefaction volumetric deformations will not induce significant effects on the shallow foundations surrounding the Terreiro do Paço site, as indicated in LSN interpretation. The relatively low values of LSN in this site are related to the presence of compacted materials near the ground surface (i.e. the embankment and pavement structure between 0 m and 8 m depth), and the masonry remains of the buildings collapsed after the 1755 earthquake —confirmed during the collecting of integral samples— that do not exhibit significant deformations during liquefaction onset due to their high stiffness. Therefore, this thick crust prevents the generation of large settlements in these sites, as verified by applying the equivalent soil profiles for liquefaction assessment proposed by Millen et al. (2021).

5.3 Liquefaction resistance assessment by advanced laboratory testing

The characterisation of the liquefaction resistance of TP-Lisbon sand was carried out by an experimental programme involving advanced testing in the laboratory, namely, cyclic triaxial (CTx) and cyclic direct simple shear (CDSS). These tests addressed the evaluation of cyclic behaviour subjected to rotation and inversion of principal stresses for different state conditions. For this characterisation, all samples were remoulded using the air pluviation method and were fully saturated. All samples were saturated by the circulation of dioxide of carbon and flushing of de-aired water, as recommended by Viana da Fonseca et al. (2021). CTx and CDSS tests focused on the liquefaction resistance of TP-Lisbon sand under different test conditions, i.e. initial relative density (or initial void ratio), stress state and cyclic stress ratios. The relative density (Dr) of all sets of tests was grouped by considering a range of $\pm 3\%$ due to the variability that can be induced during the phases before cyclic shearing. On the other hand, the experimental program involving two types of testing (i.e. CTx and CDSS) deals with the assessment of undrained cyclic behaviour by inversion of principal stresses and by the rotation of principal stresses.

For triaxial testing, the back pressure was gradually increased up to 300 kPa. This increment was applied by ensuring a difference between cell and back pressures of about 10 kPa. The full saturation condition was validated by measuring B-values and P-wave velocities (V_P), which in all tests were higher than 0.97 and 1482 m/s, respectively (Astuto et al., 2023). For CDSS testing, the degree of saturation (S_r) was estimated by monitoring the sample deformations during all test phases and measuring the water content (ω) at the end of each test (Cappellaro et al., 2021; Fanni et al., 2022). In all tests, S_r higher than 99% were reported.

The CTx tests were conducted in 30 soil specimens remoulded for relative densities of 30%, 40% and 50%. The range of relative density (D_r) and mean effective stress (p'_0) are within the in situ range estimated from CPTu results (see Figure 3.4 in Section 3.2). Besides, these samples were isotropically consolidated for p'_0 equal to 50 kPa and 100 kPa –representative of the in situ p'_0 range. After consolidation, the samples were subjected to different combinations of cyclic deviatoric stress (q) or cyclic stress ratio ($CSR_{Tx} = q/(2p'_0)$) to define the liquefaction resistance of TP-Lisbon sand. Such loading was applied to inverse the principal stresses through compression and extension symmetric cycles. Figure 5.3 illustrates the typical results obtained during CTx testing. This Figure includes plots of stress-strain response, stress path, relationship between the number of cycles (N) and axial strain (ε_a) changes, and evolution of pore pressure built-up ($r_u = \Delta u/p'_0$) during cyclic loading.

From Figure 5.3, it can be observed low deformations ($\varepsilon_a < 0.1\%$) and a progressive increment of r_u during the first cycles of loading. However, after achieving a r_u of about 0.65 (see cycle 9 in Figure 5.3), the soil showed a rapid increment of pore pressure build-up, which led to massive deformations and the total reduction of mean effective stress, causing the onset of liquefaction. Many tests exhibited $r_u > 1.0$ since the axial piston of the CTx apparatus achieved its maximum limit after liquefaction onset. This effect generated compliance issues at the end of the cyclic loading, which induced variations in the measurement of soil behaviour. However, these issues did not influence the definition/identification of liquefaction resistance of TP-Lisbon sand by CTx testing.

The CDSS tests were conducted using 24 soil specimens with D_r between 40% and 60%. These samples were consolidated by increasing the vertical load until achieving a vertical effective stress (σ'_{v0}) equal to 80 kPa and 150 kPa, corresponding to the in-situ representative stresses of sandy soil layers in the Terreiro do Paço profile. During the consolidation, the radial strains were restricted by a series of stack copper rings,

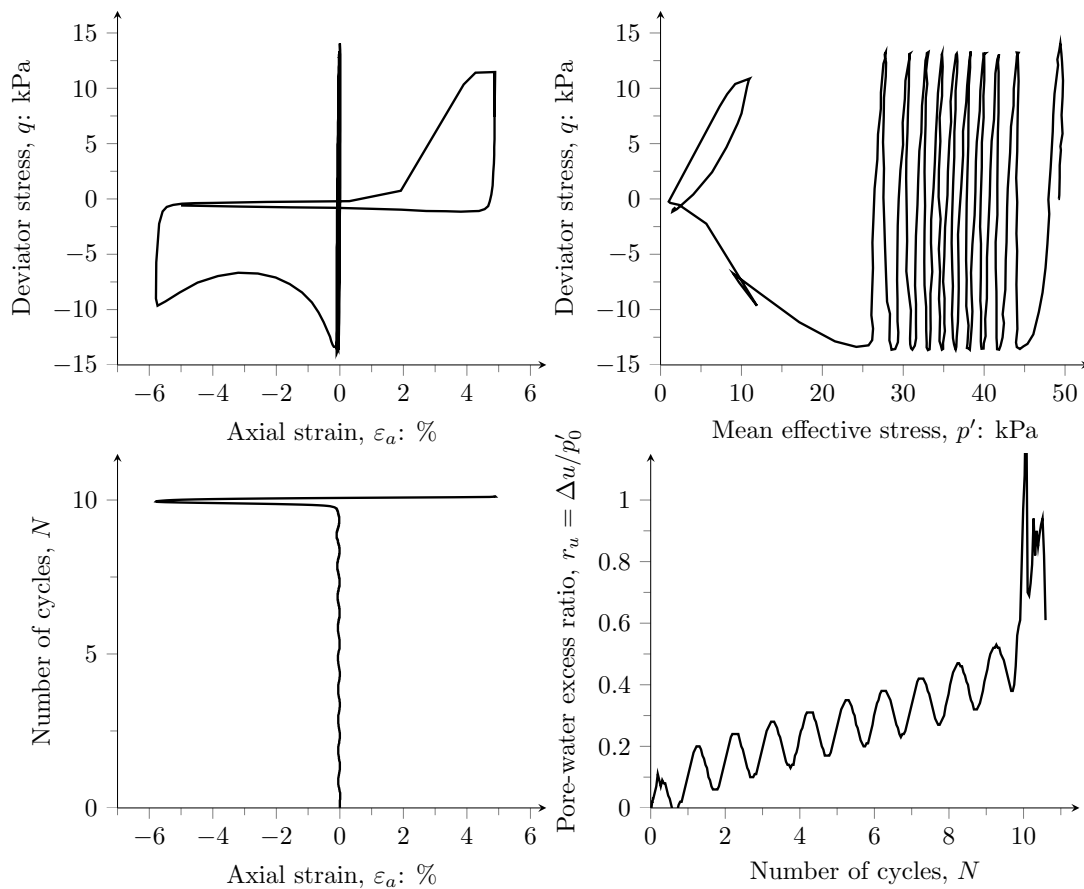


Figure 5.3: Typical results of cyclic triaxial testing ($p'_0 = 50$ kPa and $Dr = 30\%$)

inducing an anisotropic condition on the soil specimen. Such condition is equivalent to the p'_0 implemented for the CTx tests by considering the at-rest earth pressure coefficient ($K_0 = \sigma'_h/\sigma'_v$). K_0 was estimated by applying the correlation proposed by Jaky (1944):

$$K_0 = 1 - \sin \phi' \quad (5.5)$$

where ϕ' is the effective friction angle of the soil, which is a simplified approximation of the value under geostatic conditions. For TP-Lisbon sand $\phi' = 34^\circ$ was adopted (see Figure 4.8). This value is equivalent to constant volume condition and independent of Dr , representing diverse relative densities and confinement stresses as used in this research.

The cyclic loading in the CDSS tests was conducted under the constant volume condition, by keeping the specimen height constant using an active control, for

different combinations of cyclic stress ratio ($CSR_{SS} = \tau/\sigma'_{v0}$). The constant volume condition is equivalent to the undrained test condition since a decrease or increase of σ'_{v0} in a constant-volume CDSS test is essentially equal to the increase or decrease of excess pore water pressure in an undrained CDSS test (Dyvik et al., 1987). Hence, $r_u \approx 1$ is equivalent to $\sigma'_{v0} \approx 0$, which indicated liquefaction onset due to the loss of soil stiffness and stress-state.

Figure 5.4 illustrates the typical results obtained from CDSS testing, including the plots of stress-strain response, stress path, relationship between the number of cycles (N) and shear strain (γ) changes, and decreasing of vertical effective stress (σ'_{v0}) during cyclic loading. From this Figure, it can be that during the first loading cycles, the development of γ was not significant, while the σ'_{v0} reduced progressively until achieve a value of about zero, where the liquefaction was attained. After liquefaction onset (cycle 10), further reversal loading led to a partial recovery of strength and stiffness of the soil, which also manifested an increasing and decreasing of σ'_{v0} . Besides, during this phase, the area of hysteresis loops increases considerably due to the accumulation of strains along with the cyclic loading.

The results of CTx and CDSS tests allowed defining the curves of liquefaction resistance of TP-Lisbon sand (see Figure 5.5). The cyclic resistance curves are drawn based on the cyclic stress ratio (CSR) and the number of cycles of liquefaction onset. The general equation to define the liquefaction resistance curve (LRC) for each test condition adopted in this research is:

$$CSR = a(N_L)^{-b} \quad (5.6)$$

where a and b are fitting parameters and N_L represents the number of cycles of liquefaction onset.

Figure 5.5 shows the LRC derived from the results obtained during CTx and CDSS tests for TP-Lisbon sand, highlighting the testing conditions and the best fitting of LRC from experimental data. Test results indicated that the liquefaction resistance increased as the relative density increased, and it decreased as decreased the stress-state in both element test types. Furthermore, Figure 5.5 shows that all LRC reported herein have similar slopes (i.e. values of b exponent between 0.095 and 0.114), indicating that the curves of TP-Lisbon sand are parallel independently of the testing condition. This Figure revealed that the CTx results showed a higher liq-

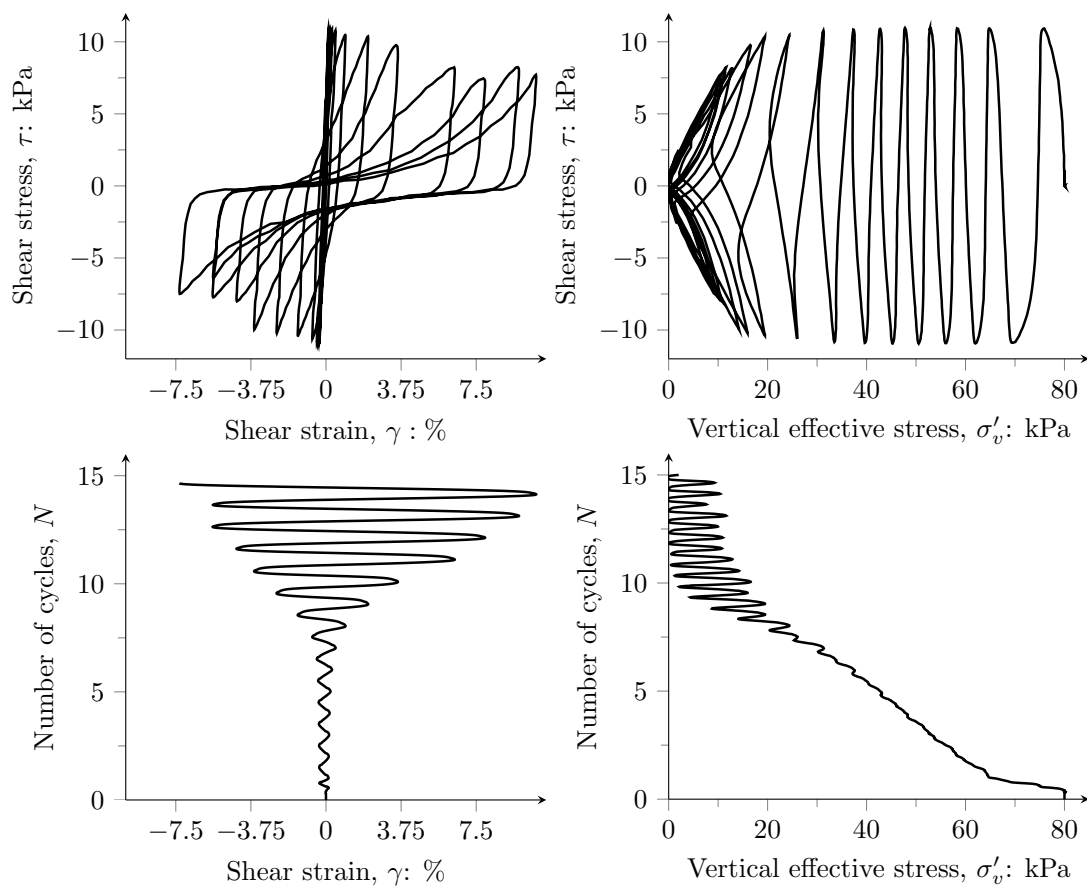
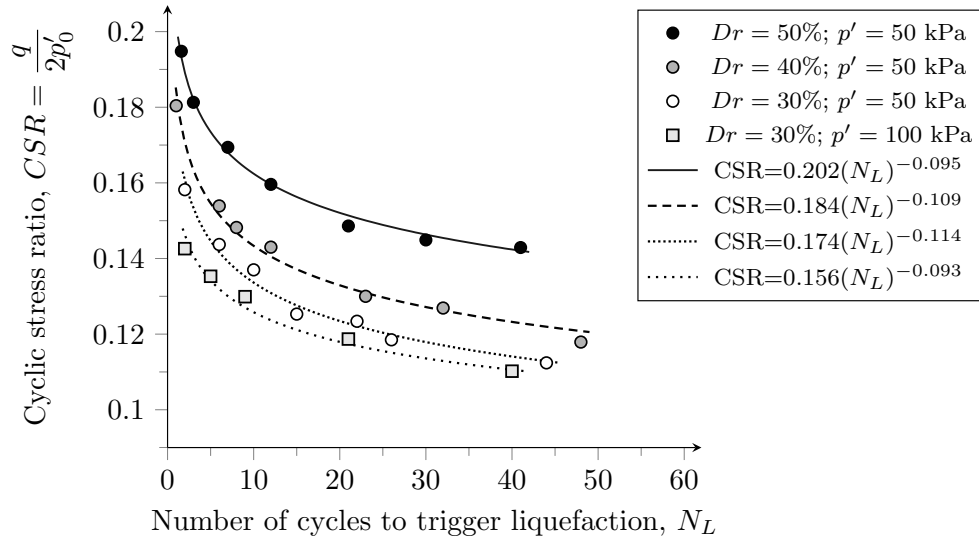


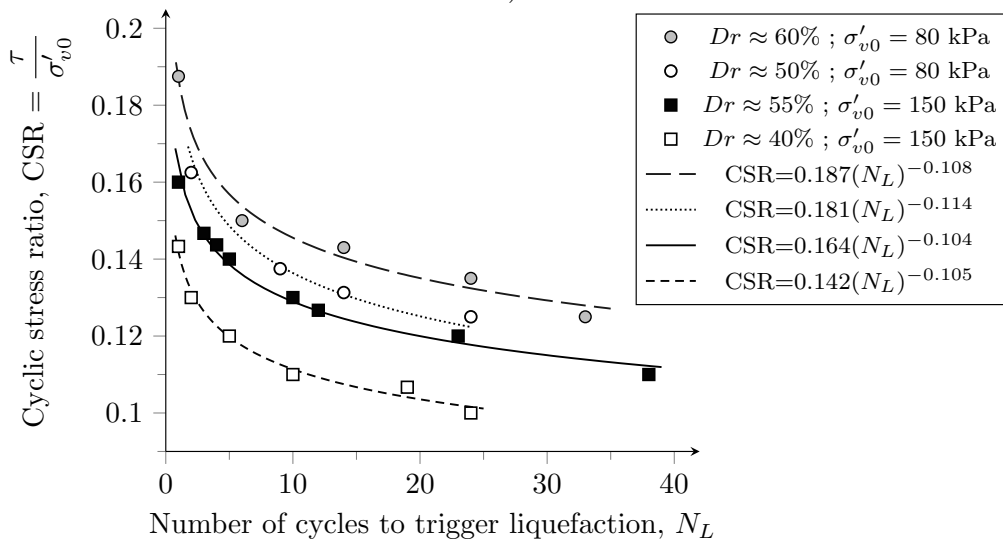
Figure 5.4: Typical results of cyclic direct simple shear testing ($\sigma'_{v0} = 50$ kPa and $Dr = 50\%$)

uefaction resistance than the CDSS results, although all CTx tests exhibited higher deformations than the CDSS tests.

The CTx and CDSS results on TP-Lisbon sand were compared against a database comprising liquefiable sands with similar intrinsic properties (see Figure 5.6). The database used compiled experimental results reported by Ishihara (1993); Kokusho et al. (2012); Jefferies and Been (2015); Mele et al. (2019); Porcino et al. (2021). Data were selected considering similar testing conditions, i.e. relative density and mean effective confinement stress. From Figure 5.6, it can be observed that liquefaction resistance of TP-Lisbon sand is lower than the compared sands under similar relative density and stress-state conditions, validating the results presented herein.



a)



b)

Figure 5.5: Liquefaction resistance curves of TP-Lisbon sand: a) CTx test results; b) CDSS test results

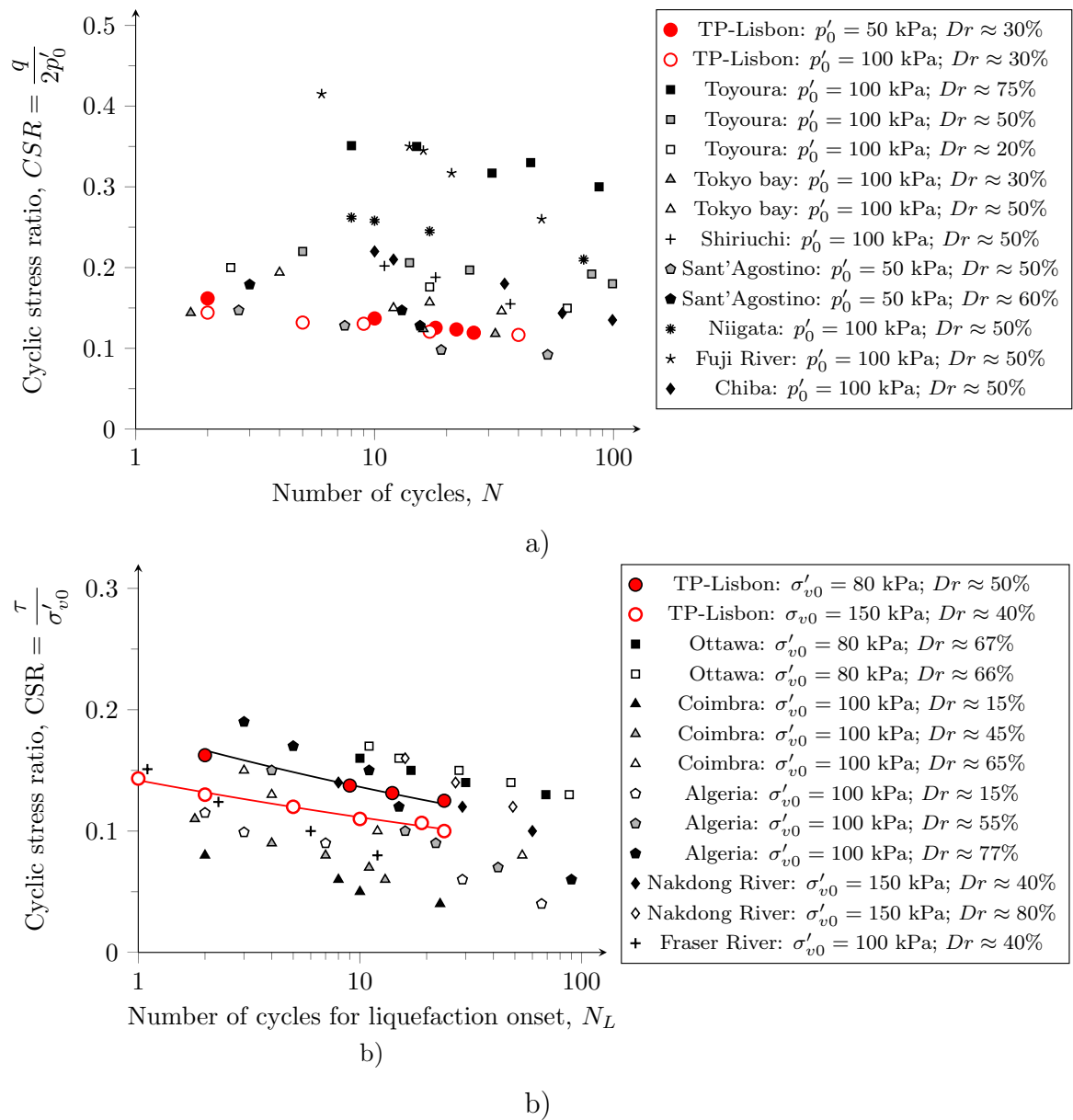


Figure 5.6: Cyclic behaviour of TP-Lisbon sand compared against other liquefiable sands: a) CTx tests; b) CDSS tests

Diverse studies have compared recently CTx and CDSS tests (Giretti and Fioravante, 2017; Khashila et al., 2021; Nong et al., 2021). The results from these testing conditions can be associated by applying correction coefficient (Cr), which transforms the liquefaction resistance obtained from the isotropic triaxial tests into liquefaction resistance for simple shear conditions:

$$CSR_{SS} = Cr \cdot CSR_{CTx} \quad (5.7)$$

Finn et al. (1971); Castro and Poulos (1977); Ishihara et al. (1985) indicated that Cr depends on the K_0 of soil. In this study, the models proposed by such authors were applied to compare the CTx and CDSS results for equivalent tests conditions, that is, $Dr = 50\%$ and $p'_0 = 50$ kPa —equivalent to $\sigma'_{v0} = 80$ kPa . However, all Cr models did not fit with the data the LCR for these conditions.

$$Cr = \frac{2 + 3K_0}{4} \quad (5.8)$$

This correlation was obtained by adjusting the experimental results by the least-square method, obtaining a correlation coefficient $R^2 = 0.92$. By using $K_0 = 1 - \sin(34^\circ)$, a Cr equal to 0.83 was obtained for TP-Lisbon sand. The Cr coefficient allowed transformed the CTx results into CDSS results properly. Figure 5.7 demonstrated that the results obtained from both test types are associated since they fall into a single LRC —denominated as LRC_{Cr} — after applying the transformation model indicated in equation 5.7. Equation 5.9 defines the best fitting of corrected liquefaction resistance of TP-Lisbon sand for $Dr = 50\%$ and $p'_0 = 50$ kPa converted for CTx loading. The parameter a and the b exponent of Equation 5.9 are within into the range values referred in Figure 5.5, validating the proposed model and describing well the liquefaction resistance of TP-Lisbon sand.

$$CSR_{Cr} = 0.171 (N_L)^{-0.101} \quad (5.9)$$

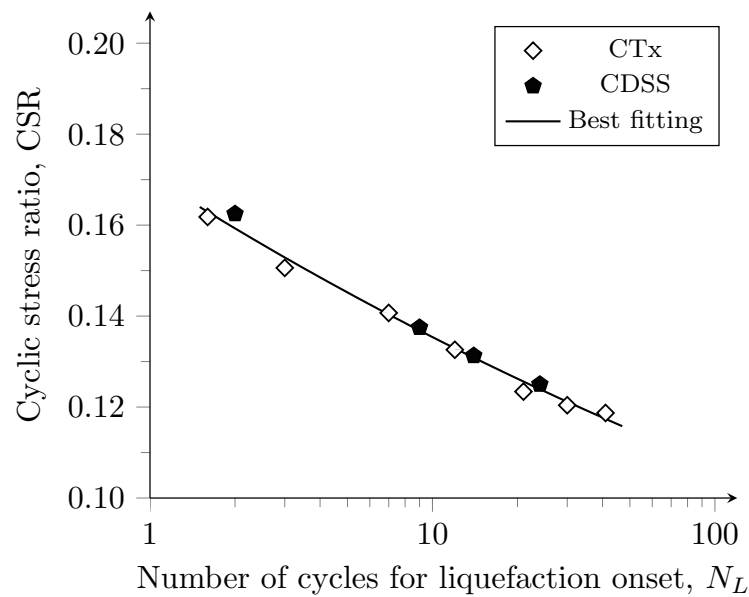


Figure 5.7: Liquefaction resistance curve of transformed for CTx loading ($p'_0 = 50$ kPa or $\sigma'_{v0} = 80$ kPa and $Dr = 50\%$)

5.4 Interpretation of liquefaction resistance within the CSSM framework

The liquefaction resistance interpretation can involve an application of the critical state soil mechanics (CSSM) framework through the estimation of the state parameter (ψ):

$$\psi = e_0 - e_{cs} \quad (5.10)$$

where e_0 is void ratio at the beginning of cyclic loading and e_{cs} is the void ratio of the critical state at the current mean stress or p'_0 . Hence, ψ represents the vertical distance between the initial state of the soil and its critical-final state.

State parameter has the advantage, in liquefaction assessment, of capturing the effect of the relative density and stress-state (Been and Jefferies, 1985). ψ was estimated by considering the critical state parameters derived from the results of monotonic triaxial tests (see Figure 4.9 in Chapter 4). The interpretation of liquefaction resistance within the CSSM was performed only using the results obtained from CTx testing was analysed since the number of combinations between Dr and p'_0 of such tests. All the specimens —tested for Dr between 30% and 50%, and p'_0 equal to

50 kPa and 100 kPa— had negative values of ψ , which lead to dilative behaviour during shearing.

The liquefaction resistance can also be described as the cyclic resistance ratio (CRR). CRR corresponds to the cyclic stress ratio (CSR) of liquefaction onset in a specific number of cycles (e.g. 10, 15 or 20 cycles). This parameter is associated with ψ for capturing the stress and state conditions, but it does not combine the initial fabric effects (Jefferies and Been, 2015). Therefore, the application of the CSSM framework to describe the liquefaction resistance of TP-Lisbon sand was carried out by estimating the ψ of the four testing conditions implemented for CTx tests and computing the CRR for 15 cycles (CRR_{15}) using the equations defining the LRR reported in Figure 5.5.a. The 15 cycles were adopted since this number has been defined as critical condition for earthquake-induced liquefaction by Seed and Idriss (1971). Moreover, for this analysis, the stress-state of LRC derived from CDSS is presented in terms of p'_0 . Table 5.1 summarises the parameters used to estimate the relationship between ψ and CRR_{15} of TP-Lisbon sand.

Table 5.1: Values for estimating the relationship between ψ and CRR_{15}

Test type	p'_0 (kPa)	e_0	e_{cs}	ψ	CRR_{15}
CTx	50	0.899	0.952	-0.053	0.128
	50	0.863	0.952	-0.089	0.137
	50	0.826	0.952	-0.126	0.158
	100	0.899	0.916	-0.017	0.101
CDSS	50	0.788	0.951	-0.163	0.14
	50	0.826	0.951	-0.125	0.133
	90	0.805	0.919	-0.114	0.124
	90	0.863	0.919	-0.056	0.107

All ψ values reported in Table 5.1 are negative, indicating dilative behaviour. Jefferies and Been (2015) stated that soils with $\psi > -0.055$ are considered susceptible to trigger liquefaction, whereas soils with $\psi < -0.055$ may exhibit cyclic mobility phenomenon. However, the liquefaction susceptibility may change according to the energy and duration of the seismic event.

Figure 5.8 presents the relationship between ψ and CRR_{15} for TP-Lisbon sand. This approach is representative for the same initial fabric (induced by the soil remoulding using the air pluviation method) since this factor influences the number of cycles for liquefaction onset. Moreover, this figure compares the results of CTx tests of this research against other results for quartz sands compiled by Jefferies and Been

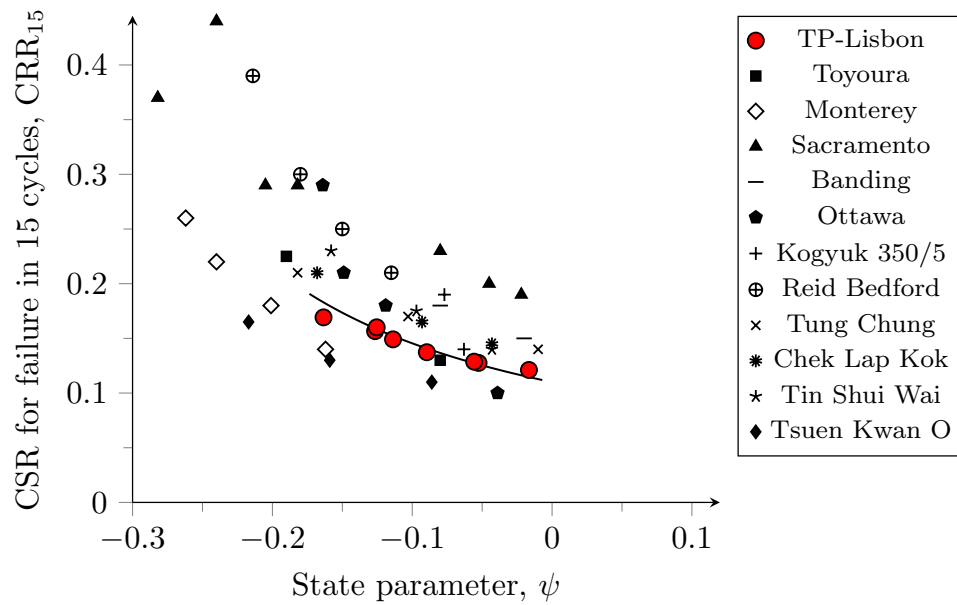


Figure 5.8: Relation between ψ and CRR_{15} (database from: [Jefferies and Been 2015](#))

(2015). The results showed a higher liquefaction resistance (i.e. CRR_{15}) as ψ became more negative, as also observed by [Giretti and Fioravante \(2017\)](#) for liquefiable soil deposits in Italy. This tendency was expected due to the increment of cyclic resistance of dilative soils. On the other hand, a unique relationship was not observed for all soils showed in Figure 5.8 since the CRR also depends on the critical friction ratio (M) ([Rahman et al., 2021](#); [Porcino et al., 2021](#)).

The data spread of Figure 5.8 is mainly linked to the uniqueness of the ψ and CRR_{15} relationship for each tested sand; thus, it can be largely attributed to differences in the initial fabric produced by the reconstitution method of each sand, which depends on its grain size distribution, particle shape and morphology. Besides, the strain level to liquefaction onset differs from that associated with critical state; typically, the liquefaction onset occurs in moderate to large strain levels ([Green et al., 2022](#)). The relationship based on ψ is not universal to describe the liquefaction resistance due to the strain level during liquefaction, which is why the derived relationships based on ψ are applicable solely, to any specific soil, but also with similar initial fabric. These results suggest that soil specimens with the same void ratio and effective confinement but with different initial fabrics may have different ψ and CRR_{15} relationships. A clear evidence of this behaviour has also been observed in the liquefaction resistance of high-quality undisturbed samples and the corresponding reconstituted specimens, where the differences are predominantly attributed to the

distinct initial fabric (Kiyota et al., 2019; Ramos, 2021). Therefore, a suitable fitting can be drawn for each sand under similar fabrics. Equation 5.11 describes the relationship between ψ and CRR_{15} for TP-Lisbon sand, as follows:

$$\text{CRR}_{15} = \frac{1.11}{1 + \frac{\psi}{0.41}} \quad (5.11)$$

By using the relationship between ψ and CRR_{15} , it is possible to compare the liquefaction resistance assessed by both in situ and laboratory testing, as validated by Giretti and Fioravante (2017), combining the ψ derived from CPT in a calibrated chamber in the centrifuge apparatus against element testing. The ψ values addressed for the characterisation of liquefaction resistance of TP-Lisbon sand in the laboratory are comparable with the ψ profile presented in Figure 3.6c (Chapter 3). This law trend line confirmed the high susceptibility of TP-Lisbon sand reported in Figures 5.1 and 5.5.

5.5 Key findings

This chapter comprehensively characterises the liquefaction resistance of a historically liquefiable soil from the Lisbon centre, denominated as TP-Lisbon sand. The liquefaction resistance was assessed through in situ and laboratory approaches based on CPTu, cyclic triaxial and cyclic simple shear test results. These were analysed by an interpretation within the critical state soil mechanics framework, namely applying the state parameter concept. From the results obtained during the experimental program, the following findings can be drawn for the development of this research:

- A critical layer composed of loose sands was identified by CPTu soundings. Such a layer is highly susceptible to liquefaction onset, although historical reports indicate that this soil has already exhibited liquefaction. Analyses of the factor of safety against liquefaction and liquefaction potential index demonstrated the current liquefaction susceptibility.
- The interpretation of the obtained values of liquefaction severity number, with values lying between 3.39 and 5.55, showed that the surrounding buildings and existing infrastructure of Terreiro do Paço site will not present significant damage or foundation settlements in case a seismic event with the local action or

similar that may occur in the Greater Lisbon Area. The possible low damages are related to the presence of shallow compacted materials and heterogeneous masonry remains (from the collapsed structures after the 1755 earthquake), which do not exhibit significant deformations during liquefaction onset due to their high stiffness.

- Liquefaction resistance curves indicated that the liquefaction resistance increases as the relative density increases. In contrast, the cyclic resistance ratio increases as the stress state decreases. Therefore, the liquefaction resistance ratio of TP-Lisbon sand depends on its state, which the state parameter concept can represent.
- The results between CTx and CDSS tests can be compared by applying a transformation based on the coefficient C_r . A new formulation to estimate C_r for TP-Lisbon sand was proposed in this study. Based on the at-rest earth pressure coefficient, the new proposal allowed CTx results to be transformed into CDSS results and vice-versa. Applying such a model in CTx and CDSS in equivalent test conditions demonstrated that such a transformation provided a reliable comparison between original and transformed data.
- A model based on the critical state soil mechanics revealed that the liquefaction resistance of TP-Lisbon sand increases as the state parameter is more negative, validating the effect of relative density and stress state on the cyclic behaviour of this soil. Such a model is consistent and reveals a lower trend line when compared to liquefiable sands with similar physical properties reported in the literature, allowing a comparison between in situ and laboratory test results.

Chapter 6

Improvement of liquefaction resistance by induced partial saturation

The main content of this chapter has been published in Molina-Gómez F., Viana da Fonseca A., Ferreira C., and Caicedo B. (2023) 'Improvement of cyclic liquefaction resistance induced by partial saturation: An interpretation using wave-based approaches', *Soil Dynamics and Earthquake Engineering*, 167, p. 107819. doi:10.1016/j.soildyn.2023.107819 and Molina-Gómez F, Viana da Fonseca A, Ferreira C, Caicedo B.(2023) Experimental Wave-Based Assessment of Liquefaction Resistance for Different Degrees of Saturation. *Geotechnical Testing Journal* 46:968–85. <https://doi.org/10.1520/GTJ20230299>.

Moreover, another paper have been submitted for publication in *Géotechnique*: Molina-Gómez, F. Ferreira C., Viana da Fonseca A., and Cascante, G. (2023) 'Use of seismic wave velocities for improved evaluation of high degrees of saturation in sands using bender elements'

6.1 Outline

This chapter presents the results of an experimental program carried out in the laboratory to assess the liquefaction resistance of TP-Lisbon sand in partially saturated conditions. The induced partial saturation was controlled by P-wave velocity measurements, which were contrasted against theoretical predictions performed in the light of Biot's theory. The procedure for estimating the degree of saturation using wave analysis is also described and validated herein. The results confirmed

that inducing partial saturation increased the liquefaction resistance. However, the findings revealed that, under the same relative density and confinement stress, the S-wave-based approach did not accurately predict the liquefaction resistance because of negligible variations in the stress state and soil stiffness at the examined degrees of saturation. In turn, the P-wave-based approach effectively predicted the increase in liquefaction resistance of TP-Lisbon sand for different degrees of saturation due to its strong dependency on P-wave propagation in fluid-saturated granular media. This effect results from the most relevant factor conditioning the pore pressure build-up in partially saturated sands, e.g., the compressibility of the occluded air bubbles, which can be detected by the P-wave and not by the S-wave.

6.2 Assessment of degree of saturation by a novel wave-based approach

The P-wave propagation is affected by the compressibility of porous fluid in the granular media. This effect offers alternatives to estimate the degree of saturation of sands by measuring the P-wave velocity. In the laboratory, such an estimation is commonly carried out by Skempton's B-value (Skempton, 1954). However, B-value is not suitable in the field due to the limitations to ensuring the undrained conditions during its measurement. An advanced method that combines the accurate measurement of the degree of saturation and the P-wave velocity (V_P) during element testing is proposed herein, providing a wave-based framework that can be applied for monitoring the degree of saturation (S_r).

6.2.1 Experimental procedure for monitoring the degree of saturation

In this research, a novel method for soil saturation is proposed. This procedure mainly involves the monitoring of the degree of saturation by measuring the evolution of P-wave velocity (V_P) during testing. However, complementary measurements of the pore pressure coefficient B or B-value (Skempton, 1954) were carried out. Physically, P-wave propagates faster through the fluid than the particles contacts (Astuto et al., 2023). Therefore, the presence of occluded air bubbles affects the V_P in porous fluid saturated media, as illustrated in Figure 6.1. Besides, an accuracy control of total and water volume changes was carried out by means of local

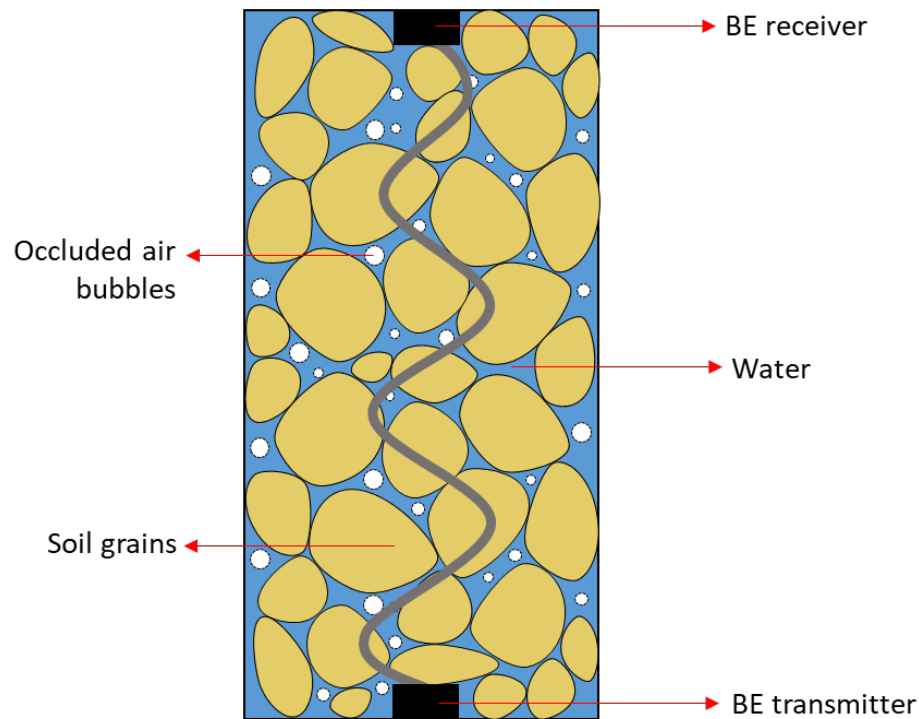


Figure 6.1: Schematic representation of P-wave propagation in porous fluid saturated media (Astuto et al., 2023)

instrumentation (Hall-Effect transducers) installed directly in the soil specimen (see Figure 3.15) and an automatic volume change gauge.

A series of soil specimens of TP-Lisbon sand with 70 mm diameter and 140 mm height were remoulded for relative densities (D_r) between 30% and 75% using the air pluviation method (Yamashita et al., 2009). Before remoulding, the soil was oven-dried to ensure $S_r = 0\%$ at the test beginning. All tests were carried out in a triaxial cell equipped with piezoelectric transducers. These piezoelectric transducers allow measuring the seismic wave velocities (i.e. V_P and V_S) through the Bender Element (BE) test procedure proposed by Ferreira et al. (2021). The triaxial cell was also instrumented with four Hall-Effect transducers –two to measure axial strains and two to measure radial strains. The Hall-Effect transducers were selected since its low weight (≈ 11 g), which is an advantage for the testing of loose sands. This configuration allows accurately monitoring the volumetric strains of soil specimen and void ratio changes during saturation process.

For soil saturation, the carbon dioxide method was implemented. This method was selected since such an inert gas is denser, less compressible and more soluble in

water than air. Therefore, the application of carbon dioxide ensures a complete replacement of the air in the soil voids. The carbon dioxide was introduced after the sample preparation under a low pressure (≈ 3 kPa) from the bottom drainage line to the top drainage line. This configuration forced the air to circulate upwards in the soil specimen until being expelled through an open tube in contact with atmospheric pressure. This tube is open and submerged underwater for controlling the bubbling velocity (e.g. one bubble per second). The flushing of the carbon dioxide was carried out until achieving a minimum of one litre of the gas, which was measured by displacing water in a bottle.

After the carbon dioxide flushing, deaired water is introduced by the bottom drainage line, allowing the water movement through the soil specimen under a constant hydraulic gradient and pushing out the carbon dioxide through the top drainage line. The water flushing covers the same connections of the carbon dioxide flushing. The water flow is the result of differential pressures at the drainage inlets, which should be reasonable to avoid the overconsolidation of the soil specimen (Viana da Fonseca et al., 2021). During this process, the cell pressure must be higher than the pressure applied internally at the bottom of the sample to ensure a positive effective confining pressure (e.g., cell pressure ≈ 20 kPa, bottom backpressure ≈ 10 kPa and the top at atmospheric pressure). To guarantee that the majority of the gas is flushed out, the volume of percolated water should be equivalent to twice the estimated volume of the voids (Soares, 2015).

The water of the soil specimen during the saturation phase was estimated by applying the mass equilibrium. Therefore, the measurement of water volume that flushed through the soil specimen was conducted using an automatic volume change gauge. The water that did not remain in the specimen was estimated by a graduated cylinder connected to the tube connected to the top drainage line, or by weighting the collected water. The water also saturated the triaxial system (i.e. pore pressure transducers, connections and tubes). Hence, the triaxial system volume was previously measured to obtain a reliable estimation of the water volume in the soil. The difference between the total flow minus the triaxial system volume and the remaining water is the water volume in the soil specimen until the end of this phase.

Occluded air bubbles may remain attached to the soil grains after carbon dioxide and water flushing. Therefore, to achieve higher degrees of saturation, the backpressure (BP) was gradually increased under a confinement pressure of about 10 kPa. V_P was measured during such increment every 50 kPa, e.g. BP equal to 0, 50, 100, 150, 200,

250 and 300 kPa, and concurrently to V_P measurements, B -value was estimated by increasing the cell pressure (CP) by 30 kPa in undrained conditions. B -value was used since this method is conventionally used to estimate S_r during triaxial testing. S_r of the soil was systematically assessed by monitoring the void ratio changes and water volume changes by the Hall-Effects transducers and the automatic volume change gauge during all phases.

To obtain a reliable V_P estimation, the axial and radial strains were monitored during all saturation phases, that is, carbon dioxide flushing (1st phase), water flushing (2nd phase) and backpressure increment (3rd phase) using the Hall-Effects readings. These measurements were also used for estimating porosity (n) from void ratio (e) derivations during testing by $n = e/(1+e)$. Figure 6.2 shows the typical void ratio changes (Δe) inferred from Hall-Effects readings. This Figure revealed a slight positive increment in Δe during the carbon dioxide flushing, which converged near 0 at the end of this phase. The maximum value in Δe was detected in the water flushing phase, corresponding to -0.0057. Such a value equalled a Dr change of 0.25%. During backpressure increment, Δe reached a value of about -0.0059, which was negligible. Therefore, significant axial and radial strains were not observed along the saturation process, which may affect the initial state of the soil specimen and the V_P measurements.

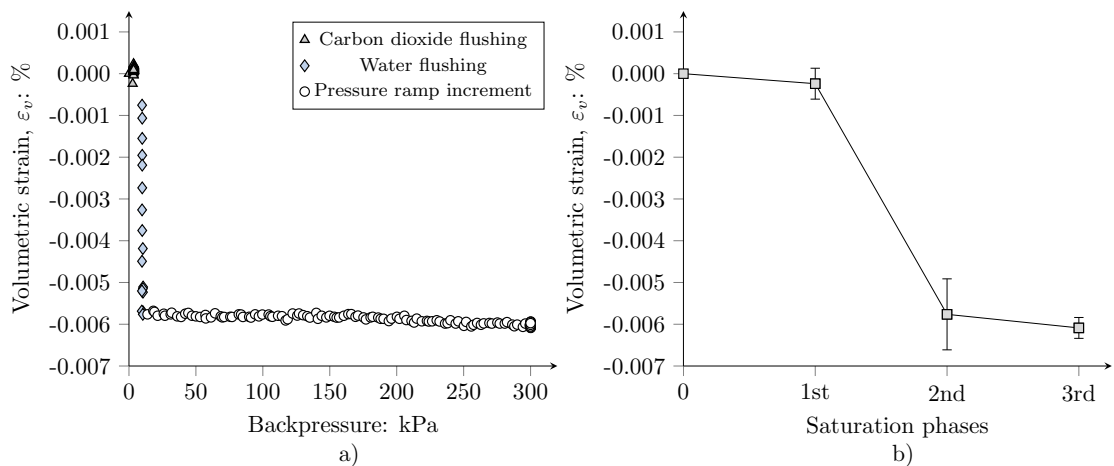


Figure 6.2: Void ratio changes inferred by Hall-Effects readings during saturation process: a) typical measurements (soil specimen with $Dr = 30\%$); b) variation of void ratio change during saturation phases, i.e. 0 (specimen assembling), 1st (carbon dioxide), 2nd water flushing and 3rd pressures increment

The soil was considered fully saturated for B -value and V_P higher than 0.98 and

near to 1500 m/s, respectively. All soil specimens reported the full saturation condition at the end of testing. Hence, the evolution of the degree of saturation was estimated based on the final water content (ω_f). To estimate ω_f , the specimens were carefully removed from the cell, avoiding possible loss of soil particles and water, as suggested by [Verdugo and Ishihara \(1996\)](#). The end-of-test soil freezing technique was not used in this study to avoid damage to the piezoelectric instruments. The procedure proposed by [Verdugo and Ishihara \(1996\)](#) allows for a reliable and consistent measurement of the void ratio after testing (e_f) based on ω_f and by applying the relation $Sr \cdot e_f = Gs \cdot \omega_f$, where Sr is considered as 100% ([Murthy et al., 2007](#); [Viana da Fonseca et al., 2021](#)).

6.2.2 Interpretation of wave signals

The BE tests to assess the relationship between Sr and V_P were carried out by applying input sine-wave pulses with four frequencies (F) between 25 and 100 kHz. The use of various frequencies allowed minimising the uncertainty and subjectivity associated with the interpretation of test results ([Viana da Fonseca et al., 2009](#)). The input frequencies varied during the saturation process to obtain the best response (or amplitude) for each Sr . On the other hand, measurements of S-wave velocity (V_S) were conducted by applying F of 2, 4, 6 and 8 kHz. All signals were interpreted by the first arrival time method, which was common to all input frequencies for both P- and S-waves (Figure 6.3).

[Ferreira et al. \(2021\)](#) demonstrated by laser measurements that input frequencies higher than 20 kHz produced vertical and horizontal polarised displacements, generating P-wave in the fluid-saturated granular media during BE tests. The simultaneous movements are due to the surrounding confinement and element inertia, which induce both perpendicular and parallel distortions that are propagated through the soil specimen. Hence, the generation of P-wave in granular media can be carried out without using other configurations or piezoelectric transducers, such as extender elements or compressional plates. Notwithstanding, in fully saturated conditions or near to full saturation, P-wave was observed for frequencies lower than 20 kHz, such as 8 kHz. The P-wave generated during BE testing exhibited lower amplitudes than S-wave ([Viana da Fonseca et al., 2009](#)).

Figure 6.3 presents the typical results of BE test using four input frequencies interpreted in both time and frequency domains. From Figures 6.3a and 6.3c, it can be observed a convergence of the arrival time in all F , for both P- and S-waves,

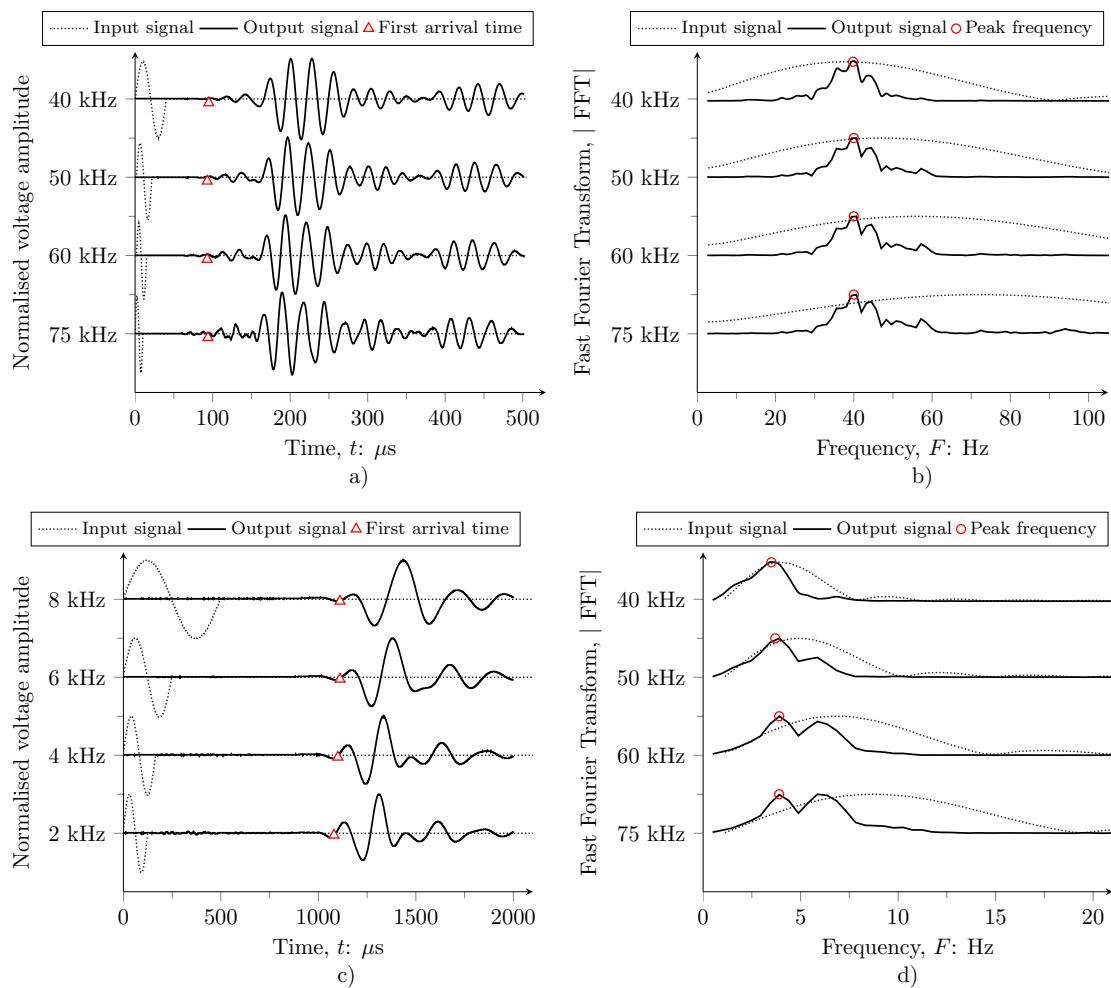


Figure 6.3: Interpretation of typical signals: a) P-wave analysis in the time-domain; a) P-wave analysis in the frequency-domain; c) S-wave analysis in the time-domain; d) S-wave analysis in the frequency-domain

validating the selection of the wave propagation travel time (t_t). Hence, based on these results, the wave velocity of each specimen was determined by computing the ratio between the BE tip-to-tip distance (L_{tt}) and the t_t (Viggiani and Atkinson, 1995). The frequency-domain analysis showed that peak frequency is in between 38 kHz and 41 kHz. Besides, the frequency-domain analysis revealed that the system response is not dependent on the excitation generated during BE testing since the frequency spectra presented similar tendencies in Figures 6.3b and 6.3d. This tendency indicated that wave propagation is transmitted through the fluid-saturated granular media.

In this study, Biot's wave was not detected due to the energy dissipation caused by the air damping present in partially saturated soils. This effect is consistent with

the rapid attenuation of such a wave-type observed by Nakagawa et al. (1997) in granular soils since the energy of Biot's wave is lower than the energy of both P- and S-waves. On the other hand, the analysis of V_P is not affected by Biot's wave since the first arrival time of P-wave is faster than the appearance of Biot's wave, independently of the degree of saturation (Astuto et al., 2023).

Before starting the experimental program, calibration tests were carried out to measure the V_P of water. For this purpose, the triaxial cell was filled with deaired and distilled water, which is the same water used for the tests of the present study. Afterwards, 300 kPa pressure was gradually applied to replicate a similar backpressure environment of soil specimens at fully saturated conditions. The average temperature of the water during testing was 23° C. On the other hand, the top-cap was fixed at 137 mm height to simulate the travel length propagation of a soil specimen during the saturation process. Figure 6.4 shows a constant P-wave arrival time ($\approx 92.5\mu s$), corresponding to a $V_P = 1475$ m/s. This result is compatible with the theoretical value reported by Santamarina et al. (2001) of 1482 m/s. The minor difference between experimental result and theoretical value was attributed to some remained pollutants in the water after the distilling process. Moreover, near-field effects and S-wave presence were not observed during the assessment of P-wave propagation tests on the water (see Figure 6.4).

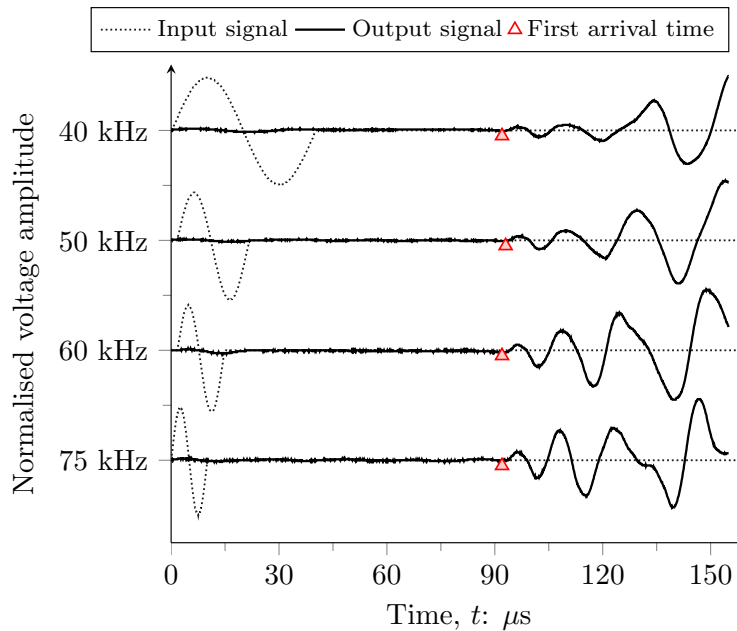


Figure 6.4: P-wave propagation in water

Figure 6.5 presents the typical P-wave signals for different degrees of saturation,

using an input frequency (F) of 40 kHz, which corresponds to a value near to the peak frequency of the system (identified in Figure 6.3b). Moreover, from Figure 6.5, it can be observed that the wave propagation time decreased with the Sr increased. These results confirmed the effects of Sr on V_P ; that is, the P-wave is faster in fully saturated conditions than in partially saturated conditions, which is consistent with the findings reported by Emerson and Foray (2006); Kumar and Madhusudhan (2012); Kim et al. (2021). In the Sr range of 97% and 100%, P-wave propagation time reduced by about $15 \mu s$ on each Sr increment of 1%. Therefore, the experimental results of this study demonstrated the high sensitivity and accuracy of V_P in detecting the evolution and small changes of Sr in partially saturated soils.

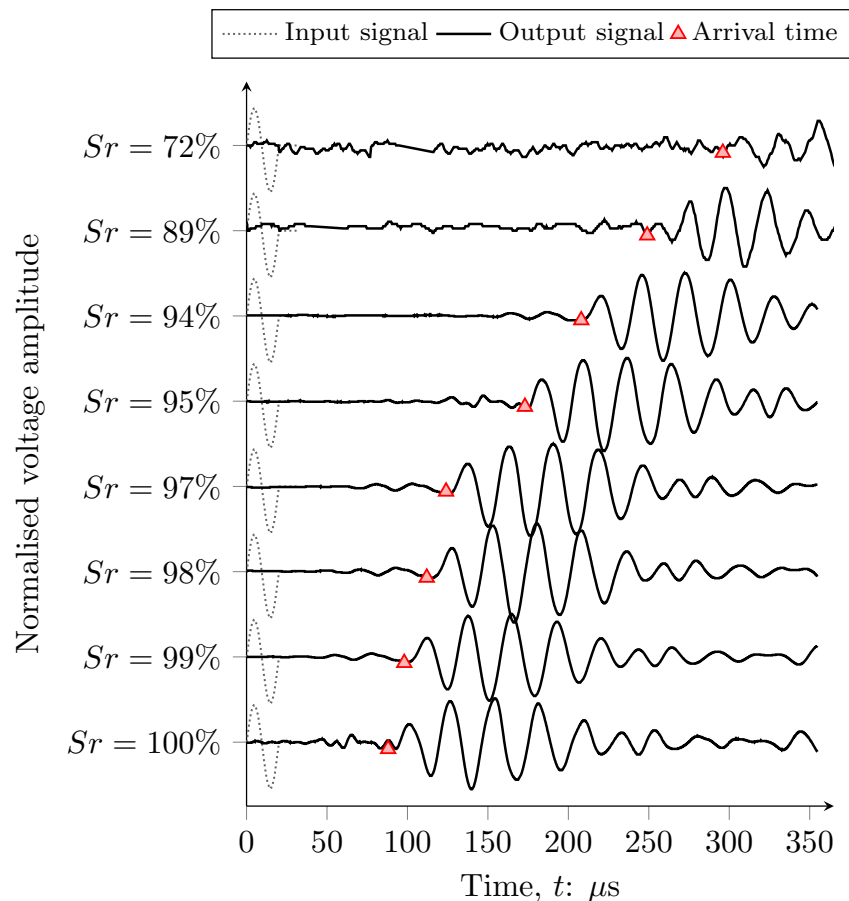


Figure 6.5: P-wave propagation for different degrees of saturation —BE tests carried out for $Dr = 30\%$ and using 40 kHz input frequency

6.2.3 Analysis of elastic waves evolution in fluid saturated granular media

In the laboratory, the full saturation condition of the soil is conventionally validated by measuring the B -value (Yang, 2002; Leong and Cheng, 2016). Hence, in this study, the relationship between concurrent measures of V_P and B -value was evaluated to correlate these parameters during the saturation process. All measurements of V_P presents such a relationship for different Dr in TP-Lisbon sand. From Figure 6.6, it can be observed a parallel evolution of V_P as a function of B -value for all Dr , indicating an effect of Dr on such relationship, where the higher values of V_P measurements for denser specimens.

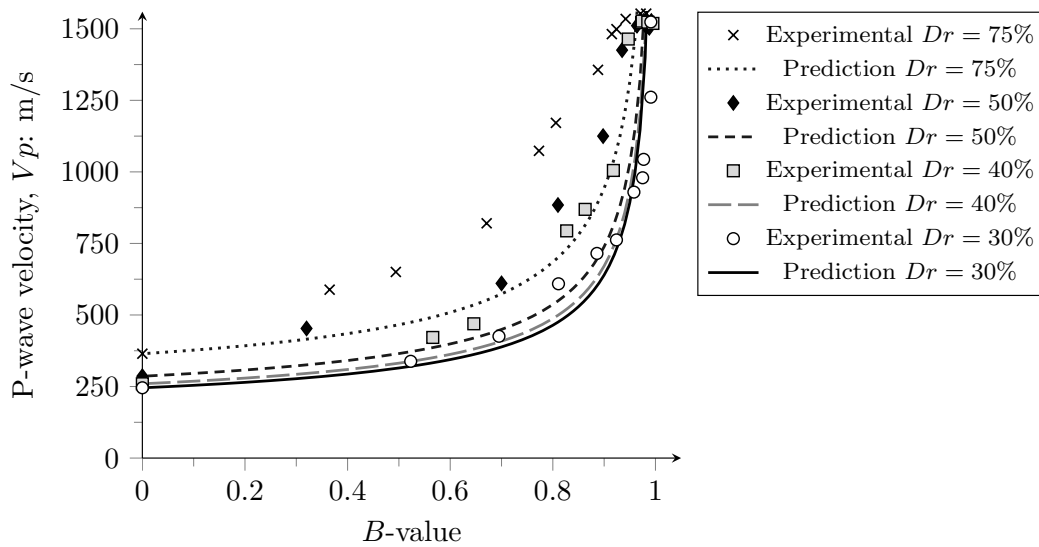


Figure 6.6: Relationship between B -value and V_P

Figure 6.6 compares experimental data against the theoretical model proposed by Yang (2002) based on the poroelastic media theory. This comparison shows that experimental results did not match the theoretical predictions for B -value between 0 and 0.75. Such a divergence was also observed for B -value between 0.60 and 0.90 by Tamura et al. (2002); Gu et al. (2021); Astuto et al. (2023). Notwithstanding, V_P in all tests increased and converged to a constant value near 1530 m/s. This value was identified in B -values from 0.97 to 1.00, confirming the full saturation condition of the soil in all Dr .

The differences between experimental results and theoretical predictions observed in Figure 6.6 were attributed to volumetric strains (ε_v) induced during the B -value tests. According to Skempton (1954), a reliable assessment of the B -value considers

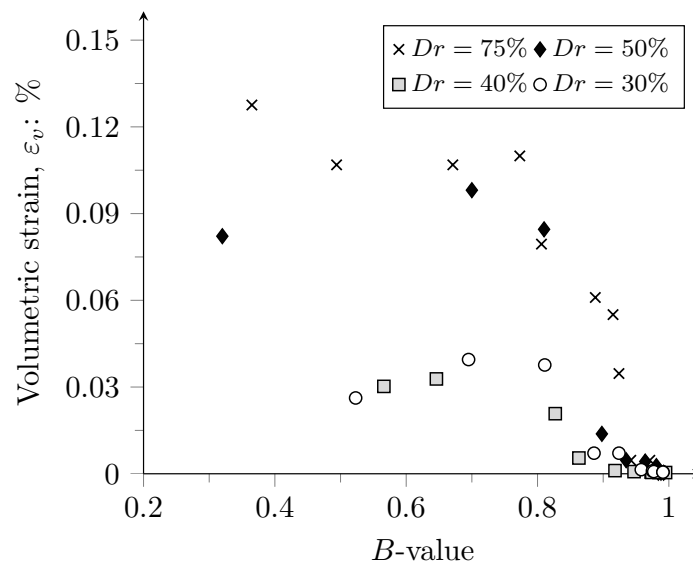


Figure 6.7: Volumetric strains reported during B-value measurements

that the soil specimen should not report volumetric strains during its measurement. Hence, ε_v may occur due to the presence of occluded air bubbles in the water, which reduce the bulk modulus of the pore fluid (K_f), affecting the pore pressure build-up during B -value testing for different Dr . Figure 6.7 presents the ε_v measured by the Hall-Effect readings during the B -value testing, showing that the soil experienced volumetric changes for B -value results lower than 0.90, validating that the volumetric strains affected the pore pressure build-up during B -value testing in partially saturated conditions.

Figure 6.8 shows the evolution of V_P as a function of the degree of saturation. The results in this figure reveal an effect of Dr on P-wave propagation during saturation since the V_P curves shifted up as Dr increased. On the other hand, Figure 6.8 compares experimental data against theoretical predictions performed based on Biot's theory (Biot, 1956a,b). For this purpose, V_S measurements carried out in dry conditions, after soil remoulding, were used for estimating the initial soil stiffness. Poisson's ratio (ν) was computed by combining the results of V_P and V_S reported during the saturation process. Besides, $K_g = 3.5 \times 10^9$ kPa were adopted, as suggested by Santamarina et al. (2005); Kumar and Madhusudhan (2012). Such computations involved the bulk modulus of liquid (water) and gas (carbon dioxide), corresponding to the soil state before the backpressure increment. The bulk modulus of carbon dioxide was $K_{CO_2} = 0.16 \times 10^6$ kPa (Adam and Otheim, 2013).

The comparison between experimental data and theoretical predictions showed that

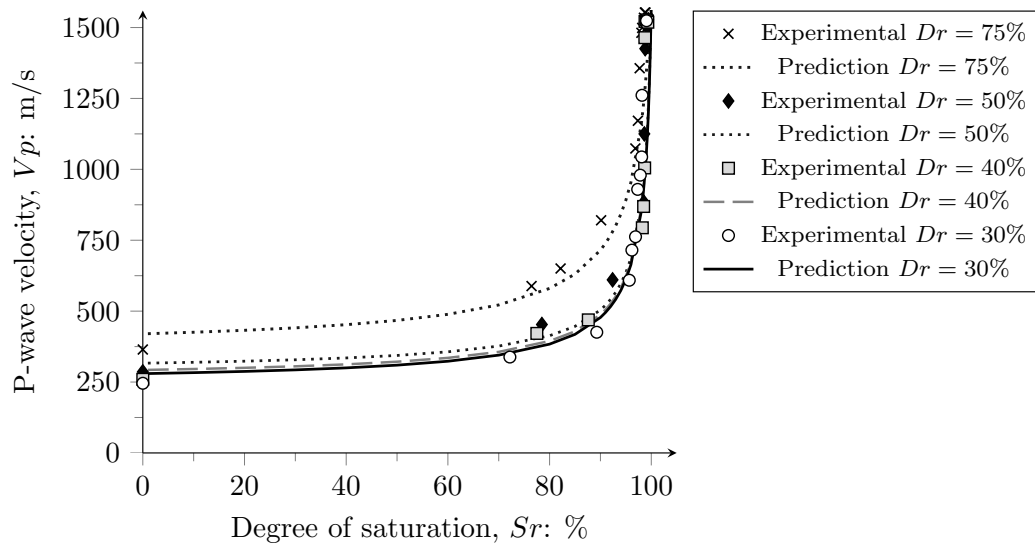


Figure 6.8: P-wave propagation for different degrees of saturation.

results agree well with the theoretical model of the tested Dr . On the other hand, it can be observed differences between V_P results from $Sr = 0\%$ until $Sr = 75\%$ obtained for different values of Dr , indicating that V_P is higher for $Dr = 50\%$ in a such Sr range. For $Sr > 75\%$, partially and fully saturated conditions, V_P suddenly increased until converging in values of about 1500 m/s for $Sr > 99.99\%$ —higher values than V_P in the water (1482 m/s). Such changes were attributed to the effects of occluded air bubbles on the propagation of P-Wave, which reduced the volumetric compressibility of the fluid in the granular medium (Leong and Cheng, 2016; Gu et al., 2021). Tamura et al. (2002) observed that bigger occluded air bubbles caused lower Sr . However, these authors recommend increasing the back-pressure to eliminate the occluded air bubbles and, thus, ensure the full saturation condition. Therefore, these findings demonstrated the sensitivity of V_P on predicting Sr in partially saturated sands.

6.3 Liquefaction resistance assessment in partially saturated conditions

Studies carried out by numerous authors (Yang et al., 2004; Mele et al., 2019; Banerjee et al., 2022; Mele et al., 2022) in sandy soils showed that the cyclic resistance ratio (CRR) increases by decreasing the degree of saturation (Sr). Saturated sands subjected to cyclic loading in undrained conditions do not present volumetric changes. The cyclic loading is transmitted to the fluid, causing a pore pressure build-up

and the loss of grain-to-grain contacts. In contrast, in partially saturated sands, the volume changes due to the compressibility of gas/air, reducing the pore pressure build-up during loading and thus increasing the liquefaction resistance of the soil. Hence, the mechanism associated with the increase in the cyclic liquefaction resistance in partially saturated sands is related to fluid compressibility since the bulk modulus of the fluid decreases significantly in the presence of occluded air bubbles.

Therefore, the techniques for inducing partial saturation of soils are considered one of the most innovative, adequate and promising for enhancing liquefaction resistance. A reduction in S_r from 100 to 98% can increase the liquefaction resistance by 30% (Mele et al., 2019). Notwithstanding, this performance may depend on the intrinsic physical properties and the relative density of each soil. The induced partial saturation techniques (IPS) rely on the generation of gas/air in the soil pores by different methods, such as water electrolysis (Yegian et al., 2007; Zhang et al., 2020), air injection (Okamura et al., 2011; Zeybek and Madabhushi, 2017), chemical desaturation (Eseller-Bayat et al., 2013; Zeybek, 2022), and microbial desaturation (Rebata-Landa and Santamarina, 2012; He et al., 2013).

An experimental program comprising an extensive number of CTx and BE tests (more than 30) was carried out to assess the improvement of cyclic liquefaction resistance induced by partial saturation. All tests were conducted under $p'_0 = 50$ kPa and relative densities of 30% and 50%, both in with a tolerance of $\pm 3\%$. In such set of CTx tests, the S_r was changed to assess the effect of the induced partial saturation on the liquefaction resistance of TP-Lisbon sand. The CTx tests carried out in partially saturated conditions analysed in this section conditions are contrasted against the CTx tests carried out in fully saturated conditions presented in Chapter 5 for each D_r . The induction of partial saturation was carried out using the procedure described in Section 6.2.1.

The S_r values were selected based on the soil-water characteristic curve (SWCC) in Figure 6.9. The SWCC was estimated by combining results from a Pressure Plate Apparatus (PPA) and Suction Plates Method (SPM), as suggested in the standard D6836 (ASTM International, 2006). PPA tests comprised the preparation of four soil specimens into four rigid stainless-steel rings using the same remolding method implemented for CTx testing. The soil specimens were placed in the pressuring chamber over a high air-entry ceramic disk. Subsequently, the soil specimens were tested using constant pressures (e.g. 1, 2, 5, 10, 20, 30, 50, 100, 200, 400, 600

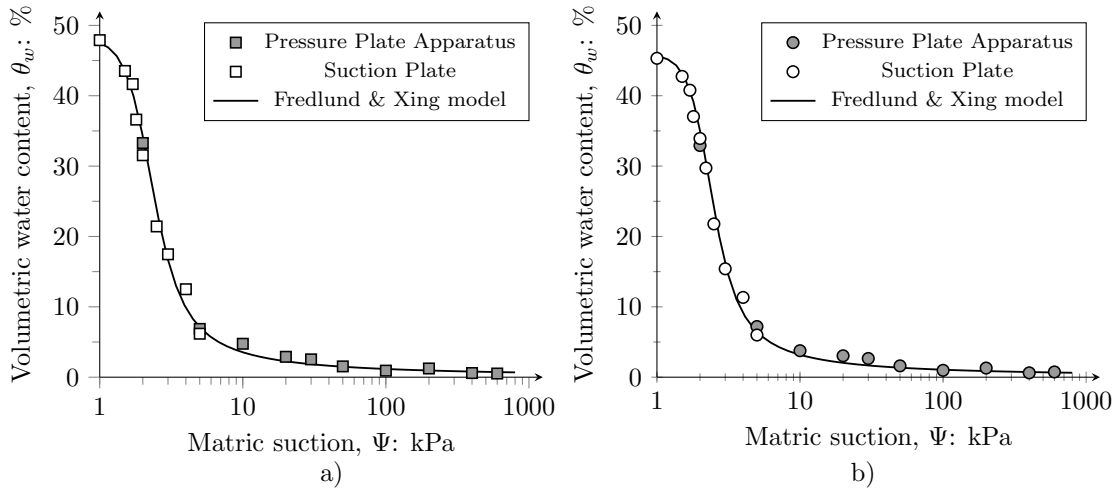


Figure 6.9: Soil-water characteristic curve of TP-Lisbon sand: a) $Dr = 30\%$; b) $Dr = 50\%$

and 700 kPa) for seven days to achieve the equilibrium between soil water and air pressure.

For the case of the SPM tests, two funnels containing a high air-entry ceramic disk were used. The funnels were positioned at different heights to ensure a fixed water height (e.g. 10, 15, 17, 18, 20, 25, 30, 40, 50, and 100 cm). These different testing heights induced different suctions, which effectively complement the PPA results (Caicedo, 2019). All samples were prepared for a relative density of $30 \pm 2\%$ and $50 \pm 2\%$ by computing the soil weight for the volume of the rigid stainless-steel rings and funnels for PPA and SPM, respectively. This procedure was applied for each pressure increment according to standard D6836 (ASTM International, 2006). After testing, the samples were weighed and oven-dried to measure the water content at the end of each suction stage.

Experimental data were contrasted against the theoretical model proposed by Fredlund and Xing (1994) to describe soil-water characteristic curve (SWCC). Equation 6.1 describes the model of SWCC:

$$\theta_w = \frac{\theta_s}{\left[\ln \left(\exp + \left(\frac{\Psi}{a} \right)^b \right) \right]^c} \quad (6.1)$$

where $\theta_w = (S_r \cdot \omega \cdot G_s) / (S_r + \omega \cdot G_s)$ is the volumetric water content, θ_s is the

saturated water content; \exp is the Euler's number (≈ 2.71828); Ψ is the applied suction; and a , b and c are fitting parameters. Table 6.1 presents the values of the parameters defining the SWCC curve of TP-Lisbon sand for Dr equal to 30% and 50%. Based on the analysis of SWCC, it was found that the air-entry value for TP-Lisbon sand is about 1.5 kPa, which corresponds to $\theta_w \pm 41\%$ (equivalent to $Sr \pm 80\%$). Therefore, from these results, it can be concluded that the Psi effects on the cyclic behaviour can be considered negligible for $Sr > 80\%$. In such a Sr range, located above the air-entry value, granular soils comprise only two phases (i.e., solid and liquid), ensuring a soil state with a continuous liquid phase, where the gas is present in the liquid as occluded air bubbles.

Table 6.1: Parameters defining the soil water characteristic curve of TP-Lisbon for different relative densities

Parameter	$Dr = 30\%$	$Dr = 50\%$
θ_s (%)	47.31	45.27
a	1.97	2.11
b	5.08	5.79
c	1.24	1.21

The occluded air bubbles do not generate suction in the soil but decrease the volumetric compressibility of the pore fluid, as observed by Okamura and Soga (2006); Zeybek (2022). Therefore, the increase in liquefaction resistance of TP-Lisbon sand for Sr higher than 80% can be attributed to the reduction of fluid compressibility (K_f) rather than Ψ . The Sr of all tests were monitored through V_P measurements during the back-pressure increment, as described in Section 6.2.1.

The V_P measurements were contrasted against a theoretical model based on the wave propagation equations proposed by Biot (1956a,b). According to Biot's theory, in fluid-saturated granular media, the P-wave propagation evolves with the variation of Sr due to the changes in the volumetric compressibility of pore fluid. Therefore, P-wave tends to be faster as Sr increases, reporting VP values above 1500 m/s for fully saturated conditions. Negligible effects of stress-state on P-wave propagation were identified due to the slight changes in V_P between the end of the backpressure increment and consolidation phases. Figure 6.10 presents the results of BE test for different Sr .

Figure 6.11 shows the results of the seismic wave velocities (V_P and V_S) as a function of Sr before cyclic loading. All Sr values were confirmed using the end-of-test procedure described in Section 3.4.2. The wave velocity values were measured under

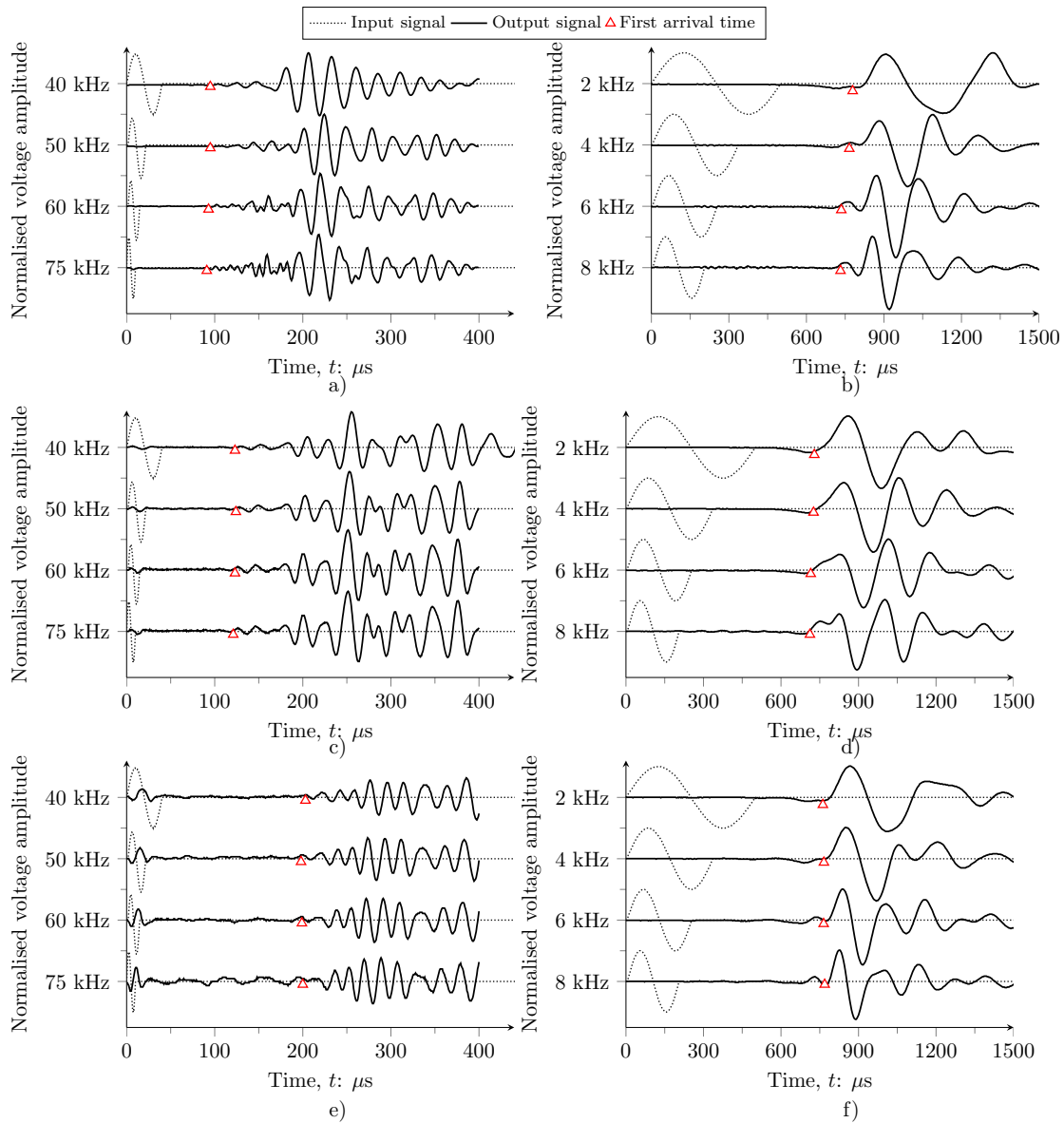


Figure 6.10: Typical signals of wave propagation ($p' = 50$ kPa and $Dr \approx 30\%$): a) P-wave for $Sr = 100\%$; b) S-wave for $Sr = 100\%$; c) P-wave for $Sr = 96\%$; d) S-wave for $Sr = 96\%$; e) P-wave for $Sr = 91\%$; f) S-wave for $Sr = 91\%$

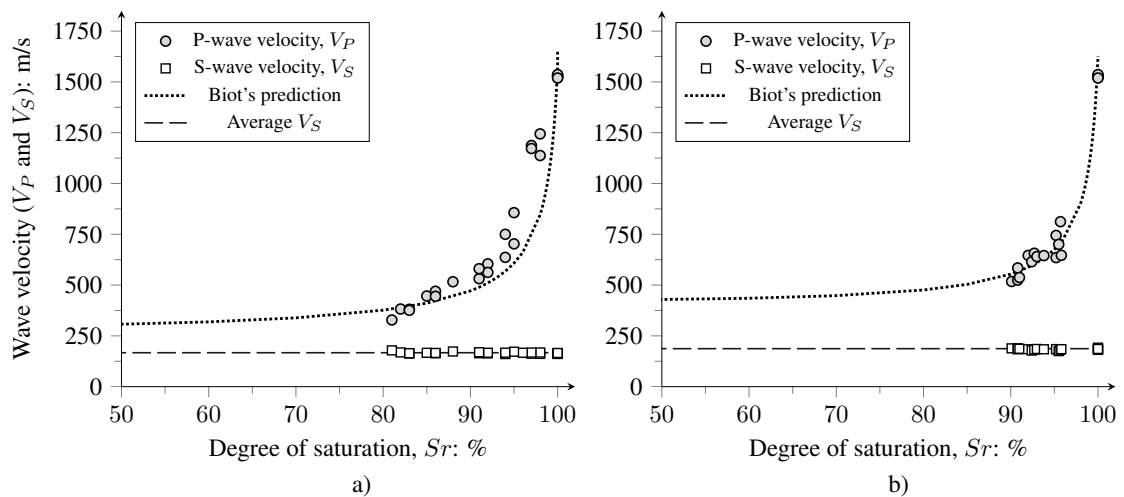


Figure 6.11: Relationship between degree of saturation and wave velocities: a) tests with $Dr \pm 30\%$; b) tests with $Dr \pm 50\%$

$p' = 50$ kPa. From Figure 6.11, it can be observed that V_S tends to be constant at 167 ± 7 m/s irrespective of the S_r . This effect can be attributed to the fact that, for S_r above 80%, the stress-state is constant, thus the stiffness of TP-Lisbon sand is unaltered. Moreover, experimental results of the S_r and V_P relationship fitted well with the theoretical predictions obtained by applying Biot's theory, providing a solid framework for estimate S_r during testing. The data trend agrees well with the results presented by Eseller-Bayat et al. (2013). Based on the results of the approach presented in Figure 6.11, S_r between 82% and 100% were grouped to cover the partially and fully saturated ranges of TP-Lisbon sand for each Dr . These values were selected considering a mean value $\pm 3\%$ for each S_r group.

Figure 6.12 contrasts the cyclic behaviour reported for three CTx tests with different S_r . Results of Figure 6.12 were obtained from CTx conducted for similar conditions of cyclic loading, that is, $CSR_{CTx} = \frac{q}{2p'_0}$ between 0.152 and 0.158, indicating important differences in cyclic behaviour can be observed for S_r of 100%, 96% and 91%. In addition, Figure 6.12 reveals that the test conducted for $S_r = 91\%$ exhibited lower axial strains (ε_a) than the other compared tests, whereas the results in fully saturated conditions showed the highest deformation after liquefaction onset. This behaviour suggested that the induction of partial saturation reduced the liquefaction-induced deformations, as also observed by Zeybek and Madabhushi (2017). However, large deformations represented by $\varepsilon_a > 5\%$ were observed in all CTx tests after liquefaction onset despite the S_r of the test.

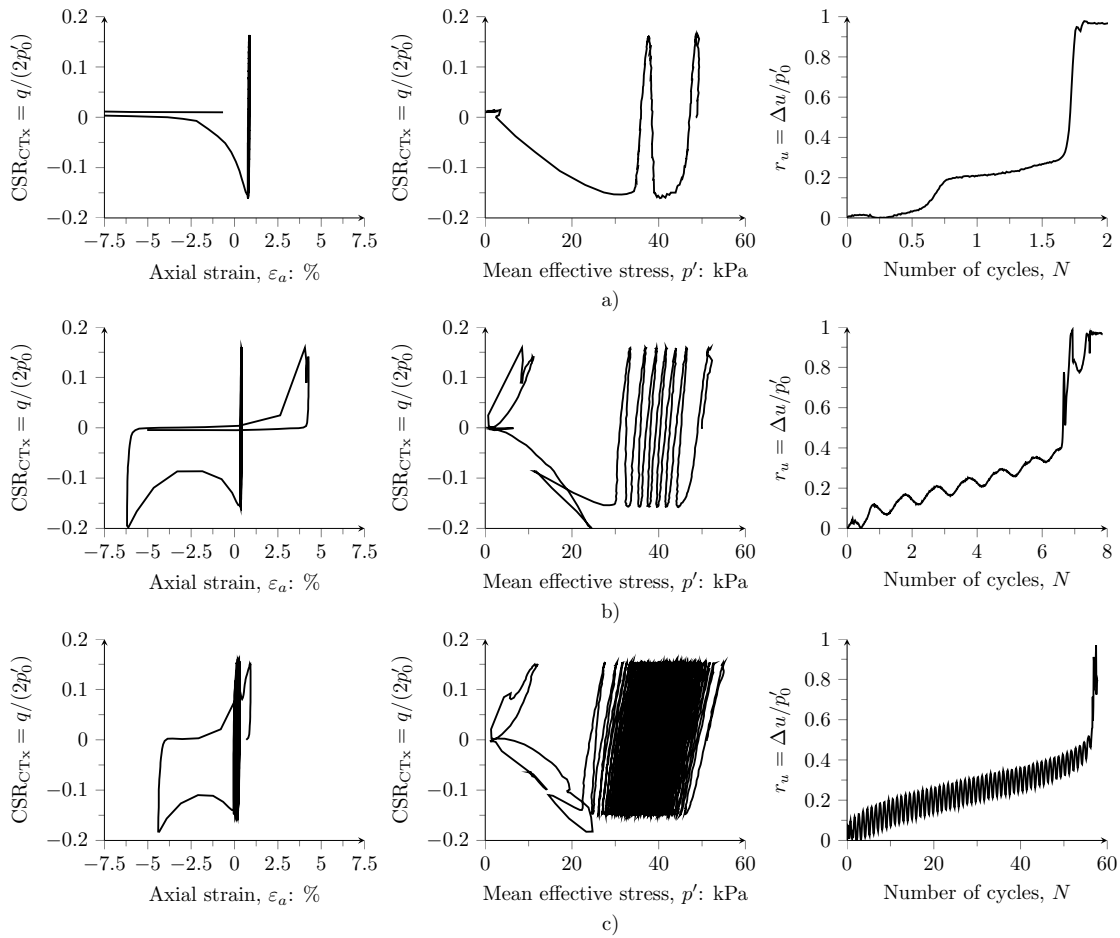


Figure 6.12: Cyclic behaviour for different degrees of saturation —typical CTx results for $Dr \pm 30\%$: a) $Sr = 100\%$; b) a) $Sr = 96\%$; c) $Sr = 91\%$

Figure 6.12 also shows that the pore pressure coefficient ($r_u = \Delta u/p'_0$) reached values higher than 0.99, even for the partially saturated specimens. Hence, in this study, the liquefaction onset for fully and partially saturated CTx tests was identified using the r_u criterion. The results in Figure 6.12 clearly reveal that the liquefaction resistance increased with the decrease of Sr . The improvement of cyclic liquefaction resistance induced by partial saturation was attributed to occluded air bubbles in the pore-fluid, which reduced the pore pressure build-up, as observed by Yegian et al. (2007). A comparison between CTx tests with very similar CSR_{CTx} indicated that a reduction in Sr by 4% tripled the number of cycles for liquefaction onset. Likewise, a decrease of Sr by 9% significantly increased the liquefaction resistance from 2 cycles to 58 cycles. Although the increment in the number of cycles to liquefaction onset (N_L) was evident, it was not possible to define a clear relationship between N_L and Sr for very similar CSR. This effect will be quantified below.

Figure 6.13 shows the liquefaction resistance curves obtained for different degrees of saturation (S_r). The degrees of saturation evaluated in this study included the full saturation condition (i.e., $S_r = 100\%$) and S_r of 97%, 95%, 91%, 86%, 82%. Experimental data allowed defining the liquefaction resistance curves (LRC) of each S_r . The LRC exhibited a linear trend in the $\text{CSR} : \log N_L$ space, which followed a power law. Table 6.2 summarises the average results of CTx and BE tests per S_r , including LRC, wave velocities (V_P and V_S) and Poisson's ratio (ν) representative for all S_r . From Figure 6.13 and also from the derived exponents of the power laws in Table 6.2, it can be observed that the liquefaction resistance curves for different degrees of saturation are nearly parallel. As expected, the lowest position corresponds to the results for $S_r = 100\%$, as also observed in studies carried out in fine poorly-graded sands (Banerjee et al., 2022; Mele et al., 2022). These results validated the improvement of cyclic liquefaction resistance induced by partial saturation.

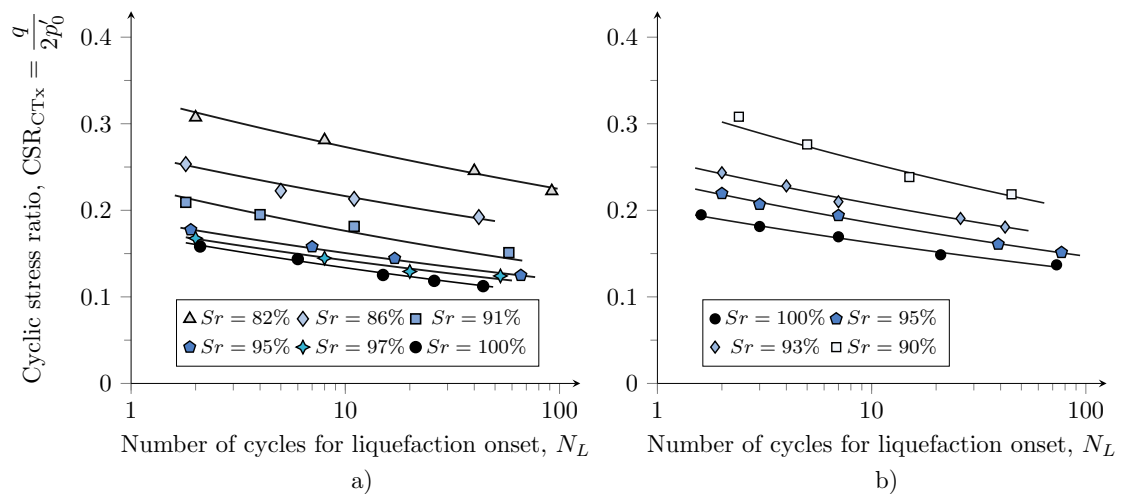


Figure 6.13: Liquefaction resistance curves for different S_r : a) test results under $Dr \pm 30\%$; b) test results under $Dr \pm 50\%$

Based on the observed parallel tendencies within the cyclic liquefaction resistance curves of TP-Lisbon sand for the testing conditions addressed in this study, a series of correlations between the intercept coefficient (a) and degree of saturation S_r were estimated to describe the evolution of liquefaction resistance with the change in S_r . Figure 6.14 presents the results of such an analysis. This figure reveals a good fitting between the a) and S_r for the two relative densities (Dr) investigated in the CTx testing. In Figure 6.14, it can be observed that the results with higher Dr are positioned at elevated points, confirming that the liquefaction resistance increases with the increment in Dr , as also observed by Giretti et al. (2018). Table

Table 6.2: Summary of average CTx and BE test results

Dr (%)	Sr (%)	Liquefaction resistance curve	V_P (m/s)	V_S (m/s)	$\frac{V_P}{V_S}$	ν
± 30	100	$CSR_{CTx} = 0.174(N_L)^{-0.114}$	1521	165	9.22	0.4949
	97	$CSR_{CTx} = 0.179(N_L)^{-0.101}$	1187	162	7.33	0.4908
	95	$CSR_{CTx} = 0.189(N_L)^{-0.101}$	803	172	4.67	0.4765
	91	$CSR_{CTx} = 0.229(N_L)^{-0.113}$	562	167	3.37	0.4518
	86	$CSR_{CTx} = 0.266(N_L)^{-0.089}$	470	164	2.87	0.4319
	82	$CSR_{CTx} = 0.322(N_L)^{-0.085}$	382	169	2.26	0.3783
± 50	100	$CSR_{CTx} = 0.202(N_L)^{-0.108}$	1532	182	8.42	0.4952
	95	$CSR_{CTx} = 0.234(N_L)^{-0.101}$	723	184	4.12	0.4653
	93	$CSR_{CTx} = 0.259(N_L)^{-0.096}$	641	183	3.51	0.4546
	90	$CSR_{CTx} = 0.325(N_L)^{-0.108}$	541	187	2.87	0.4318

6.3 presents the models with the best fitting describing the relationships between the intercept coefficient and degree of saturation.

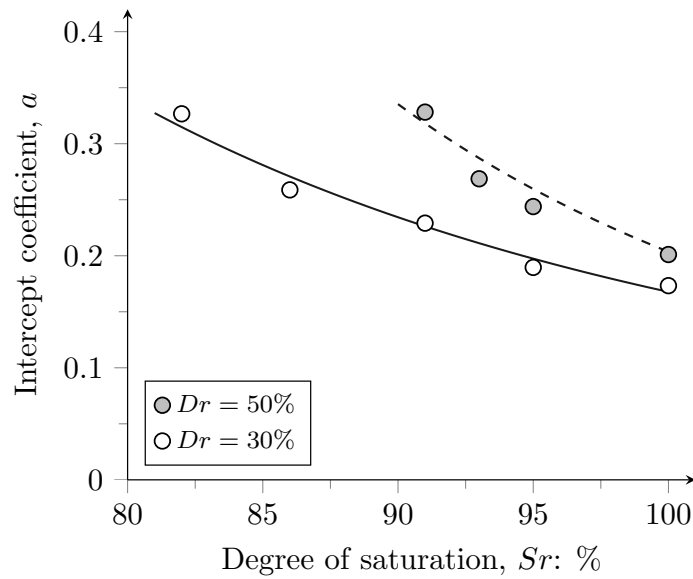


Figure 6.14: Relationships between intercept coefficient and degree of saturation

Table 6.3: Best fitting between intercept coefficient and degree of saturations

Sand	Dr (%)	Best fitting
TP-Lisbon	30	$a = (3.7 \times 10^5)Sr^{-3.172}$
	50	$a = (6.0 \times 10^8)Sr^{-4.735}$

The results in Figure 6.14 and Table 6.3 confirm the relation between the evolution of cyclic strength curves with Sr . However, the results representation of Figure 6.14 does not quantitatively characterise the liquefaction resistance improvement

provided by IPS. In order to address this limitation, the CTx and BE test results will be subjected to further interpretation in the next section, utilising an approach that allows a better characterisation of the liquefaction resistance increment of TP-Lisbon sand.

6.4 Analysis of liquefaction resistance improvement by wave-based approaches

The liquefaction resistance can be correlated with elastic wave velocities (Andrus and Stokoe, 2000; Tsukamoto et al., 2002; Zhou and Chen, 2007; Hossain et al., 2013; Kayen et al., 2013; Porcino and Tomasello, 2019; Kiyota et al., 2019). Therefore, the application of wave-based approaches provides alternative methods to assess the improvement of cyclic liquefaction induced by partial saturation. For this purpose, two methods were implemented in this study. The first method correlates the cyclic stress ratio with V_S measurements (CEN, 2010). CSR covered the CTx results referred in Figure 6.13 for each Sr . The second method correlates the liquefaction resistance ratio (LRR) with V_P measurements. The LRR was estimated by:

$$\text{LRR} = \frac{\text{CSR}_{\text{part}}}{\text{CSR}_{\text{sat}}} \quad (6.2)$$

where CSR_{part} is the cyclic stress ratio in partially saturated conditions, and CSR_{sat} is the cyclic stress ratio in fully saturated conditions. These values were estimated by replacing N_L in the liquefaction resistance curve the ratio between the CSR for each Sr over the CSR for fully saturated conditions (i.e. $Sr = 100\%$).

The analysis of liquefaction resistance involving the correlation between CRR_{20} and V_S was carried out by applying a V_S normalisation in terms of the overburden stress, as follows:

$$V_{S1} = V_S \left(\frac{\text{Pa}}{p'_0} \right)^{0.25} \quad (6.3)$$

where V_{S1} represents the overburden stress-corrected S-wave velocity; and Pa is the atmospheric pressure, typically 100 kPa.

The experimental results were contrasted against models reported in the literature,

namely Andrus and Stokoe (2000); Zhou and Chen (2007); Kayen et al. (2013). All estimations were performed for sands with FC lower than 5% and considering an earthquake magnitude of $M_w = 7.5$, which corresponds to the local seismic action type 1 of Lisbon (CEN, 2010). Figure 6.15 presents the results of the correlation between CSR_{CTx} and V_{S1} of TP-Lisbon sand. This figure includes the experimental results for the studied Sr and the boundaries of liquefaction and non-liquefaction for clean sands reported in the literature (Andrus and Stokoe, 2000; Zhou and Chen, 2007; Kayen et al., 2013).

The results of Figure 6.15 indicate that CSR_{CTx} increased with the decrease in Sr for similar V_{S1} (near the threshold value of 200 m/s). Besides, from Figure 6.15, it can be observed that the CSR_{CTx} fitted with all liquefaction boundaries for $Sr \leq 90\%$. On the contrary, the comparison between the boundaries and the experimental results for $Sr > 91\%$ are not suitable to assess the improvement of liquefaction resistance induced by partial saturation of TP-Lisbon sand. Therefore, the correlation between CSR_{CTx} and V_{S1} did not describe well the improvement of cyclic liquefaction resistance induced by partial saturation since V_S is not affected by the changes in Sr , especially for partially saturated conditions, above the air-entry value.

Studies developed by Yoshimi et al. (1989); Ishihara et al. (2001); Tsukamoto et al. (2002); Yang et al. (2004) have recognised that the use of V_P allows for a more suitable quantification of liquefaction resistance increase by inducing partial saturation than V_S . Such recommendation was attributed to the fact that V_S is more sensitive to suction, which changes the stress state of soils, than to the compressibility of pore-fluid –a fundamental component for the generation of the pore pressure build-up in sandy soils. Hence, an approach based on the liquefaction resistance ratio (LRR) was applied to describe the liquefaction resistance for different Sr as a function of V_P . The LRR was estimated by computing the ratio between the CSR_{CTx} applied during CTx testing in partially saturated conditions and the CSR_{CTx} derived for fully saturated conditions using the CSR_{CTx} derived from experimental results reported in Table 2.3), where N_L corresponds to the number of cycles to liquefaction measured in the partially saturated CTx tests. Hence, the normalised cyclic strength for partially saturated tests tends to yield values higher than one. Figure 6.16 presents the variation of LRR as a function of V_P . The results of Figure 6.16 show an increment in LRR with the decreasing of V_P (an indicator of Sr), demonstrating the suitability of this approach in predicting and quantifying the performance of IPS in

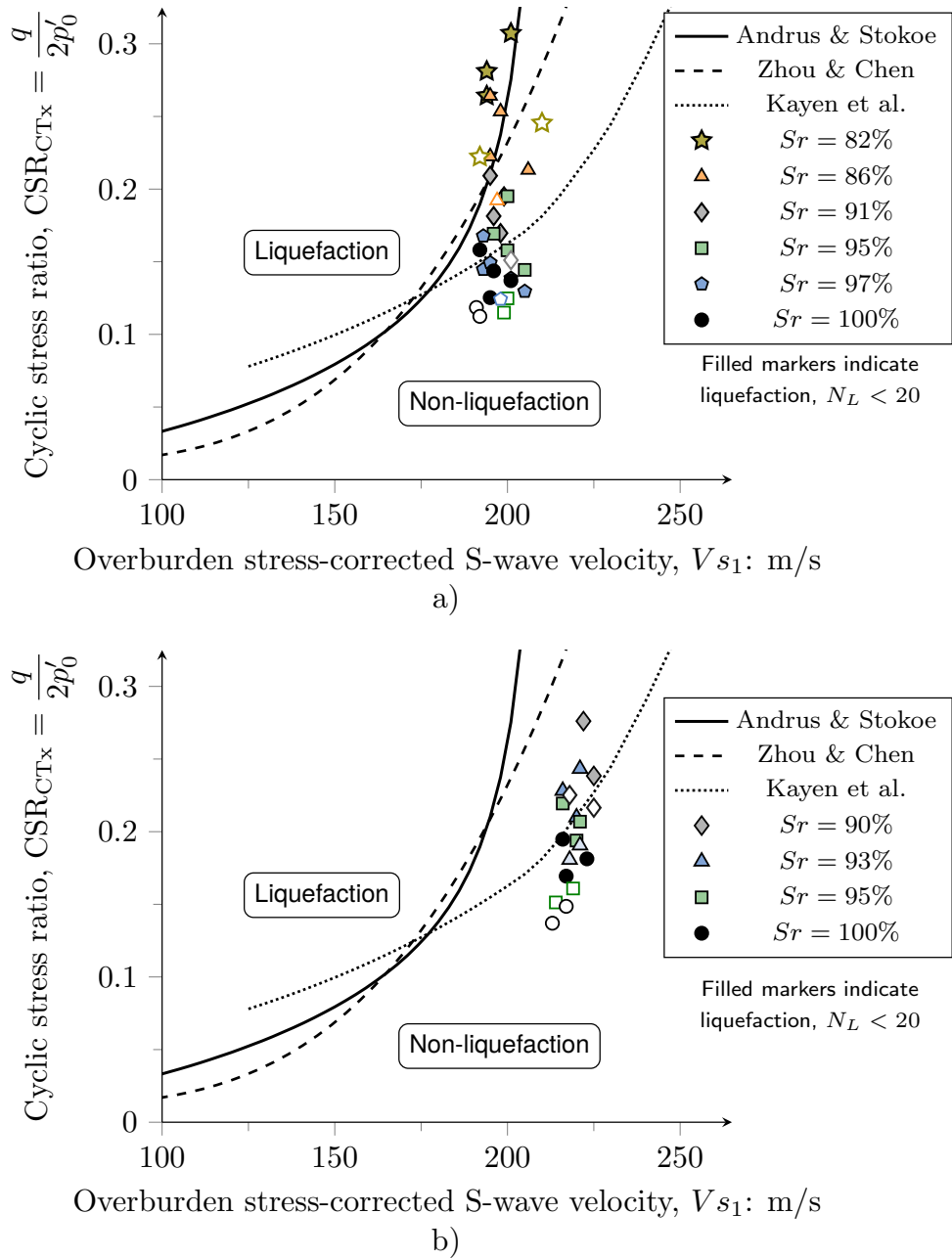


Figure 6.15: $CSR_{CTx} : V_{s1}$ relationship for different Sr : a) test results under $Dr \pm 30\%$; b) test results under $Dr \pm 50\%$

the liquefaction resistance improvement.

The results of P-wave-based approach allow a better quantification of the improvement of liquefaction resistance by inducing partial saturation than V_S since P-wave propagation depends on the compressibility of pore-fluid in sands. Hence, an approach to assess the liquefaction resistance as a function of V_P was applied to analyse the improvement induced by varying the degree of saturation. Figure 6.17 presents the relationship between LRR_{20} and V_P for TP-Lisbon sand and other Japanese liquefiable sands (namely Koshigaya, Niigata and Toyoura sands), and compares the experimental data against a non-linear regression model proposed by Hossain et al. (2013):

$$LRR_{20} = 0.95 + \exp^{[2-1.95 \ln(V_P/100-1.3)]} \quad (6.4)$$

The non-linear model of Equation 6.4 was obtained with a correlation coefficient of 0.85 for a confidence interval of 95%. Notwithstanding, this model was limited for V_P until 1400 m/s since the authors indicated that more complex regression equations are required to describe LRR_{20} , considering $LRR_{20} = 1$ for $V_P > 1400$ m/s. Since the model proposed by Hossain et al. (2013) was obtained by a non-linear regression correlation, it was adapted for the experimental data of TP-Lisbon sand, reporting a correlation coefficient of 0.97. Equation 6.5 describes the $LRR_{20} : V_P$ relationship proposed herein. Nevertheless, Equation 6.5 was limited for $V_P < 1480$ m/s due to V_P results higher of such a value corresponds to fully saturated conditions, where the P-wave is propagated through the water, as demonstrated in Figure 6.17, where for V_P values higher than 1480 m/s, LRR_{20} is 1.

$$LRR_{20} = 0.97 + \exp^{[1.9-2.1 \ln(V_P/100-1.3)]} \quad (6.5)$$

The results of Figure 6.17 exhibit a good agreement between experimental data and non-linear models, showing minor differences between the model proposed in this study and the model proposed by Hossain et al. (2013). Therefore, these comparisons have demonstrated that the P-wave-based approach provided a reliable estimation of the liquefaction resistance improvement induced by partial saturation of TP-Lisbon sand. However, studies carried out by numerous authors Kiyota et al. (2019); Porcino and Tomasello (2019); Viana da Fonseca et al. (2015) have demonstrated

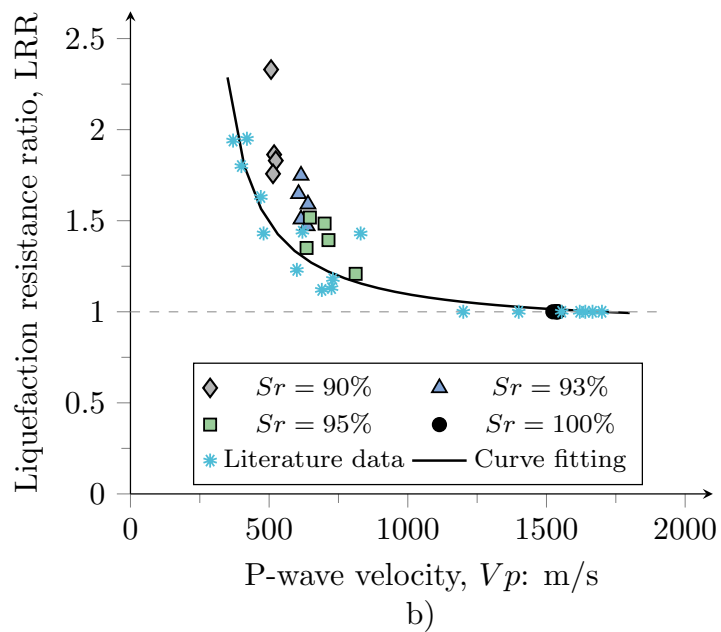
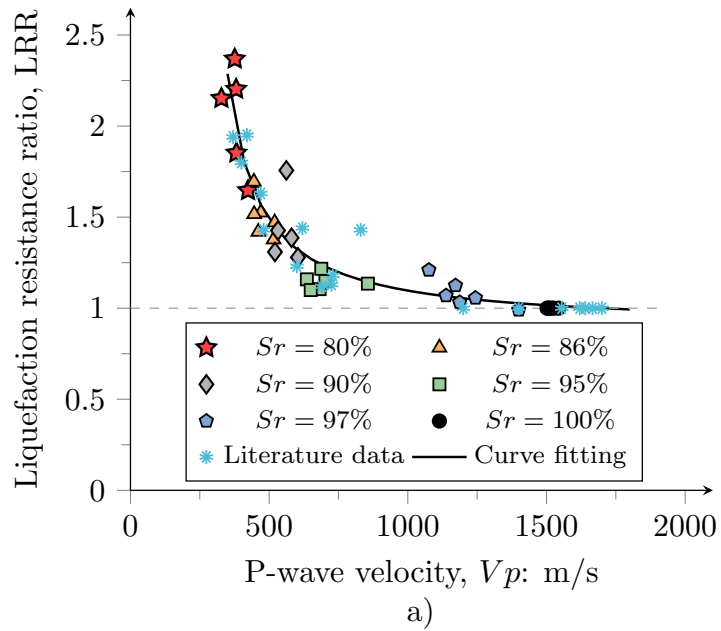


Figure 6.16: Liquefaction resistance ratio as a function of V_P for different S_r in TP-Lisbon sand: a) test results under $Dr \pm 30\%$; b) test results under $Dr \pm 50\%$

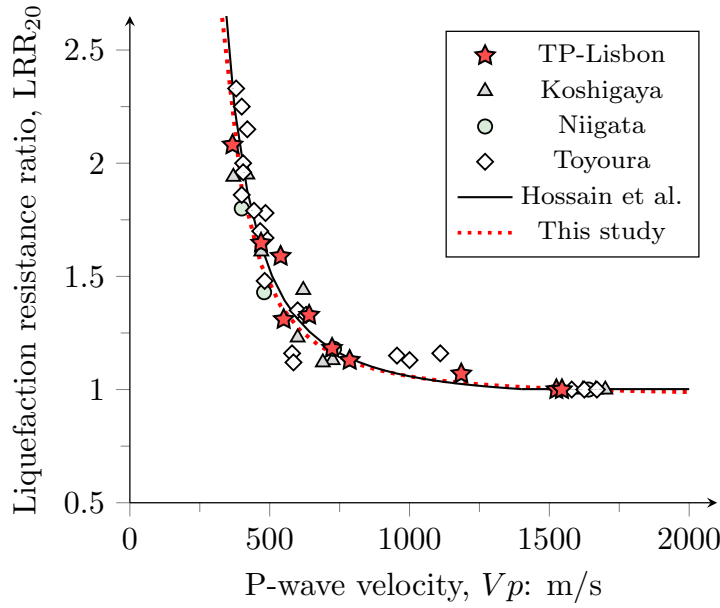


Figure 6.17: Normalised cyclic strength ratio as a function of V_P

that liquefaction resistance is highly affected by Dr . In this case and under the same confinement, the liquefaction resistance of dense sands is higher than loose sands, as demonstrated in Figure 5.8. The effect of Dr on soil behaviour can be described by the V_S of the soil (Yamashita et al., 2009). Hence, a model based on the algebraic manipulation of Biot's theory for describing the relationship between LRR_{20} and V_P/V_S is proposed in Equation 6.6.

$$LRR_{20} = \exp \left[\frac{\alpha \cdot R}{\left(\frac{V_P}{V_S}\right)^2 + \frac{4}{3}} \right] \quad (6.6)$$

where α is the ratio between V_P and V_S in dry conditions; and R is a parameter dependent on the Poisson's ratio, ν , in dry conditions using (Yang et al., 2004):

$$R = \frac{2(1 + \nu)}{3(1 - 2\nu)} \quad (6.7)$$

In this study, the ν value in dry conditions was computed using a relation between wave velocities (see Equation 2.29), where the values of V_P and V_S were estimated utilising their stress-dependency law referred in Table 4.5. Figure 6.18 shows the

results of the $LRR_{20} : V_P/V_S$ relationship for TP-Lisbon sand and the liquefiable Japanese sands to validate the model proposed in Equation 6.2. The R parameter and ν values for TP-Lisbon sand were obtained from the BE test results reported in Figure 4.24. For the case of the liquefiable Japanese sands, these values were obtained by analysing the results reported by [Ishihara et al. \(2001\)](#); [Tsukamoto et al. \(2002\)](#); [Nakazawa et al. \(2004\)](#). Besides, this figure compares all experimental data against the regression curve by [Hossain et al. \(2013\)](#).

Figure 6.18 reveals that this approach is suitable for analysing and quantifying the improvement of cyclic liquefaction resistance induced by partial saturation in different sands. The model expressed in Equation 6.6 provided a reliable liquefaction resistance assessment of partially saturated sands, which was validated by the good agreement between experimental data and the results of the model computation. This agreement can be attributed to the incorporation of the effects of degree of saturation and small-strain stiffness on liquefaction resistance by integrating both V_P and V_S . The application of this wave-based approach indicated that it is suitable for different Dr , as demonstrated by examining the data of Toyoura sand.

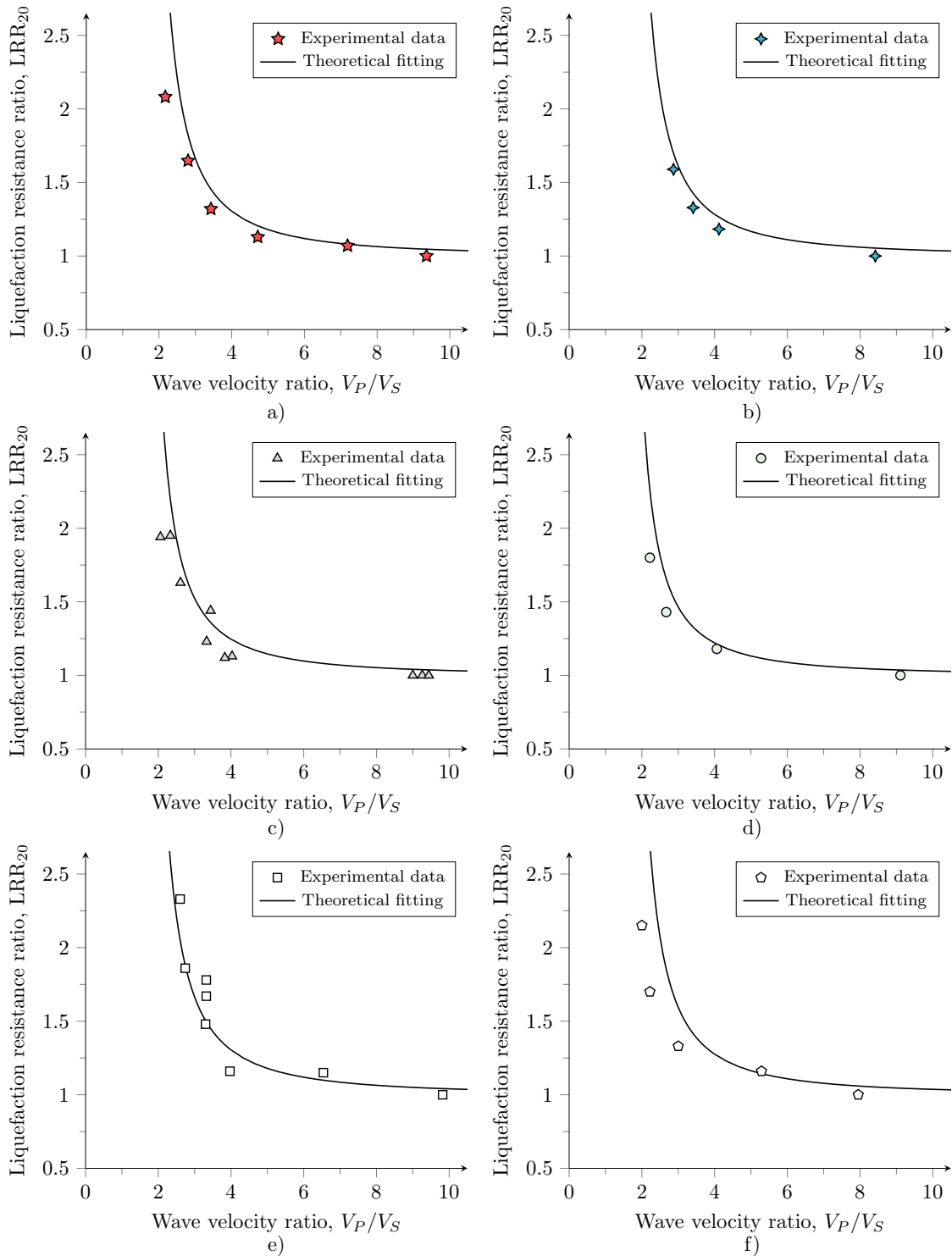


Figure 6.18: $LRR_{20} : V_P$ relationship for different liquefiable soils: a) TP-Lisbon sand $-Dr = 30\%$; b) TP-Lisbon sand $-Dr = 50\%$; c) Koshigaya sand; d) Niigata sand; e) Toyoura sand $-Dr = 40\%$; f) Toyoura sand $-Dr = 70\%$

6.5 Key findings

This chapter presented the results of a series of cyclic triaxial tests of TP-Lisbon sand in partially saturated conditions. The degree of saturation was monitored by P-wave measurements and interpreted in the light of wave propagation theory in fluid-saturated media (Biot, 1956a,b). The experimental results indicate that the liquefaction resistance of TP-Lisbon sand increases as the degree of saturation decreases. The wave-based approaches estimated the liquefaction resistance improvement. From the obtained results, the following findings can be drawn:

- The measurement of V_P allows for a more accurate estimation of the Sr during element testing, mainly in partially saturated conditions of the soil (i.e. $Sr > 75\%$) than B -value measurements. These differences are attributed to the effects of the volumetric compressibility of the fluid on the propagation of P-wave in granular media and pore pressure build-up. These factors are highly affected by occluded air bubbles, as validated by theoretical predictions derived from applying the wave propagation theory of fluid-saturated media (Biot, 1956a,b).
- Cyclic triaxial tests showed that the liquefaction resistance of TP-Lisbon increases with the decrease in Sr . The liquefaction resistance curves outlined for the examined Sr exhibited parallel trends, where the lowest position was observed for $Sr = 100\%$. Despite the different Sr , all tests reported pore pressure coefficients higher than 0.99. These coefficients demonstrated that the liquefaction onset in partially saturated sands is triggered by pore pressure build-up rather than accumulated strains. However, differences in axial strain were observed for the examined Sr , showing that the highest strains obtained for the tests in fully saturated conditions.
- The analysis of shear wave velocities before cyclic loading revealed that this parameter is unsuitable for the liquefaction resistance assessment when varying the degree of saturation. Despite the increment in CSR to trigger liquefaction in partially saturated sands, the experimental data corresponding to the critical condition for earthquake-induced liquefaction ($N_L < 20$) did not match the theoretical boundary proposed by Andrus and Stokoe (2000) for Sr above 88%. These effects have been attributed to the presence of occluded air bubbles in the pore-fluid, which the V_S cannot realistically detect. However, for a degree of saturation of 100% and different relative densities, the S-wave

approach showed a good agreement with experimental data. Such an agreement was attributed to the capacity of S-wave velocity to detect the changes in porosity and initial soil stiffness, which complement the characterisation of liquefaction resistance by estimating the soil state.

- In turn, the liquefaction resistance ratio as a function of P-wave velocity provided a reliable approach to describe the increase of liquefaction resistance by varying the degree of saturation. Hence, this approach is considered appropriate for comparing the liquefaction resistance at different degrees of saturation. The experimental results fit well with a non-linear regression model. This model indicates that, for V_P lower than 1400 m/s, corresponding to degrees of saturation below 98%, the liquefaction resistance of TP-Lisbon sand can be effectively increased. In turn, for V_P lower than 600 m/s, the liquefaction resistance ratio of TP-Lisbon sand increased sharply, achieving values that doubled the liquefaction resistance in fully saturated conditions.

Chapter 7

Site response of TP-Lisbon sand for different S_r by centrifuge testing

A version with the main content of this chapter has been submitted for publication to *Journal of Geotechnical and Geoenvironmental Engineering*: Molina-Gómez, F.; Caicedo, B; Monroy, J.; Carrilho Gomes, R.; Viana da Fonseca A. Site response assessment of shallow sandy soil deposits with different degrees of saturation by centrifuge tests.

7.1 Outline

This chapter presents the results of an experimental program focused on analysing the site response of shallow sandy soil deposits with different degrees of saturation using a novel testing approach. The partial saturation was induced by desaturating the soil using the suction plates method. The approach integrates a micro shaking table and geotechnical centrifuge apparatuses to induce a series of in-flight cyclic loading with a wide frequency range using a micro shaking table. The soil samples were tested in a laminar box, which deforms laterally at very low friction, accurately replicating the seismic motion during testing. The approach introduced herein allows estimating the amplification factor spectra for Peak Ground Acceleration and volumetric strains of the soil for various depths with different degrees of saturation — including the dry, partially and fully saturated conditions. In turn, the results revealed important effects of the degree of saturation on the frequency amplification spectrum relevant to the performance and design of geotechnical structures.

7.2 Features of site response in partially saturated sands

Earthquakes generate seismic waves in the bedrock, propagating through the soil deposit until the ground surface. The composition and distribution of the soil deposit (i.e. layering) influence the free-field seismic response since the distortion generated in the bedrock can be altered in terms of intensity, frequency content and duration as it travels through the overlaying soil (Rayhani and El Naggar, 2008). This transition is commonly evaluated using ‘site response analysis’, which is fundamental in the soil-structure systems assessment. Therefore, local site conditions (i.e. soil stiffness, damping, relative density, unit weight and plasticity) have important effects on the site response (Borcherdt, 1994; Afacan et al., 2014; Quintero et al., 2023).

The degree of saturation (S_r) affects the site response since it affects the wave propagation, whether the soil is fully saturated, partially saturated, unsaturated or dry (Leong and Cheng, 2016; Gu et al., 2021). These effects can be attributed to variations in the stress state caused by inter-particle suction and changes in soil compressibility for different S_r , affecting the stiffness and damping of the soil (Kumar and Madhusudhan, 2012; Hoyos et al., 2015). As a result, seismic wave propagation mechanisms may vary along partially saturated soil layers, leading to a different site response (Yang and Sato, 2001; Ghayoomi et al., 2011). Although the differences in soil behaviour under various degrees of saturation regarding cyclic response have been identified through element testing, only a few studies have addressed the differences in site response for different degrees of saturation (S_r).

Partial saturation in sandy soils with low range suction level (e.g. $\Psi < 10$ kPa) resulted in higher amplifications, while in silty soils with high suction range (e.g. $\Psi > 70$ kPa), the partial saturation led to a lower amplification and lateral deformations in comparison with those of dry soil layers (Mirshekari and Ghayoomi, 2017). Besides, S_r affects the natural frequency and Peak Ground Acceleration (PGA) in soil layers composed of granular materials subjected to earthquake loading (Yang, 2006). S_r also influence the settlements on the ground surface, as observed by Ghayoomi et al. (2013); Zeybek and Madabhushi (2020). These authors conducted a series of centrifuge testing in F75 Ottawa sand and Huston HN31 sand, respectively, to assess the earthquake-induced settlement under diverse S_r . These authors identified that the larger surface settlement occurred in the middle range of studied S_r .

Therefore, there is an influence of Sr on the site response of sandy soil deposits. However, these effects have yet to be studied in detail due to a lack of in situ data and limited experimental capabilities to evaluate site response under these specific conditions. This chapter describes the development of a new experimental approach to characterise the site response of a sandy soil deposit representative of the Terreiro do Paço site under different Sr conditions. The approach is based on a novel procedure using shaking table tests in the geotechnical centrifuge, allowing a comprehensive analysis of Sr effects on site response by applying a cyclic loading in-flight with a wide frequency range.

7.3 Experimental procedures

7.3.1 Centrifuge testing

The centrifuge testing aims to model of geotechnical problems in a reduced-scale model $1/N$ by generating an acceleration field that is N times Earth's gravity (Caicedo and Thorel, 2014). When the centrifuge model is subjected to an inertial acceleration field of N times Earth's gravity, the vertical stress at depth, h_m , will be identical to that in the corresponding prototype at depth, h_p (see Equation 7.1).

$$h_p = N \cdot h_m \quad (7.1)$$

The change in Earth's gravity produces an increment of the soil stress state, which affects the behaviour of the model. Therefore, the centrifuge test results of such a model are compared with the prototype response by applying the scaling factors. The gravity is increased by the same geometric factor N relative to the normal Earth's gravity field, which is $1g$ (Taylor, 1995; Madabhushi, 2014). The mini geotechnical centrifuge of Universidad de los Andes can increase the inertial radial acceleration field up to $400g$; that is, it allows for conducting tests 400 times stronger than the gravity of Earth. Table 7.1 presents the Scaling factors for centrifuge modelling.

Table 7.1: Scaling factors for centrifuge modelling (Taylor, 1995; Madabhushi, 2014)

Type of event	Parameter	Scaling law (model/prototype)	Units
All events	Stress	1	N/m ²
	Strain	1	-
	Length	1/ N	m
	Time (diffuse)	1/ N	s
Dynamic events	Frequency	N	1/s
	Velocity	1	m/s
	Acceleration	N	1/s ²
	Time	1/ N^2	s
	Displacement	1/ N	m

In this research, numerous centrifuge tests were performed to assess the site response under different Sr under effective centrifuge accelerations of 30g, 60g and 80g to induce stress states representative of the soil profile at the Terreiro do Paço site. The centrifuge testing was carried out with the same setup and instrumentation described in section 3.3.5. Therefore, cyclic loading was applied by generating continuous sinusoidal signals with frequencies between 20 Hz and 600 Hz. The amplitude of the signal was produced by a fixed voltage of 0.5 V generated by the function generator, which was amplified by the ‘Cedrat’ device. This amplitude induced the initial displacements at the shaking table base. However, these displacements varied with the signal frequency and effective centrifuge acceleration. The acceleration \ddot{u} and displacements (u) induced in the system can be expressed by the simple harmonic motion model, using Equations 7.2 and 7.3, respectively.

$$u = u(0) \sin f t \quad (7.2)$$

$$\ddot{u} = \frac{\partial^2 u}{\partial t^2} = -f^2 u(0) \sin f t \quad (7.3)$$

where $u(0)$ is the initial displacement (controlled by the input voltage), f represents the input frequency applied by the Piezoelectric actuator, and t is the time.

The effects of the degree of saturation (Sr) on Site response analysis were assessed using remoulded soil samples of TP-Lisbon sand. The samples were prepared using the air pluviation method, which allowed for the remoulding of samples with a height of approximately 72 mm, corresponding to the height of the accelerometer located

at the top of the micro shaking table. A dry soil mass of 420 g per sample was used to achieve a dry density (ρ_{dry}) of 1.4 g/cm^3 , equivalent to a relative density (Dr) of 30%. The soil remoulding was carried out directly in the centrifuge apparatus to avoid further vibrations during the transport of the equipment, which could compact (or densify) the soil sample. Such a handling procedure allows for the preservation of Dr and confirms the versatility of soil testing using the micro shaking table and mini centrifuge at UniAndes.

On the other hand, seismic wave velocities were measured in a series of parallel in-flight tests using a container equipped with piezoelectric transducers to conduct Bender Elements (BE) tests. This container has the exact internal dimensions as the laminar box to obtain a reliable characterisation of soil response during centrifuge testing by both containers. The setup for BE testing covers a pair of piezoelectric transducers with 6.4 mm length and 13.2 mm width, a function generator (Protek B8000FD), an output amplifier (Cedrat LC75C) and an oscilloscope (Tektronix TBS 1102). The signals were acquired directly from the oscilloscope using a pen drive after each wave measurement. Figure 7.1 presents the setup for dynamic centrifuge and in-flight BE testing at UniAndes.

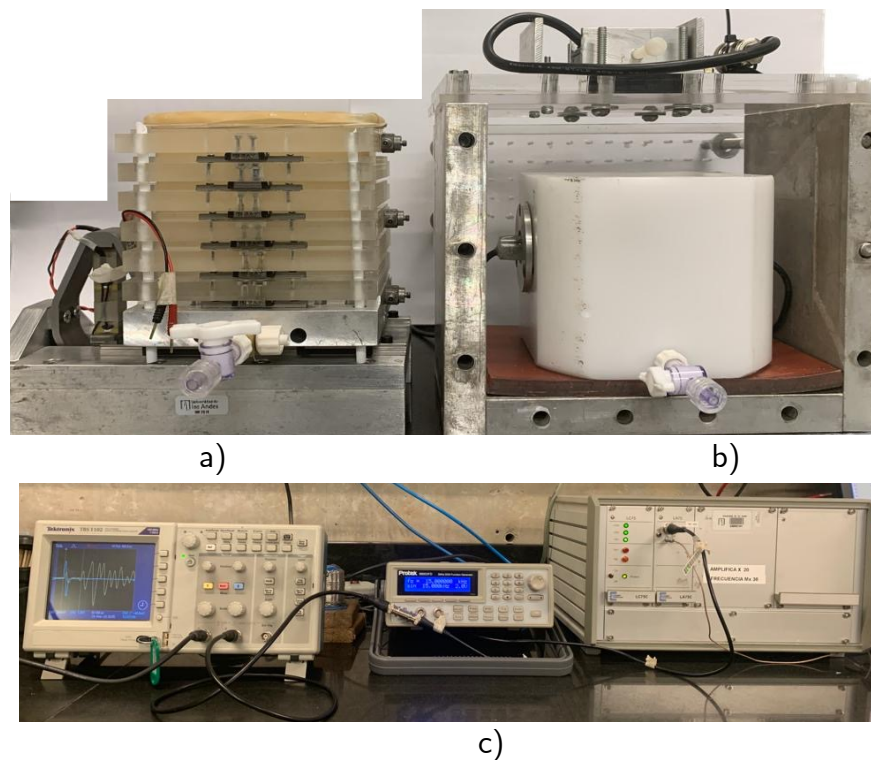


Figure 7.1: Centrifuge testing in-flight setup: a) Micro shaking table; b) Container with piezoelectric transducers; c) Oscilloscope, Function generator and Amplifier

7.3.2 Saturation and induction of partial saturation

The saturation process involved flushing 300 cm³ of deaired and demineralised water from the bottom to the soil surface. To maintain a low hydraulic gradient, the water level was positioned 5 cm above the container top (see Figure 7.2). The excess water was carefully collected using a syringe to prevent damage to the piezoelectric actuator and accelerometers during this process. Moreover, the partial saturation of the soil was induced by applying a fixed suction using the suction plate method. The suction level was controlled by adjusting the height of the suction plate below the soil model, as illustrated in Figure 7.3.

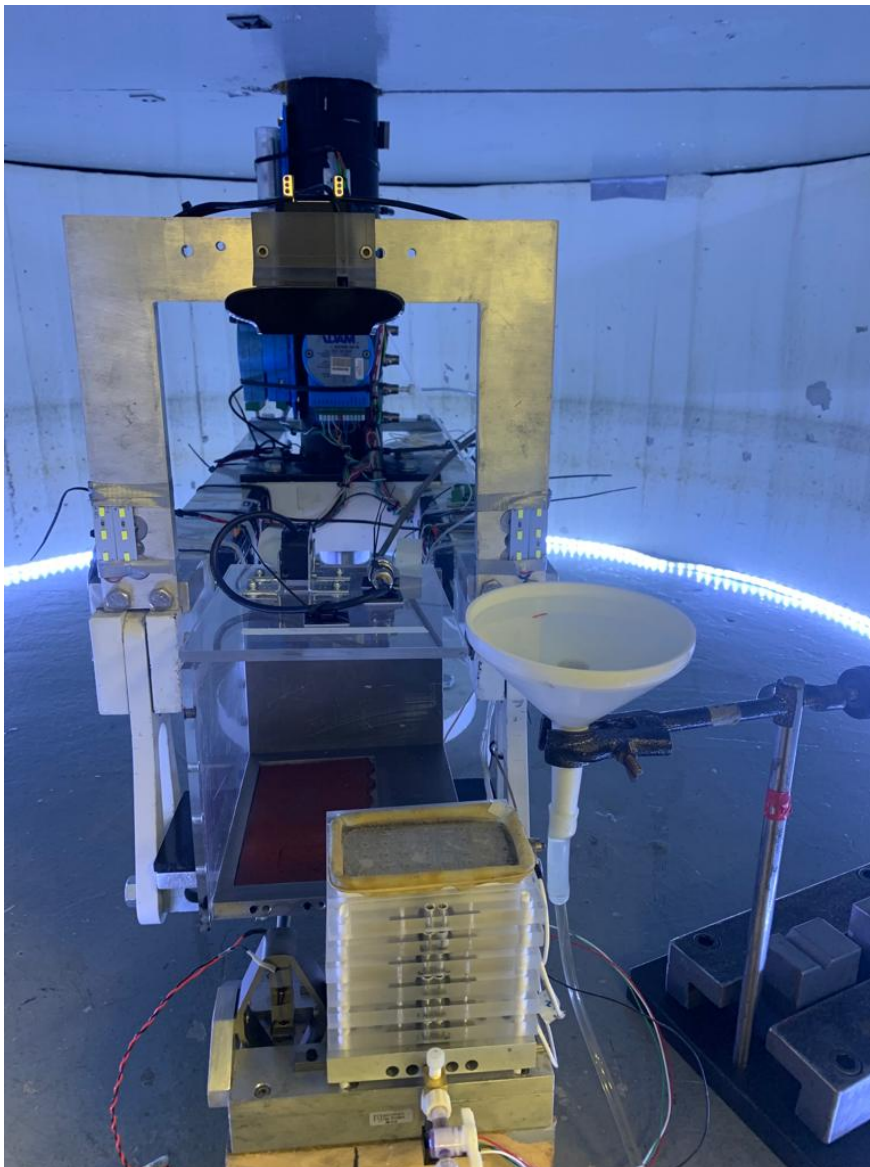


Figure 7.2: Illustration of saturation process in the geotechnical centrifuge



Figure 7.3: Illustration of the induced partial saturation process in the geotechnical centrifuge by soil desaturation

The induction of partial saturation was carried out by applying suctions (Ψ) equal to 2 and 3 kPa. The Ψ were obtained by positioning the suction plate at 20 cm and 30 cm height. The combination of soil remoulding, sample saturation, and induced partial saturation, the site response allowed for the assessment of S_r of 100%, 87%, 71% and 0%. The S_r values were confirmed by measuring the sample volume and water content at the beginning and end of each test, resulting in a difference of approximately 2% for all tests, where the lower value corresponded to the S_r at end-of-test.

The applied suction was confirmed by comparing the S_r of testing against the soil water characteristic curve (SWCC) derived using the model proposed by Fredlund and Xing (1994) for TP-Lisbon sand under $Dr = 30\%$. Figure 7.4 presents the S_r obtained by inducing partial saturation and their comparison with the SWCC derived using the model of Fredlund and Xing (1994). This figure indicates the variability in the volumetric water content (ω_w), showing a low variation for the S_r values studied in this research.

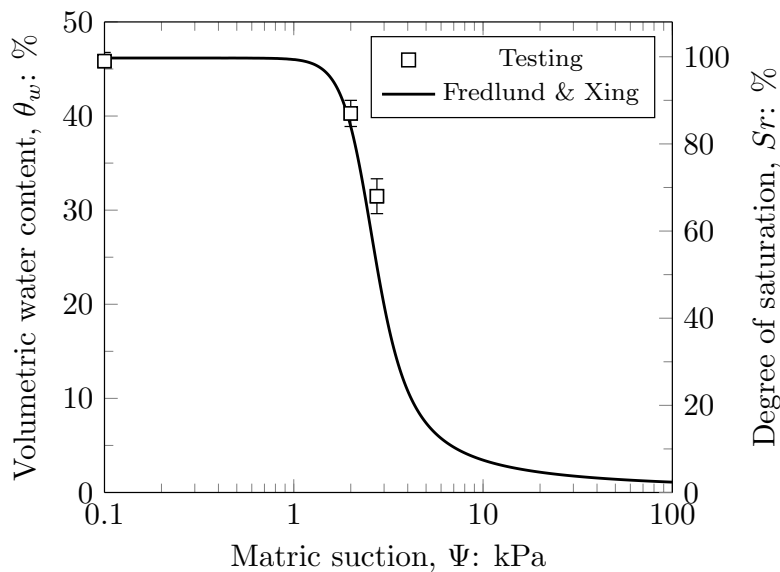


Figure 7.4: Results of the degree of saturation after induced partial saturation compared against the soil water characteristic curve

The S_r results were confirmed by P-wave velocity (V_P) measurements through BE tests. In these tests, P-wave was generated by applying input sine-wave pulses with four input frequencies ranging from 50 to 150 kHz, as described in Section 6.2.1. These measurements were contrasted against the wave propagation theory of fluid-saturated media (Biot, 1956a,b). Figure 7.5 presents the results of the relationship between V_P and S_r obtained during centrifuge testing. The results in Figure 7.5 confirm the efficiency of the experimental method to induce partial saturation in the soil samples.

7.4 Evaluation of stress-strain behaviour

The stress-strain behaviour of the soil during centrifuge-shaking-table (C-ST) testing was evaluated by estimating the horizontal displacements ($\delta_H = u$) and shear stresses (τ) induced by the cyclic loading. The motion of the laminar box was considered as

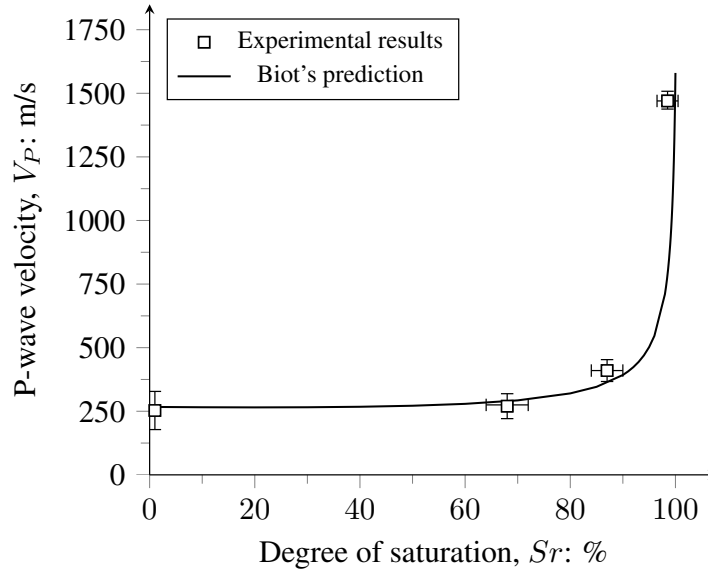


Figure 7.5: Variation of V_P as a function of S_r

the motion of a single degree of freedom (SDOF) system due to the linear constraints of this device. Therefore, the displacements from the acceleration records were calculated using the Duhamel integral:

$$u(t) = \frac{1}{m f_d} \int_0^t Q(\tau) e^{-\xi f(t-\tau)} \sin f_d(t-\tau) d\tau \quad (7.4)$$

Duhamel integral is complex to solve analytically, but it can be solved by the convolution integral using numerical methods (Kramer, 1996). Based on this method, u was estimated by finding the second integral of the acceleration (\ddot{u}). Equation 7.5 shows the numerical method for finding the first integral of \ddot{u} (i.e. the velocity, \dot{u}) and Equation 7.6 shows the method for estimating the second integral of \ddot{u} in a time interval Δt :

$$\Delta \dot{u} = \ddot{u}(\tau) \Delta t + \Delta \ddot{u}(\tau) \frac{\Delta t}{2} \quad (7.5)$$

$$\Delta u = \dot{u}(\tau) \Delta t + \Delta \dot{u}(\tau) \frac{\Delta t^2}{2} + \Delta \ddot{u}(\tau) \frac{\Delta t^2}{6} \quad (7.6)$$

Molina-Gómez et al. (2019) validated that the numerical convolution of the Duhamel integral provides a reliable estimate of u by comparing the numerical results with

displacements measured with a high-precision Eddy-Current transducer. From the u results at different depths Z (i.e. the base and top of the laminar box), the shear strains (γ) of the soil under cyclic loading were estimated as follows:

$$\gamma = \frac{\partial u}{\partial Z} \quad (7.7)$$

From Equation 7.7, the average shear strain at depth Z (γ_Z) can be calculated using:

$$\gamma_Z(t) = \frac{u_i - u_{i+1}}{\Delta Z_i + Z_{i+1}} \quad (7.8)$$

Assuming 1D wave propagation conditions in a medium with constant density (ρ), the shear stress τ caused by the horizontal cyclic load (S) in a time t can be described by:

$$\frac{\partial \tau}{\partial Z} = \rho \frac{\partial^2 S}{\partial t^2} \quad (7.9)$$

Zeghal and Elgamal (1994) proposed a simplified method to estimate τ by integrating the equation of an idealised 1-shear beam as:

$$\tau(z, t) = \int_0^Z \rho \ddot{u} \, dz \quad (7.10)$$

Equation 7.10 can be solved by numerical integration using:

$$\tau_i(t) = \sum_{k=0}^{i-1} \rho \frac{\ddot{u}_k + \ddot{u}_{k+1}}{2} \Delta Z_k \quad (7.11)$$

The procedure presented here for estimating the stress-strain behaviour by in-flight testing has also been applied by other authors in the analysis and characterisation of diverse soils (Rayhani and El Naggar, 2008; Turan et al., 2009; Afacan et al., 2014; Zeybek and Madabhushi, 2017). Moreover, this procedure allows for comparing experimental data and seismic loading, and offers valuable insights into predicting soil response during earthquakes through centrifuge testing. The results obtained in

the laboratory have practical implications for mitigating damages caused by seismic events, which contribute to hazard mitigation strategies and the design of resilient infrastructures.

The movement of the system corresponds to the configuration of a single degree of freedom (SDOF) due to the configuration restrictions of the shaking table and laminar box. As a result, the displacements during testing can be assumed to follow a linear horizontal pattern. At the same time, the cyclic loading imparted by the piezoelectric actuator on the soil can be considered as pure shear. Figure 7.6 gives an example of the vibration modes of the laminar box with the soil sample at three different frequencies: one before resonance, one at resonance, and one after resonance. These vibration modes were estimated using accelerometer measurements and equations 7.5 to 7.8. From Figures 7.6.a and 7.6.b, it can be observed that the displacement increases nearly linearly from the base to the top of the container, indicating the first vibration mode. After reaching resonance, the displacement at the middle and top of the laminar box move in opposite directions, indicating the system transition to the second vibration mode, as demonstrated in Figures 7.6.c.

Figure 7.7 shows the typical stress-strain behaviour during C-ST testing for different loading frequencies using hysteresis loops. These frequencies are model frequencies, not prototype frequencies; thus, the frequencies are not scaled. The analysis of the stress-strain behaviour indicates that the soil tested using the micro shaking table device in the geotechnical centrifuge is in the medium strain level, i.e. γ is in the range of 10^{-5} to 10^{-4} . This strain level is representative of wave propagation in earthquakes (Vucetic, 1994; Ishihara, 1996). The stress-strain behaviour observed in the tests covers the elastoplastic soil response. The shape of the hysteresis loops can confirm such a response, which is not linearly elastic.

Both γ and τ exhibit a progressive increase as the frequency (f) increases in the range from 20 Hz to 300 Hz. This observation highlights the influence of frequency on stress-strain behaviour. However, for frequencies higher than 300 Hz, both γ and τ decrease compared to the values observed at frequencies below 300 Hz. This decrease can be attributed to the deamplification of the pseudo-acceleration at these frequencies, as indicated by an amplification factor (AF) lower than 1 for $f > 300$ Hz. On the other hand, the hysteresis loops showed that the τ applied during the test was below 5 kPa, which corresponds to a low cyclic stress ratio (CSR) that does not lead to the onset of liquefaction under fully and partially saturated conditions at centrifuge accelerations of 30g, 60g and 80g.

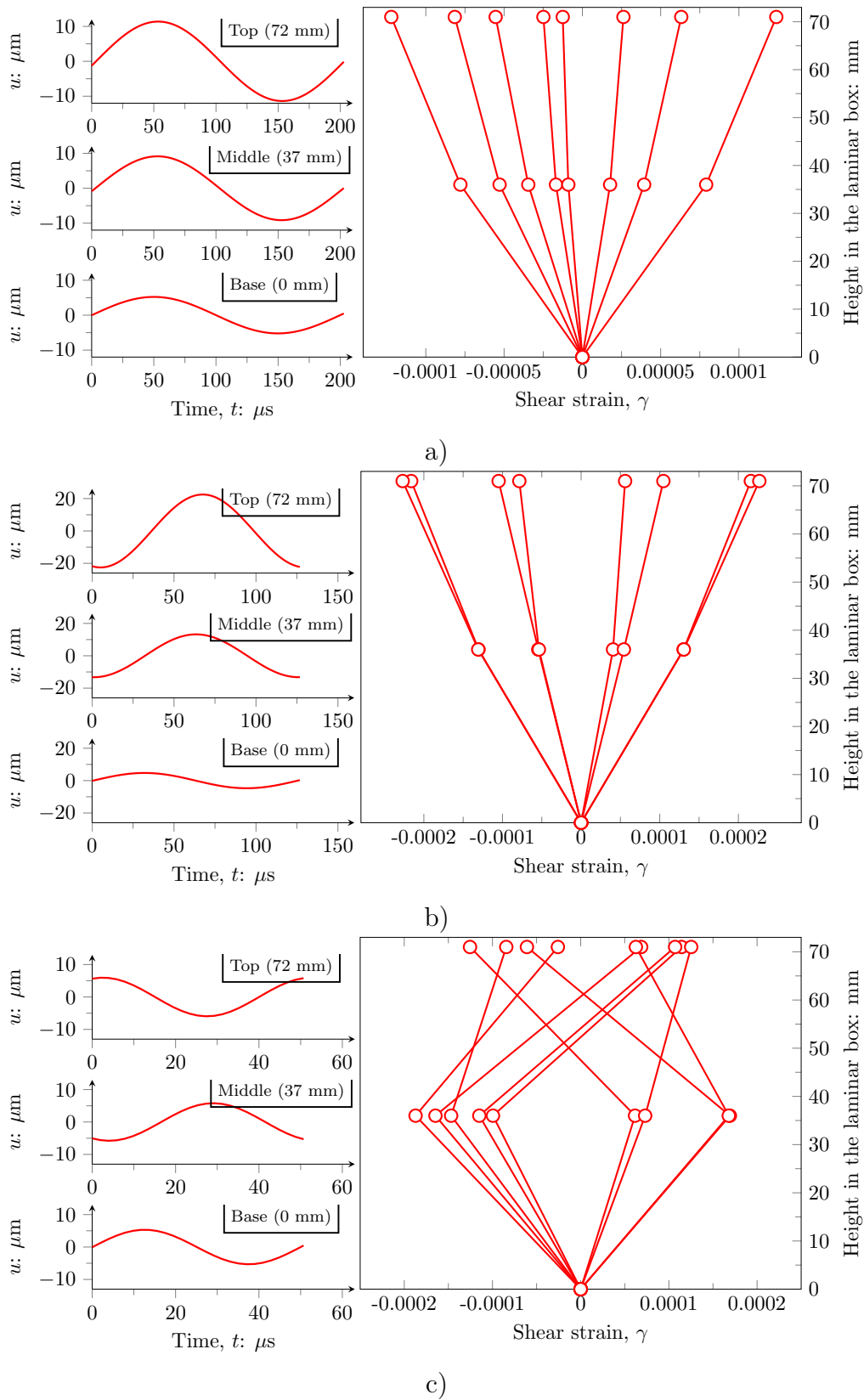


Figure 7.6: Vibration modes of the laminar box — results of a dry sample tested at 30 g: a) 50 Hz (before resonance); b) 100 Hz (resonance); c) 200 Hz (after resonance)

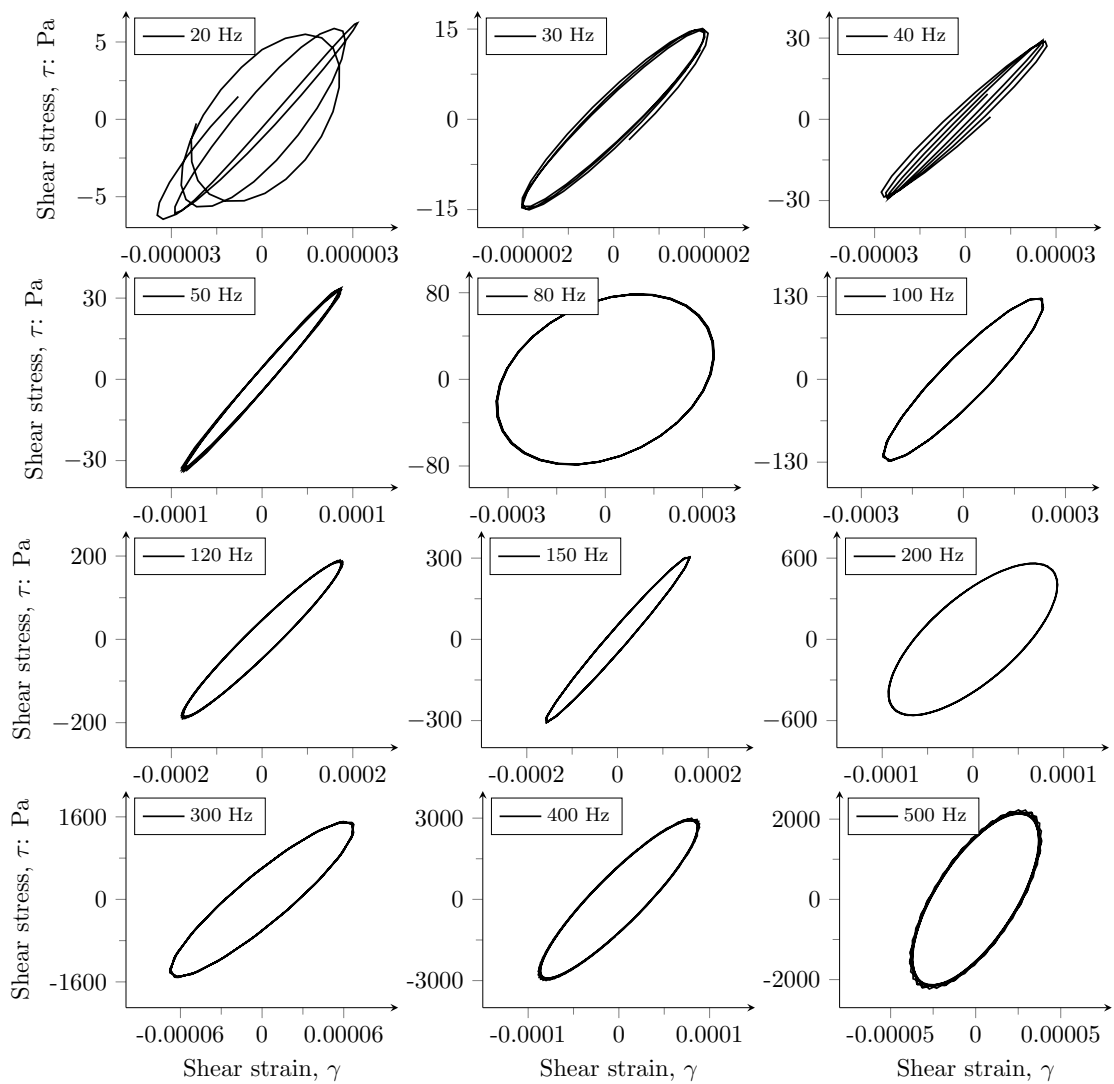


Figure 7.7: Stress-strain loops for different frequencies —results of a dry sample tested at 30 g

Figure 7.8 presents the results of the liquefaction susceptibility analysis using the state parameter (ψ) approach proposed in Section 5.4. The cyclic loading conditions of C-ST testing were assumed to be equivalent to the conditions of the direct simple shear tests. Therefore, the approach was performed by estimating the stress state of fully saturated tests (critical condition for the liquefaction onset) and the CSR induced by $\tau = 5$ kPa (maximum stress at $f > 500$ Hz). The results in Figure 7.8 confirm that the tests carried out under 30g, 60g and 80g do not cause the onset of liquefaction in the Sr studied herein. Values of pore pressure build-up (r_u) lower than 0.12 were registered during testing, revealing no liquefaction onset during the dynamic centrifuge testing, which may affect the site response results.

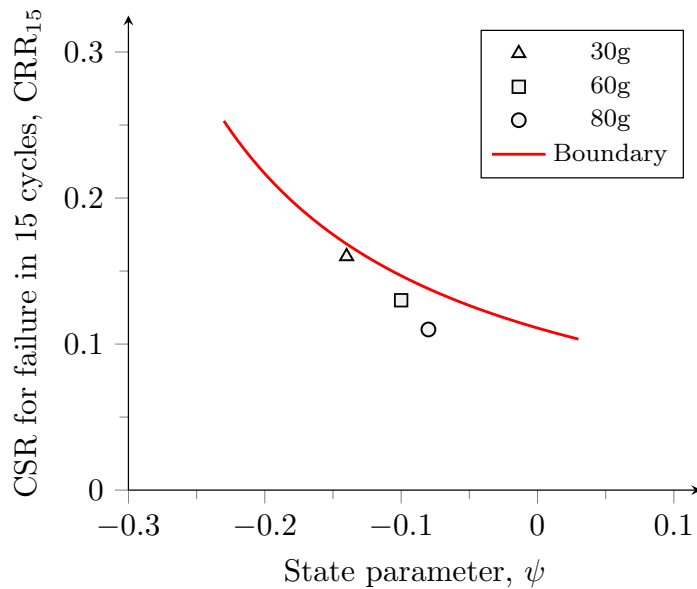


Figure 7.8: Relation of CSR failure and state parameter for different effective centrifuge accelerations under fully saturated conditions

The soil stiffness degrades as increases the cyclic loading (controlled by the input frequency and base acceleration) in the centrifuge-shaking-table (C-ST) tests. Hence, an analysis of the evolution of the stiffness degradation curves was carried out. This analysis covers an estimation of the normalised shear modulus (i.e. G/G_0) curves by computing the scant shear modulus of the stress-strain loops reported in the C-ST tests (Brennan et al., 2005). To validate the C-ST results, the normalised shear modulus curves were contrasted against the Resonant-Column (RC) referred in Figure 4.18. Both curves were also contrasted against the hyperbolic fitting proposed by Ishibashi and Zhang (1993) for sands, which is commonly used in engineering practice. This approach also helps to calibrate and perform numerical analyses of geotechnical structures subjected to seismic action, as demonstrated in previous

studies (Conti and Viggiani, 2012; Afacan et al., 2014). Figure 7.9 presents an example of the shear degradation curves by addressing the C-ST results conducted under an effective acceleration of 30g and the RC results under a level of 30 kPa, both for dry conditions. The experimental data in Figure 7.9 were contrasted with the hyperbolic fitting.

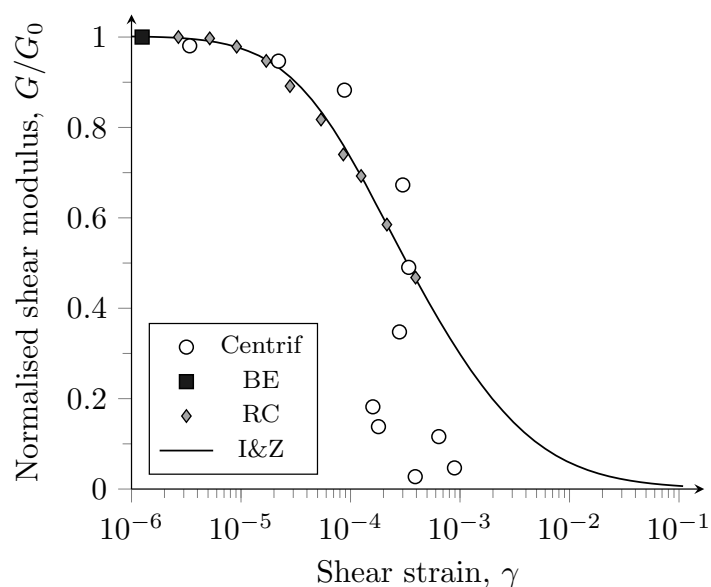


Figure 7.9: Stiffness degradation curves; comparison between C-ST tests against other testing methods and hyperbolic fitting by Ishibashi and Zhang (1993) for dry conditions and 30 kPa confinement

The results in Figure 7.9 show a good agreement between experimental data and hyperbolic fitting. The best adjustment is observed for the RC results and C-ST in the small strain range (i.e. $\gamma < 10^{-4}$). These results are comparable with the behaviour observed by Brennan et al. (2005); Conti and Viggiani (2012). The C-ST results for $\gamma < 10^{-4}$ exhibit scatter since the system reached the second vibration mode in this strain range. Consequently, this distortion generated in the second vibration mode leads to considerable variation in tests conducted after resonance. The C-ST results, coupled with the comparison against the RC tests and the hyperbolic fitting, provide a suitable estimation of soil stiffness subjected to the seismic action (or stress-strain combinations) induced during C-ST testing or when assessing site response using different frequencies. Nevertheless, it is important to note that this approach is best suited for predicting soil stiffness before the system resonance.

7.5 Site response analysis

The site response analysis by centrifuge testing aims to reproduce the soil behaviour of a prototype by a scaled model. The effective centrifuge accelerations applied in this study were 30g, 60g and 80g. This allows for evaluating sandy soil deposits with different depths by applying the scaling factors in Table 7.1. Table 7.2 summarises the prototype to model depths similitude used for the site response analysis by centrifuge testing.

Table 7.2: Depth similitude of sandy soil deposit between prototype and model

Model	Effective acceleration	Prototype
0.072 m	30g	2.16 m
	60g	4.32 m
	80g	5.76 m

The site response of this study aims to evaluate the amplification factor (AF) for different degrees of saturation of shallow sandy soil deposits. AF refers to the ratio between the peak ground acceleration at the ground surface (PGA_{GS}) and the peak ground acceleration at the bedrock (PGA_B) (Kramer, 1996). The AF assessment was performed by estimating the maximum amplitude of the fast Fourier transform (FFT) of the accelerations measured at the top and base of the laminar box. The acceleration measurements at these locations represent the motions at the ground surface and bedrock in natural soil deposits. Besides, the FFT analysis allowed confirm the frequency (f) of both PGA_{GS} and PGA_B are the same. Figure 7.10 shows the procedure for estimating the AF from shaking table testing. The linear frequency (f), time (t) and acceleration (\ddot{u}) values were suitably scaled using the scaling law, with the model/prototype factors referred to in Table 7.1, to accurately represent the response of shallow sandy soil deposits under cyclic loading conditions.

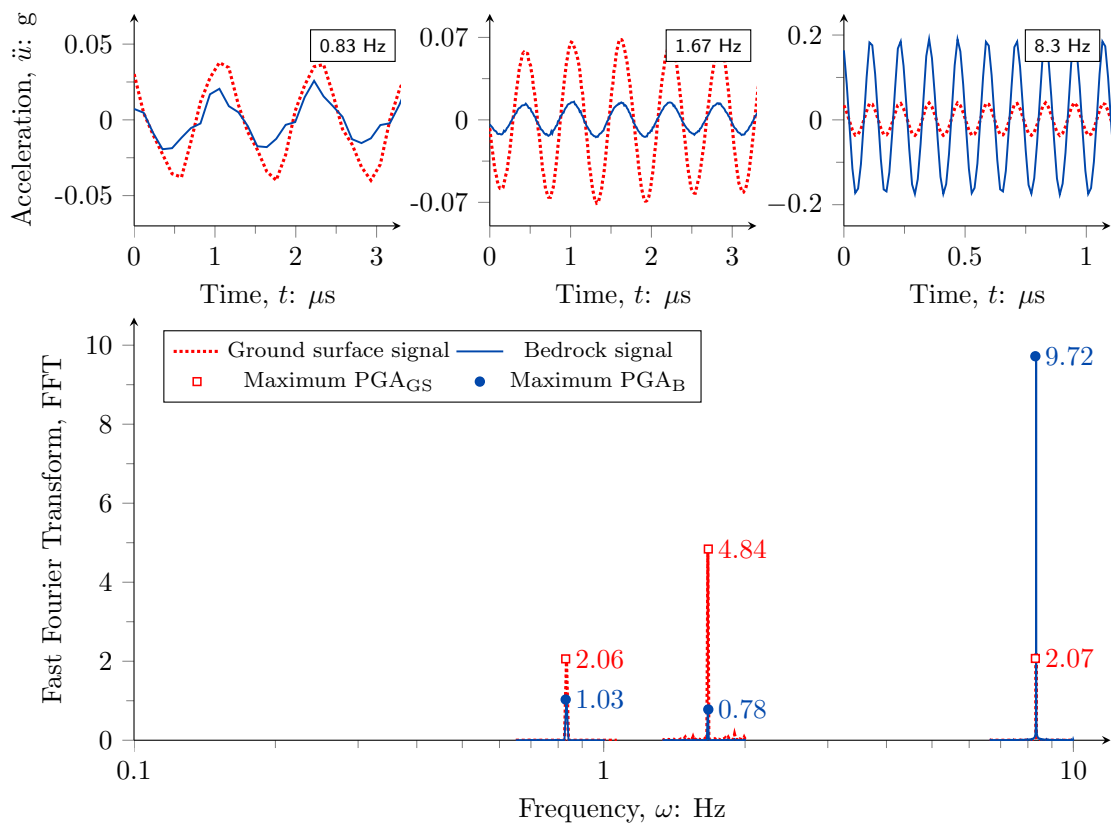


Figure 7.10: Example of amplification factor estimating —results of a sample with 87% degree of saturation and tested under 60g

Figure 7.11 presents the results of frequency amplification spectrum for various S_r and effective centrifuge accelerations. From Figures 7.11.a, c and e, similar trends can be observed from the amplification factor (AF) results. The AF remains relatively flat for frequencies (f) below 1 Hz and ranges from 1 to 1.5. Subsequently, the AF increases sharply until it reaches the resonant frequency (f_R), which falls between 1.5 and 3.0 Hz depending on the S_r and g level. The shape frequency spectra and f_R results are consistent with the values reported by [Conti and Viggiani \(2012\)](#), specifically for dry and saturated sands. At the resonant frequency, the AF can reach values up to 3.2. In the higher frequency range of the spectra, a decrease in AF is observed after f_R , with the values of AF falling below 1 towards the end of the spectra (i.e. $f > 3.75$ Hz). This behaviour is expected due to the vibrations modes induced by the cyclic loading with different frequencies, as demonstrated in Figure 7.6. This indicated that higher intensity earthquake motion leads to higher strain-dependent damping and lower strain-dependent shear modulus, reducing the AF after f_R ([Mirshakari and Ghayoomi, 2017](#)).

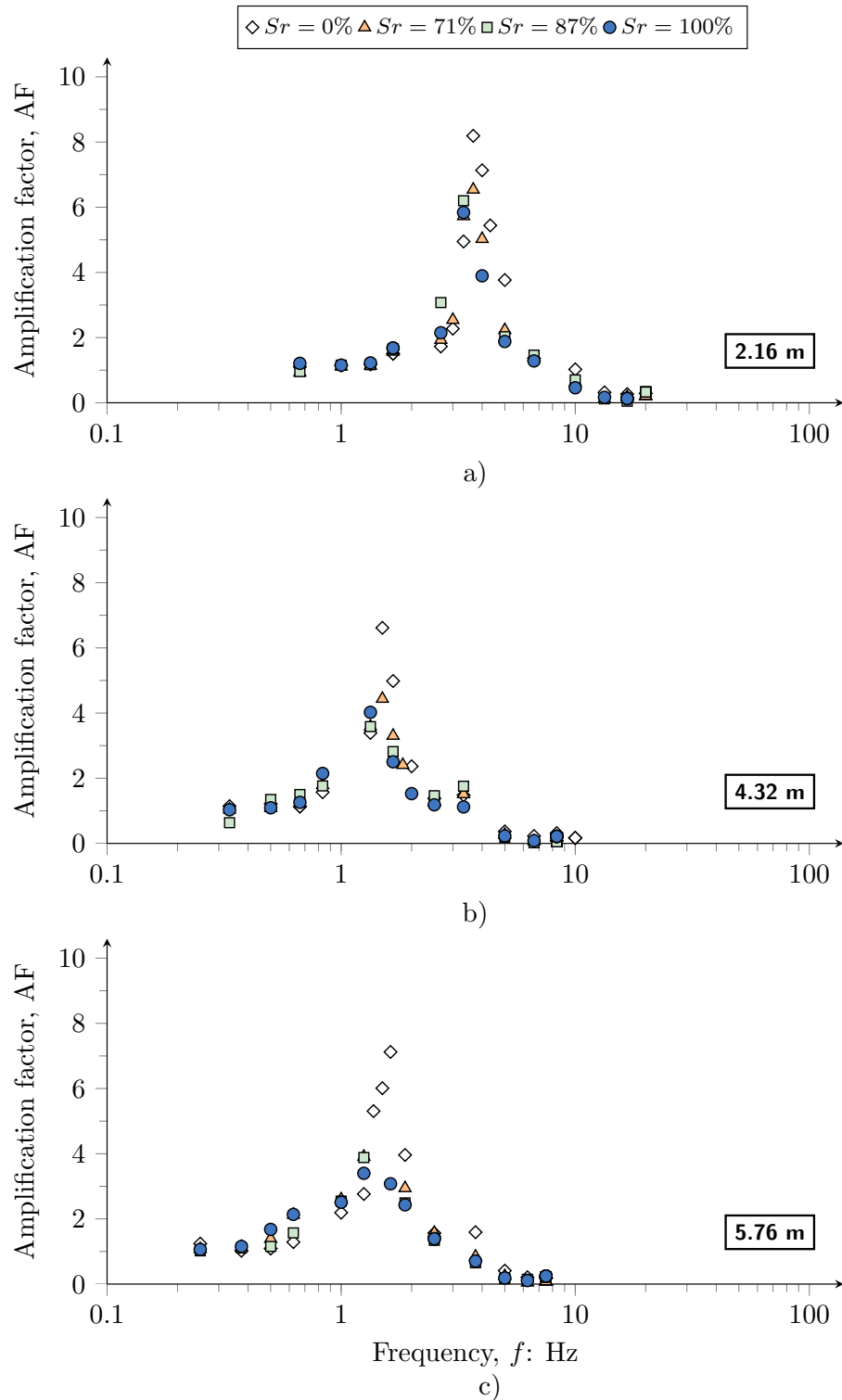


Figure 7.11: Frequency-dependent of AF for various Sr : a) results under 30g; b) results under 60g; c) results under 80g

Figure 7.12 shows the site response analysis by comparing the relationships between maximum AF and f_R for different combinations of Sr and centrifuge accelerations. The results in Figures 7.12.a and 7.12.b reveal that maximum AF decreases as the Sr decreases in all centrifuge accelerations. This behaviour aligns with the expected effects resulting from variations in soil density and the propagation of mechanical waves affected by the water content change, which leads to higher peak ground amplifications with the Sr reduction. Previous numerical validations performed by Yang and Sato (2001) support the notion that the Sr reduction leads to higher AF. Figures 7.12.c and 7.12.d also indicate that f_R values are within the range of typical values of predominant earthquakes frequencies, namely a range between 1 Hz to 5 Hz (Yang, 2006; Molina-Gómez et al., 2019). However, a strong dependency of soil depth on f_R was observed, indicating that soil deposits with lower depths have a higher f_R . In contrast, no significant effects of Sr on f_R were identified.

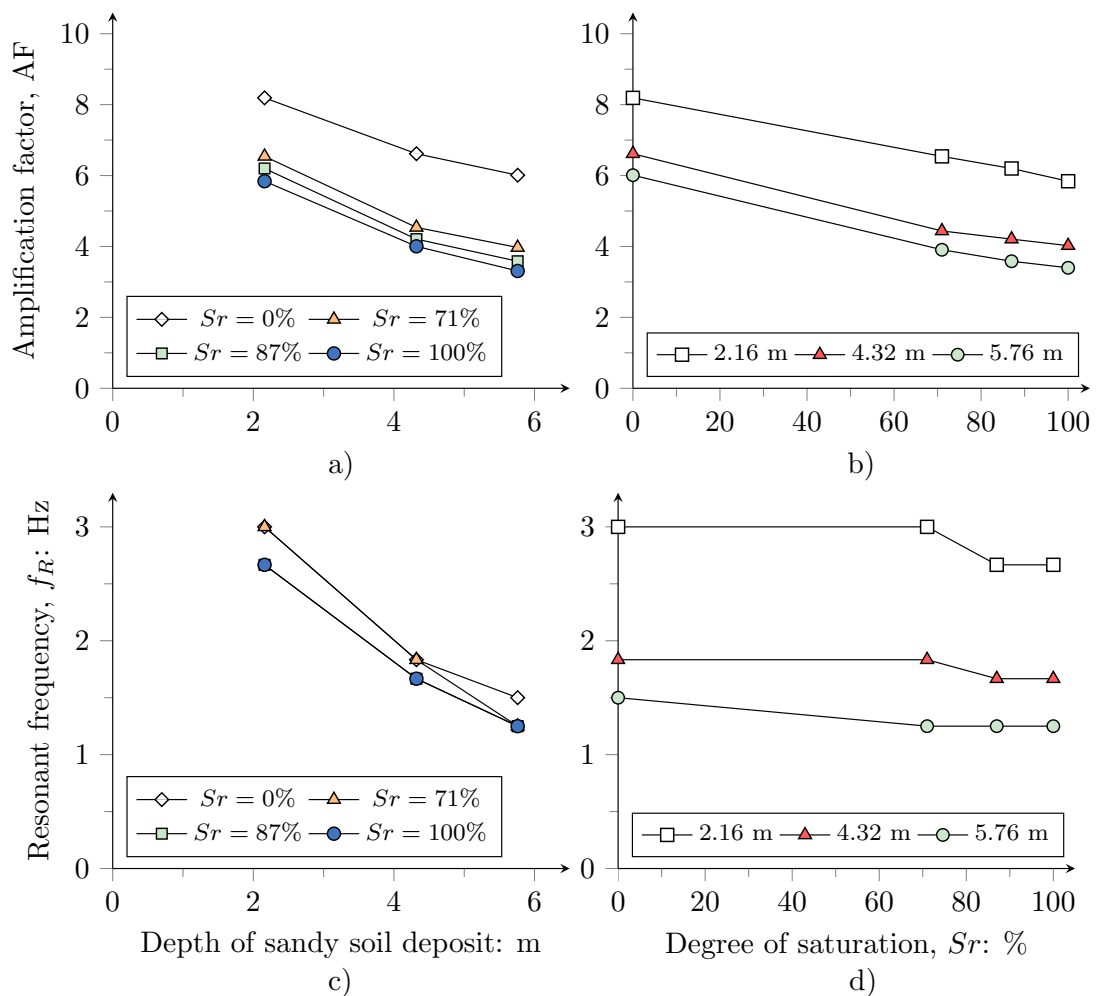


Figure 7.12: Site response analysis: a) maximum AF vs. depth; b) maximum AF vs. Sr ; c) f_R vs. depth; d) f_R vs. Sr

7.6 Volumetric strains

The soil surface settlement during and after an earthquake is a significant cause of damage to the built environment [Zeybek and Madabhushi \(2020\)](#). Hence, predicting the earthquake-induced volumetric strains (ε_v) is an important aspect of the site response assessment. In this study, the (ε_v) induced by the cyclic loading was assessed by measuring settlement at the surface using a laser and comparing it with the initial height of the soil before the test. This estimation is valid due to the limited lateral deformations allowed by the laminar box during testing ([Rayhani and El Naggari, 2008](#); [Soriano Camelo et al., 2022](#)). Figure 7.13 illustrates the typical progression of surface settlement during cyclic loading in the geotechnical centrifuge reported by the laser transducer. In Figure 7.13, the dashed line represents an idealised settlement trend. Such a trend indicates an initial increase in the surface settlement at the beginning of the test, followed by a stabilisation of surface settlement towards the end of the cyclic loading.

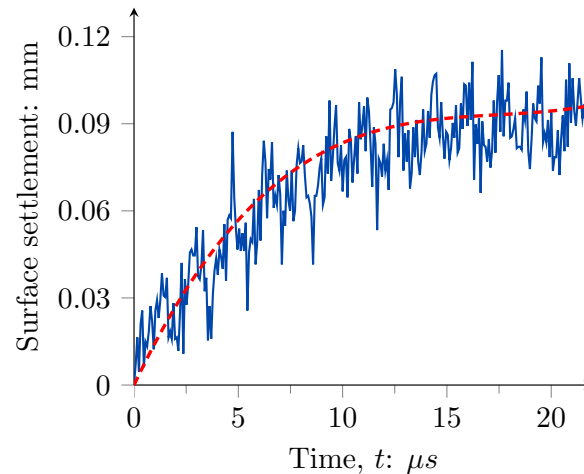


Figure 7.13: Typical measurements of surface settlements —results of a sample with 87% degree of saturation tested under 60 g and 500 Hz loading frequency

Figure 7.14 shows the ε_v variation for all f under different S_r and effective centrifuge accelerations. This figure reveals several trends from ε_v plots, which do not suggest specific patterns in the variation of ε_v with respect to f for the studied S_r and effective centrifuge accelerations. However, the highest volumetric strain results were identified for the tests in dry and fully saturated conditions. In the case of the tests under S_r of 70% and 87%, the ε_v results are lower since sands in partially saturated conditions exhibit higher volume than the soils in dry and fully saturated conditions. In all S_r cases, the results revealed dilative and contractile before and after f_R , respectively.

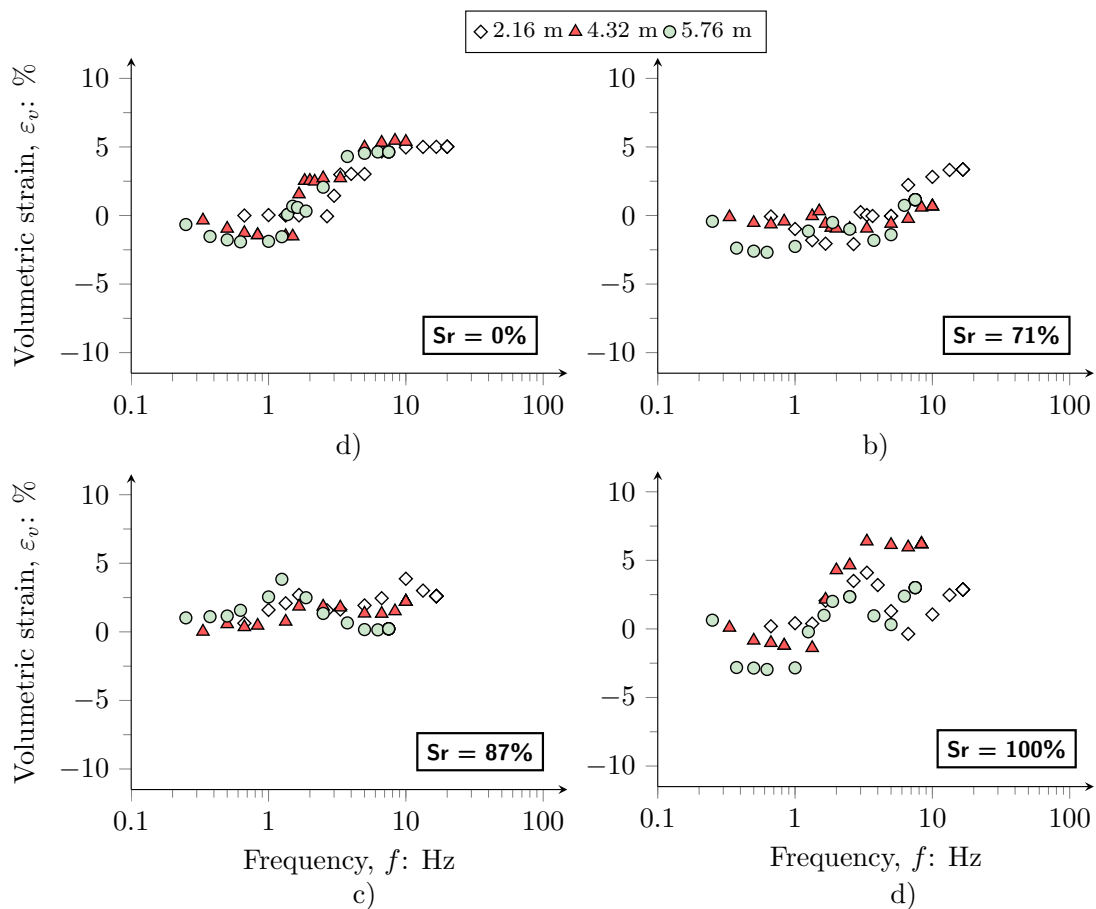


Figure 7.14: Frequency-dependent volumetric strain variation for various effective centrifuge accelerations: a) $S_r = 0\%$; b) $S_r = 71\%$; c) $S_r = 87\%$; d) $S_r = 100\%$

The trend patterns in Figure 7.14 agree with the experimental result reported by Ghayoomi et al. (2013); Mirshekari and Ghayoomi (2017) since these authors also reported lower deformations for partially saturated conditions since the higher ε_v values were observed herein for dry and fully saturated conditions. The volumetric strains are caused by the rapid dissipation of possible pore pressure build-up during cyclic loading due to the free-field condition of the soil model. Zeybek and Madabhushi (2020) indicate that the response of partially saturated sands to seismic shaking differs from dry or saturated soils due to two factors: (i) air-filled voids may compress and change differently during cyclic loading than water-filled voids during cyclic loading; (ii) the mechanisms for generating and dissipating excess pore water pressure may be different. However, the settlements caused by post-cyclic reconsolidation under partially and fully saturated conditions can be considered negligible since the cyclic loading did not cause liquefaction. Therefore, the volumetric strains during the shaking table tests in the geotechnical centrifuge were

caused by the compression of the particles during cyclic loading, as described by [Sawada et al. \(2006\)](#). The agreement of experimental data with previous research reinforces the consistency of the obtained results and contributes to the understanding of the cyclic behaviour of the shallow sandy soil deposits under different degrees of saturation.

7.7 Key findings

This chapter presented a site response analysis of shallow sandy soil deposits for different degrees of saturation. The analysis comprises an innovative testing approach that combines shaking table and centrifuge testing methodologies. By means of this integrated approach, a comprehensive characterisation of the dynamic response of sandy soil deposits with different degrees of saturation. The analysis focused on the frequency amplification spectra for different testing conditions. The spectra considered different effective centrifuge accelerations and degrees of saturation, which cover the dry, partially and fully saturated conditions. From the experimental results, the following findings can be drawn:

- A novel procedure to saturate and induce partial saturation in sands was introduced. This procedure allowed for the testing of uniform loose soil samples with specific degrees of saturation (i.e. 0%, 71%, 87% and 100%) with a relatively small variation of about 3%. The induced partial saturation was conducted using the plate suction method and validated by the wave propagation theory in fluid-saturated media.
- The combination of the micro shaking table and the mini centrifuge apparatuses provided an accurate experimental method to assess the cyclic behaviour of shallow soil deposits. This integrated approach allows a detailed investigation of the seismic response of the soil under different loading conditions due to its relatively fast and numerous testing of physical models with diverse stress and state conditions.
- The in-flight tests delved into the dynamic behaviour of soils subjected to cyclic loading. This novel testing approach allows for assessing the evolution of stiffness degradation. The results obtained in the centrifuge-shaking-table tests were validated by contrasting Resonant-Column data. The excellent agreement between our results and the hyperbolic fitting method proposed by

Ishibashi and Zhang (1993) underscores the robustness of our approach. This alignment is particularly evident in the small strain range (i.e. $\gamma < 10^{-4}$) since the effects of the second vibration mode of the system highly affect the stiffness estimation after the resonance.

- Experimental results allow deriving a series of frequency-dependent amplification spectra. These spectra demonstrated the effects of the degree of saturation and stress state on the amplification factor. Besides, the spectra indicated that the maximum amplification factor decreases as the degree of saturation increases, introducing the potentiality of evaluating the seismic behaviour of partially saturated soils.
- The measurements of surface settlements revealed distinct patterns in the relationship between ε_v and f for the investigated Sr and effective centrifuge accelerations. Due to the differences in these patterns, it was not possible to establish a clear tendency to describe the evolution of volumetric strains as a function of the loading frequency. However, the experimental results indicated that higher volumetric strains occur in dry and fully saturated conditions, aligning with the experimental findings reported in the literature.

Chapter 8

Conclusions and further research

8.1 Concluding remarks

The conclusions derived from this research research systematically presented at the end of each chapter. This section summarises and encapsulates the main contributions of the thesis, showing that the objectives of this research have been achieved.

- The intrinsic properties, including particle morphology and packing, have a strong influence on the mechanical and dynamic behaviour of granular soils. In the case of TP-Lisbon, the particle shape induce a high position of critical state locus when comparing against other natural sands. In addition, these properties govern the frictional stable state at constant volume (i.e. effective friction angle at critical state) and the small strain behaviour (represented by the normalised shear modulus). These observations establish correlations between the critical state behaviour and the small-strain parameters with the particle shape parameter and granular packing characteristics of TP-Lisbon.
- There are relevant effects on the liquefaction resistance of this soil associated with the type of solicitation; that is, the rotation or inversion of principal stresses during cyclic loading. Experimental evidence showed a higher liquefaction resistance for the cyclic triaxial test results (i.e. inversion of principal stresses) than the cyclic direct simple shear (i.e. rotation of principal stresses). However, these testing conditions can be compared by analysing the results in the invariant spaces and using the state parameter concept.

- The measurement of P-wave velocity by bender element tests provides a reliable approach for estimating the degree of saturation in fully and partially saturated sands. The applicability of this procedure was validated by a good agreement between experimental results and wave propagation predictions based on the wave propagation theory of fluid-saturated media. The predictions depend on the relative density of the sand, showing the highest position for the denser sands. This approach demonstrates that the evolution of P-wave velocity as a function of the degree of saturation is significantly affected by the compressibility of the pore fluid type and the distribution of gas bubbles (occluded or in a continuous phase) in the soil skeleton. Therefore, in fully saturated conditions, the P-wave velocity converges to a value near or above 1500 m/s, corresponding to a value slightly higher than the P-wave velocity of the water.
- The experimental results indicate that the liquefaction resistance of TP-Lisbon sand increases as the degree of saturation decreases, accentuating the effectiveness of induced partial saturation as a method for mitigating the liquefaction phenomenon. To quantify this liquefaction resistance improvement provided by induced partial saturation, a novel parameter denominated as 'liquefaction resistance ratio' was applied and correlated with the degree of saturation and the P-wave velocity. The non-linear model relating normalised cyclic resistance as a function of P-wave velocity provided a reliable prediction of the effects of the degree of saturation in liquefaction resistance. This model is a suitable alternative approach for comparing the liquefaction resistance and cyclic behaviour of sands at different degrees of saturation.
- The analysis of shear wave velocities before cyclic loading revealed that this parameter is unsuitable for the liquefaction resistance assessment when varying the degree of saturation in granular soils. These effects have been attributed to occluded air bubbles in the pore-fluid, which cannot be realistically detected by the S-wave velocity, especially in sandy soils with degrees of saturation where the matric suction is negligible. However, for a degree of saturation of 100% and different relative densities, the S-wave can be applied due to its capabilities to detect the changes in porosity and initial soil stiffness, which complement the characterisation of liquefaction resistance by estimating the soil state.

- An integrated experimental approach that combines shaking table and centrifuge testing provided a reliable characterisation of the cyclic/dynamic behaviour of shallow sandy soil deposits. This approach demonstrated its adaptability for assessing earthquake-induced damage since its versatility in testing small models. The micro shaking table simulates seismic motions through diverse combinations of cyclic loading thanks to the capabilities of an integrated piezoelectric transducer, while the mini centrifuge reproduces the effects of gravity and scaled accelerations.
- A series of frequency-dependent amplification spectra revealed the influence of the degree of saturation on the site response of shallow sandy soil deposits. The experimental results consistently indicate that the maximum amplification factor decreases as the degree of saturation increases. Moreover, the results highlight that higher volumetric strains occur in both dry and fully saturated conditions, which aligns with the experimental findings reported in the existing literature.

In summary, this research has explored the performance of induced partial saturation in improving the liquefaction resistance of sandy soils, demonstrating its efficiency by experimental evidence. Wave-based approaches can quantify this improvement and the degree of saturation. Therefore, this research highlights the potential of combining P-wave and S-wave propagation measurements with cyclic testing. The results obtained in the laboratory have practical implications for mitigating damages caused by seismic events, which contribute to hazard mitigation strategies and the design of resilient infrastructures due to the effects of the degree of saturation on the cyclic behaviour in fluid-saturated granular media. The findings presented in this research provide a better understanding of the potential use of induced partial saturation in practical engineering applications.

8.2 Further works

The innovations derived from this thesis have suggested new ideas, which can be explored in future research.

- The intrinsic properties of sands were correlated with the critical state parameters. These properties can be correlated with the factors affecting the instability of non-plastic soils, providing new criteria for developing innovative

criteria and methodologies to more accurately estimate the susceptibility to soil liquefaction in diverse geomaterials.

- This research has contributed to the development of a comprehensive experimental database that can be valuable for numerical analyses and the design of geotechnical structures subjected to monotonic, cyclic or seismic loading. The results presented in this study can serve as a valuable resource for calibrating numerical and constitutive models, thereby enhancing their accuracy and reliability.
- The effects of inversion and rotation of principal stresses on liquefaction resistance were experimentally explored herein. The assessment of combined axial and torsional loading can replicate better the liquefaction onset in soils under seismic action by multiaxial testing devices.
- Cyclic triaxial tests in partially saturated sands validated the effectiveness of induced partial saturation in mitigating earthquake-induced liquefaction. Due to the implementation of local instrumentation for monitoring the volumetric strains in partially saturated sands, the energy-based approaches can be used to compare the experimental results against field case histories.
- The induced partial saturation improves the shear strength of granular soils. This method can be studied under monotonic conditions to assess the instability and critical state locus of granular soils.
- Occluded air bubbles have an important effect on the cyclic behaviour of granular soils. Hence, the characterisation of stiffness degradation and damping evolution can be investigated.
- The experimental procedures implemented herein provided reliable and accurate results of the cyclic undrained behaviour of TP-Lisbon sand. These procedures can be employed to assess the performance of specific techniques to induce partial saturation, such as denitrification or to assess the liquefaction resistance of gassy soils.
- P-wave velocity measurements provided a reliable approach to estimate the degree of saturation in sands, as validated by the wave propagation theory of fluid-saturated media. This approach can be applied in field trials or study sites by in situ geophysical testing.

- The application of other methods and theories based on electrical or thermal conductivity can also be used to assess the degree of saturation, especially in ranges for which the P-wave propagation is unsuitable for such a purpose.
- The calibration and implementation of constitutive models comprising the effect of fluid compressibility for the prediction of pore pressure evolution (e.g. Biot's theory) can be explored to propose strategies for liquefaction mitigation by varying the degree of saturation.
- The integration of the mini shaking table in the geotechnical centrifuge apparatus provided valuable experimental evidence of the seismic response of shallow sandy soils. This approach can be implemented to assess the effects of seismic wave propagation during liquefaction onset, which is a gap in the current state-of-art. This assessment will provide relevant insights into the evolution of site response during the state transition of soils during liquefaction.
- Dynamic centrifuge testing can be applied to characterise the seismic response of other soil types (e.g. clays and tailings). Besides, the incorporation of viscous fluids during testing will provide relevant insights about the liquefaction onset in free field conditions.
- The ground surface or volumetric strains can be explored in the dynamic geotechnical centrifuge apparatus under historical seismic records to provide methodologies to mitigate earthquake-induced damage.
- This research addressed and interpreted experimental results of site response using the geotechnical centrifuge. The frequency amplification spectra for various degrees of saturation and stress level can be compared against coupled numerical models involving such testing conditions.

*'No llores porque ya se terminó,
sonríe porque sucedió.'*

Gabriel García Márquez

References

- Adam, L. and Otheim, T. Elastic laboratory measurements and modeling of saturated basalts. *Journal of Geophysical Research: Solid Earth*, 118(3):840–851, 2013. doi: 10.1002/jgrb.50090.
- Afacan, K. B., Brandenberg, S. J., and Stewart, J. P. Centrifuge Modeling Studies of Site Response in Soft Clay over Wide Strain Range. *Journal of Geotechnical and Geoenvironmental Engineering*, 140(2), 2014. doi: 10.1061/(ASCE)GT.1943-5606.0001014.
- Alavi, A. H. and Gandomi, A. H. Energy-based numerical models for assessment of soil liquefaction. *Geoscience Frontiers*, 3(4):541–555, 2012. doi: 10.1016/j.gsf.2011.12.008.
- Altuhafi, F.N., Coop, M.R., and Georgiannou, V.N. Effect of Particle Shape on the Mechanical Behavior of Natural Sands. *Journal of Geotechnical and Geoenvironmental Engineering*, 142(12):04016071, 2016. doi: 10.1061/(ASCE)GT.1943-5606.0001569.
- Andrus, R. D. and Stokoe, K. H. Liquefaction Resistance of Soils from Shear-Wave Velocity. *Journal of Geotechnical and Geoenvironmental Engineering*, 126(11):1015–1025, 2000. doi: 10.1061/(ASCE)1090-0241(2000)126:11(1015).
- Archie, G.E. The Electrical Resistivity Log as an Aid in Determining Some Reservoir Characteristics. *Transactions of the AIME*, 146(01):54–62, 1942. ISSN 0081-1696. doi: 10.2118/942054-G.
- ASTM International. D6913 – Standard Test Method for Particle-Size Distribution (Gradation) of Soils Using Sieve Analysis, 2007.
- ASTM International. D4253 – Test Methods for Maximum Index Density and Unit Weight of Soils Using a Vibratory Table, 2016a.
- ASTM International. D4254 – Standard Test Methods for Minimum Index Density and Unit Weight of Soils and Calculation of Relative Density, 2016b.
- ASTM International. ASTM D5778 – Standard Test Method for Electronic Friction Cone and Piezocone Penetration Testing of Soils), 2017.

- ASTM International. C702 – Standard Practice for Reducing Samples of Aggregate to Testing Size, 2018.
- ASTM International. ASTM D6836 – Standard Test Methods for Determination of the Soil Water Characteristic Curve for Desorption Using Hanging Column, Pressure Extractor, Chilled Mirror Hygrometer, or Centrifuge), 206.
- Astuto, G. *Bio-induced partial saturation as liquefaction mitigation technique*. Phd thesis, University of Napoli Federico II, 2021.
- Astuto, G., Molina-Gómez, F., Bilotta, Emilio, Viana da Fonseca, A., and Flora, A. Some remarks on the assessment of P-wave velocity in laboratory tests for evaluating the degree of saturation. *Acta Geotechnica*, 2023. doi: 10.1007/s11440-022-01610-9.
- Azeiteiro, R. J.N., Coelho, P. A.L.F., Taborda, D. M.G., and Grazina, J. C.D. Energy-based evaluation of liquefaction potential under non-uniform cyclic loading. *Soil Dynamics and Earthquake Engineering*, 92, 2017. doi: 10.1016/j.soildyn.2016.11.005.
- Banerjee, A., Puppala, A. J., and Hoyos, L. R. Liquefaction Assessment in Unsaturated Soils. *Journal of Geotechnical and Geoenvironmental Engineering*, 148(9), 2022. doi: 10.1061/(ASCE)GT.1943-5606.0002851.
- Bao, X., Jin, Z., Cui, H., Chen, X., and Xie, X. Soil liquefaction mitigation in geotechnical engineering: An overview of recently developed methods. *Soil Dynamics and Earthquake Engineering*, 120:273–291, 2019. doi: 10.1016/J.SOILDYN.2019.01.020.
- Been, K. and Jefferies, M. A state parameter for sands. *Géotechnique*, 35(2):99–112, 1985. doi: 10.1680/geot.1985.35.2.99.
- Been, K and Jefferies, M. G. Stress-dilatancy in very loose sand. *Canadian Geotechnical Journal*, 41(5):972–989, 2004. doi: 10.1139/T04-038.
- Been, K., Jefferies, M. G., and Hachey, J. The critical state of sands. *Géotechnique*, 41(3):365–381, 1991. doi: 10.1680/geot.1991.41.3.365.
- Bertalot, D., Brennan, A.J., and Villalobos, F.A. Influence of bearing pressure on liquefaction-induced settlement of shallow foundations. *Géotechnique*, 63(5): 391–399, 2013. doi: 10.1680/geot.11.P.040.
- Biot, M. A. Theory of Propagation of Elastic Waves in a Fluid-Saturated Porous Solid I. Low-Frequency Range. *Journal of the Acoustical Society of America*, 28: 168–178, 1956a. doi: 10.1121/1.1908239.
- Biot, M. A. Theory of Propagation of Elastic Waves in a Fluid-Saturated Porous

- Solid II. Higher Frequency Range. *Journal of the Acoustical Society of America*, 28:179–191, 1956b. doi: 10.1121/1.1908241.
- Bishop, A. W. and Blight, G. E. Some Aspects of Effective Stress in Saturated and Partly Saturated Soils. *Géotechnique*, 13(3):177–197, 1963. doi: 10.1680/GEOT.1963.13.3.177.
- Booker, J.R., Rahman, M.S., and Seed, H.B. GADFLEA—a computer program for the analysis of pore pressure generation and dissipation during cyclic or earthquake loading. Technical report, Earthquake Engineering Center, University of California, Berkeley, CA, 1976.
- Borcherdt, R. D. Estimates of Site-Dependent Response Spectra for Design (Methodology and Justification). *Earthquake Spectra*, 10(4):617–653, 1994. doi: 10.1193/1.1585791.
- Boulanger, R. W. and Idriss, I. M. CPT and SPT based liquefaction triggering procedures. Technical report, Center for Geotechnical Modeling, Department of Civil and Environmental Engineering, University of California, Davis, 2014.
- Boulanger, R.W. Liquefaction in the 2011 Great East Japan Earthquake: Lessons for U.S. Practice. In *International Symposium on Engineering Lessons Learned from the Giant Earthquake*, pages 655–664, Tokyo - Japan, 2012. URL <https://www.geoengineer.org/publications/online-library?keywords{%}5B0{%}5D=Liquefactioninthe2011GreatEastJapanEarthquake{%}3ALessonsforU.S.Practice>.
- Bray, J.D. and Sancio, R.B. Assessment of the Liquefaction Susceptibility of Fine-Grained Soils. *Journal of Geotechnical and Geoenvironmental Engineering*, 132(9):1165–1177, 2006. doi: 10.1061/(ASCE)1090-0241(2006)132:9(1165).
- Brennan, A. J., Thusyanthan, N. I., and Madabhushi, S. P. Evaluation of Shear Modulus and Damping in Dynamic Centrifuge Tests. *Journal of Geotechnical and Geoenvironmental Engineering*, 131(12):1488–1497, 2005. doi: 10.1061/(ASCE)1090-0241(2005)131:12(1488).
- Cabrera, M.A., Caicedo, B., and Thorel, L. Dynamic actuator for centrifuge modeling of soil-structure interaction. *Geotechnical Testing Journal*, 35(4):539–547, 2012. doi: 10.1520/GTJ104353.
- Caicedo, B. and Thorel, L. Centrifuge modelling of unsaturated soils. *Journal of Geo-Engineering Sciences*, 2(1-2):83–103, 2014. doi: 10.3233/JGS-130013.
- Caicedo, Bernardo. *Geotechnics of Roads: Fundamentals*. CRC Press/Balkema, 2019. ISBN 9780429025914.

- Camacho-Tauta, J. *Evaluation of the small-strain stiffness of soil by non-conventional dynamic testing methods*. Phd thesis, Instituto Superior Técnico da Universidade Técnica de Lisboa, 2011.
- Camacho-Tauta, J., Cascante, G., Viana da Fonseca, A., and Santos, J. A. Time and frequency domain evaluation of bender element systems. *Géotechnique*, 65(7):548–562, 2015. doi: 10.1680/geot.13.P.206.
- Cambridge, M. and Shaw, D. Preliminary reflections on the failure of the Brumadinho tailings dam in January 2019. *Dams and Reservoirs*, 29(3):113–123, 2019. doi: 10.1680/jdare.19.00004.
- Cappellaro, C., Cubrinovski, M., Bray, J., Chiaro, G., Riemer, M., and Stringer, M. Liquefaction resistance of Christchurch sandy soils from direct simple shear tests. *Soil Dynamics and Earthquake Engineering*, 141:106489, 2021. doi: 10.1016/j.soildyn.2020.106489.
- Carrera, A., Coop, M.R., and Lancellota, R. Influence of grading on the mechanical behaviour of Stava tailings. *Géotechnique*, 61(11):935–946, 2011. doi: 10.1680/geot.9.P.009.
- Cascante, G. and Santamarina, J. C. Interparticle contact behavior and wave propagation. *Journal of Geotechnical Engineering*, 122:831–839, 1996. doi: 10.1061/(ASCE)0733-9410(1996)122:10(831).
- Castro, G. and Poulos, S. J. Factors Affecting Liquefaction and Cyclic Mobility. *Journal of the Geotechnical Engineering Division*, 103(6):501–506, 1977. doi: 10.1061/AJGEB6.0000433.
- CEN. Eurocode 8: Design of structures for earthquake resistance, 2010.
- Cetin, K. O., Seed, R. B., Der Kiureghian, A., Tokimatsu, K., Harder, L. F., Kayen, R. E., and Moss, Robert E. S. Standard Penetration Test-Based Probabilistic and Deterministic Assessment of Seismic Soil Liquefaction Potential. *Journal of Geotechnical and Geoenvironmental Engineering*, 130(12):1314–1340, 2004. doi: 10.1061/(ASCE)1090-0241(2004)130:12(1314).
- Chen, R., Chen, Y., Liu, H., Zhang, K., Zhou, Y., Xu, S., and Wu, K. In situ desaturation tests by electrolysis for liquefaction mitigation. *Canadian Geotechnical Journal*, 58:1744–1756, 2021. doi: 10.1139/cgj-2020-0580.
- Chiaradonna, A. and Flora, A. On the estimate of seismically induced pore-water pressure increments before liquefaction. *Geotechnique Letters*, 10(2):128–134, 2020. doi: 10.1680/jgele.19.00032.
- Chiaradonna, A., Tropeano, G., D’Onofrio, A., and Silvestri, F. Development of a simplified model for pore water pressure build-up induced by cyclic load-

- ing. *Bulletin of Earthquake Engineering*, 16(9):3627–3652, 2018. doi: 10.1007/s10518-018-0354-4.
- Cho, G-C., Dodds, J., and Santamarina, J.C. Particle Shape Effects on Packing Density, Stiffness, and Strength: Natural and Crushed Sands. *Journal of Geotechnical and Geoenvironmental Engineering*, 132(5):591–602, 2006. doi: 10.1061/(ASCE)1090-0241(2006)132:5(591).
- Consentini, R.M. and Foti, S. Evaluation of porosity and degree of saturation from seismic and electrical data. *Géotechnique*, 64(4):278–286, 2014. doi: 10.1680/geot.13.P.075.
- Conte, E., Cosentini, R. M., and Troncone, A. Shear and dilatational wave velocities for unsaturated soils. *Soil Dynamics and Earthquake Engineering*, 29(6):946–952, 2009. doi: 10.1016/J.SOILDYN.2008.11.001.
- Conti, Riccardo and Viggiani, Giulia M. B. Evaluation of Soil Dynamic Properties in Centrifuge Tests. *Journal of Geotechnical and Geoenvironmental Engineering*, 138(7):850–859, 2012. doi: 10.1061/(ASCE)GT.1943-5606.0000659.
- Couto, R., Bento, R., and Gomes, R.C. Seismic performance and fragility curves of historical residential buildings in Lisbon downtown affected by settlements. *Bulletin of Earthquake Engineering*, 18(11):5281–5307, 2020. doi: 10.1007/s10518-020-00906-z.
- Cubrinovski, M., B., Jonathan D., Taylor, M., Giorgini, S., Bradley, B., Wotherpoon, L., and Zupan, J. Soil liquefaction effects in the central business district during the February 2011 Christchurch earthquake. *Seismological Research Letters*, 82(6):893–904, 2011. doi: 10.1785/gssrl.82.6.893.
- Cubrinovski, M., Rhodes, A., Ntritsos, N., and Van Ballegooy, S. System response of liquefiable deposits. *Soil Dynamics and Earthquake Engineering*, 124:212–229, 2019. doi: 10.1016/J.SOILDYN.2018.05.013.
- Cubrinovski, Misko and Ishihara, Kenji. Maximum and minimum void ratio characteristics of sands. *Soils and Foundations*, 42(6):65–78, 2002. doi: 10.3208/sandf.42.6_65.
- Dashti, S., Bray, J.D., Pestana, J.M., Riemer, M., and Wilson, D. Centrifuge Testing to Evaluate and Mitigate Liquefaction-Induced Building Settlement Mechanisms. *Journal of Geotechnical and Geoenvironmental Engineering*, 136(7):918–929, 2010. doi: 10.1061/(ASCE)GT.1943-5606.0000306.
- Dhakal, R., Cubrinovski, M., and Bray, J. D. Geotechnical characterization and liquefaction evaluation of gravelly reclamations and hydraulic fills (Port of Wellington, New Zealand). *Soils and Foundations*, 60(6):1507–1531, 2020. doi: 10.1016/j.sandf.2020.10.001.

- Dief, H.M and Figueroa, J. L. Liquefaction assessment by the energy method through centrifuge modeling. In Zeng, X.W., editor, *Proceedings of the NSF International Workshop on Earthquake Simulation in Geotechnical Engineering, CWRU*, pages 1–15, Cleveland, OH, 2001. URL <https://engineering.case.edu/eciv/proceedings/iwes/paper/dief.pdf>.
- Dyvik, R., Berre, T., Lacasse, S., and Raadim, B. Comparison of truly undrained and constant volume direct simple shear tests. *Géotechnique*, 37(1):3–10, mar 1987. doi: 10.1680/geot.1987.37.1.3.
- Emerson, M. and Foray, P. Laboratory P-wave measurements in dry and saturated sand. *Acta Geotechnica*, 1(3):167–177, 2006. doi: 10.1007/s11440-006-0015-7.
- Eseller-Bayat, E., Yegian, M. K., Alshawabkeh, A., and Gokyer, S. Liquefaction Response of Partially Saturated Sands. I: Experimental Results. *Journal of Geotechnical and Geoenvironmental Engineering*, 139(6):863–871, 2013. doi: 10.1061/(ASCE)GT.1943-5606.0000815.
- Esmailpour, P., Mamazizi, A., and Madabhusi, G. S.P. An overview of the model container types in physical modeling of geotechnical problems. *Soil Dynamics and Earthquake Engineering*, 168:107827, 2023. doi: 10.1016/j.soildyn.2023.107827.
- Fanni, R., Reid, D., and Fourie, A. On reliability of inferring liquefied shear strengths from simple shear testing. *Soils and Foundations*, 62(3):101151, 2022. doi: 10.1016/j.sandf.2022.101151.
- Fasano, G., De Sarno, D., Bilotta, E., and Flora, A. Design of horizontal drains for the mitigation of liquefaction risk. *Soils and Foundations*, 59(5):1537–1551, 2019. doi: 10.1016/J.SANDF.2019.07.004.
- Fernandes, M. *Mecânica dos Solos: Conceitos e Princípios Fundamentais*. Faculdade de Engenharia da Universidade do Porto, Porto, 5th edition, 2017. ISBN 9789897461453.
- Ferreira, C. *The use of seismic wave velocities in the measurement of stiffness of a residual soil*. Phd thesis, IUniversidade do Porto, 2009.
- Ferreira, C., Viana da Fonseca, A., Ramos, C., Saldanha, A. S., Amoroso, S., and Rodrigues, C. Comparative analysis of liquefaction susceptibility assessment methods based on the investigation on a pilot site in the greater Lisbon area. *Bulletin of Earthquake Engineering*, 18:109–138, 2020. ISSN 1570-761X. doi: 10.1007/s10518-019-00721-1.
- Ferreira, C., Díaz-Durán, F., Viana da Fonseca, A., and Cascante, G. New approach to concurrent V_s and V_p measurements using bender elements. *Geotechnical Testing Journal*, 44(6), 2021. doi: 10.1520/GTJ20200207.

- Figuroa, J. L., Saada, A. S., Liang, L., and Dahisaria, N. M. Evaluation of Soil Liquefaction by Energy Principles. *Journal of Geotechnical Engineering*, 120(9): 1554–1569, 1994. doi: 10.1061/(ASCE)0733-9410(1994)120:9(1554).
- Figuroa, J. L., Saada, A. S., and Rokoff, M. D. Influence of grain-size characteristics in determining the liquefaction potential of a soil deposit by the energy method. *Physics and mechanics of soil liquefaction. Proceedings of the international workshop, Baltimore, September 1998.*, pages 237–245, 1999. doi: 10.1201/9780203743317-21.
- Finn, W.D. Liam, Pickering, Dennison J., and Bransby, Peter L. Sand Liquefaction in Triaxial and Simple Shear Tests. *Journal of the Soil Mechanics and Foundations Division*, 97(4):639–659, 1971. doi: 10.1061/JSFEAQ.0001579.
- Fioravante, V., Giretti, D., Airoidi, S., and Moglie, J. Effects of seismic input, fine crust and existing structure on liquefaction from centrifuge model tests. *Bulletin of Earthquake Engineering*, 19(10):3807–3833, 2021. doi: 10.1007/s10518-021-01139-4.
- Flora, A., Bilotta, E., Chiaradonna, A., Lirer, S., Mele, L., and Pingue, L. A field trial to test the efficiency of induced partial saturation and horizontal drains to mitigate the susceptibility of soils to liquefaction. *Bulletin of Earthquake Engineering*, pages 1–30, 2020. doi: 10.1007/s10518-020-00914-z.
- Foti, S., Lai, C. G., and Lancellotta, R. Porosity of fluid-saturated porous media from measured seismic wave velocities. *Géotechnique*, 52(5):359–373, 2002. doi: 10.1680/geot.2002.52.5.359.
- Fredlund, D. G. Unsaturated Soil Mechanics in Engineering Practice. *Journal of Geotechnical and Geoenvironmental Engineering*, 132(3):286–321, 2006. doi: 10.1061/(ASCE)1090-0241(2006)132:3(286).
- Fredlund, D. G and Rahardjo, R. *Soil Mechanics for Unsaturated Soils*. John Wiley & Sons INC, 1993. ISBN 9780471850083.
- Fredlund, D. G. and Xing, A. Equations for the soil-water characteristic curve. *Canadian Geotechnical Journal*, 31(4):521–532, 1994. doi: 10.1139/T94-061.
- Fundação Luso-Americana, F. L. A. *1755 o Grande Terramoto de Lisboa – Vol 1 Descrições*. FLAD e Público editions, Lisboa, Portugal, 2005. ISBN 989-619-013-5.
- Gajo, A. and Wood, D. Muir. A kinematic hardening constitutive model for sands: the multiaxial formulation. *International Journal for Numerical and Analytical Methods in Geomechanics*, 23(9):925–965, 1999. doi: 10.1002/(SICI)1096-9853(19990810)23:9<925::AID-NAG19>3.0.CO;2-M.

- Garzón, L. X., Caicedo, B., Sánchez-Silva, M., and Phoon, K-K. Physical modelling of soil uncertainty. *International Journal of Physical Modelling in Geotechnics*, 15(1):19–34, 2015. doi: 10.1680/ijpmg.14.00012.
- Geyin, M. and Maurer, B.W. Fragility Functions for Liquefaction-Induced Ground Failure. *Journal of Geotechnical and Geoenvironmental Engineering*, 146(12):04020142, 2020. doi: 10.1061/(ASCE)GT.1943-5606.0002416.
- Ghayoomi, M., McCartney, J., and Ko, H.-Y. Centrifuge Test to Assess the Seismic Compression of Partially Saturated Sand Layers. *Geotechnical Testing Journal*, 34(4):103355, 2011. doi: 10.1520/GTJ103355.
- Ghayoomi, M., McCartney, J. S., and Ko, H-Y. Empirical Methodology to Estimate Seismically Induced Settlement of Partially Saturated Sand. *Journal of Geotechnical and Geoenvironmental Engineering*, 139(3):367–376, 2013. doi: 10.1061/(ASCE)GT.1943-5606.0000774.
- Giretti, D. and Fioravante, V. A correlation to evaluate cyclic resistance from CPT applied to a case history. *Bulletin of Earthquake Engineering*, 15(5):1965–1989, 2017. doi: 10.1007/s10518-016-0057-7.
- Giretti, D., Fioravante, V., Been, K., and Dickenson, S. Mechanical properties of a carbonate sand from a dredged hydraulic fill. *Géotechnique*, 68(5):410–420, 2018. doi: 10.1680/jgeot.16.P.304.
- Gomes Correia, A., Barros, J.M.C., Santos, J. A., and Sussumu, N. An approach to predict shear modulus of soils in the range of 10^{-6} to 10^{-2} strain levels. In *Proceedings of the Fourth International Conference on Recent Advances in Geotechnical Earthquake Engineering and Soil Dynamics*, San Diego, California, USA, 2001.
- Goudarzy, M., Konig, D., and Schanz, T. Small and intermediate strain properties of sands containing fines. *Soil Dynamics and Earthquake Engineering*, 132:110–20, 2018. doi: 10.1016/J.SOILDYN.2018.02.020.
- Green, R. A., Mitchell, J. K., and Polito, C. P. An Energy-Based Pore Pressure Generation Model for Cohesionless Soils. In *John Booker Memorial Symposium – Developments in Theoretical Geomechanics*, Sydney, Australia, 2000. Balkema.
- Green, R.A. *Energy-Based Evaluation and Remediation of Liquefiable Soils*. Phd thesis, Virginia Polytechnic Institute and State University, 2001. URL <https://vtechworks.lib.vt.edu/handle/10919/28641>.
- Green, R.A., Bradshaw, A.S., and Baxter, C.D.P. Accounting for Intrinsic Soil Properties and State Variables on Liquefaction Triggering. *Journal of Geotechnical and Geoenvironmental Engineering*, 148(7), 2022. doi: 10.1061/(ASCE)GT.1943-5606.0002823.

- Gu, X., Zuo, K., Tessari, A., and Gao, G. Effect of saturation on the characteristics of P-wave and S-wave propagation in nearly saturated soils using bender elements. *Soil Dynamics and Earthquake Engineering*, 145:106742, 2021. doi: 10.1016/J.SOILDYN.2021.106742.
- Hardin, B. O. and Drnevich, V. P. Shear modulus and damping in soils: design equations and curves. *Soil Mechanics and Foundations Division*, 98:667–692, 1972. doi: 10.1017/S000748530002229X.
- Hardin, B. O. and Richart, F. Elastic wave velocities in granular soils. *Soil Mechanics and Foundations Division*, 89:33–65, 1963.
- He, J., Chu, J., and Ivanov, V. Mitigation of liquefaction of saturated sand using biogas. *Géotechnique*, 63(4):267–275, 2013. doi: 10.1680/GEOT.SIP13.P.004.
- He, J., Chu, J., and Liu, H. Undrained shear strength of desaturated loose sand under monotonic shearing. *Soils and Foundations*, 54(4):910–916, 2014. doi: 10.1016/J.SANDF.2014.06.020.
- Hossain, A. M., Andrus, R. D., and Camp, W. M. Correcting Liquefaction Resistance of Unsaturated Soil Using Wave Velocity. *Journal of Geotechnical and Geoenvironmental Engineering*, 139(2):277–287, 2013. doi: 10.1061/(ASCE)GT.1943-5606.0000770.
- Hoyos, L. R., Suescún-Florez, E. A., and Puppala, A. J. Stiffness of intermediate unsaturated soil from simultaneous suction-controlled resonant column and bender element testing. *Engineering Geology*, 188:10–28, 2015. doi: 10.1016/j.enggeo.2015.01.014.
- Hu, X., Li, D., Peng, E., Hou, Z., Sheng, Y., and Chou, Y. Long-term sustainability of biogas bubbles in sand. *Scientific Reports*, 10:12680, 7 2020. doi: 10.1038/s41598-020-69324-0.
- Huang, Y. and Wen, Z. Recent developments of soil improvement methods for seismic liquefaction mitigation. *Natural Hazards*, 76(4):1927–1938, 2015. doi: doi.org/10.1007/s11069-014-1558-9.
- Ishibashi, I. and Zhang, X. Unified dynamic shear moduli and damping ratios of sand and clay. *Soils and Foundations*, 33(1):182–191, 1993. doi: 10.3208/sandf1972.33.182.
- Ishihara, K. Approximate forms of wave equations for water-saturated porous materials and related dynamic modulus. *Soils and Foundations*, 10(4):10–38, 1970. doi: 10.3208/sandf1960.10.4_10.
- Ishihara, K. Liquefaction and flow failure during earthquakes. *Géotechnique*, 43(3): 351–451, 1993. ISSN 0016-8505. doi: 10.1680/geot.1993.43.3.351.

- Ishihara, K. Liquefaction in Tokyo bay and Kanto regions in the 2011 great east Japan earthquake. In *Proceedings of the International Symposium on Engineering Lessons Learned from the 2011 Great East Japan Earthquake, March 1-4, 2012, Tokyo, Japan*, pages 63–82, Tokio, Japan, 2012.
- Ishihara, K., Yamazaki, A., and Haga, K. Liquefaction of K0-Consolidated Sand Under Cyclic Rotation of Principal Stress Direction With Lateral Constraint. *Soils and Foundations*, 25(4):63–74, 1985. doi: 10.3208/sandf1972.25.4_63.
- Ishihara, K., Huang, Y., and Tsuchiya, H. Liquefaction resistance of nearly saturated sand as correlated with longitudinal wave velocity. In *Poromechanics: A tribute to Maurice A. Biot*, pages 583–586, 1998.
- Ishihara, K., Tsuchiya, H., Huang, Y., and Kamada, K. Keynote Lecture: Recent Studies on Liquefaction Resistance of Sand-Effect of Saturation. *International Conferences on Recent Advances in Geotechnical Earthquake Engineering and Soil Dynamics*, mar 2001. URL <https://scholarsmine.mst.edu/icrageesd/04icrageesd/session00/30>.
- Ishihara, K., Harada, K., Lee, W.F., Chan, C.C., and Safiullah, A.M.M. Post-liquefaction settlement analyses based on the volume change characteristics of undisturbed and reconstituted samples. *Soils and Foundations*, 56(3):533–546, 2016. doi: 10.1016/J.SANDF.2016.04.019.
- Ishihara, Kenji. *Soil Behaviour in Earthquake Geotechnics*. Oxford, 1 edition, 1996. ISBN 0198562241.
- Ishihara, M, Okamura, M, and Oshita, T. Desaturating sand deposit by air injection for reducing liquefaction potential. In *Pacific Conference on Earthquake Engineering*, pages paper–89, 2003.
- ISO. ISO/TS 17892–9:2004, 2004: Geotechnical Investigation and Testing - Laboratory Testing of Soil – Part 9: Consolidated Triaxial Compression Tests on Water-Saturated Soils, 2004.
- Iwasaki, T., Tatsuoka, F., Tokida, K., and Yasuda, S. A practical method for assessing soil liquefaction potential based on case studies at various sites in Japan. In *Proceedings of the 2nd international conference on microzonation*, pages 885–896, San Diego, California, USA, 1978.
- Jafarzadeh, F. and Sadeghi, H. Experimental study on dynamic properties of sand with emphasis on the degree of saturation. *Soil Dynamics and Earthquake Engineering*, 32:26–41, 2012. doi: 10.1016/j.soildyn.2011.08.003.
- Jaky, J. The coefficient of earth pressure at rest. In Hungarian "A nyugalmi nyomas tenyezoje". *Journal Society Hungarian Engineering and Architecture*, pages 355–358, 1944.

- Japanese Geotechnical Society. JGS 0161 - Test methods for minimum and maximum densities of sands, 2009.
- Jara, A., Cabrera, M., and Caicedo, B. A micro laminar box coupled with a piezoelectric shaking table for centrifuge testing. *Measurement*, under review, 2020.
- Jefferies, M. Nor-Sand: a simple critical state model for sand. *Géotechnique*, 43(1): 91–103, 1993. doi: 10.1680/geot.1993.43.1.91.
- Jefferies, M. and Been, K. Implications for critical state theory from isotropic compression of sand. *Géotechnique*, 50(4):419–429, 2000. doi: 10.1680/geot.2000.50.4.419.
- Jefferies, M. and Been, K. *Soil Liquefaction: A Critical State Approach*. CRC Press, 2 edition, 2015. ISBN 9781482213683.
- Jiang, M. D., Yang, Z. X., Barreto, D., and Xie, Y. H. The influence of particle-size distribution on critical state behavior of spherical and non-spherical particle assemblies. *Granular Matter*, 20(4):80, 2018. doi: 10.1007/s10035-018-0850-x.
- Jorge, C. *Zonation of Liquefaction Potential. Application Attempt to the Portuguese Territory*. Msc, New University of Lisbon., 1993.
- Jorge, C. and Vieira, A. M. Liquefaction potential assessment: Application to the Portuguese territory and to the town of Setubal. In Seco and Pinto, P. S., editors, *Earthquake geotechnical engineering: Seismic behaviour of ground and geotechnical structures*, page 401, Hamburg, Germany, 1997. A.A. Balkema. ISBN 9054108878.
- Kayen, R., Moss, R. E. S., Thompson, E. M., Seed, R. B., Cetin, K. O., Kiureghian, A. Der, Tanaka, Y., and Tokimatsu, K. Shear-Wave Velocity-Based Probabilistic and Deterministic Assessment of Seismic Soil Liquefaction Potential. *Journal of Geotechnical and Geoenvironmental Engineering*, 139(3):407–419, 2013. doi: 10.1061/(ASCE)GT.1943-5606.0000743.
- Khan, Z., El Naggar, M.H., and Cascante, G. Frequency dependent dynamic properties from resonant column and cyclic triaxial tests. *Journal of the Franklin Institute*, 348(7):1363–1376, 2011. doi: 10.1016/J.JFRANKLIN.2010.04.003.
- Khashila, M., Hussien, M. N., Karray, M., and Chekired, M. Use of pore pressure build-up as damage metric in computation of equivalent number of uniform strain cycles. *Canadian Geotechnical Journal*, 55(4):538–550, 2018. doi: 10.1139/cgj-2017-0231.
- Khashila, M., Hussien, M. N., Chekired, M., and Karray, M. On the Dynamic Soil Behavior under Triaxial and Simple Shear Modes. *International Journal of Geomechanics*, 21(8):04021134, 2021. doi: 10.1061/(ASCE)GM.1943-5622.0002085.

- Kim, J., Won, J., and Park, J. Effects of water saturation and distribution on small-strain stiffness. *Journal of Applied Geophysics*, 186:104278, 2021. doi: 10.1016/J.JAPPGEO.2021.104278.
- Kiyota, T., Maekawa, Y., and Wu, C. Using in-situ and laboratory-measured shear wave velocities to evaluate the influence of soil fabric on in-situ liquefaction resistance. *Soil Dynamics and Earthquake Engineering*, 117:164–173, 2019. doi: 10.1016/J.SOILDYN.2018.11.016.
- Kokusho, T. Correlation of pore-pressure B-value with P-wave velocity and Poisson's ratio for imperfectly saturated sand or gravel. *Soils and Foundations*, 40(4):95–102, 2000. ISSN 00380806. doi: 10.3208/sandf.40.4_95.
- Kokusho, T. Liquefaction potential evaluations: energy-based method versus stress-based method. *Canadian Geotechnical Journal*, 50(10):1088–1099, 2013. doi: 10.1139/cgj-2012-0456.
- Kokusho, T., Ito, F., Nagao, Y., and Green, A. R. Influence of Non/Low-Plastic Fines and Associated Aging Effects on Liquefaction Resistance. *Journal of Geotechnical and Geoenvironmental Engineering*, 138(6):747–756, 2012. doi: 10.1061/(ASCE)GT.1943-5606.0000632.
- Kramer, S. L. *Geotechnical Earthquake Engineering*. Prentice Hall, New Jersey, 1 edition, 1996. ISBN 978-0133749434.
- Kumar, J. and Madhusudhan, B. N. Dynamic properties of sand from dry to fully saturated states. *Géotechnique*, 62(1):45–54, 2012. doi: 10.1680/geot.10.P.042.
- Ladd, R. S. Specimen preparation and cyclic stability of sands. *Journal of Geotechnical and Geoenvironmental Engineering*, 103(6):535—547, 1977.
- Lai, C. G., Bozzoni, F., Conca, D., Famà, A., Özcebe, A. G., Zuccolo, E., Meisina, C., Bonì, R., Bordoni, M., Cosentini, R. M., Martelli, L., Poggi, V., Viana da Fonseca, A., Ferreira, C., Rios, S., Cordeiro, D., Ramos, C., Molina-Gómez, F., Coelho, C., Logar, J., Maček, M., Oblak, A., Ozcep, F., Bozbey, I., Oztoprak, S., Sargin, S., Aysal, N., Oser, C., and Kelesoglu, M. K. Technical guidelines for the assessment of earthquake induced liquefaction hazard at urban scale. *Bulletin of Earthquake Engineering*, pages 1–45, 2020. doi: 10.1007/s10518-020-00951-8.
- Lashkari, A., Falsafizadeh, S. R., Shourijeh, P. T., and Alipour, M. J. Instability of loose sand in constant volume direct simple shear tests in relation to particle shape. *Acta Geotechnica*, 15(9):2507–2527, 2020. doi: 10.1007/s11440-019-00909-4.
- Lee, J-S and Santamarina, J. C. Bender Elements: Performance and Signal Interpretation. *Journal of Geotechnical and Geoenvironmental Engineering*, 131(9): 1063–1070, 2005. doi: 10.1061/(ASCE)1090-0241(2005)131:9(1063).

- Lee, K.L. and Albaisa, A. Earthquake induced settlements in saturated sands. *Journal of Soil Mechanics and Foundations Division*, 100:387–406, 1974.
- Leong, E. C. and Cheng, Z. Y. Effects of Confining Pressure and Degree of Saturation on Wave Velocities of Soils. *International Journal of Geomechanics*, 16(6): D4016013, 2016. doi: 10.1061/(ASCE)GM.1943-5622.0000727.
- Li, W., Coop, M.R., Senetakis, K., and Schnaid, F. The mechanics of a silt-sized gold tailing. *Engineering Geology*, 241:97–108, 2018. doi: 10.1016/j.enggeo.2018.05.014.
- Li, X. S. Thermodynamics-based constitutive framework for unsaturated soils. 1: Theory. *Géotechnique*, 57(5):411–422, 2007. doi: 10.1680/geot.2007.57.5.411.
- Liang, Liquan. *Development of an energy method for evaluating the liquefaction potential of a soil deposit*. Phd thesis, Case Western Reserve University, 1995. URL <https://www.proquest.com/openview/3af9011b4f5260f682b802463616a5e8/1?pq-origsite=gscholar{%&}cbl=18750{%&}diss=y>.
- Lirer, S. and Mele, L. On the apparent viscosity of granular soils during liquefaction tests. *Bulletin of Earthquake Engineering*, 17(11):5809–5824, 2019. doi: 10.1007/s10518-019-00706-0.
- Liu, T., Jardine, R. J., Vinck, K., and Ackerley, S. K. Optimization of Advanced Laboratory Monotonic and Cyclic Triaxial Testing on Fine Sands. *Geotechnical Testing Journal*, 45(6):20210190, 2022. doi: 10.1520/GTJ20210190.
- Liu, X. and Yang, J. Shear wave velocity in sand: effect of grain shape. *Géotechnique*, 68(8):742–748, 2018. doi: 10.1680/jgeot.17.T.011.
- Lo Presti, D. C. F., Jamiolkowski, M., Pallara, O., Cavallaro, A., and Pedroni, S. Shear modulus and damping of soils. *Géotechnique*, 47:603–617, 1997. doi: 10.1680/geot.1997.47.3.603.
- Lunne, T., Knudsen, S., Blaker, Vestgården, T., Powell, J. J.M., Wallace, C. F., Krogh, L., Thomsen, N. V., Yetginer, G., and Ghanekar, R. K. Methods used to determine maximum and minimum dry unit weights of sand: Is there a need for a new standard? *Canadian Geotechnical Journal*, 56(4):536–553, 2019. doi: 10.1139/cgj-2017-0738.
- Madabhushi, G.S.P. *Centrifuge Modelling for Civil Engineers*. CRC Press, New York, 2014. ISBN 0203126823.
- Marasini, N.P. and Okamura, M. Air injection to mitigate liquefaction under light structures. *International Journal of Physical Modelling in Geotechnics*, 15(3): 129–140, 2015. doi: 10.1680/jphmg.14.00005.

- Marulanda, C., Culligan, P. J., and Germaine, J. T. Centrifuge modeling of air sparging — a study of air flow through saturated porous media. *Journal of Hazardous Materials*, 72:179–215, 2 2000. doi: 10.1016/S0304-3894(99)00140-5.
- Mele, L. and Flora, A. On the prediction of liquefaction resistance of unsaturated sands. *Soil Dynamics and Earthquake Engineering*, 125:105689, 2019. doi: 10.1016/j.soildyn.2019.05.028.
- Mele, L., Tian, J. Tan, Lirer, S., Flora, A., and Koseki, J. Liquefaction resistance of unsaturated sands: Experimental evidence and theoretical interpretation. *Géotechnique*, 69(6):541–553, 2019. doi: 10.1680/jgeot.18.P.042.
- Mele, L., Chiaradonna, A., Lirer, S., and Flora, A. A robust empirical model to estimate earthquake-induced excess pore water pressure in saturated and non-saturated soils. *Bulletin of Earthquake Engineering*, pages 1–29, 2020. ISSN 15731456. doi: 10.1007/s10518-020-00970-5.
- Mele, L., Lirer, S., and Flora, A. An Energetic Interpretation of Liquefaction Laboratory Tests on Partially Saturated Soils. *Journal of Geotechnical and Geoenvironmental Engineering*, 148(10), 2022. doi: 10.1061/(ASCE)GT.1943-5606.0002881.
- Meslem, A., Iversen, H., Kaschwich, T., Iranpour, K., and Drange, L. S. LIQUEFACT Software — Technical Manual and Application. Technical report, Derivable D6.6 of the European H2020 LIQUEFACT Research Project, 2019. URL <http://www.liquefact.eu/wp-content/uploads/2020/03/D6.6.pdf>.
- Mesri, G and Vardhanabhuti, B. Compression of granular materials. *Canadian Geotechnical Journal*, 46(4):369–392, 2009. doi: 10.1139/T08-123.
- Millen, M., Rios, S., Quintero, J., and Viana da Fonseca, A. Prediction of time of liquefaction using kinetic and strain energy. *Soil Dynamics and Earthquake Engineering*, 128:105898, 2020. doi: 10.1016/j.soildyn.2019.105898.
- Millen, M., Viana da Fonseca, A., Quintero, J., Ferreira, C., Oztoprak, S., Oser, C., Bozbey, I., Aysal, N., Kosič, M., and Logar, J. Site classification using equivalent soil profiles for building-liquefaction interaction. *Bulletin of Earthquake Engineering*, 19(10):3987–4012, 2021. doi: 10.1007/s10518-020-00967-0.
- Miranda, L., Caldeira, L., Serra, J., and Carrilho Gomes, R. Dynamic behaviour of Tagus River sand including liquefaction. *Bulletin of Earthquake Engineering*, pages 1–30, 2020. doi: 10.1007/s10518-020-00881-5.
- Mirshekari, M. and Ghayoomi, M. Centrifuge tests to assess seismic site response of partially saturated sand layers. *Soil Dynamics and Earthquake Engineering*, 94: 254–265, 2017. doi: 10.1016/j.soildyn.2017.01.024.
- Molina-Gómez, F., Caicedo, B., and Viana da Fonseca, A. Physical modelling of

- soil liquefaction in a novel micro shaking table. *Geomechanics and Engineering*, 19(3):229–240, 2019. doi: 10.12989/gae.2019.19.3.229.
- Monaco, Paola, de Magistris, Filippo Santucci, Grasso, Salvatore, Marchetti, Silvano, Maugeri, Michele, and Totani, Gianfranco. Analysis of the liquefaction phenomena in the village of Vittorito (L’Aquila). *Bulletin of Earthquake Engineering*, 9(1):231–261, 2011. doi: 10.1007/s10518-010-9228-0.
- Moss, R. E., Seed, R. B., Kayen, R. E., Stewart, J. P., Der Kiureghian, A., and Cetin, K. O. CPT-Based Probabilistic and Deterministic Assessment of In Situ Seismic Soil Liquefaction Potential. *Journal of Geotechnical and Geoenvironmental Engineering*, 132(8):1032–1051, 2006. doi: 10.1061/(ASCE)1090-0241(2006)132:8(1032).
- Mousavi, S. and Ghayoomi, M. Seismic Compression of Unsaturated Silty Sands: A Strain-Based Approach. *Journal of Geotechnical and Geoenvironmental Engineering*, 147(5):04021023, 2021. doi: 10.1061/(ASCE)GT.1943-5606.0002507.
- Mousavi, S., Ghayoomi, M., and Jones, S. H. Compositional and geoenvironmental factors in microbially induced partial saturation. *Environmental Geotechnics*, 8(4):282–294, 2021. doi: 10.1680/jenge.18.00087.
- Murillo, C., Thorel, L., and Caicedo, B. Spectral analysis of surface waves method to assess shear wave velocity within centrifuge models. *Journal of Applied Geophysics*, 68:135–145, 2009. doi: 10.1016/J.JAPPGEO.2008.10.007.
- Murthy, T. G., Loukidis, D., Carraro, J. A.H., Prezzi, M., and Salgado, R. Undrained monotonic response of clean and silty sands. *Géotechnique*, 57(3):273–288, 2007. doi: 10.1680/geot.2007.57.3.273.
- Naesgaard, E., Byrne, P. M., and Wijewickreme, D. Is P-Wave Velocity an Indicator of Saturation in Sand with Viscous Pore Fluid? *International Journal of Geomechanics*, 7(6):437–443, 2007. doi: 10.1061/(asce)1532-3641(2007)7:6(437).
- Nakagawa, K., Soga, K., and Mitchell, J. K. Observation of Biot compressional wave of the second kind in granular soils. *Géotechnique*, 47(1):133–147, 1997. doi: 10.1680/geot.1997.47.1.133.
- Nakazawa, H., Ishihara, K., Tsukamoto, Y., and Kamata, T. Case studies on evaluation of liquefaction resistance of imperfectly saturated soil deposits. In Triantafyllidis, T., editor, *Cyclic Behaviour of Soils and Liquefaction Phenomena: Proceedings of the international conference on cyclic behaviour of soils and liquefaction phenomena*, pages 295–304, Bochum, Germany, 2004.
- NASEM. *State of the Art and Practice in the Assessment of Earthquake-Induced Soil Liquefaction and Its Consequences*. National Academies of Sciences, Engineering, and Medicine, Washington, DC, 2016. ISBN 978-0-309-44027-1. doi: 10.17226/

23474.

- Nateghi, A. and Shamy, U. El. Numerical modeling of the effect of desaturation on liquefaction hazard mitigation. *Geosciences*, 13:15, 12 2022. ISSN 2076-3263. doi: 10.3390/geosciences13010015.
- Nemat-Nasser, S. and Shokoh, A. A unified approach to densification and liquefaction of cohesionless sand in cyclic shearing. *Canadian Geotechnical Journal*, 16 (4):659–678, 1979. doi: 10.1139/t79-076.
- Nguyen, H.B.K., Rahman, M., and Fourie, A. How particle shape affects the critical state, triggering of instability and dilatancy of granular materials – results from a DEM study. *Géotechnique*, pages 1–16, 2020. doi: 10.1680/jgeot.18.p.211.
- Nong, Z. Z., Park, S. S., and Lee, D. E. Comparison of sand liquefaction in cyclic triaxial and simple shear tests. *Soils and Foundations*, 61(4):1071–1085, 2021. doi: 10.1016/J.SANDF.2021.05.002.
- Nova, R. A constitutive model for soil under monotonic and cyclic loading. In Pande, GN and Zienkiewicz, OC, editors, *Soil Mechanics – Transient and Cyclic Loads*, pages 343–373, Chichester, UK, 1982. Wiley.
- Okamura, M. and Soga, Y. Effects of pore fluid compressibility on liquefaction resistance of partially saturated sand. *Soils and Foundations*, 46(5):695–700, 2006. doi: 10.3208/sandf.46.695.
- Okamura, M., Takebayashi, M., Nishida, K., Fujii, N., Jinguji, M., Imasato, T., Yasuhara, H., and Nakagawa, E. In-Situ Desaturation Test by Air Injection and Its Evaluation through Field Monitoring and Multiphase Flow Simulation. *Journal of Geotechnical and Geoenvironmental Engineering*, 137(7):643–652, 2011. doi: 10.1061/(ASCE)GT.1943-5606.0000483.
- Olarte, J., Paramasivam, B., Dashti, S., Liel, A., and Zannin, J. Centrifuge modeling of mitigation-soil-foundation-structure interaction on liquefiable ground. *Soil Dynamics and Earthquake Engineering*, 97:304–323, 2017. doi: 10.1016/J.SOILDYN.2017.03.014.
- Oliveira, C. S. Review of the 1755 Lisbon Earthquake Based on Recent Analyses of Historical Observations. In Fréchet, J., Meghraoui, M., and Stucchi, M., editors, *Historical Seismology: Interdisciplinary Studies of Past and Recent Earthquakes*, pages 261–300. Springer, 2008. doi: 10.1007/978-1-4020-8222-1_13.
- Oztoprak, S. and Bolton, M.D. Stiffness of sands through a laboratory test database. *Géotechnique*, 63(1):54–70, 2013. doi: 10.1680/geot.10.P.078.
- Park, J. and Santamarina, J.C. Revised Soil Classification System for Coarse-Fine Mixtures. *Journal of Geotechnical and Geoenvironmental Engineering*, 143(8):

- 04017039, 2017. ISSN 1090-0241. doi: 10.1061/(ASCE)GT.1943-5606.0001705.
- Park, S-S. and Kim, Y-S. Liquefaction Resistance of Sands Containing Plastic Fines with Different Plasticity. *Journal of Geotechnical and Geoenvironmental Engineering*, 139(5):825–830, 2013. doi: 10.1061/(ASCE)GT.1943-5606.0000806.
- Park, T., Park, D., and Ahn, J. K. Pore pressure model based on accumulated stress. *Bulletin of Earthquake Engineering*, 13(7):1913–1926, 2015. doi: 10.1007/s10518-014-9702-1.
- Pestana, J. M. and Whittle, A. J. Compression model for cohesionless soils. *Géotechnique*, 45(4):611–631, 1995. doi: 10.1680/geot.1995.45.4.611.
- Pietruszczak, S. and Pande, G. N. Constitutive Relations for Partially Saturated Soils Containing Gas Inclusions. *Journal of Geotechnical Engineering*, 122(1): 50–59, 1996. doi: 10.1061/(ASCE)0733-9410(1996)122:1(50).
- Pietruszczak, S., Pande, G. N., and Oulapour, M. A hypothesis for mitigation of risk of liquefaction. *Géotechnique*, 53(9):833–838, 2003. doi: 10.1680/GEOT.2003.53.9.833.
- Polito, C., Green, R. A., Dillon, E., and Sohn, C. Effect of load shape on relationship between dissipated energy and residual excess pore pressure generation in cyclic triaxial tests. *Canadian Geotechnical Journal*, 50(11):1118–1128, 2013. doi: 10.1139/cgj-2012-0379.
- Polito, C.P., Green, R.A., and Lee, J. Pore Pressure Generation Models for Sands and Silty Soils Subjected to Cyclic Loading. *Journal of Geotechnical and Geoenvironmental Engineering*, 134(10):1490–1500, 2008. doi: 10.1061/(asce)1090-0241(2008)134:10(1490).
- Porcino, D. and Tomasello, G. Shear wave velocity-based evaluation of liquefaction resistance for calcareous sands of different origin. *Soil Dynamics and Earthquake Engineering*, 122:235–247, 2019. doi: 10.1016/j.soildyn.2019.03.019.
- Porcino, D., Triantafyllidis, T., Wichtmann, T., and Tomasello, G. Application of critical state approach to liquefaction resistance of sand-silt mixtures under cyclic simple shear loading. *Journal of Geotechnical and Geoenvironmental Engineering*, 147(3):04020177, 2021. doi: 10.1061/(ASCE)GT.1943-5606.0002470.
- Qadimi, A. and Coop, M. R. The undrained cyclic behaviour of a carbonate sand. *Géotechnique*, 57(9):739–750, 2007. doi: 10.1680/geot.2007.57.9.739.
- Quintero, J., Gomes, R. C., Rios, S., Ferreira, C., and Viana da Fonseca, A. Liquefaction assessment based on numerical simulations and simplified methods: A deep soil deposit case study in the Greater Lisbon. *Soil Dynamics and Earthquake Engineering*, 169:107866, 2023. doi: 10.1016/j.soildyn.2023.107866.

- Rahman, M. M., Nguyen, H. B. K., Fourie, A. B., and Kuhn, M. R. Critical state soil mechanics for cyclic liquefaction and postliquefaction behavior: Dem study. *Journal of Geotechnical and Geoenvironmental Engineering*, 147(2):04020166, 2021. doi: 10.1061/(ASCE)GT.1943-5606.0002453.
- Ramos, C. *Cyclic liquefaction susceptibility of soils from field and laboratory tests – Methodologies and critical analyses*. Phd thesis, Universidade do Porto, 2021.
- Ramos, C., Ferreira, C., Molina-Gómez, F., and Viana da Fonseca, A. Critical State Lines of Portuguese liquefiable sands. *E3S Web of Conferences*, 92:06003, 2019. doi: 10.1051/e3sconf/20199206003.
- Rayhani, M. H.T. and El Naggar, M. H. Seismic response of sands in centrifuge tests. *Canadian Geotechnical Journal*, 45(4):470–483, 2008. doi: 10.1139/T07-097.
- Rebata-Landa, V. and Santamarina, J. C. Mechanical Effects of Biogenic Nitrogen Gas Bubbles in Soils. *Journal of Geotechnical and Geoenvironmental Engineering*, 138(2):128–137, 2012. doi: 10.1061/(ASCE)GT.1943-5606.0000571.
- Reid, D., Fourie, A., Ayala, J. L., Dickinson, S., Ochoa-Cornejo, F., Fanni, R., Garfias, J., Viana da Fonseca, A., Ghafghazi, M., Ovalle, C., Riemer, M., Rismanchian, A., Olivera, R., and Suazo, G. Results of a critical state line testing round robin programme. *Géotechnique*, 71(7):616–630, 2021. doi: 10.1680/jgeot.19.p.373.
- Rio, J. F. *Advances in laboratory geophysics using bender elements*. Ph.d thesis, University College of London, 2006.
- Rios, S., Millen, M., Quintero, J., and Viana da Fonseca, A. Analysis of simplified time of liquefaction triggering methods by laboratory tests, physical modelling and numerical analysis. *Soil Dynamics and Earthquake Engineering*, 157:107261, 2022. doi: 10.1016/j.soildyn.2022.107261.
- Robertson, P.K. Soil classification using the cone penetration test. *Canadian Geotechnical Journal*, 27(1):151–158, 1990. doi: 10.1139/t90-014.
- Robertson, P.K. Interpretation of cone penetration tests - a unified approach. *Canadian geotechnical journal*, 46(11):1337–1355, 2009. doi: 10.1139/T09-065.
- Robertson, P.K., Viana da Fonseca, A., Ulrich, B., and Coffin, J. Characterization of unsaturated mine waste: a case history. *Canadian Geotechnical Journal*, 54(12):1752–1761, 2017. doi: 10.1139/cgj-2017-0129.
- Rollins, K.M., Evans, M.D., and N.B., Diehl. Shear Modulus and Damping Relationships for Gravels. *Journal of Geotechnical and Geoenvironmental Engineering*, 124(5):396—405, 1998. doi: 10.1061/(ASCE)1090-0241(1998)124:5(396).

- Salgado, F. Siting-Downtown Lisbon Metro blue line. In *Lecture. MERCEA08, Seismic Engineering International Conference commemorating the 1908 Messina and Reggio Calabria Earthquake*, Calabria, Italy, 2009.
- Salgado, F. Liquefaction - Causes and effects. In Silvestri, F and Moraci, N, editors, *Earthquake Geotechnical Engineering for Protection and Development of Environment and Constructions*, pages 415–422, Rome, Italy, 2019. CRC Press/Balkema.
- Salvatore, E., Modoni, G., Mascolo, M. C., Grassi, D., and Spagnoli, G. Experimental Evidence of the Effectiveness and Applicability of Colloidal Nanosilica Grouting for Liquefaction Mitigation. *Journal of Geotechnical and Geoenvironmental Engineering*, 146(10):04020108, 2020. doi: 10.1061/(ASCE)GT.1943-5606.0002346.
- Santamarina, J. C., Klein, K. A., and Fam, M.A. *Soils and waves*. John Wiley & Sons, 2001. ISBN 9780471490586.
- Santamarina, J. Carlos and Cho, G.C. Soil behaviour: The role of particle shape. In Jardine, R. J., Potts, D. M., and Higgins, K. G., editors, *Advances in geotechnical engineering: The Skempton conference*, volume 1, pages 604–617. Thomas Telford, London, 2004. ISBN 978-0727732644. doi: 10.1680/AIGEV1.32644.0035.
- Santamarina, J. Carlos, Rinaldi, Victor A., Fratta, Dante, Klein, Katherine A., Wang, Yu-Hsing, Cho, Gye Chun, and Cascante, Giovanni. A Survey of Elastic and Electromagnetic Properties of Near-Surface Soils. In Butler, Dwain K., editor, *Near-Surface Geophysics*, pages 71–87. Society of Exploration Geophysicists, 2005. doi: 10.1190/1.9781560801719.ch4.
- Santos, J. A. *Soil characterization by dynamic and cyclic torsional shear test. Application to study of piles under static and dynamic horizontal loading*. Phd thesis, Instituto Superior Técnico da Universidade Técnica de Lisboa, 1999.
- Santos, J. A. and Gomes Correia, A. Reference threshold shear strain of soil. Its application to obtain an unique strain-dependent shear modulus curve for soil. In *Proceedings of the 15th International Conference on Soil Mechanics and Geotechnical Engineering*, Istanbul, Turkey, 2001.
- Sarkar, D., Goudarzy, M., König, D., and Wichtmann, T. Influence of particle shape and size on the threshold fines content and the limit index void ratios of sands containing non-plastic fines. *Soils and Foundations*, 60(3):621–633, 2020. doi: 10.1016/j.sandf.2020.02.006.
- Sawada, S., Tsukamoto, Y., and Ishihara, K. Residual deformation characteristics of partially saturated sandy soils subjected to seismic excitation. *Soil Dynamics and Earthquake Engineering*, 26:175–182, 2006. doi: 10.1016/j.soildyn.2004.11.024.
- Seed, H.B. and Idriss, I.M. Simplified procedure for evaluating soil liquefaction

- potential. *Journal of the Soil Mechanics and Foundations Division*, 97(9):1249–1273, 1971.
- Seed, H.B., Martin, P.P., and Lysmer, J. The generation and dissipation of pore water pressures during soil liquefaction. Technical report, Earthquake Engineering Center, University of California, Berkeley, CA, 1975.
- Senetakis, K., Anastasiadis, A., K., Pitilakis, and Coop, M.R. The Small-Strain Shear Modulus and Damping Ratio of Quartz and Volcanic Sands. *Soil Dynamics and Earthquake Engineering*, 45:70–79, 2013. doi: 10.1016/j.soildyn.2012.11.009.
- Seyedi-Viand, S. M. and Eseller-Bayat, E. E. Partial Saturation as a Liquefaction Countermeasure: A Review. *Geotechnical and Geological Engineering 2021*, pages 1–32, 2021. doi: 10.1007/S10706-021-01926-5.
- Sherif, M. A., Tsuchiya, C., and Ishibashi, I. Saturation effect on initial soil liquefaction. *Journal of the Geotechnical Engineering Division*, 103(8):914–917, 1977.
- Silva, J., Azenha, M., Gomes Correia, A., and Ferreira, C. Continuous stiffness assessment of cement-stabilised soils from early age. *Geotechnique*, 63: 1419–1432, 2013. doi: 10.1680/GEOT.13.P.021/ASSET/IMAGES/SMALL/GEOT63-1419-F16.GIF.
- Skempton, A. W. The Pore-Pressure Coefficients A and B. *Géotechnique*, 4(4): 143–147, 1954. doi: 10.1680/geot.1954.4.4.143.
- Soares, M. *Evaluation of soil liquefaction potential based on laboratory data Major factors and limit boundaries*. Phd thesis, Universidade do Porto, 2015. URL <http://hdl.handle.net/10216/78425>.
- Soares, M and Viana da Fonseca, A. Factors Affecting Steady State Locus in Triaxial Tests. *Geotechnical Testing Journal*, 39(6):20150228, 2016. ISSN 01496115. doi: 10.1520/GTJ20150228.
- Soriano Camelo, C. Y., de Almeida, M. C. F., de Almeida, M. de S. S., Madabhushi, G. S. P., and Stanier, S. Centrifuge Modeling of the Seismic Behavior of Soft Clay Slopes. *Journal of Geotechnical and Geoenvironmental Engineering*, 148 (11), 2022. doi: 10.1061/(ASCE)GT.1943-5606.0002884.
- Tamura, S., Tokimatsu, K., Abe, A., and Sato, M. Effects of air bubbles on B-value and P-wave velocity of a partly saturated sand. *Soils and Foundations*, 42(1): 121–129, 2002. doi: 10.3208/sandf.42.121.
- Tatsuoka, F., Ochi, K., Fujii, S., and Okamoto, M. Cyclic undrained triaxial and torsional shear strength of sands for different sample preparation methods. *Soils and Foundations*, 26(3):23–41, 1986. ISSN 0385-1621. doi: 10.3208/sandf1972.26.3_23.

- Taylor, R. N. *Geotechnical Centrifuge Technology*. CRC Press, 1995. ISBN 0203210530.
- Teves-Costa, P. and Batlló, J. The 23 April 1909 Benavente earthquake (Portugal): macroseismic field revision. *Journal of Seismology*, 15(1):59–70, 2011. doi: 10.1007/s10950-010-9207-6.
- Teves-Costa, P., Almeida, I. M., and Silva, P. L. Microzonation of Lisbon: 1-D theoretical approach. *Pure and Applied Geophysics*, 158(12):2579–2596, 2001. doi: 10.1007/pl00001187.
- Tonkin & Taylor. Canterbury earthquakes 2010 and 2011. Land report as at 29 February 2012. Technical report, Tonkin & Taylor Ltd, 2013.
- Torres-Cruz, L.A. and Santamarina, J.C. The critical state line of non-plastic tailings. *Canadian Geotechnical Journal*, 57:1508–1517, 2020. doi: 10.1139/cgj-2019-0019.
- Towhata, I. Features of liquefaction-induced damages. *Springer Series in Geomechanics and Geoengineering*, 1:343–368, 2008. ISSN 18668755. doi: 10.1007/978-3-540-35783-4_17.
- Towhata, I. Liquefaction Mitigation Measures: A Historical Review. In Sitharam, T. G., Jakka, Ravi, and Kolathayar, Sreevalsa, editors, *Latest Developments in Geotechnical Earthquake Engineering and Soil Dynamics*, pages 41–86. Springer, 2021. doi: 10.1007/978-981-16-1468-2_3.
- Tsuchida, H. Prediction and countermeasure against the liquefaction in sand deposits. *Abstract of the Seminar in the Port and Harbor Research Institute*, pages 31–333, 1970. URL <http://ci.nii.ac.jp/naid/10007805219/en/>.
- Tsukamoto, Y. Degree of saturation affecting liquefaction resistance and undrained shear strength of silty sands. *Soil Dynamics and Earthquake Engineering*, 124: 365–373, 2019. doi: 10.1016/J.SOILDYN.2018.04.041.
- Tsukamoto, Y., Ishihara, K., Nakazawa, H., Kamada, K., and Huang, Y. Resistance of partly saturated sand to liquefaction with reference to longitudinal and shear wave velocities. *Soils and Foundations*, 42(6):93–104, 2002. doi: 10.3208/sandf.42.6_93.
- Tsukamoto, Y., Kawabe, S., Matsumoto, J., and Hagiwara, S. Cyclic resistance of two unsaturated silty sands against soil liquefaction. *Soils and Foundations*, 54(6):1094–1103, 2014. doi: 10.1016/J.SANDF.2014.11.005.
- Turan, A., Hinchberger, S. D., and El Naggar, M. H. Design and commissioning of a laminar soil container for use on small shaking tables. *Soil Dynamics and Earthquake Engineering*, 29(2):404–414, 2009. doi: 10.1016/j.soildyn.2008.04.003.

- Unno, T., Kazama, M., Uzuoka, R., and Sentos, N. Liquefaction of Unsaturated Sand Considering the Pore Air Pressure and Volume Compressibility of the Soil Particle Skeleton. *Soils and Foundations*, 48(1):87–99, 2008. doi: 10.3208/SANDF.48.87.
- Valle-Molina, C. and Stokoe, K.H. Seismic measurements in sand specimens with varying degrees of saturation using piezoelectric transducers. *Canadian Geotechnical Journal*, 49(6):671–685, 2012. doi: 10.1139/t2012-033.
- Vardanega, P.J. and Bolton, M.D. Stiffness of clays and silts: Normalizing shear modulus and shear strain. *Journal of Geotechnical and Geoenvironmental Engineering*, 139(9):1575–89, 2013. doi: 10.1061/(ASCE)GT.1943-5606.0000887.
- Verdugo, R. and Ishihara, K. The Steady State of Sandy Soils. *Soils and Foundations*, 36(2):81–91, 1996. doi: 10.3208/sandf.36.2_81.
- Viana da Fonseca, A., Ferreira, C., and Fahey, M. A Framework Interpreting Bender Element Tests, Combining Time-Domain and Frequency-Domain Methods. *Geotechnical Testing Journal*, 32(2):100974, 2009. doi: 10.1520/GTJ100974.
- Viana da Fonseca, A., Soares, M., and Fourie, A.B. Cyclic DSS tests for the evaluation of stress densification effects in liquefaction assessment. *Soil Dynamics and Earthquake Engineering*, 75:98–111, 2015. doi: 10.1016/J.SOILDYN.2015.03.016.
- Viana da Fonseca, A., Millen, M., Gómez, F., Romão, X., Quintero, J., Molina-Gómez, F., Costa, P., Rios, S., Kosič, M., Dolšek, M., Logar, J., Oztoprak, S., Bozbey, I., Kelesoglu, K., Ozcep, F., Flora, A., Rasulo, A., Modoni, G., and Croce, P. State of the art review of numerical modelling strategies to simulate liquefaction-induced structural damage and of uncertain/random factors on the behaviour of liquefiable soils. Technical report, LIQUEFACT Deliverable D3.1, 2017. URL <http://www.liquefact.eu/wp-content/uploads/2018/12/D3.1-State-of-the-art-review-of-numerical-modelling-strategies-...pdf>.
- Viana da Fonseca, A., Ferreira, C., Coelho, C., Quintero, J., Rios, S., Millen, M., and Cordeiro, D. D2.7—Part 2: Methodology for assessment of earthquake-induced risk liquefaction at the four European testing sites (microzonification). Technical report, Derivelable D2.7 of the European H2020 LIQUEFACT Research Project, 2019. URL <http://www.liquefact.eu/wp-content/uploads/2020/03/D2.7{ }ter.pdf>.
- Viana da Fonseca, A., Cordeiro, D., and Molina-Gómez, F. Recommended Procedures to Assess Critical State Locus from Triaxial Tests in Cohesionless Remoulded Samples. *Geotechnics*, 1(1):95–127, 2021. doi: 10.3390/GEOTECHNICS1010006.

- Vieira Faria, N., Viana da Fonseca, A., and Ferreira, C. Proceso de saturación de ensayos triaxiales. *Geotecnia*, 104:31–42, 2006.
- Viggiani, G. and Atkinson, J. H. Interpretation of bender element tests. *Géotechnique*, 45(1):149–154, 1995. doi: 10.1680/geot.1997.47.4.873.
- Villamor, P., Almond, P., Tuttle, M. P., Giona-Bucci, M., Langridge, R. M., Clark, K., Ries, W., Bastin, S. H., Eger, A., Vandergoes, M., Quigley, M. C., Barker, P., Martin, F., and Howarth, J. Liquefaction features produced by the 2010–2011 Canterbury earthquake sequence in southwest Christchurch, New Zealand, and preliminary assessment of Paleoliquefaction features. *Bulletin of the Seismological Society of America*, 106(4):1747–1771, 2016. ISSN 19433573. doi: 10.1785/0120150223.
- Vucetic, M. Cyclic threshold shear strains in soils. *Journal of Geotechnical Engineering*, 120:2208–2228, 1994. doi: 10.1061/(ASCE)0733-9410(1994)120:12(2208).
- Wang, H., Koseki, J., Sato, T., Chiaro, G., and Tan Tian, J. Effect of saturation on liquefaction resistance of iron ore fines and two sandy soils. *Soils and Foundations*, 56(4):732–744, 2016. doi: 10.1016/J.SANDF.2016.07.013.
- Wang, K., Chu, J., Wu, S., and He, J. Stress–strain behaviour of bio-desaturated sand under undrained monotonic and cyclic loading. *Géotechnique*, 71(6):521–533, 2020. doi: 10.1680/JGEOT.19.P.080.
- Wei, L.M. and Yang, J. On the role of grain shape in static liquefaction of sand–fines mixtures. *Géotechnique*, 64(9):740–745, 2014. doi: 10.1680/geot.14.T.013.
- Winter, M. J., Hyodo, M., Wu, Y., Yoshimoto, N., Hasan, M. B., and Matsui, K. Influences of particle characteristic and compaction degree on the shear response of clinker ash. *Engineering Geology*, 230:32–45, 2017. doi: 10.1016/j.enggeo.2017.09.019.
- Xiao, Y., Long, L., Matthew Evans, T., Zhou, H., Liu, H., and Stuedlein, A. W. Effect of Particle Shape on Stress-Dilatancy Responses of Medium-Dense Sands. *Journal of Geotechnical and Geoenvironmental Engineering*, 145(2):04018105, 2019. doi: 10.1061/(asce)gt.1943-5606.0001994.
- Yamashita, S., Kawaguchi, T., Nakata, Y., Mikamt, T., Fujiwara, T., and Shibuya, S. Liquefaction resistance of sand in relation to P-wave velocity. *Soils and Foundations*, 49(4):631–650, 2009. doi: 10.3208/sandf.49.631.
- Yang, J. Liquefaction resistance of sand in relation to P-wave velocity. *Géotechnique*, 52(4):295–298, 2002. doi: 10.1680/geot.2002.52.4.295.
- Yang, J. Frequency-Dependent Amplification of Unsaturated Surface Soil Layer. *Journal of Geotechnical and Geoenvironmental Engineering*, 132(4):526–531, 2006.

- ISSN 1090-0241. doi: 10.1061/(ASCE)1090-0241(2006)132:4(526).
- Yang, J. and Luo, X.D. Exploring the relationship between critical state and particle shape for granular materials. *Journal of the Mechanics and Physics of Solids*, 84: 196–213, 2015. doi: 10.1016/j.jmps.2015.08.001.
- Yang, J. and Sato, T. Analytical study of saturation effects on seismic vertical amplification of a soil layer. *Géotechnique*, 51(2):161–165, 2001. doi: 10.1680/geot.2001.51.2.161.
- Yang, J. and Wei, L.M. Collapse of loose sand with the addition of fines: the role of particle shape. *Géotechnique*, 62(12):1111–1125, 2012. doi: 10.1680/geot.11.P.062.
- Yang, J., Savidis, S., and Roemer, M. Evaluating Liquefaction Strength of Partially Saturated Sand. *Journal of Geotechnical and Geoenvironmental Engineering*, 130(9):975–979, 2004. doi: 10.1061/(ASCE)1090-0241(2004)130:9(975).
- Yasuda, S., Towhata, I., Ishii, I., Sato, S., and Uchimura, T. Liquefaction-induced damage to structures during the 2011 great east japan earthquake. *Journal of JSCE*, 1(1):181–193, 2013. doi: 10.2208/journalofjsce.1.1_181.
- Yegian, M. K., Eseller-Bayat, E., Alshawabkeh, A., and Ali, S. Induced-Partial Saturation for Liquefaction Mitigation: Experimental Investigation. *Journal of Geotechnical and Geoenvironmental Engineering*, 133(4):372–380, 2007. doi: 10.1061/(ASCE)1090-0241(2007)133:4(372).
- Yoshimi, Y. and Kuwabara, F. Effect of Subsurface Liquefaction on the Strength of Surface Soil. *Soils and Foundations*, 13(2):67–81, 1973. doi: 10.3208/sandf1972.13.2_67.
- Yoshimi, Y. and Tokimatsu, K. Settlement of buildings on saturated sand during earthquakes. *Soils and Foundations*, 17(1):23–38, 1977. doi: 10.3208/sandf1972.17.23.
- Yoshimi, Y., Tanaka, K., and Tokimatsu, K. Liquefaction resistance of a partially saturated sand. *Soils and Foundations*, 29(3):157–162, 1989. doi: 10.3208/sandf1972.29.3_157.
- Zeghal, M. and Elgamal, A.-W. Analysis of Site Liquefaction Using Earthquake Records. *Journal of Geotechnical Engineering*, 120(6):996–1017, 1994. doi: 10.1061/(ASCE)0733-9410(1994)120:6(996).
- Zeybek, A. Suggested Method of Specimen Preparation for Triaxial Tests on Partially Saturated Sand. *Geotechnical Testing Journal*, 45(2):20210168, 2022. doi: 10.1520/GTJ20210168.
- Zeybek, A. and Madabhushi, G.S.P. Physical modelling of air injection to remediate

- liquefaction. *International Journal of Physical Modelling in Geotechnics*, 18(2): 68–80, 2018. doi: 10.1680/jphmg.16.00049.
- Zeybek, A. and Madabhushi, G.S.P. Closure to “Simplified Procedure for Prediction of Earthquake-Induced Settlements in Partially Saturated Soils” by Abdülhakim Zeybek and Santana Phani Gopal Madabhushi. *Journal of Geotechnical and Geoenvironmental Engineering*, 147(1):07020027, 2020. doi: 10.1061/(ASCE)GT.1943-5606.0002437.
- Zeybek, A. and Madabhushi, S.P.G. Centrifuge testing to evaluate the liquefaction response of air-injected partially saturated soils beneath shallow foundations. *Bulletin of Earthquake Engineering*, 15(1):339–356, 2017. doi: 10.1007/s10518-016-9968-6.
- Zhang, B., Muraleetharan, K. K., and Liu, C. Liquefaction of Unsaturated Sands. *International Journal of Geomechanics*, 16(6), 2016. ISSN 1532-3641. doi: 10.1061/(ASCE)GM.1943-5622.0000605.
- Zhang, N., Liu, X., and Lan, H. Characterizing saturation state of loess using P-wave velocity. *Engineering Geology*, 290:106207, 2021. doi: 10.1016/J.ENGGEOL.2021.106207.
- Zhang, Z., Chen, Y., Liu, H., Zhou, Y., and Zhou, X. Resistivity characteristics during horizontal-layered electrolysis desaturation of calcareous sand. *Engineering Geology*, 279:105899, 2020. ISSN 00137952. doi: 10.1016/j.enggeo.2020.105899.
- Zheng, J. and Hryciw, R. D. Index Void Ratios of Sands from Their Intrinsic Properties. *Journal of Geotechnical and Geoenvironmental Engineering*, 142(12): 06016019, 2016. doi: 10.1061/(asce)gt.1943-5606.0001575.
- Zheng, J and Hryciw, RD. Traditional soil particle sphericity, roundness and surface roughness by computational geometry. *Géotechnique*, 65(6):494–506, 2015. doi: 10.1680=geot.14.P.192.
- Zheng, J., Hryciw, R.D., and Ventola, A. Compressibility of Sands of Various Geologic Origins at Pre-crushing Stress Levels. *Geotechnical and Geological Engineering*, 35(5):2037–2051, 2017. doi: 10.1007/s10706-017-0225-9.
- Zhou, Y-G. and Chen, Y-M. Laboratory Investigation on Assessing Liquefaction Resistance of Sandy Soils by Shear Wave Velocity. *Journal of Geotechnical and Geoenvironmental Engineering*, 133(8):959–972, 2007. doi: 10.1061/(ASCE)1090-0241(2007)133:8(959).